SLAC-R-968
June 2011

# Papers from U.S. Department of Energy

# Science Undergraduate Laboratory Internship Program (SULI 2010)

*SLAC National Accelerator Laboratory, Stanford University, Menlo Park, CA 94025*

---

Work supported by Department of Energy contract DE-AC02-76SF00515.

# Solvation Sphere of $I^-$ and $Br^-$ in Water

Matthew D. Antalek

Office of Science, Science Undergraduate Laboratory Internship (SULI)

Stanford Synchrotron Radiation Lightsource

Stanford, CA

August 20, 2010

Prepared in partial fulfillment of the requirements of the Office of Science, Department of Energy's Science Undergraduate Laboratory Internship under the direction of Ritimukta Sarangi at the Structural Molecular Group, Stanford Synchrotron Radiation Lightsource.

Participant: _____

Signature

Research Advisor: _____

Signature

Work supported in part by US Department of Energy contract DE-AC02-76SF00515.

# TABLE OF CONTENTS

# ABSTRACT

Solvation Sphere of $I^-$ and $Br^-$ in Water. MATTHEW D. ANTALEK (
, Binghamton, NY 13902) RITIMUKTA SARANGI (Structural Molecular Group, Stanford Synchrotron Radiation Lightsource, Stanford, CA 94025)

The solvation sphere of halides in water has been investigated using a combination of extended x-ray absorption fine structure (EXAFS) and x-ray absorption near-edge structure (XANES) analysis techniques. The results have indicated that $I^-$ and $Br^-$ both have an asymmetric, 8 water molecule primary solvation spheres. These spheres are identical, with the $Br^-$ sphere about .3 Å smaller than the $I^-$ sphere. This study utilized near-edge analysis to supplement EXAFS analysis which suffers from signal dampening/broadening due to thermal noise.

# 1.0 INTRODUCTION

Halide ions are of fundamental importance to many chemical and biological systems. They play essential roles in protein activation/deactivation, determination of acid-base equilibria, ion transport across cell membranes, and electrolytic and osmological balance found in all organisms [1]. For these reasons it is central to biology and biochemistry to understand the solvation of halide ions in water. In particular knowledge of the the number and coordination geometry of the water molecules around the halide ions will help shed light on their roles in biological systems. The solvation sphere of $I^-$ and $B^-$ have been extensively studied using both computational and experimental methods. However, studies of these systems, particularly in the solution phase is no trivial undertaking. Thermal motion, as well as dynamic solvation shells make these studies particularly challenging.

To this point, a variety of methods have been used to probe the solvation shell structures of $I^-$and $Br^-$ solvated in water. These include studies in extended x-ray absorption fine structure (EXAFS), quantum mechanical (QM) simulations, infrared spectroscopy, molecular dynamics (MD) simulations, and density functional theory (DFT) calculations [2],[1],[3]. However, experimental techniques suffer from large errors in determining the coordination number and geometric structure of solvation shells. Studies in x-ray and neutron diffraction, although powerful for probing structures with uniform surfaces and orientations, lack the ability to study dynamic systems such as ions in bulk solution phase. Computational simulations rely on theoretical parameterized inputs and are approximate at producing statistically reliable information on the structural properties of these solvation spheres [3]. As a result, the latest reported aqueous coordination numbers of $I^-$ and $Br^-$ are 7.3 to 9.7 and 5.8 to 6.2, water molecules, respectively [2],[3]. These results agree with the established chemical theory that larger ions have larger solvation shells. This study attempts to analyze these solvation spheres with more rigor and precision than previous studies.

In this study, a combination of data analysis techniques was used to study the solvation

shells of $I^-$ and $Br^-$ in water. Using bromide K-edge and iodide L1-edge EXAFS and near-edge data, structural analysis was performed. EXAFS analysis is a standard structural determination technique, which can be used to probe the local geometric structure near a central absorbing element [4],[5],[6],[7]. EXAFS analysis requires less computational time than near-edge analysis, so this data was fit first to generate models for the near edge analysis. EXAFS fits were used to test structural models (4, 6, 8, and 10 coordinate geometries), which were subsequently used to fit the near-edge data. MXAN has the advantage that it mostly independent of thermal noise/Debye-Waller factors, which lead to EXAFS signal dampening and broadening. Near-edge analysis was performed using MXAN, a data analysis software that employs full multiple scattering theory, to reproduce the x-ray absorption near edge spectrum (XANES) and the EXAFS region out to 150 eV, using input structural and non-structural parameters[8],[9]. The near-edge analysis used by MXAN is very sensitive to local geometries and can furnish accurate three-dimensional structural information[8],[9],[6]. It is best to use a combination of these data analysis techniques because these methods are complementary and optimize structural model-building.

## 2.0 MATERIALS AND METHODS

*2.1 Sample preparation*

A 500 mM solution of KI in de-ionized (DI) water was prepared by mixing solid KI in DI water until completely dissolved. A 500 mM solution of KBr in DI water was prepared by mixing solid KBr in DI water until completely dissolved.

*2.2 Data collection*

Iodide L1-edge XAS data were collected on the 20-pole 2T wiggler unfocused beamline 4-3 under the standard ring operating condition of 3 GeV and 200 mA ring current. A fully tuned Si(111) double crystal monochromator was used for energy selection. Other upstream optics included a Ni-coated vertically collimating and harmonic rejection mirror.

Room temperature measurements were performed on the sample in fluorescence mode using a passivated implanted planar silicon (PIPS) detector. The samples were housed in a teflon cell with 5 $\mu$m polypropylene windows. The cell was sealed with 37 $\mu$m Kapton tape. Energy calibration was achieved by setting the first inflection point at 5280 eV [10]. Bromide K-edge data was previously collected on BL 9-3 by Dr. Ritimukta Sarangi.

*2.3 Data analysis*

Before analysis the data was processed to remove background radiation. To accomplish this, each spectrum was viewed using MVIEW, a program in the suite EXAFSPAK, to check the quality of data files. The spectra were then added together and averaged. A second degree polynomial was then fit to the pre-edge region of the averaged data using PySpline. This polynomial was then subtracted from then entire spectrum as background. This process was used to normalize both the I- and Br- data.

Theoretical EXAFS phase and amplitude parameters were calculated using *FEFF* (version 7.0), and fit to the experimental data using EXAFSPAK. Hydrogen atoms were excluded during the fitting process because of their minor contribution to the overall EXAFS signal. Structural parameters that were varied during the fitting process included bond distance (R) and bond variance ($\sigma^2$), which is related to the Debye-Waller factor, resulting from thermal motion. The nonstructural parameter $E_0$, (the energy where $k$=0), was also varied between fits but was linked for every component in a given fit. Coordination numbers were varied but remained constant in a given fit. The reduced error ($\chi^2$) and visual analysis were used to determine the goodness of the fits. The $I^-$ spectrum was fit over k=2-10.1 $Å^{-1}$. The $Br^-$ spectrum was fit over k=2-12.5 $Å^{-1}$.

Experimental XAS spectra were theoretically modeled using MXAN, which performs full multiple scattering analysis to obtain structural information [8],[9]. Starting structures were taken from the best three-dimesional models that included the coordination numbers 4, 6, 8, and 10 with radial metrics obtained from EXAFS analysis. The data were fit over a $E$-$E-0$ range of -6.5 eV to 120 eV for $I^-$ and -6.0 eV to 120 eV for $Br^-$. After each

step of structural parameter refinement a step of non-structural parameter refinement was performed. Refinements were closely monitored for large fluctuations in both the structural parameters and non-structural parameters. No such fluctuations were observed. The least squares error and visual analysis were used to determine the accuracy of the fits.

## 3.0 RESULTS

*3.1 Iodide*

In $I^-$ EXAFS analysis, the best fit was achieved with a coordination number of 8 water molecules, as the reduced $\chi^2$ error was 0.000672 (see Table 1, Figure 3). However, the fit with 10 water molecules coordinated to the I- anion also yielded a very low error with reduced $\chi^2$ error = 0.000884 (see Table 1, Figure 4). Both fits used two iodide-oxygen paths in which one path was about 0.3 Å longer than the other (see Table 1). Both fits correlated well with coordination numbers and distances suggested in previous studies [3]. Due to the similarities between the two fits it was impossible to distinguish between the two models. Fits with coordination numbers of 6 and 4 yielded much higher error (see Table 1).

In XANES analysis, the best fit was achieved with a coordination number of 8 water molecules with the $\sum$ square residuals = 0.57718 (see Figure 7). In this particular model, the four water molecules in a plane with the central anion were coordinated over a range of distances (see Figure 9), from 3.30 to 3.70 Å from the central $I^-$ to the O of the water molecules. The two remaining pairs of water molecules had distances of 3.54 Å from the I-ion to the O of the water molecule. These distances agree with findings in previous studies as well as distances observed in EXAFS analysis [3]. The fit with a coordination number of 10 yielded a fit that was about three times poorer than a coordination number of 8 with $\sum$ square residuals = 1.8835 (see Figure 7). Coordination numbers of 4 and 6 yielded poor fits to the data (see Figure 7).

*3.2 Bromide*

In bromide EXAFS analysis the best fit was achieved with coordination number of 10 water molecules with a reduced $\chi^2$ error of 0.0167 ( see Table 2, Figure 5). The fit with coordination number of 8 was slightly poorer with a reduced $\chi^2$ error of 0.0189 (see Table 2, Figure 6). Due to the similarities between these two fits,and since the Debye-Waller factors make coordination number determination difficult, both 8 and 10 coordinated models must be regarded as feasible structural models for the $Br^-$ solvation sphere. Fits with coordination numbers of 4 and 6 water molecules did not fit the data well (see Table 2).

The MXAN analysis resulted in a much clearer pattern. The fit with 8 water molecules coordinated to the central $Br^-$ anion yielded the best fit and the $\sum$ square residuals was 2.9440. Structurally, this model is similar to the $I^-$ model with 8 water molecules, however the distances between the central anion and the O of the water molecules is slightly shorter (see Figure 10). The four water molecules in a plane with the central $Br^-$ anion have a distance of 3.25-3.44 $\mathring{A}$ from the Br- ion to the O of the water molecules. The two remaining pairs of water molecules are placed such that the Br-O distances are 3.30 Å in three of the water molecules and 3.63 Å in the remaining water molecule. These distances agree with previous studies, as well as distances observed in EXAFS analysis [3]. The fit with 10 water molecules coordinated to a central $Br^-$ anion produced a fit about three times worse than the fit with 8 water molecules (see Figure 8).

## 4.0 DISCUSSION

The solvation sphere of $I^-$ and $Br^-$ has been determined using a combination of EXAFS and MXAN data analysis techniques. Both anions have an asymmetric eight coordinate solvation sphere (see Figures 9,10). In the $I^-$ model, 4 of the water molecules lie in a plane around the central anion, with the oxygen atoms between 3.30 Å and 3.72 Å from the iodide anion. The remaining four molecules are in pairs above and below the central plane with the oxygen atoms approximately 3.54 Å from the iodide anion (see Figure 9). This model is consistent

with both the EXAFS and MXAN analysis and correlates strongly to distances obtained in previous studies[3].

The $Br^-$ solvation shell is nearly structurally identical to the $I^-$ solvation shell (see Figure 10). Four water molecules lie in a plane about the central $Br^-$ anion with the oxygen atoms between 3.26 Å and 3.44 Å from the central $Br^-$ anion. The remaining four water molecules are in pairs oriented in orthogonal planes to each other, with the oxygen atoms between 3.27 Å and 3.63 Å from the central $Br^-$ anion(see Figure 10). This is a strong model because the Br-O distances match what previous literature suggested, as well as correlating strongly to the results we saw in both EXAFS and XANES analysis [2], [3]. Although some aspects of this study correlate to reported values in previous literature, the structural results described in this study are different from earlier EXAFS publications [3] [2]. This study especially contrasts previous reported values with respect to coordinate geometry of the water molecules.

The use of MXAN which includes the XANES region of the absorption spectrum, was a very powerful tool in this study. MXAN allows the optimization of a wider variety of structural and non-structural parameters. MXAN includes edge region, where effects from Debye-Waller broadening and dampening are minor, which uniquely allows inclusion of geometric structure analysis. While EXAFS analysis using FEFF is a very powerful technique for local structure determination, the error associated with EXAFS especially in room temperature data studies does not allow the precise determination geometric structures because EXAFS is only capable of giving radial information. The EXAFS equation does not include an angular dependence term. A combination of these data analysis techniques is a more powerful way to analyze XAS data and determine geometric structures. EXAFS analysis can produce starting models with the correct coordination number and bond distances relatively quickly. MXAN can then be used to optimize the geometry as well as non-structural parameters not included in EXAFS analysis.

Near-edge XAS investigation has determined that the solvation spheres of both $I^-$ and

$Br^-$ are nearly identical in geometry and number. This is counterintuitive since a large anion might be expected to have a larger solvation sphere by classical chemistry. The data show that although the coordination number remains the same, the bond distances for $Br^-$ are shorter by 0.24 Å, indicating the decrease in ionic radii in $Br^-$. These data indicate that the classical theory of increasing the number of solvating water molecules with increasing ionic radius must be revisited. Other reasons, such as charge delocalization, charge density and steric hindrance effects of nearby water molecules may play major roles in determining the solvation sphere. We are currently exploring the solvation sphere of $Cl^-$ to get a more complete understanding of solvation in halides.

This study of the first solvation shell of $I^-$ and $Br^-$ is of fundamental importance to the bio-chemical community. Knowledge of the solvation sphere gives us a better understanding of how these anions interface with other molecules in aqueous systems. This is of particular importance in biological systems, since how these anions interact with proteins as well as how they determine equilibria may be related to the solvation sphere that surrounds these anions in aqueous systems. In addition, the impact of halide solvation on the structure of water can now proceed from a geometrically explicit solvation model. Further studies could look at how this solvation structure changes in protein solution, and if the presence of a protein matrix decreases the number of solvated water molecules.

## 5.0 CONCLUSION

This paper has reported on the solvation first sphere of $I^-$ and $Br^-$ in water. Using EXAFS and XANES analysis, strong models which describe the geometric configuration of water molecules coordinated to a central anion have been developed. The combination of these techniques has provided us with a more substantiated argument than relying solely on one or the other. An important finding of this study is that the size of the anion plays a smaller role than previously assumed in determining the number of coordinating water molecules.

Further experimental and theoretical invesigation is required to understand why the size of the anion plays a minor role in determining the number of water molecules bound.

## 6.0 ACKNOWLEDGMENTS

I would like to thank Dr. Ritimukta Sarangi for mentoring me on this project and contributing the KBr K-edge data used. I would also like to thank Dr. Maurizo Benfatto for the resources and expertise he has provided in using MXAN. I would like to thank Dr. Steven Rock for the direction and organization he has provided, as well as the other staff who have helped run the SULI program at SLAC. I would also like to thank Dr. Patrick Frank for his guidance and input on this manuscript. This research was funded by the U.S. Department of Energy, the Stanford Linear Accelerator Center and the Stanford Synchrotron Radiation Lightsource. The calculations were carried out at the computing center in Frascati, Italy, at the Instituto Nazionale di Fiscia Nucleare.

## REFERENCES

[1] K.J.Tielrooij *et al.*, "Cooperativity in ion hydration," *Science*, vol. 328, pp. 1006–1009, 2010.

[2] S. Raugei and M. L. Klein, "An ab initio study of water molecules in the bromide ion solvation shell," *Journal of Chemical Physics*, vol. 116, no. 1, pp. 196–202, 2002.

[3] V.T.Pham *et al.*, "The solvent shell structure of aqueous iodide: X-ray absorption spectroscopy and classical, hybrid qm/mm and full quantum molecular dynamics simulations," *Journal of Chemical Physics*, vol. 371, pp. 24–29, 2010.

[4] B. Teo, *EXAFS: Basic Principles and Data Analysis.* New York: Springer-Verlag, 1986.

[5] J. M. de Leon *et al.*, "Ab initio curved-wave x-ray-absorption fine structure," *Physical Review, B: Condensed Matter*, vol. 44, no. 9, pp. 4146–4156, 1991.

[6] E. Stern, *In EXAFS, SEXAFS and XANES*, D. Konsinberger, Ed. New York: John Wiley and Sons, 1988, vol. 1.

[7] G. George, "Exafspak and edgefit," Stanford Synchrotron Radiation Laboratory, Stanford Linear Acclerator Center, Stanford University, Stanford, CA, 2000.

[8] M. Benfatto and S. D. Longa, "Geometrical fitting of experimental xanes spectra by a full multiple-scattering procedure," *Journal of Synchrotron Radiation*, vol. 8, pp. 1087–1094, 2001.

[9] M. Benfatto *et al.*, "Advances in the theoretical analysis of the xanes (x-ray absorption near edge structure) energy region for quantitative structural use," *Physica Scripta*, vol. T115, p. 28, 2005.

[10] F. E. Huggins *et al.*, "Modes of occurrence of trace elements in coal from xafs spectroscopy," *International Journal of Coal Geology*, vol. 32, no. 1, pp. 31–53, 1996.

# FIGURES

| Coordination# | *R* (Å) | $\sigma^2$ | $E_0$ (eV) | Reduced Error ($X^2$) |
|---|---|---|---|---|
| 4 | 3.51 | 0.02347 | -3.9119 | 0.0015 |
| 6 | 3.54 | 0.03378 | -2.9505 | 0.00208 |
| 8 | 3.52 | 0.02149 | -1.3404 | 0.000672 |
| | 3.83 | 0.04573 | | |
| 10 | 3.54 | 0.0248 | -1.1247 | 0.000884 |
| | 3.87 | 0.04474 | | |

Figure 1: Table 1 displays coordination number, bond distances, Debye-Waller factors, E0, and Reduced Error ($\chi^2$) for EXAFS fits with iodide. Note that two paths were used for fits with 8 and 10 water molecules coordinated.

| Coordination# | *R* (Å) | $\sigma^2$ | $E_o$ (eV) | Reduced Error ($X^2$) |
|---|---|---|---|---|
| 4 | 3.27 | 0.01328 | -5.5179 | 0.0718 |
| 6 | 3.27 | 0.01209 | -5.6423 | 0.0407 |
| 8 | 3.27 | 0.02514 | -5.6574 | 0.0189 |
| 10 | 3.27 | 0.02113 | -5.7119 | 0.0167 |
| | 3.6 | 0.04452 | | |

Figure 2: Table 2 displays coordination number, bond distances, Debye-Waller factors, E0, and Reduced Error ($\chi^2$) for EXAFS fits with bromide. Note that two paths were used for fit with 10 water molecules coordinated.

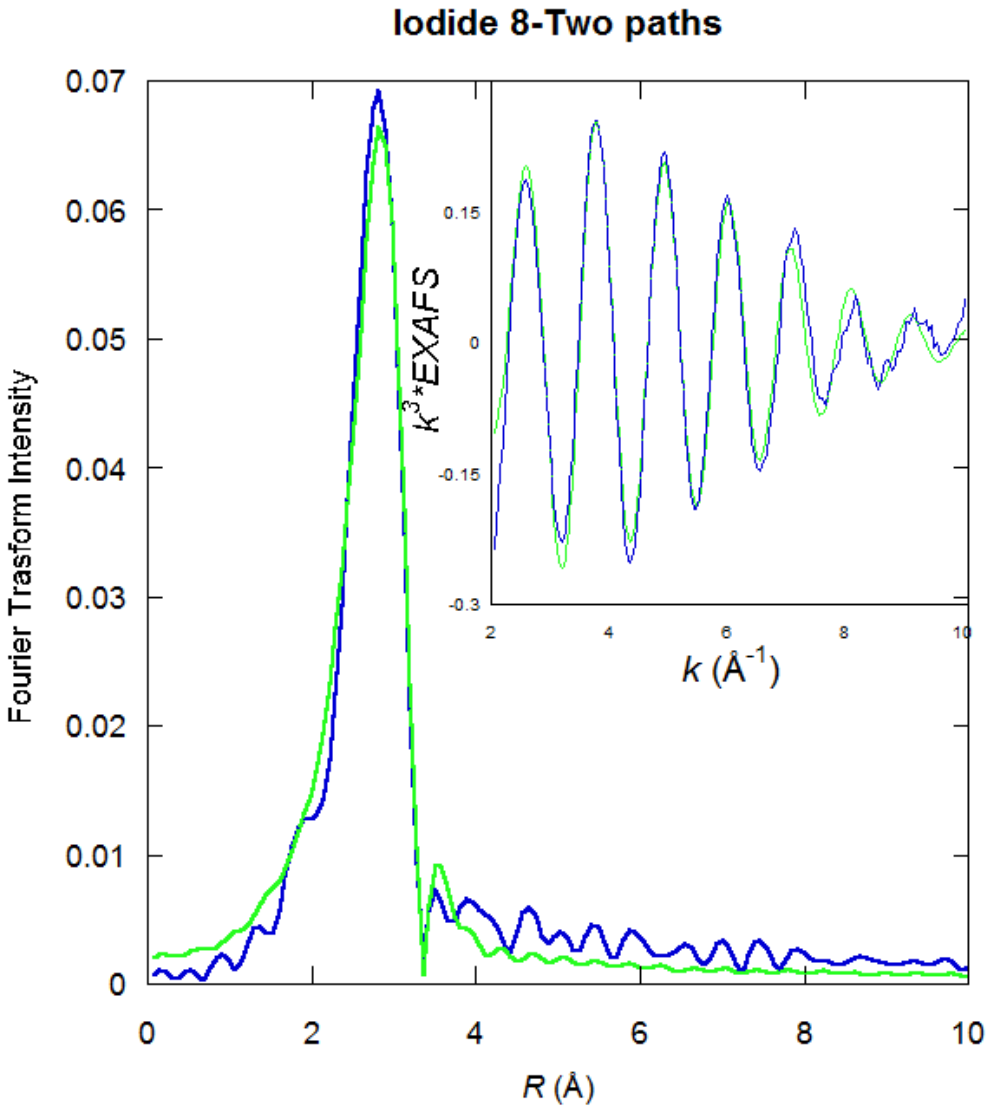


Figure 3: Fourier Tranform and EXAFS data, Iodide coordination number 8. Blue lines indicate experimental data, green lines indicate theoretically reproduced spectra.

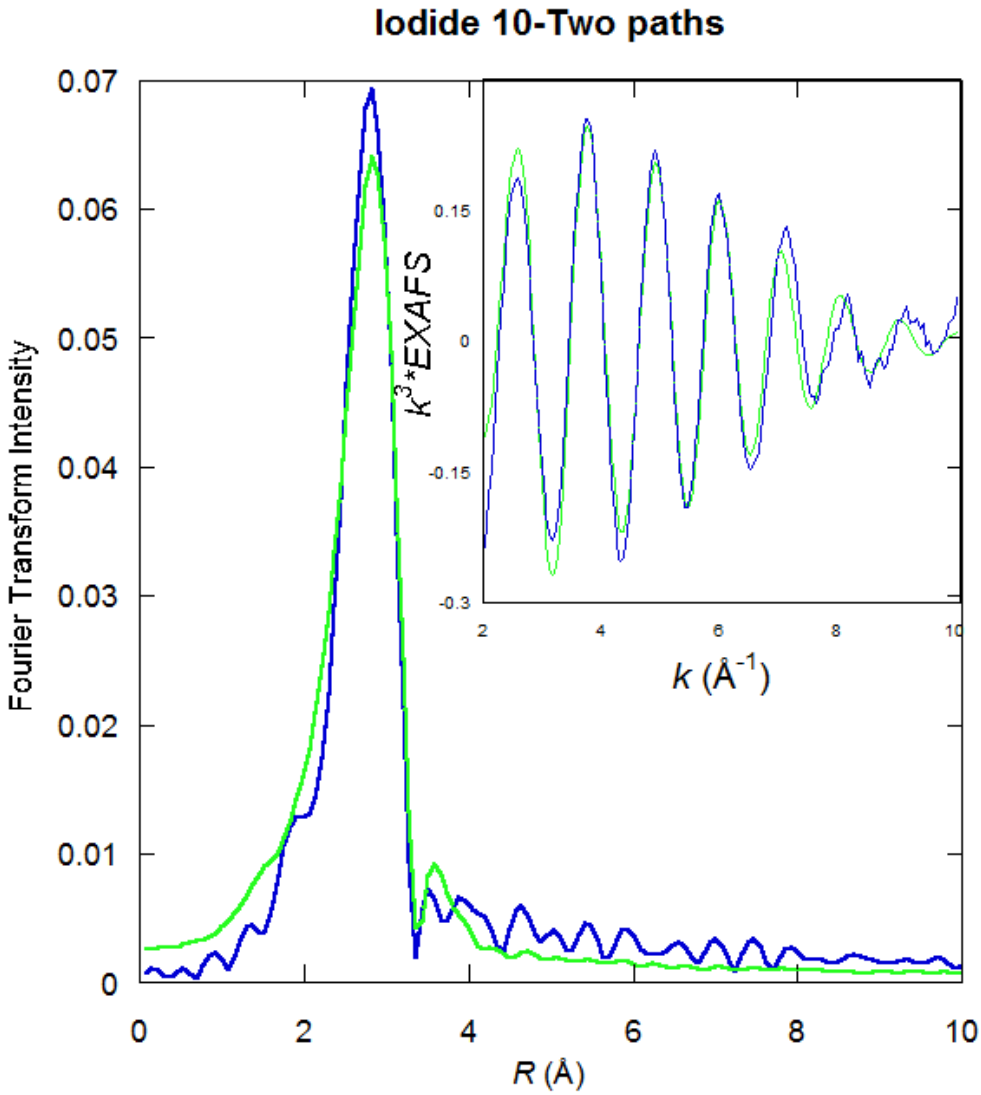


Figure 4: Fourier Tranform and EXAFS data, Iodide coordination number 10. Blue lines indicate experimental data, green lines indicate theoretically reproduced spectra.

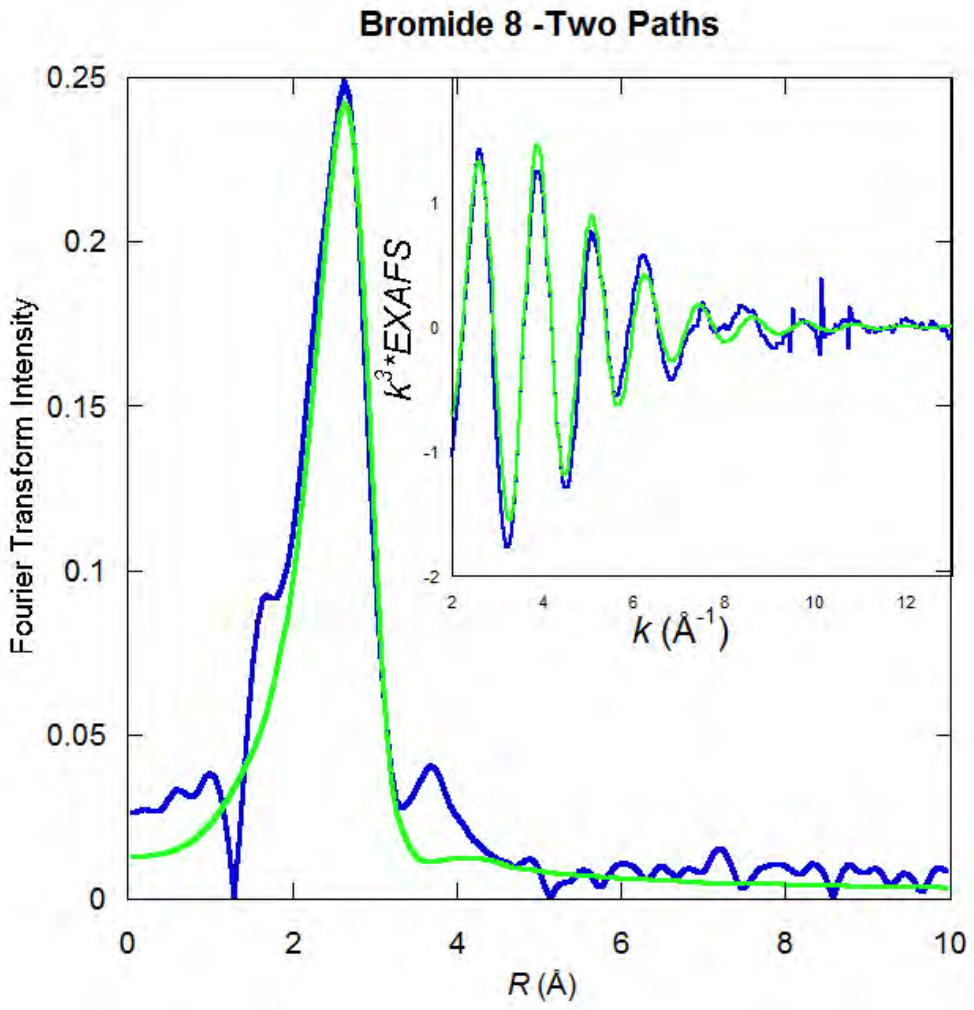


Figure 5: Fourier Tranform and EXAFS data, Bromide coordination number 8. Blue lines indicate experimental data, green lines indicate theoretically reproduced spectra.

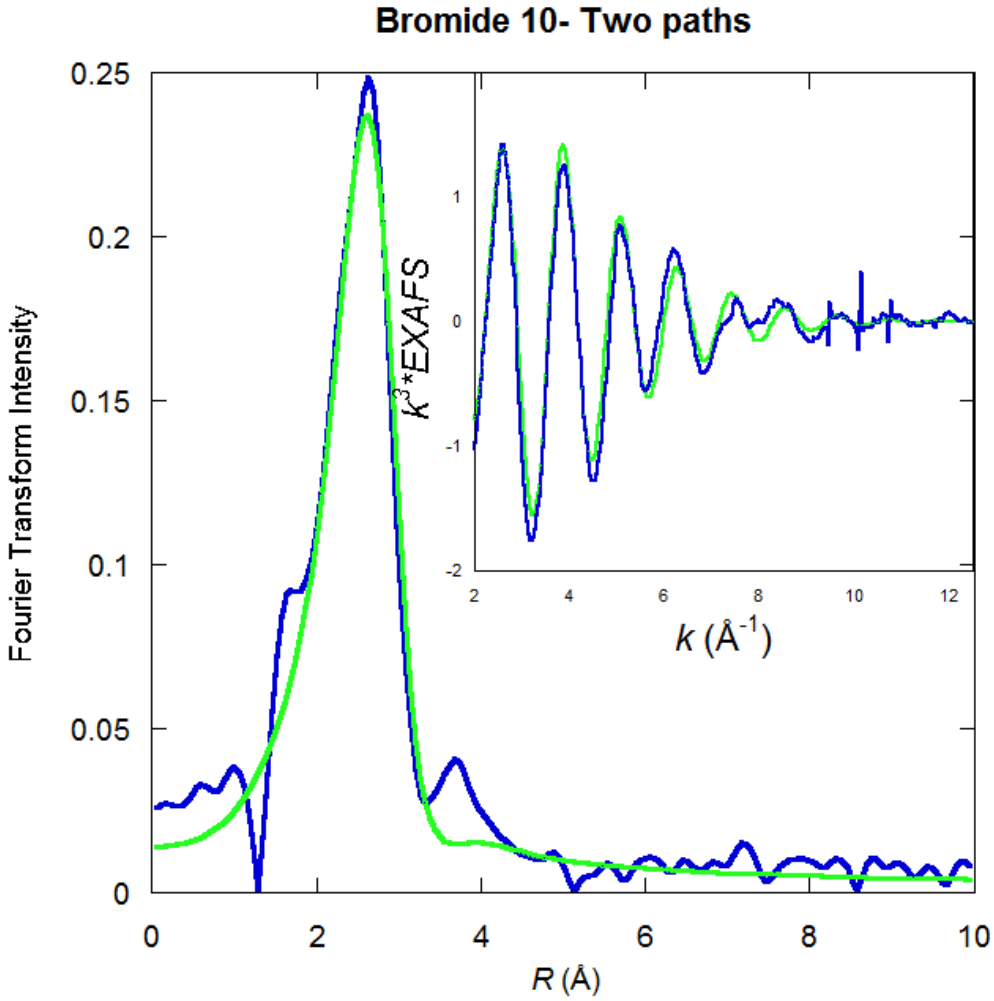


Figure 6: Fourier Tranform and EXAFS data, Bromide coordination number 10. Blue lines indicate experimental data, green lines indicate theoretically reproduced spectra.

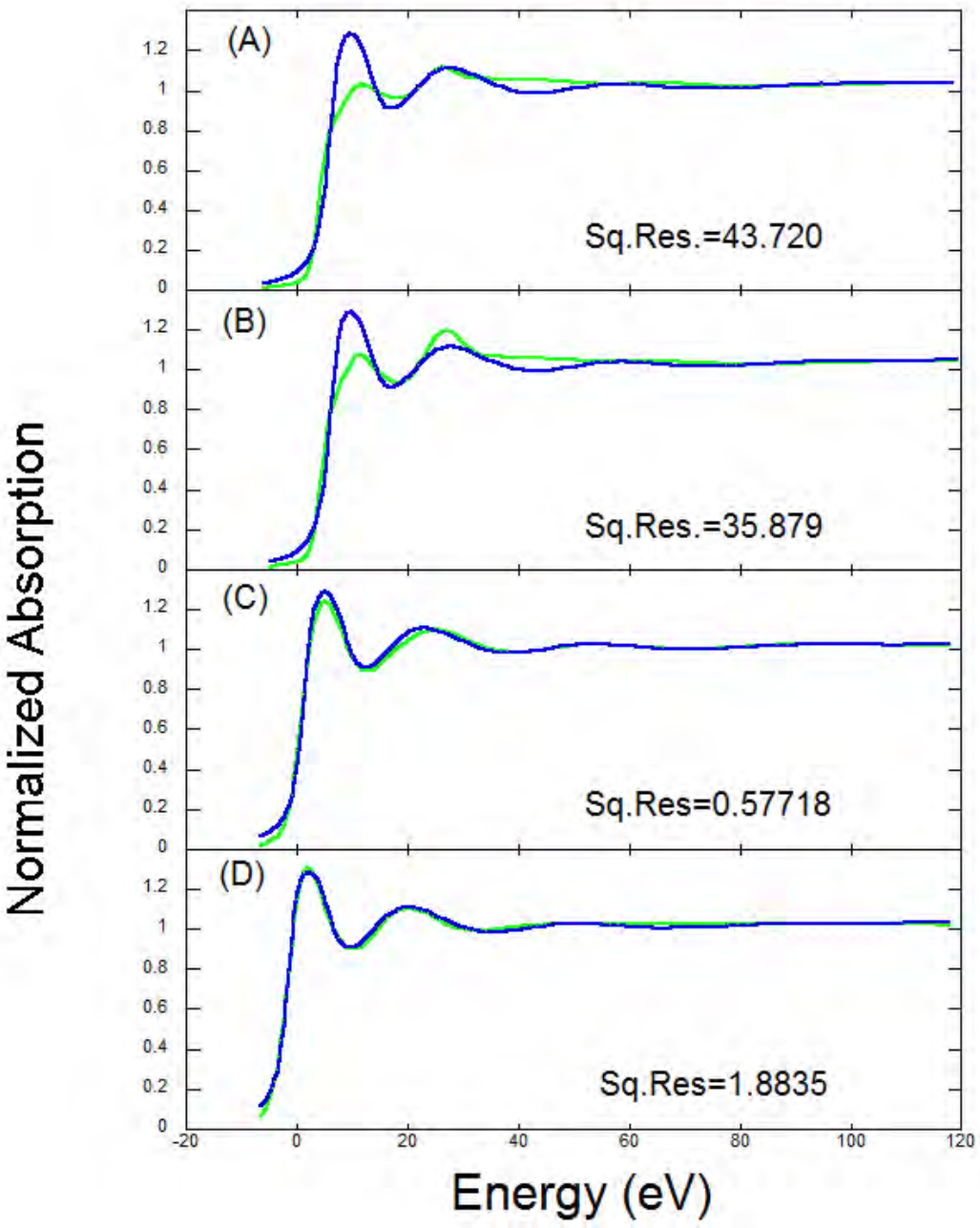


Figure 7: XANES data ans MXAN fits for Iodide. Blue lines indicate experimental data, green lines indicate theoretically reproduced spectra. (A): coordination number= 4, (B) coordination number= 6, (C) coordination number= 8, (D) coordination number= 10.

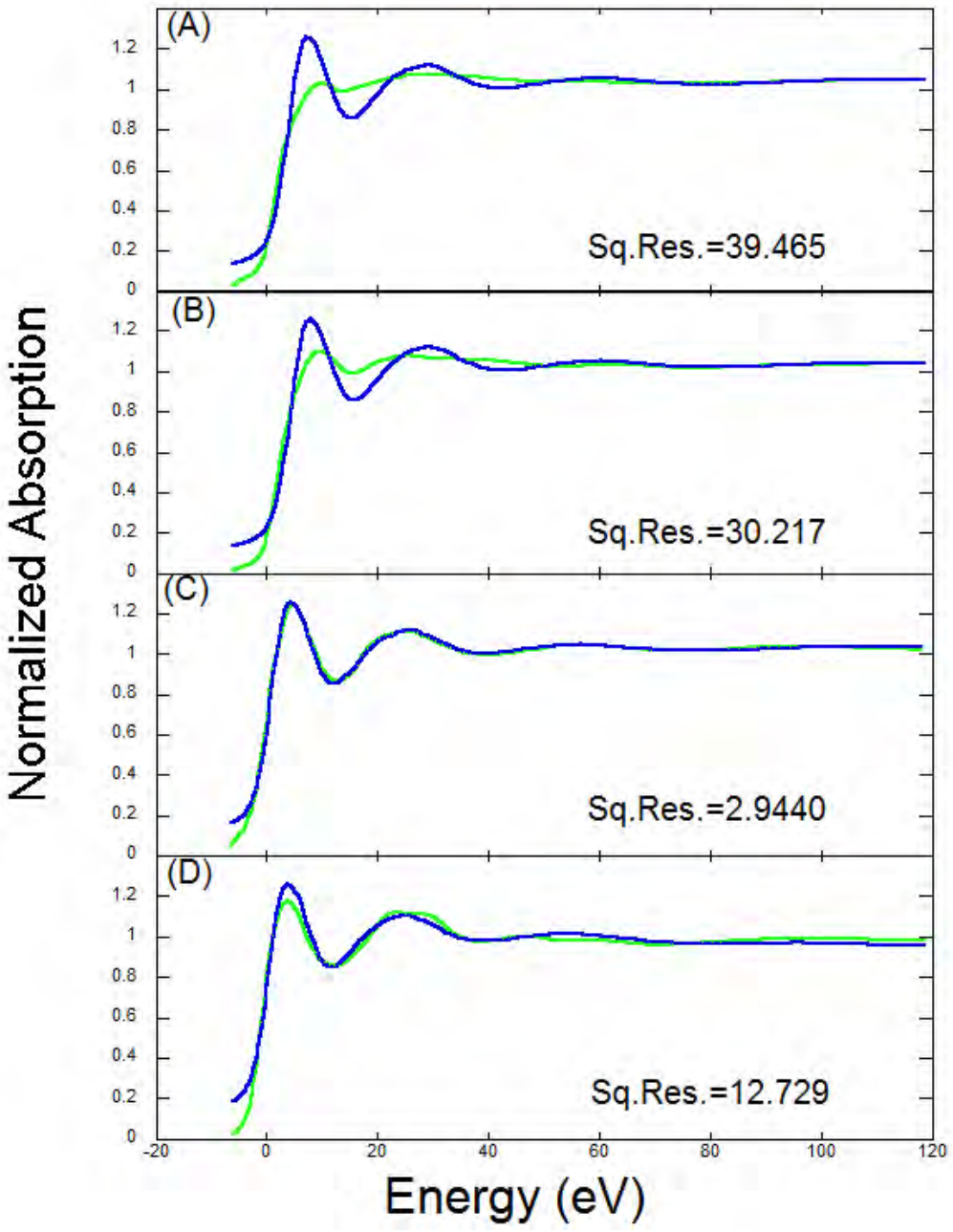


Figure 8: XANES data and MXAN fits for Bromide. Blue lines indicate experimental data, green lines indicate theoretically reproduced spectra.(A) coodination number= 4, (B) coordination number= 6, (C) coordination number= 8, (D) coordination number= 10

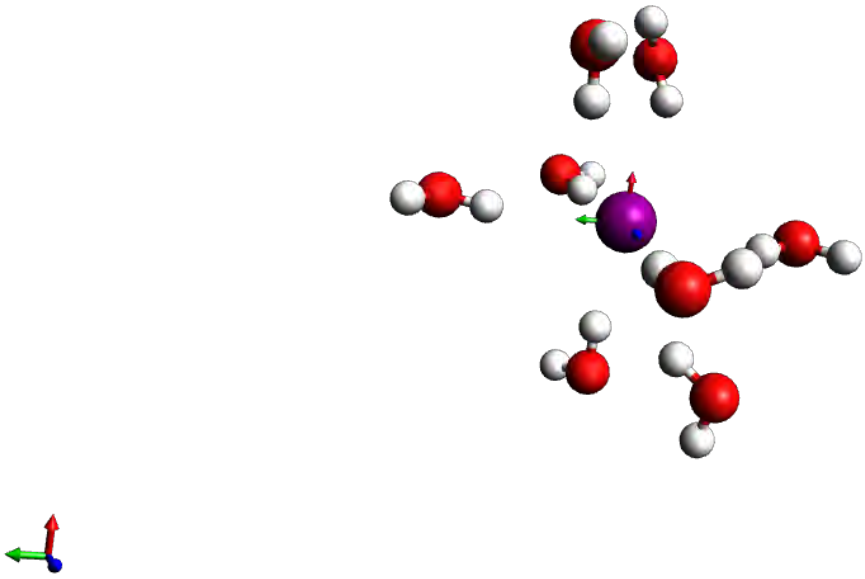

Figure 9: Model of Iodide coordination number= 8.

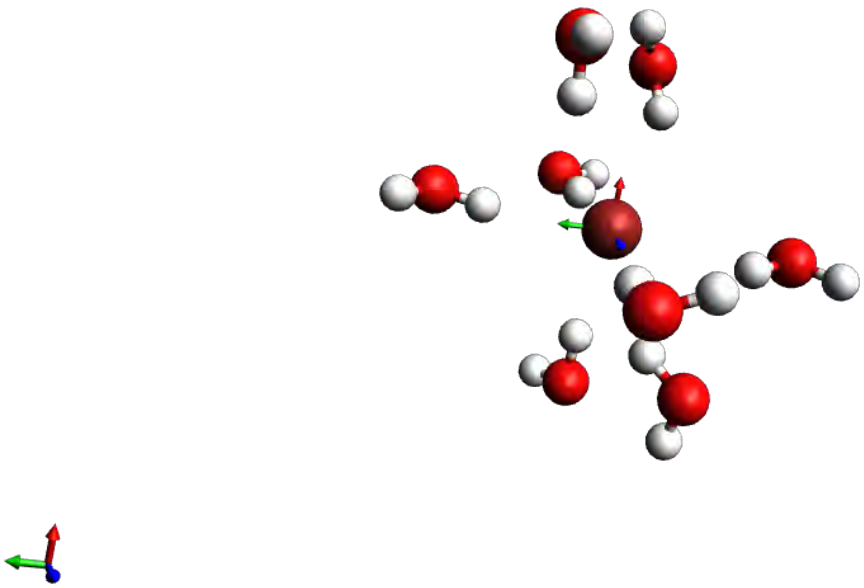

Figure 10: Model of Bromide coordination number= 8.

# Clicks versus Citations:
# Click Count as a Metric in High Energy Physics Publishing

Ayelet Bitton

Office of Science, Science Undergraduate Laboratory Internship (SULI)

University of California, San Diego

SLAC National Accelerator Laboratory

Stanford, CA

August 20, 2010

Prepared in partial fulfillment of the requirements of the Office of Science, Department of Energy's Science Undergraduate Laboratory Internship under the direction of Travis Brooks at the SPIRES/INSPIRES Group, SLAC National Accelerator Laboratory.

Participant: _____

Signature

Research Advisor: _____

Signature

Work supported in part by US Department of Energy contract DE-AC02-76SF00515.

# TABLE OF CONTENTS

# ABSTRACT

Clicks versus Citations: Click Count as a Metric in High Energy Physics Publishing. AYELET BITTON (University of California, San Diego, La Jolla, CA 92093) TRAVIS BROOKS (SPIRES/INSPIRES Group, SLAC National Accelerator Laboratory, Menlo Park, CA 94025)

High-energy physicists worldwide rely on online resources such as SPIRES and arXiv to perform gather research and share their own publications. SPIRES is a tool designed to search the literature within high-energy physics, while arXiv provides the actual full-text documents of this literature. In high-energy physics, papers are often ranked according to the number of citations they acquire — meaning the number of times a later paper references the original. This paper investigates the correlation between the number of times a paper is clicked in order to be downloaded and the number of citations it receives following the click. It explores how physicists truly read what they cite.

# INTRODUCTION

Traditionally, costly journals have ruled the world of published research papers. However, in high-energy physics (HEP), free online paper repositories have led to a huge change in how physicists perform research and share their findings. With the invention of the internet, the transmission of information — including research results — has moved online. Within the world of science, and particularly HEP, scientists are now able to reach more information than ever before, at tremendously increased speeds.

HEP is unique in that its participants have access to a majority of the field's literature online, free of cost. Over two decades ago, the first website in the United States came online: SPIRES, a database designed to effectively search HEP papers [1]. This open access resource initiated a change in the way scientists normally interact with research publication. It also provides a unique means of studying how a community with such infrastructure operates. This method of sharing and accessing information has already led to numerous changes in the publishing habits of high-energy physicists.

Past research has already shown that in the two decades since the invention of the internet, the field norms have moved to the point that over 95 percent of the HEP community publishes its papers online [2]. These papers are submitted in the form of preprints to arXiv — a database that stores the actual copies of the papers SPIRES allows users to search for [3]. Preprints await journal review, but are often still of a high caliber due to "the invisible hand of peer review" [4]. Papers that are published to arXiv later tend to be cited over 14 times on average, while papers not submitted to arXiv receive less than four citations on average [2].

Currently, a citation count — the number of times a specific paper is referenced by a later paper — acts as the sole objective metric for measuring a paper's or author's success and influence. SPIRES simplifies this by offering citation statistics, displaying a specific

author's or paper's citation count alongside the article's information. In this paper, we shall investigate whether the number of clicks a paper receives in any way correlates with the number of citations it later receives. For the purposes of this paper, the word "click" represents only clicks on the SPIRES website that led to an actual download of a paper, which was then theoretically read by the user. To simplify the question: are researchers clicking (and therefore reading) what they cite from SPIRES and arXiv? If so, a paper's click count may also serve as a metric for relevance, and may be worth considering alongside its citation count. Certain paper repositories have already implemented a display of a paper's click counts [5], but as of this point, no concrete research has commenced the search for a correlation between clicks and citations. Should such a correlation exist, it could be a further adjustment that SPIRES and other online repositories have had on the way high-energy physicists perform their research.

## METHODS AND MATERIALS

SPIRES is a database holding the metadata for over 750,000 scientific papers, including papers published in journals and online repositories such as arXiv[1]. It features a search system for finding papers, and provides links to the journals and databases where these papers are available. SPIRES works hand in hand with arXiv, which provides the actual preprints of papers, offering a free alternative to costly journal versions of papers. High energy physicists worldwide rely on SPIRES and arXiv as a resource to perform research and access their colleagues' findings. The data in this paper is drawn from log files created over a six month period in 2009 consisting of all clicks made on the SPIRES website during that time, as well as the same data drawn from arXiv over the same six month period.

The SPIRES log files allow us to create different data sets to demonstrate various relationships between clicks and citations. About 87 percent of the links within the log file could

be associated with a paper record identification number within the SPIRES system, while the remaining 13 percent were left aside, unable to be disambiguated. From the SPIRES record identification numbers, we are able to fetch various pieces of information about each paper clicked by a SPIRES user, such as its citation count, its topic, its year published, etc. Accordingly, we are able to plot different sets of the clicked papers. By plotting the number of clicks against the number of citations the paper received after the initial click, we can determine if any correlation between clicks and citations exist. To narrow the data in search of the specific click versus citation correlation, only papers that were published within three months of the recorded click were plotted; moreover, only their citations that occurred within the following year were plotted as well, to ensure that the citation followed a user accessing the paper and theoretically led to a citation (Figure 1). We generated the same plots for the arXiv data set. In order to reduce error, we compiled a list of the IP addresses drawn from each line of the log file, and removed computerized users such as Google Bot which had logged thousands of faux clicks.

In addition to plotting the clicks versus citations data set, we calculated the expected value of both clicks and citations for each point. This was calculated by determining the number of clicks versus its frequency (Figure 3) and the number of citations versus its frequency (Figure 4). From these two data sets, we were able to determine the expected value at each point on the original plot, and then found the difference between the actual and expected value, plotting the result (Figure 2). This allowed us to examine where the data deviates from the calculated expectation or null hypothesis — what we would expect to find should no correlation exist.

Finally, to find a statistical representation of the data, we calculated Pearson's rho a correlation coefficient that fluctuates between -1 and 1. Values near 0 indicate a lack of a correlation, while positive results correspond to a positive correlation and negative results correspond with negative values. In addition to calculating Pearson's rho for the data,

we took a hundred sets of randomized data reassigning all x- and y-values to a new pair, recalculated the correlation coefficient, and averaged the resulting values. This would allow us to determine whether the resultant coefficient from the actual data is in fact remarkable in any way, or whether it is irrelevant — similar to the resultant coefficient from the randomized data.

## RESULTS

Upon examination, the SPIRES and arXiv data revealed a consistent correlation between clicks and citations. Both data sets revealed remarkably similar plots. While the initial plot of the six months of SPIRES data (Figure 1) plotting only papers published within three months of their click and their citations within the next year looks mundane, the secondary plot displaying the difference between the actual and expected values clearly shows the correlation (Figure 2). It eliminates papers alongside both axes, dividing the data into three distinct areas the blue area along the x-axis, the blue area along the y-axis, and the central colored region. The area along the x-axis (or click-axis) represents an area of papers that are highly clicked but rarely cited, the area along the y-axis (or cite-axis) represents papers that are heavily cited but not often clicked, and the center region represents everything in between.

Pearson's correlation coefficient supports this finding. While the calculated coefficient for the six months of data was 0.34, which initially seemed too near to zero to indicate a correlation, the averaged, randomized data set consistently returned a correlation coefficient of $0 \pm 0.002$. This indicates that the method is not generating the correlation of 0.34, strengthening the idea of a correlation. To quantify this reading, we calculated a naive confidence interval of rho, which confirmed that zero was not within the confidence interval of the limits of rho, supporting a true, significant correlation.

# CONCLUSION

While there are numerous outlier papers, the SPIRES and arXiv data still indicate a correlation between downloads and citations. Rather than simply clicking around, physicists utilize the papers they click and cite them in their own published research. This shows the unique role that SPIRES plays in the realm of HEP; SPIRES is an important tool for high-energy physicists to find relevant background for their own projects.

Proprietors of databases such as SPIRES must consider whether it is worthwhile to introduce a new form of competition for physicists. While many physicists place great weight on their citation counts, it can not be a true form of evaluating the worth, value, or influence of a paper or author. The same can be said of downloads. The addition of a new statistic to the competitive number game may in actuality produce extraneous rivalry within the field — an effect that may not be beneficial to physicists.

***Future Work*** Additional work is needed to determine individual characteristics that define which papers lie within each of the three sections revealed in the difference plot. One strategy may be to plot papers according to topic, review, an author's overall cite count, or a number of other categories. Another statistical form of analyzing the data may be to calculate Spearman's rank, to pair with Pearson's rho and the confidence interval. A final means of quantifying an author's work, as proposed by John Beacom, would be to investigate plotting an author's accumulated citations within the past five years versus the author's overall citations for each year throughout the author's career.

# FIGURES

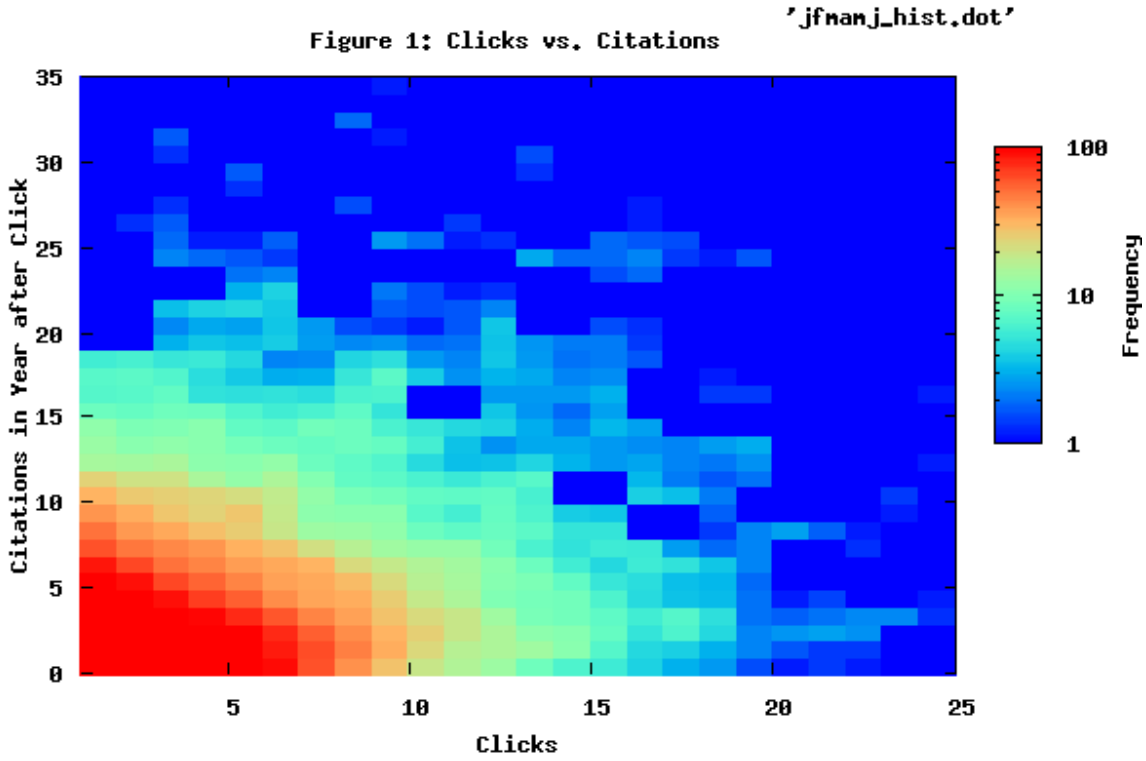


**Figure 1**

Clicks vs. Citations. Six months of 2009 SPIRES data narrowed to display only papers published within 3 months of the initial click and citations occurring in the year following the click.

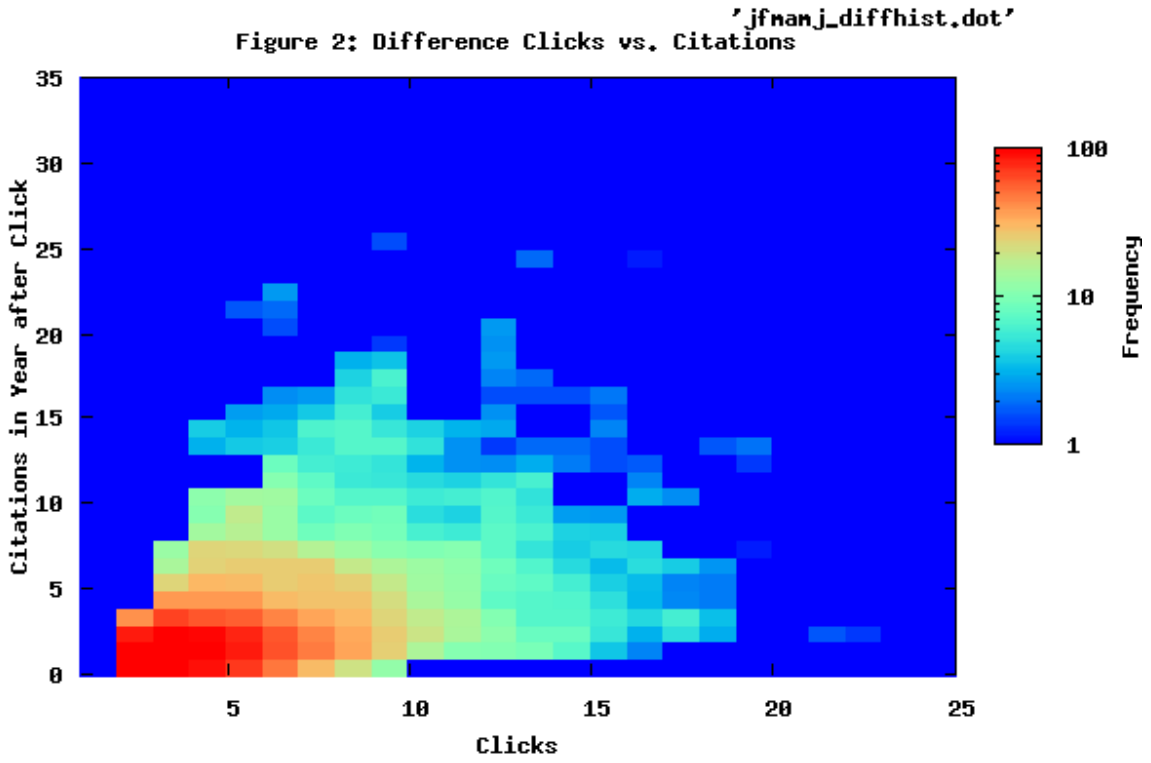


**Figure 2**

Difference of Actual Value and Expected Value Clicks vs. Citations. The difference of the six months of SPIRES data (shown in Figure 1) and the calculated expected value from the six month data set.

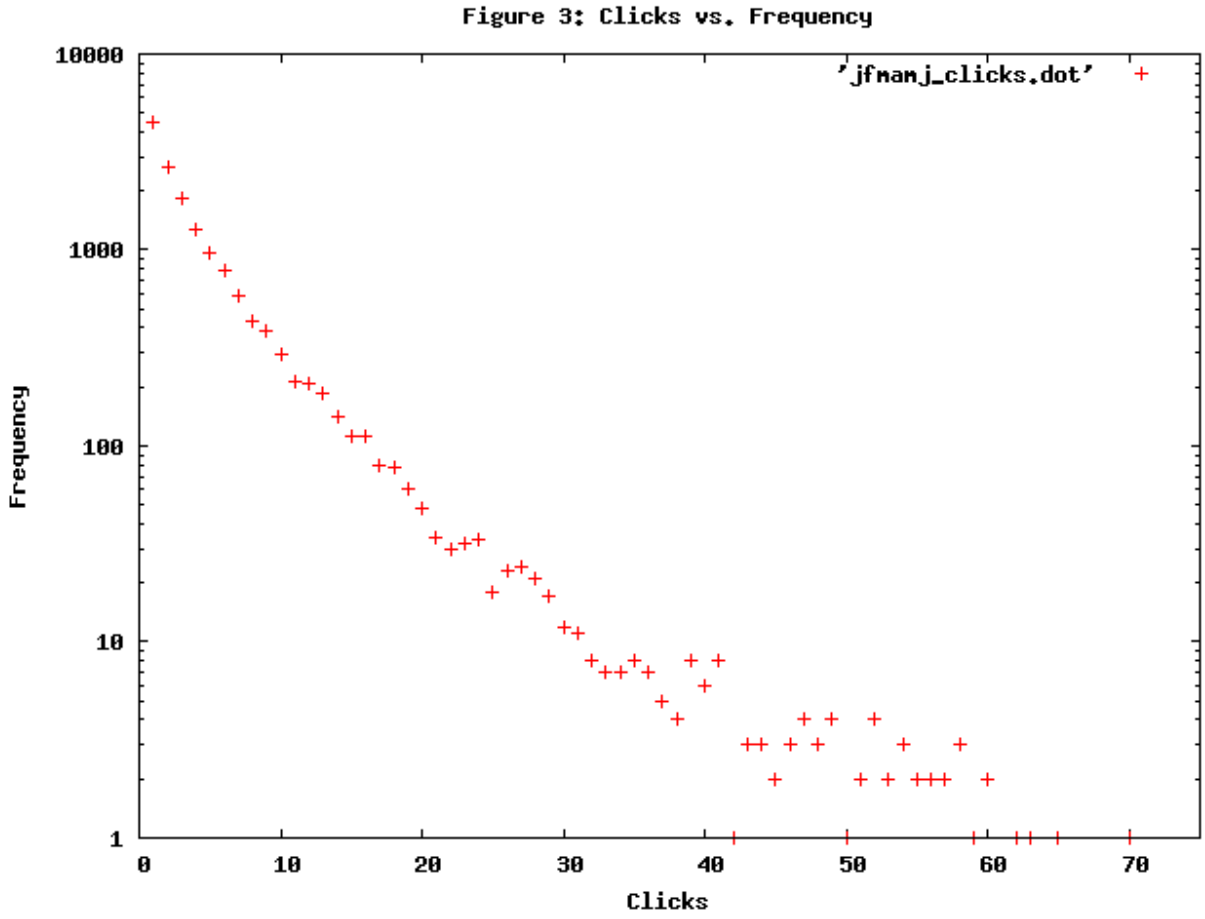


**Figure 3**

Clicks vs. Frequency. Used to calculate expected value.

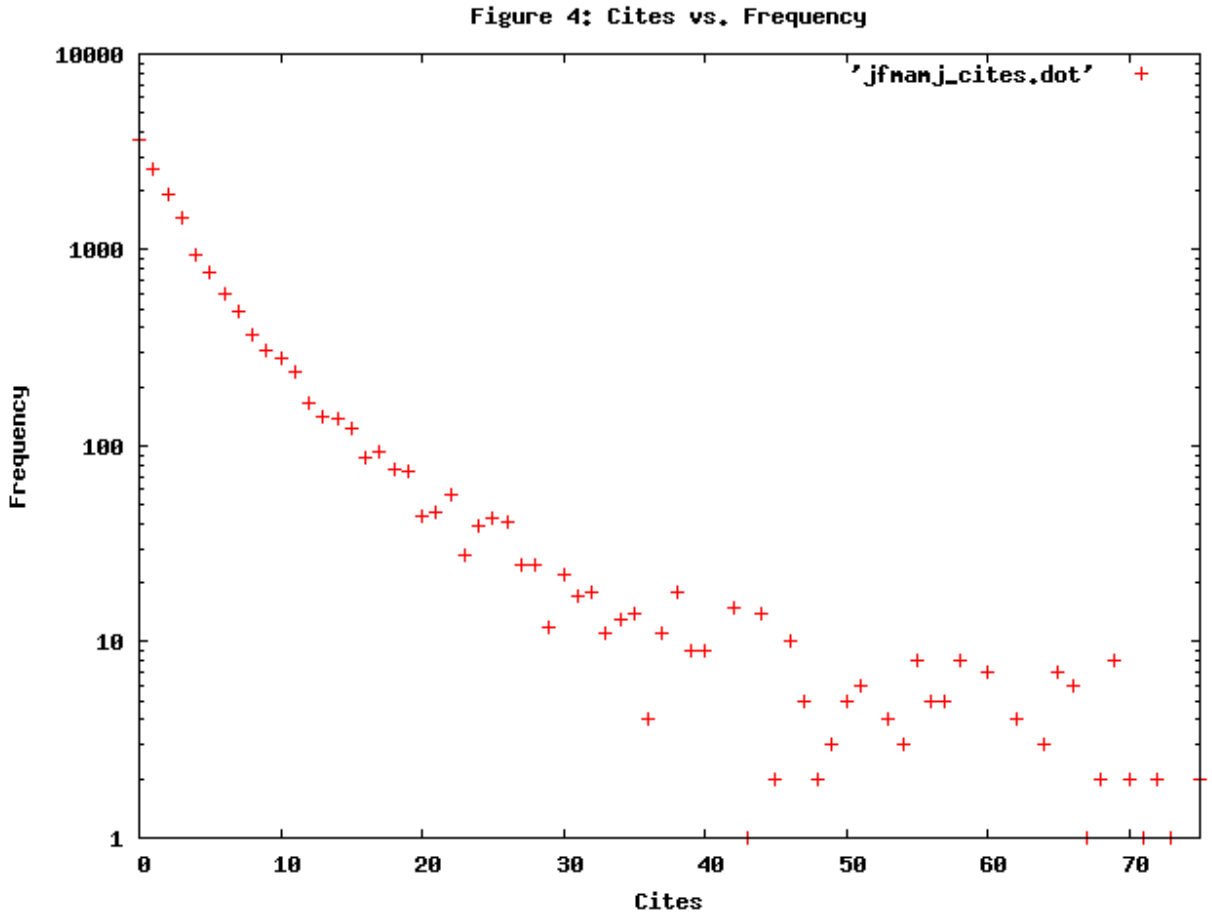


**Figure 4**

Cites vs. Frequency. Used to calculate expected value.

## ACKNOWLEDGEMENTS

This research was conducted at SLAC National Accelerator Laboratory. I would like to thank my mentor, Travis Brooks, who has shown me the value of computer science and the sort of research I did, and has instilled in me an excitement for the field. I would also like to especially thank Joseph Blaylock for his consistent support, assistance, and teaching. Further thanks to the SPIRES staff both at SLAC and abroad. Finally, thank you to SLAC and the Department of Energy for supporting the SULI Program and offering me this invaluable

opportunity.

## REFERENCES


[1] SPIRES Website http://www.slac.stanford.edu/spires [Last visited August 20, 2010]

[2] A. Gentil-Beccot, S. Mele, T. C. Brooks, "Citing and Reading Behaviours in High-Energy Physics. How a Community Stopped Worrying about Journals and Learned to Love Repositories," Scientometrics **84**, 345 (2010). [arXiv:0906.5418 [cs.DL]]

[3] arXiv Website http://arxiv.org/ [Last visited August 20, 2010]

[4] Harnad, S. (2000). The invisible hand of peer review. Exploit Interactive. http://www.exploit-lib.org/issue5/peer-review/.

[5] SSRN Website http://www.ssrn.com/ [Last visited August 20, 2010]

# Diborane Electrode Response in 3D Silicon Sensors for the CMS and ATLAS Experiments

Emily R. Brown

Office of Science, Science Undergraduate Laboratory Internship (SULI)

Reed College

Stanford Linear Accelerator Center

Menlo Park, CA

August 31, 2010

Prepared in partial fulfillment of the requirements of the Office of Science, Department of Energy's Science Undergraduate Laboratory Internship under the direction of Chris Kenney at the Particle Physics and Astrophysics Elec. and SW Eng. Dept., Stanford Linear Accelerator Center.

Participant: _____

Signature

Research Advisor: _____

Signature

Work supported in part by US Department of Energy contract DE-AC02-76SF00515.

# TABLE OF CONTENTS

# ABSTRACT

Diborane Electrode Response in 3D Silicon Sensors for the CMS and ATLAS Experiments. EMILY R. BROWN (Reed College, Portland, OR 97202) CHRIS KENNEY (Particle Physics and Astrophysics Elec. and SW Eng. Dept., Stanford Linear Accelerator Center, Menlo Park, CA 94025)

Unusually high leakage currents have been measured in test wafers produced by the manufacturer SINTEF containing 3D pixel silicon sensor chips designed for the ATLAS (A Toroidal LHC ApparatuS) and CMS (Compact Muon Solenoid) experiments. Previous data has shown the CMS chips as having a lower leakage current after processing than ATLAS chips. Some theories behind the cause of the leakage currents include the dicing process and the usage of copper in bump bonding, and with differences in packaging and handling between the ATLAS and CMS chips causing the disparity between the two. Data taken at SLAC from a SINTEF wafer with electrodes doped with diborane and filled with polysilicon, before dicing, and with indium bumps added contradicts this past data, as ATLAS chips showed a lower leakage current than CMS chips. It also argues against copper in bump bonding and the dicing process as main causes of leakage current as neither were involved on this wafer. However, they still display an extremely high leakage current, with the source mostly unknown.

# INTRODUCTION

## Semiconductor Theory

The basic theory of semiconductor detectors centers around the small ionization current caused when a charged particle loses part of its energy through elastic collisions with electrons as it travels through a material [1]. Most semiconductor detectors consist of a silicon crystal wafer doped and reverse biased, which makes it a diode. Doping refers to the addition of an impurity to the pure semiconducting material in order to change its electrical properties. For silicon, adding a column V impurity, such as phosphorus, donates an electron to the semiconductor, creating an n-type semiconductor. Adding a column III impurity, such as boron, creates an excess hole, or lack of an electron, forming a p-type semiconductor [2]. Various patterns of doping are used in detectors for different purposes and to various degrees of effectiveness. For a more detailed explanation, see textbooks by Sze, Grove or Lutz.

Originally, semiconductors were doped only on the surface of the silicon, or using planar technology. In contrast, doping of the detectors in ATLAS and those used in many other situations penetrates into the substrate of the silicon. Electrodes are etched, doped and filled in various patterns which determine maximum drift and depletion distances. Figure 1.1 displays an ionizing particle traveling through a planar detector, while Figure 1.2 is a diagram of 3D electrodes. Advantages of three-dimensional (3D) electrodes include a greater resistivity to radiation damage, they read out faster and that the shape of the detector is not restricted to a square [3]. However, because the 3D etching process essentially turns the silicon into a sponge-like shape, it is more difficult to keep clean as there are more places for contaminants to settle. The manufacturing process itself is also more difficult than those of planar technologies.

## ATLAS

ATLAS, or A Toroidal LHC Apparatus, is one of the six particle detectors on the Large

Hadron Collider (LHC) at CERN in Geneva. It is designed to be a general-purpose detector, combining an inner detector to precisely record position of particles with outer layers of calorimeters, toroids and muon spectrometers to measure momentum and energy of particles resulting from a proton-proton collision [Fig. 2.1] [4]. The goals of the experiment range from completing the standard model to looking for evidence of dark matter, the Higgs boson, and supersymmetry, amongst other theories. The high energy capacity of the LHC (14 TeV) provides a unique opportunity to study never-before-seen physical phenomena, and the ATLAS experiment strives to gather as much information from the collisions in the LHC as is currently possible.

The very innermost layer of ATLAS is comprised of semiconducting silicon pixel detectors which precisely record the positions and vertices of charged particles resulting from the collision [Fig. 2.2]. These detectors need to be as precise as possible in order to detect potential particle decays by showing particle paths not originating from the position of the original collision. These decays can happen in a scale of nanometers, so reducing the noise to signal ratio is incredibly important.

The barrel and end disks of the pixel detector are made up of 1744 modules consisting of a silicon n+ on n sensor, 16 front end (FE) chips, and a module control chip (MCC) [Fig. 2.3]. The silicon sensor is what detects all of the particles that come in contact with the detector, and every pixel of the sensor is connected to a pixel on the front-end chip. The front end chip is a 3-D silicon chip that is a charge sensitive amplifier with leakage current subtraction, signal shaping, a programmable threshold discriminator, and Time over Threshold (ToT), i.e., an 8 bit measurement for charge amplitude. After the FE chip initially sifts through the data, it is sent to the MCC which combines the individual events and distributes trigger and command signals. The silicon sensor is glued to a kapton-flex hybrid and bump bonded to the FE chip, and the MCC and FE chips are connected through pigtail connectors [5, 6]

**CMS**

CMS, or the Compact Muon Solenoid, is another general purpose detector on the LHC with similar experimental goals as ATLAS. It consists of a large superconducting solenoid with calorimeters and muon chambers, and an inner core consisting of pixel detectors [Fig. 3.1] [7]. It also has three barrel layers of modules but has only two end-cap disks with modules tilted at 20 degrees to form a fan shape, in contrast to the ATLAS detector which has three flat end cap disks on each end [Fig. 3.2]. This layout is used to induce charge sharing so that the drift direction is not parallel to the magnetic field [8].

The CMS modules are also very similar to those of ATLAS, consisting of an n+ on n silicon sensor bump bonded to 3-D silicon readout chips (ROCs) glued to a high-density interconnect (HDI) which holds the Token Bit Manager Chip (TBM). The ROCs have similar functions to the FE chips on the ATLAS modules, and the TBMs control the readout of the ROCs, again similar to the MCCs on ATLAS. The main differences between the two experiments are in the designs of each of the components and in their size. For example, the ROCs on CMS have 80 x 52 pixels, and a pixel size of 100 $\mu$m x 150 $\mu$m, while the FE chips on ATLAS have 160 x 18 pixels and a pixel size of 50 $\mu$m x 400 $\mu$m. Both have a resolution of 10 $\mu$m in the $r\phi$ coordinate system, but the chip design clearly differs [8, 9]. The two experiments are intended to complement each other in their searches for physical phenomena.

**SINTEF Wafer Problems**

Wafers made at SINTEF in Norway have been found to have an extremely high leakage current for an unknown reason. The leakage current is large enough to occupy most and sometimes all of the dynamic range of the detector. The dynamic range is the maximum signal that the detector can handle, so if the signal is occupied by leakage current, the detector will not be able to sense any signal from particles. High leakage currents in the detector also cause it to draw a great deal of power, which should be reduced to save operating costs. In an effort to understand this, both ATLAS and CMS chips made at SINTEF have been

tested at various stages in the manufacturing process. The CMS chips have been showing significantly less leakage current than the ATLAS chips, so this has led some to theorize that differences in the packaging and handling or the intrinsic geometry of the two have caused this disparity. Figures 4.1 and 4.2 show some past data on the ATLAS and CMS chips taken after bumps had been added but before the chips were diced.

## MATERIALS AND METHODS

In order to add some insight into the problem, a wafer from SINTEF sent to SLAC that had only one edge cut and indium bumps added was tested. Voltage probes with an optical microscope were used to measure the leakage current in the different chip designs on different areas of the chips. The areas tested on each chip differs and a bias voltage of 10-50V in intervals of 10 was used. The wafer was tested at roughly room temperature in a non-clean environment.

**Types of Chips on SINTEF Wafer [Fig. 5.1]**

- "Baby ATLAS" – These are small versions of the sensors that match the FEI3 chips, the front end chips currently in the ATLAS detector, created to study their behavior in smaller sizes. These range from having 1 to 5 (1E-5E) columns per pixel, and all of the pixels are connected together. They are located mainly along the edges of the top half of the wafer. The leakage current between the active edges and the chip's test pad was tested [Fig. 5.2].

- FEI3 – These match the FE chips currently in the ATLAS detector, which have a range of 1E-5E. They are located on the bottom half of the wafer. The leakage current between the active edge and the top right, center and bottom right pixels was tested by making contact with the voltage probe and the indium bump for that pixel.

- FEI4 – These are larger versions of the FEI3s, possibly to be incorporated into the next ATLAS upgrade, both of which are 2E. They are the two largest chips in the center of the top half of the wafer. The leakage currents between the top right pixel, the center pixel and the bottom right pixel and the active edge were tested.

- CMS – The current sensors in the CMS experiment which are either 2E or 4E types. They are located on the right side of the top half of the wafer. Again, the leakage current between the top right and bottom right pixels and the active edge was tested. A second set of data on the leakage current between the edge, top right, center and bottom right pixels was taken.

# RESULTS

**Baby ATLAS**

Table 1.1 shows the total number of each kind of chip and the number and percent that broke down. The chips with the higher numbers of electrodes broke down more frequently than the others. However, this could be because those were most frequently along the edges of the wafer and many appeared to be damaged.

Table 1.2 and Figure 6 show the average leakage current by the number of electrodes per pixel. As the number of electrodes per pixel increases, so does the leakage current. The leakage current on almost all of the chips fluctuated widely, with some decreasing in current by about 30 nA per minute.

**FEI3**

Table 2.1 shows the number of each kind of chip on the wafer and the number and percent that broke down. Only two FEI3s broke down, possibly due to damage as one was along the sliced edge.

Table 2.2 and Figure 7 display the average leakage current by the number of electrodes

per pixel. Once more, we see an increasing leakage current with an increasing number of electrodes per pixel. The 4Es on this chip were consistently unstable at higher voltages with some decreasing by about 10 to 30 nA per minute at 50 V. The area and number of pixels measured with the technique of contacting the voltage probe with an indium bump is unclear, so it is difficult to compare these measurements to the those on the "Baby ATLAS" chips, the FEI4s and the CMS chips, but a similarity in behavior with the CMS chips will be assumed.

**FEI4**

Only two FEI4 chips were on the wafer tested, and neither broke down. However, the bottom right pixel of the FEI4 on the top had an extremely high leakage current which showed a more exponential shape. The bottom right pixel of that chip also had a rapidly fluctuating current, that differed around 10 nA. Comparing the leakage current measurements of these chips is difficult, as it is unclear how many pixels were measured. Table 3.2 and Figure 8 shows the leakage currents of the two chips at each of the pixels measured.

**CMS**

Table 4.1 shows the number of CMS chips on the wafer of each type as well as the number and percent that broke down. Only one CMS chip broke down, which could have also been due to damage, as the chip was along the top edge.

Table 4.2 and Figure 9 display the average leakage currents for the chips by number of electrodes per pixel. Figure 9 separates the data by which pixel the data was taken from. The top right pixels of the 2E chips all showed a rapidly increasing leakage current with an exponential shape, while the data from the other pixels on all of the other chips kept a much lower leakage current with a more linear shape. The 4Es also were unstable at higher voltages, decreasing in current from 10 to 40 nA per minute at 50 V.

# DISCUSSION AND CONCLUSIONS

## Discussion

*FEI3 vs. FEI4*

Figure 10 shows the average leakage current over the three points taken on the chip of the 2E FEI3s and the two FEI4s. The bottom right pixel of the top FEI4 was not included as it showed break down level leakage current while the bottom right pixel of the other did not. The FEI4s had about 3 times as more leakage current. However, it is difficult to know how many pixels the data includes so because the FEI4 pixels are smaller than those on the FEI3s; the data taken could be including more pixels on the FEI4s than the FEI3s. Additionally, a statistics issue needs to be taken into account since the sampling of FEI4s was much smaller than that of the FEI3s.

*FEI3 vs. CMS*

Figures 11 and 12 show the average leakage current over the three points taken on the chip of the FEI3s and the CMS chips separated by the number of electrodes per pixel. On both chip types, the FEI3s showed a lower leakage current than the CMS chips, contradicting past data. Again, there could be an issue with sample size because there were about twice as much FEI3s than CMS chips, so the CMS data could be more skewed. The chips that broke down of either type were not included in the averages.

## Conclusion

The SINTEF wafer shows completely different behavior than the others, as the FEI3s actually performed better than the CMS chips. Therefore this data argues against the differences in packaging and handling or the intrinsic geometry of the two as a cause in the disparity between the leakage currents of the chips. Even though the leakage current in the FEI3s overall is lower, the current is still significant enough to cause problems. As this wafer was not diced, nor had it any copper added for bump bonding, this data argues against the

dicing and bump bonding as causes for leakage curent.

To compliment this information, more data will be taken on the efficiency of the individual electrodes of the ATLAS and CMS chips on this wafer. The electrodes will be shot perpendicularly with a laser to test the efficiency across the width of the electrode. A mask with pinholes has been made to focus the laser to a beam smaller than the width of an electrode in order to properly scan it. This will provide more information on whether something in the electrodes, such as the polysilicon filling, is contributing to the leakage current or if there is another cause to be found. It will also reveal whether the diborane doping method and the new polysilicon filling has increased the electrode efficiency as expected. Thus, the cause of these leakage currents on the wafers from SINTEF has yet to be definitively found.

# FIGURES AND TABLES

## Figures

Fig. 1.1 - Ionizing Particle Traveling Through a Planar Detector

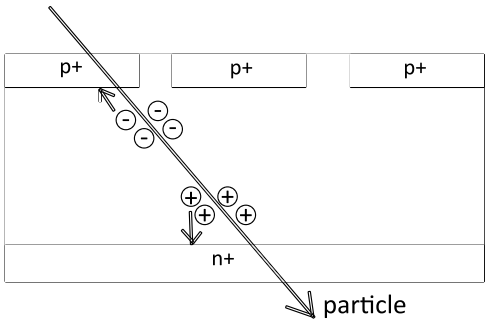

Fig. 1.2 - Three-dimensional view of electrodes in a 3-D detector [10]

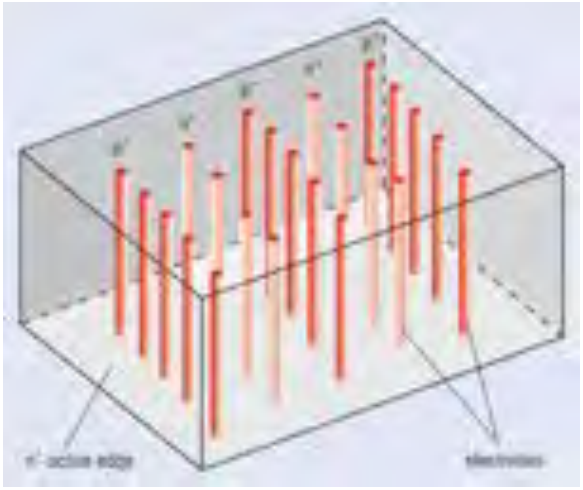

Fig. 2.1 - Overall ATLAS Diagram [4]

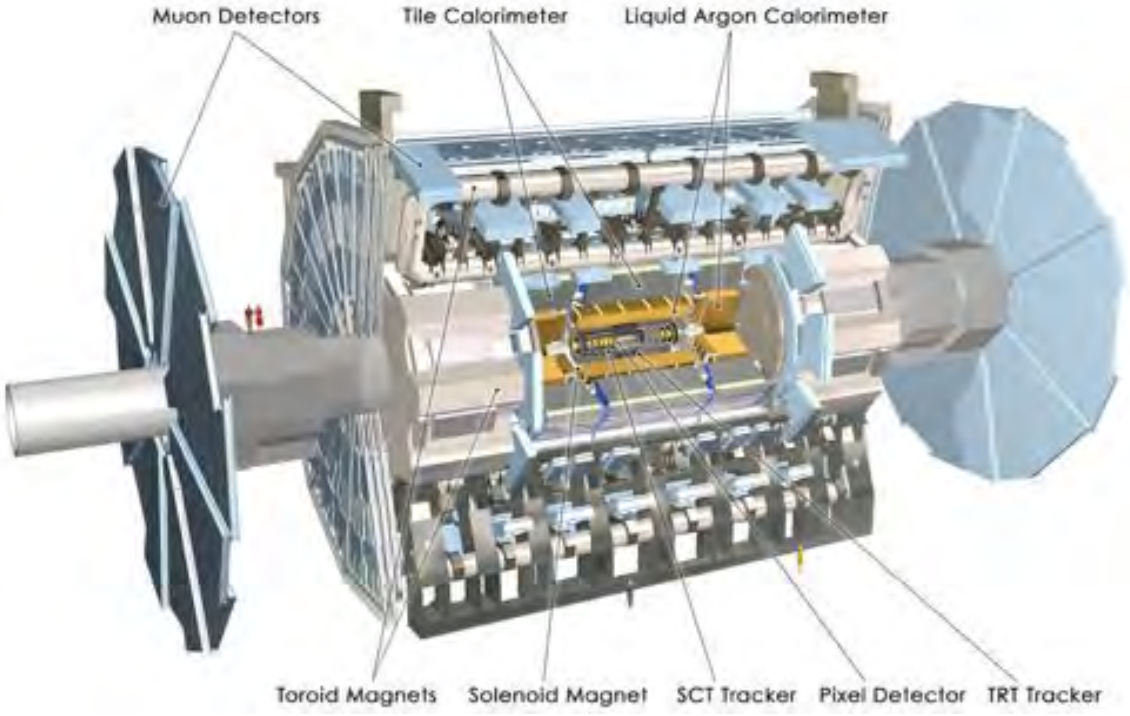

Fig. 2.2 - ATLAS Inner detector [11]

Fig. 2.3 - ATLAS Module [9, 6]

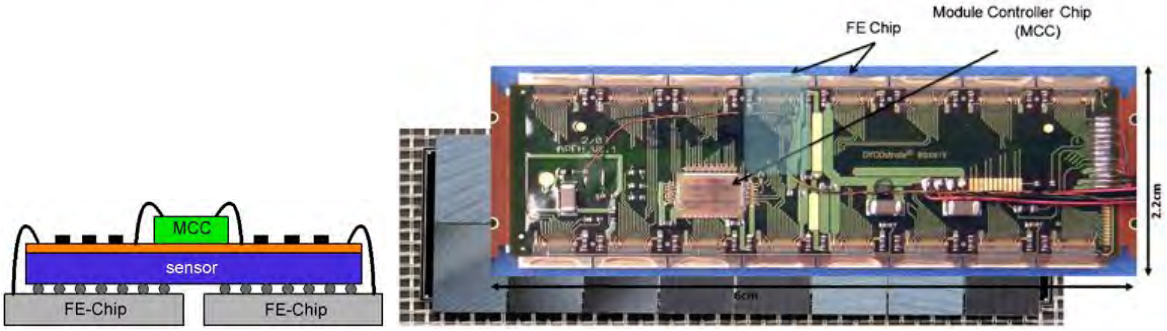


Fig. 3.1 - CMS detector [12]

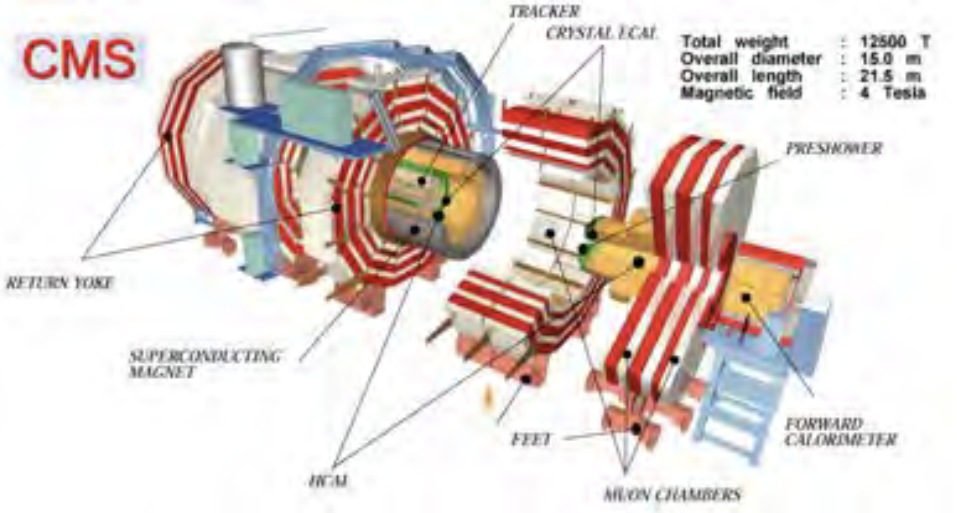

Fig. 3.2 - CMS inner detector [7]

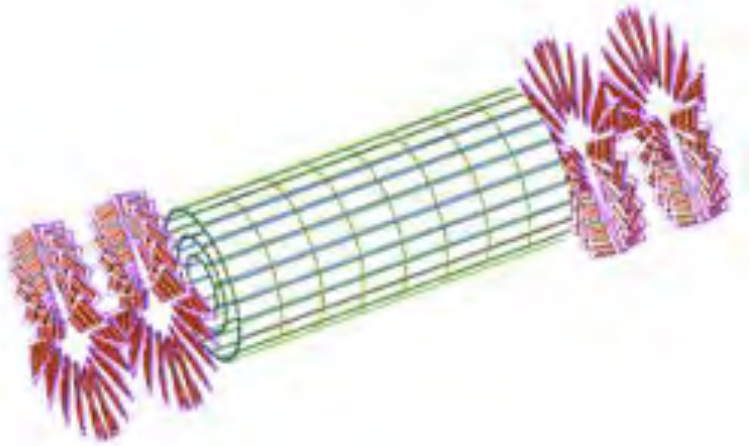

Fig. 4.1 - FEI3 data taken at SINTEF with bump-bonding [13]

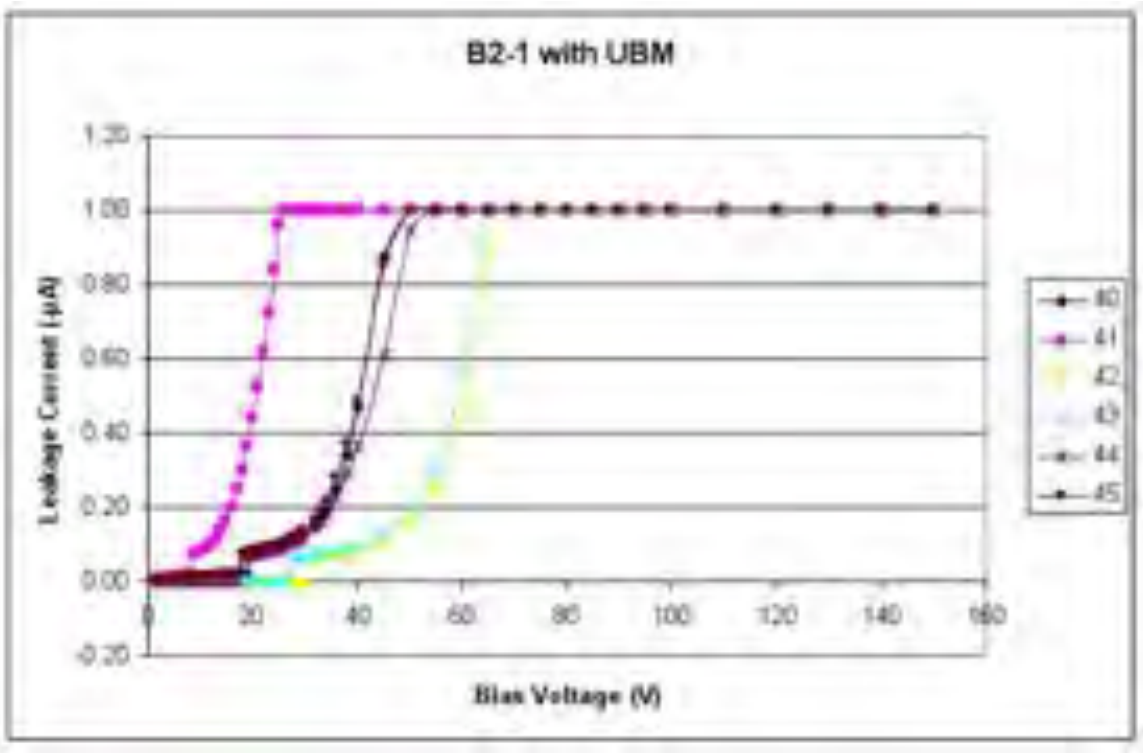

Fig. 4.2 - CMS data taken by Purdue and Fermilab [13]

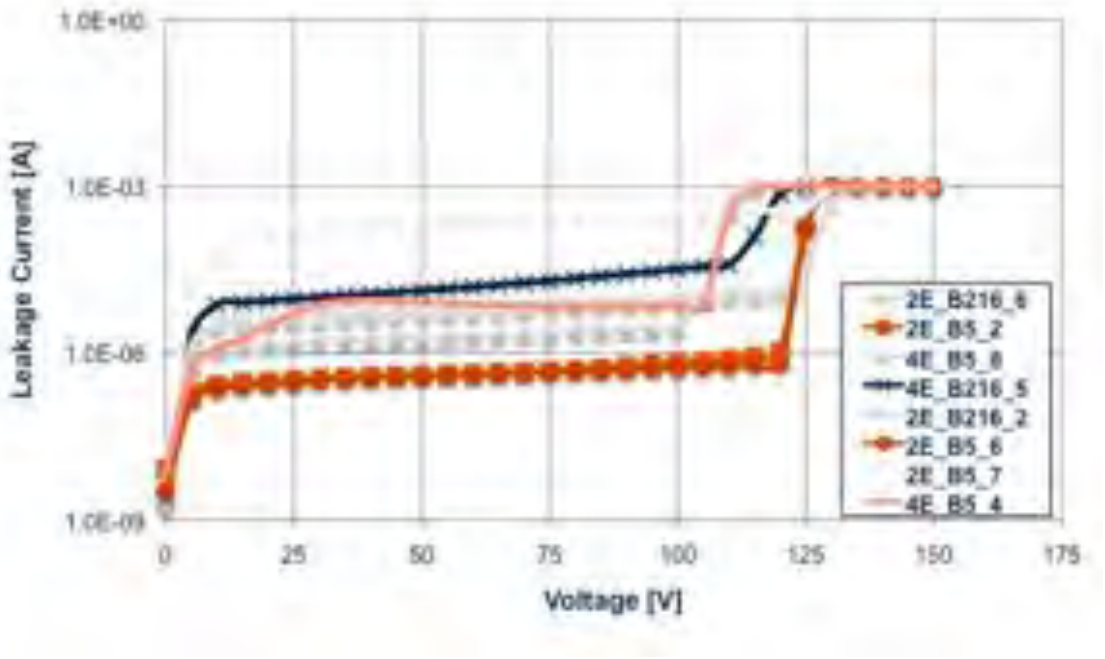


Fig. 5.1 - SINTEF Test Wafer

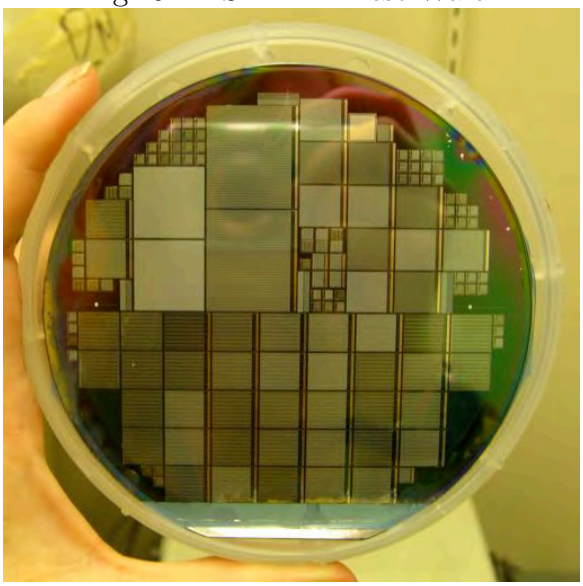

Fig. 5.2 - “Baby ATLAS” [13]

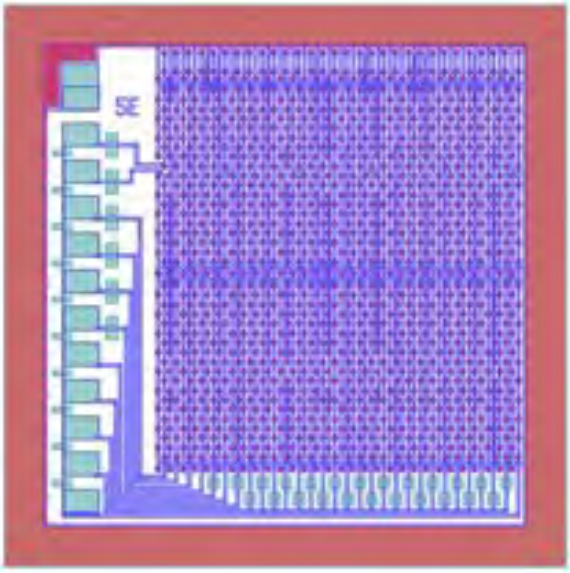


Fig. 6 -“Baby ATLAS” Average Leakage Current

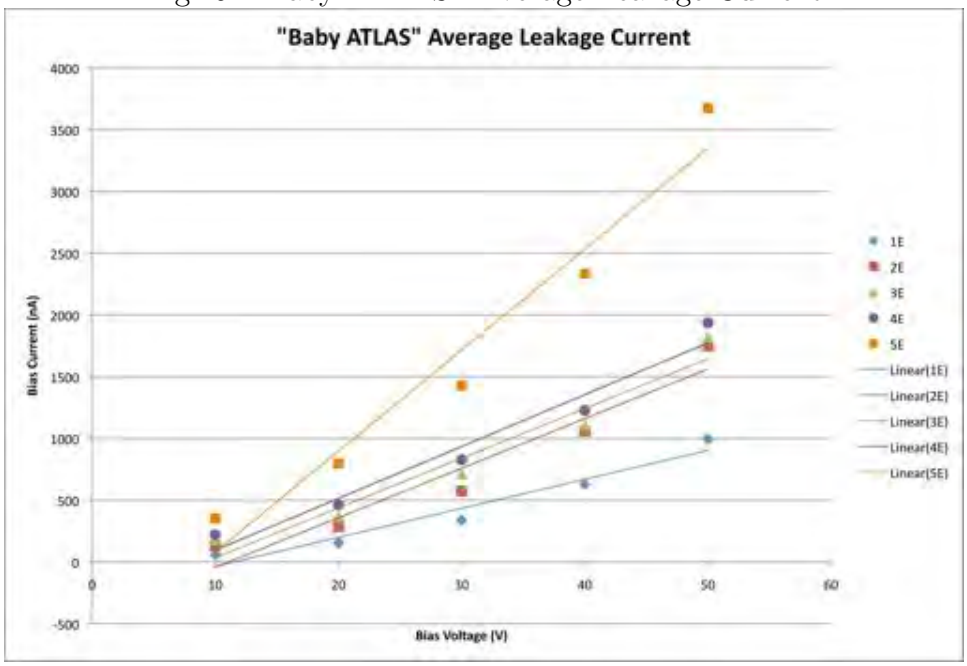

Fig. 7 - FEI3 Average Leakage Current

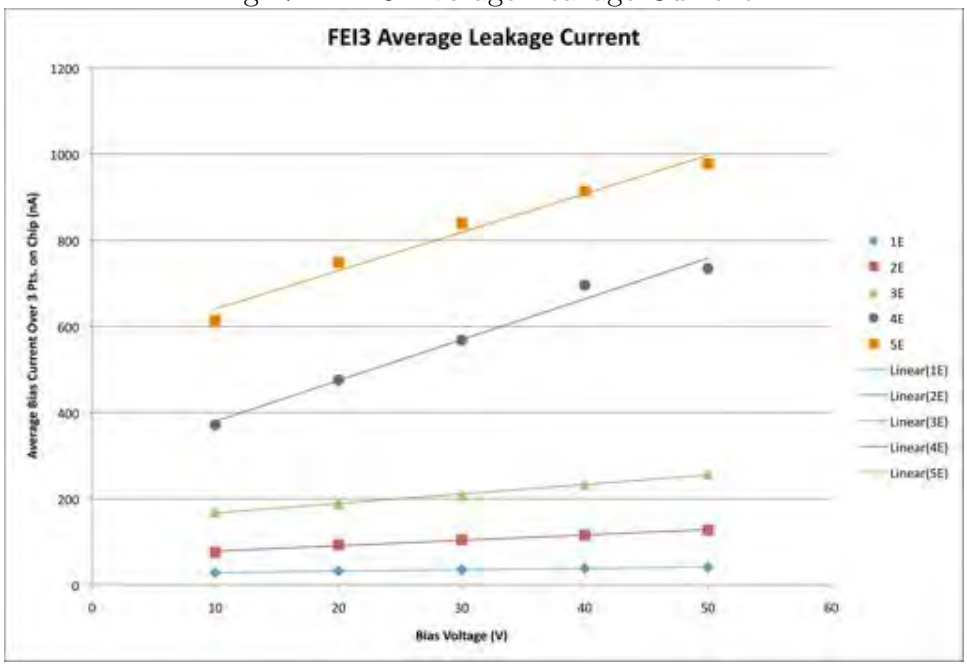


Fig. 8 - FEI4 Leakage Current

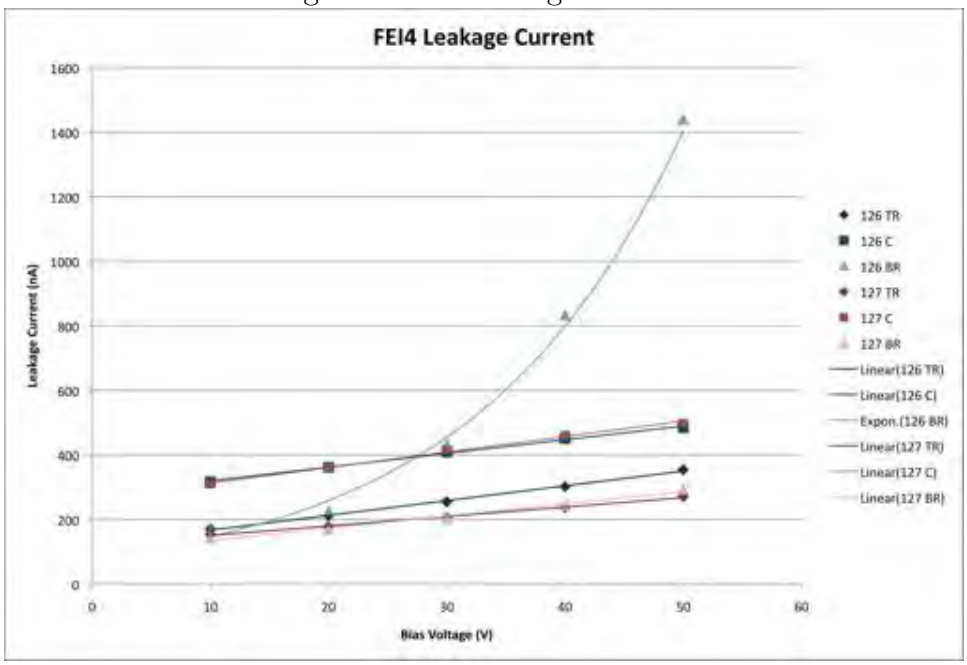

Fig. 9 - CMS Average Leakage Current

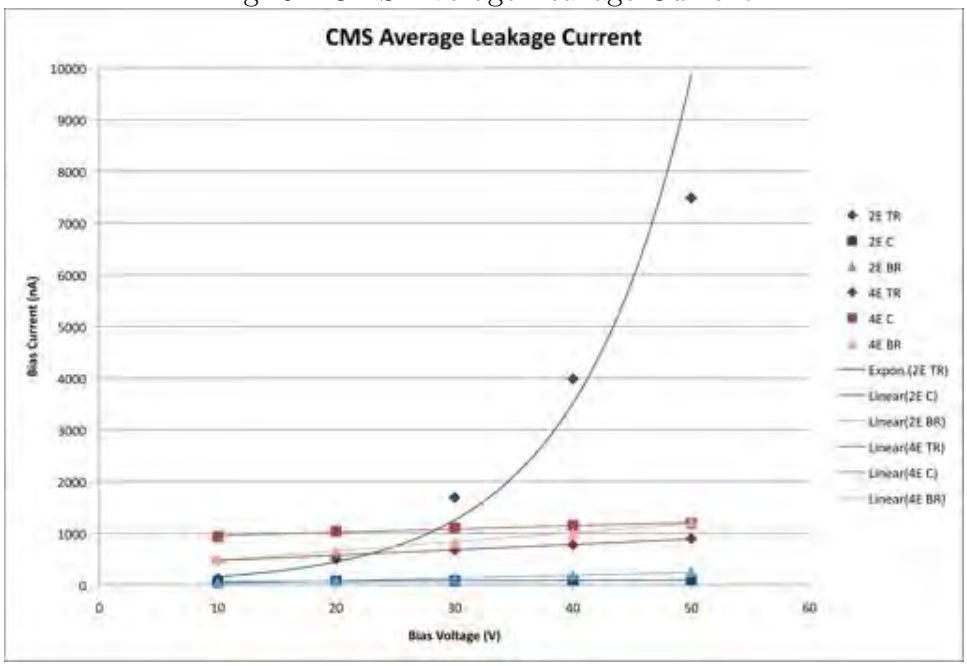


Fig. 10 - FEI3 vs. FEI4 Average Leakage Current

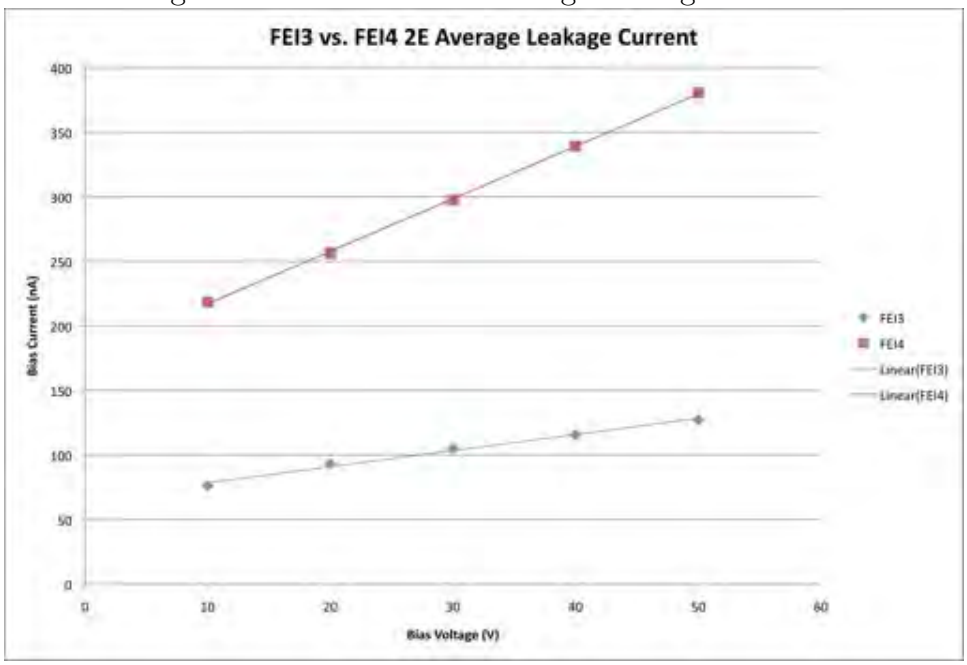

Fig. 11 - FEI3 vs. CMS 2E

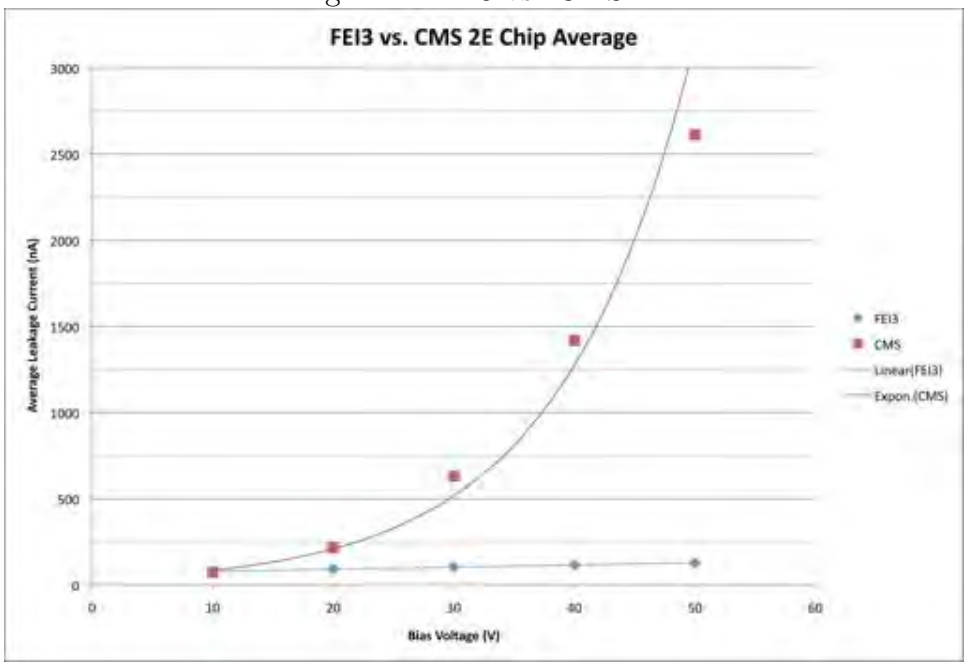


Fig. 12 - FEI3 vs. CMS 4E

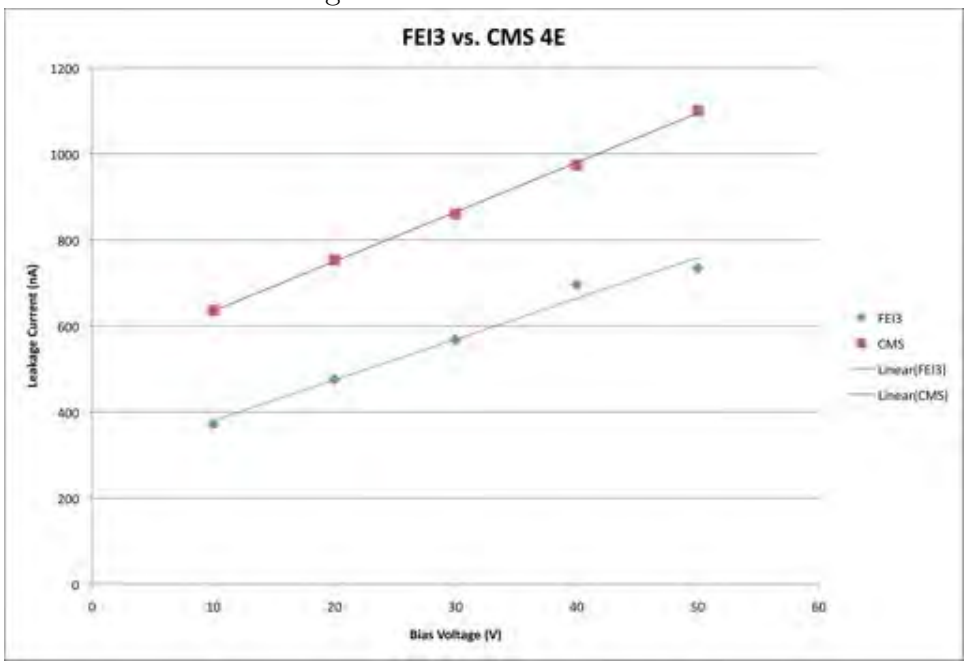

**Tables**

Table 1.1 - "Baby ATLAS" Table of % Break Down

| # of Columns | # on Wafer | #BD | % BD of Total |
|---|---|---|---|
| 1E | 12 | 1 | 8% |
| 2E | 12 | 4 | 33% |
| 3E | 12 | 2 | 17% |
| 4E | 13 | 3 | 23% |
| 5E | 12 | 5 | 42% |
| Total | 61 | 15 | 25% |

Table 1.2 - "Baby ATLAS" Average Leakage Current (nA) Separated by # of Electrodes

| # of Columns | 10 V | 20 V | 30 V | 40 V | 50 V |
|---|---|---|---|---|---|
| 1E | 58.182 | 154 | 337.455 | 626.364 | 995.455 |
| 2E | 130.125 | 282 | 575.375 | 1059.5 | 1748.75 |
| 3E | 179 | 371.2 | 714.5 | 1113.5 | 1821 |
| 4E | 220 | 462.1 | 828.1 | 1226.9 | 1936 |
| 5E | 351.714 | 796.571 | 1427.143 | 2332.857 | 3672.857 |

Table 2.1 - FEI3 Table of % Break Down

| # of Columns | # on Wafer | #BD | % BD of Total |
|---|---|---|---|
| 1E | 2 | 0 | 0% |
| 2E | 10 | 0 | 0% |
| 3E | 6 | 0 | 0% |
| 4E | 11 | 2 | 18% |
| 5E | 2 | 0 | 0% |
| Total | 31 | 2 | 6% |

Table 2.2 - FEI3 Average Leakage Current (nA) Separated by # of Electrodes

| # of Columns | 10 V | 20 V | 30 V | 40 V | 50 V |
|---|---|---|---|---|---|
| 1E | 28.333 | 32.333 | 35.667 | 38.167 | 41.167 |
| 2E | 76.033 | 93.1 | 105.1 | 115.567 | 127.267 |
| 3E | 169.333 | 188.444 | 208.056 | 232.389 | 257.5 |
| 4E | 371.467 | 475.633 | 568.233 | 696.033 | 734.348 |
| 5E | 614 | 748.833 | 839.333 | 913.667 | 977.5 |

Table 3.1 - FEI4 Leakage Current (nA) On Different Areas of Chip

| Die # | Test Pixel | 10 V | 20 V | 30 V | 40 V | 50 V |
|---|---|---|---|---|---|---|
| 126 | TR | 170 | 212 | 255 | 302 | 354 |
| 126 | C | 317 | 362 | 409 | 451 | 485 |
| 126 | BR | 165 | 227 | 433 | 834 | 1440 |
| 127 | TR | 154 | 178 | 206 | 237 | 271 |
| 127 | C | 309 | 361 | 415 | 462 | 499 |
| 127 | BR | 143 | 170 | 203 | 244 | 294 |

Table 4.1 - CMS Table of % Break Down

| # of Columns | # on Wafer | #BD | % BD of Total |
|---|---|---|---|
| 2E | 5 | 0 | 0% |
| 4E | 6 | 1 | 17% |
| Total | 11 | 1 | 9% |

Table 4.2 - CMS Average Leakage Current (nA) Separated by # of Electrodes

| # of Columns | 10 V | 20 V | 30 V | 40 V | 50 V |
|---|---|---|---|---|---|
| 2E | 73.067 | 216.267 | 630.8 | 1418.467 | 2612.2 |
| 4E | 635.8 | 753.4 | 860.667 | 974 | 1100.6 |

## ACKNOWLEDGMENTS

I would like to first thank Chris Kenney, my mentor, for all of the help he's given me this past summer and for trying his best to give me a great project. I'd also like to thank John Morse, Steven Veljovic and Philippe Grenier for helping me out. Also, Steve Rock, Eric Shupert and Christine Green have done a wonderful job organizing the SULI Program this summer, and I'm grateful for the work they've done. Last but not least, I'd like to thank all of the SLAC SULI students this summer, since they've really helped make my summer great and because we've all been so supportive of each other. Thanks everyone.

## REFERENCES

[1] G. Lutz, *Semiconductor Radiation Detectors.* Springer, 1999.

[2] A. S. Grove, *Physics and Technology of Semiconductor Devices.* Wiley, 1967.

[3] J. S. Christopher Kenney, Sherwood Parker and C. Storment, "Silicon detectors with 3-d electrode arrays: Fabrication and initial test results," *IEEE Transactions on Nuclear Science*, vol. 46, no. 4, 1999.

[4] G. Aad *et al.*, "Atlas fact sheet," 2010. [Online]. Available: http://atlas.ch/pdf/atlas_factsheet_all.pdf

[5] J. Grosse-Knetter, "The atlas pixel detector," *Nuclear Instruments and Methods in Physics Research A*, vol. 568, 2006.

[6] W. Fernando, "Overview and status of atlas pixel detector," *Nuclear Instruments and Methods in Physics Research A*, vol. 596, 2008.

[7] A. Dominguez, "The cms pixel detector," *Nuclear Instruments and Methods in Physics Research A*, vol. 581, 2007.

[8] D. Bortoletto, "The cms pixel system," *Nuclear Instruments and Methods in Physics Research A*, vol. 579, 2007.

[9] M. Cristinziani, "The atlas pixel detector," *Nuclear Instruments and Methods in Physics Research A*, vol. 582, 2007.

[10] C. DaVia, "Radiation hard silicon detectors lead the way," *CERN Courier*, 2003. [Online]. Available: http://cerncourier.com/cws/article/cern/28790

[11] G. Gagliardi, "The atlas pixel detector: A hundred million channels vertex detector for lhc," *Nuclear Instruments and Methods in Physics Research A*, vol. 546, 2005.

[12] "Cms detector drawings," 2010. [Online]. Available: http://cms.web.cern.ch/cms/Resources/Website/Media/Images/Detector/DetectorDrawings/CMSnc.jpg

[13] A. Kok *et al.*, "3d processing status at sintef," powerpoint Presentation.

SLAC-TN-11-004

# Comparing the Calibration and Simulation Data of the Cryogenic Dark Matter Search

Anthony DiFranzo

Office of Science, Science Undergraduate Laboratory Internship (SULI)

Rensselaer Polytechnic Institute

SLAC National Accelerator Laboratory

Menlo Park, CA

August 20, 2010

Prepared in partial fulfillment of the requirements of the Office of Science, Department of Energy's Science Undergraduate Laboratory Internship under the direction of Rudy Resch at the Kavli Institute for Particle Astrophysics and Cosmology, Stanford Linear Accelerator Center.

Participant: _____

Signature

Research Advisor: _____

Signature

Work supported in part by US Department of Energy contract DE-AC02-76SF00515.

# TABLE OF CONTENTS

# ABSTRACT

Comparing the Calibration and Simulation Data of the Cryogenic Dark Matter Search. ANTHONY DIFRANZO (Rensselaer Polytechnic Institute, Troy, NY 12180) RUDY RESCH (Kavli Institute for Particle Astrophysics and Cosmology, Stanford Linear Accelerator Center, Stanford, CA 94025)

The Cryogenic Dark Matter Search, or CDMS, collaboration is preparing a new experiment called SuperCDMS. CDMS uses Germanium detectors to attempt the direct detection of dark matter. To do this, they measure the ionization and heat produced during an event where a WIMP scatters off of germanium crystal lattice. To prepare for the experiment the detectors are calibrated with various radioactive sources. The response of the detectors is also modeled by a Monte Carlo simulation. These simulations include modeling everything from the radiation production to the raw data collected by the detector. The experimental data will be used to validate the results of the detector simulation.

This research will look only at the phonons produced during events that occur very close to the detector surface. From the raw data and simulation output three parameters will be determined: the rise time, the decay time, and time to position independence. It was found that the simulation's risetime and time to position independence was generally smaller than that of the data, while the decay time was found to be larger in the simulation than in the data. These differences show that the simulation is not complete. The difference in risetime implies that the phonons are not spread out enough when they reach the detector walls, which would be improved by a look at the Luke phonon and charge transport. The long decay time in the simulation implies that the rate phonons are being absorbed is underestimated. Finally, the small time to position independence in the simulation could be due to a low phonon scattering rate. A simple solution may be to alter the parameters that control the simulation, while still remaining physically sensible, to help match simulation and data.

# INTRODUCTION

In 1934, Dark Matter was first hypothesized by Fritz Zwicky after approximating the mass of galaxies in the Coma Cluster. This average mass was two orders of magnitude greater than expected from the cluster's luminosity, he attributed the difference to what he called dark matter[1]. In 1959, Louise Volders discovered that the rotation curve of the spiral galaxy M33 did not match the predictions given by Newtonian Dynamics[2], see Figure 1 for a comparison of the expected and measured rotation curves. The two main hypotheses that resulted to explain these discoveries were the Modified Newtonian Dynamics, or MOND, and Dark Matter. MOND assumes that Newton's laws are incorrect at large distances, and the Dark Matter hypothesis says that there is invisible matter that is altering the gravitational field of a galaxy[3]. In 2006, a study was conducted on the Bullet Cluster, which consists of two galaxy cluster colliding. The visible matter, such as interstellar gas, was mapped using x-rays, while the total mass is mapped using gravitational lensing techniques, see Figure 2 for an image of this cluster. It was found that light was being bent where there was not very much visible matter, MOND is not able to explain this. It is believed that the collision separated the visible matter from the dark matter, which appears to have been formed in a halo around the galaxies.

Assuming Dark Matter exists, the first question one must ask is what is Dark Matter made of? It doesn't interact via the electromagnetic force, since we are not able to probe it with light. Dark Matter appears to be nearly non-interacting and predominantly non-relativistic, often referred to as cold. Of the many candidates, Weakly Interacting Massive Particles or WIMPs are the most prominent. A WIMP is a hypothetical class of particles and that are believed to interact only through the weak force and gravity include the neutralino, Kaluza-Klein particle, and branon[4]. The discovery of neutralinos would be particularly exciting as it would give credibility to the Supersymmetric model[5].

Now the hypothesis must be tested; how will WIMPs be detected? In a collider, WIMPs,

like neutrinos, must be found through the missing energy and momentum of a collision, as WIMPs will not interact well with detectors. Neutralinos are the most hoped for as constituents of dark matter. The neutralino is classified as a WIMP and is the supersymmetric partner of the neutrino, with an intrinsic spin of 3/2 as determined by supersymmetry. The highest energies are currently attained with hadron, rather than lepton, colliders. Since hadrons are not elementary, the momenta of their constituents are not very well defined. Therefore, colliders can introduce some complications, however this is still a viable route. Indirect detection is also possible by looking for WIMP pair annihilation in space; however this is accompanied by other difficulties. The third option is direct detection which looks for the elastic scattering of WIMPs with the nuclei of a particle detector[5].

The Cryogenic Dark Matter Search, or CDMS, is an experiment looking to directly observe these particles and hopefully determine their candidacy as constituents of Dark Matter. The experiment consists of germanium detectors, which must be held at millikelvin temperatures, to detect an interaction between a dark matter particle and a Ge nucleus. Since dark matter is believed to be spread throughout our galaxy and is slowly moving we can move the detectors through space to attain collisions. As the Earth and our solar system move through the dark matter halo of the Milky Way Galaxy, the detectors will hopefully interact with a Dark Matter particle[5].

Data has been taken on the detector and a simulation has been developed to as closely as possible represent the conditions under which the data was taken. The purpose of the research discussed here is to compare the data with the simulation of the detector. This will either validate our model or tell us what needs to be improved or changed.

The detector geometry used in this experiment is known as an Interleaved Z-sensitive Ionization and Phonon, or iZIP. The top and bottom of the Ge detectors have contacts to collect charge and phonons. Figure 3 shows an image of the iZIP detector mask. These contacts are partitioned into regions, in order to gain information about the location of an interaction. Sensitivity to both the distribution and timing of phonon collection between

each region determines where in the detector the event occurred. The phonon and charge channels allow us to determine the amount of energy in an interaction and are used to distinguish between nuclear and electron recoil, which is crucial in discriminating between signal and background. To further help with discrimination, these detectors are housed underground to reduce background events involving cosmic radiation.

Keeping the detectors at low temperatures has a dual purpose. First, a warm crystal lattice will naturally contain a high density of thermal phonons, which would swamp out any meaningful signal that might be present. Therefore, the detectors are held at millikelvin temperatures to minimize any presence of thermal phonons. Second, this low temperature is also required for our method of phonon detection. The phonon detection relies on Transition Edge Sensors, or TES, which need to be kept at the temperature where it transitions from a superconducting to normal state. Phonons are absorbed by the Quasiparticle-trap-assisted Electrothermal-feedback Transition-edge-sensor, or QET, a phonon will then break a cooper pair, which consists of two electrons bound together in a superconductor. The broken cooper pair releases quasiparticles which the QET is able to focus onto the TES at its center. The TES's heat up, bringing the sensor out of its superconducting state[6]. This transition is accompanied by a sharp, measurable increase in the resistance of the sensor, which is recorded as part of our data collection.

There are three forms of phonons in our detector that we must study to properly analyze the data. The first are called Luke phonons, these are radiated from charged particles that move greater than the speed of sound within that medium. This is analogous to Cherenkov radiation, where a charged particle radiates light when it moves faster than the speed of light in that medium. The second types are called intrinsic phonons, which are released at the position of the interaction. They usually undergo anharmonic decay, where a phonon will split into two phonons each with about half the energy of the parent phonon. The mean free path of this type of decay scales inversely to the phonon energy. Phonons with low enough energy will have a mean free path larger than the size of the detector. At this

point, the phonons are called ballistic; they bounce around the detector without scattering until it is absorbed. The third are known as recombination phonons[5]. These are released when electrons and holes recombine, often through a defect states rather than a direct transition across the band gap, known as Shockley Reed Hall recombination. The defect state population is usually greater at the edges of a crystal lattice; therefore most recombination phonons are created at the surfaces of the detector.

Charge transport will also be integral to modeling our detectors. An electric field is applied across the detector to draw electrons and holes to opposite sides of the detector. However, an important process to account for is oblique propagation. Here electrons will not travel in a straight line following the electric field. Instead, they will follow "energy valleys" within the germanium, this makes them travel at an angle to the electric field. However, the energy valleys for the holes are aligned with the electric field lines, so they do not experience this angled transportation described here.

## MATERIALS AND METHODS

The Monte Carlo simulation of the events serves as a way for us to prove we understand the detector. There are three distinct components to this simulation: radiation scattering, transport, and measurement. In the first step GEANT4 places the source near to one face of the detector, masks can be placed between the source and detector in the program to better replicate the experimental setup. The incident particles are then allowed to scatter within the Ge. GEANT4 simulates the positions and energies of these scattering events. In the second step, these positions and energies are used to determine the initial number and locations of the phonons and charges. These phonons and charges propagate through the detector and undergo the transport processes previously discussed. Finally, when they reach the surface the phonons are collected. For simplicity in the simulation, the detector faces are divided into regions. The number of phonons incident on each region are counted and

put through a simulation of the QET system. The final result is a pulse that models the output of the actual detector during a calibration data run.

In order to validate the simulation, we can compare to a calibration dataset on the detectors to which we will compare the simulation. The detectors are calibrated with radioactive sources such as Barium-133, Californium-252, and Cadmium-109. Each of these calibration sources provide a different type of event that we are interested in. Ba-133 produces relatively high energy electron and gamma rays, this will produce bulk electron recoils. Cf-252 produces neutrons which will produce nuclear recoils. Cd-109 produces lower energy electron and gamma rays, which produce electromagnetic events that occur very close to the surface of our detector[7]. We are specifically interested in surface events for this project, meaning Cd-109 will be used as the source for our data analysis. To ensure that the simulation and data are actually measuring the same thing, we can help ensure this by applying quality cuts to our data that remove events that do not match what the simulation is attempting to model. For example, we may be only looking at a certain energy range or perhaps we want to isolate surface events.

Both the data and simulation output raw pulses. These raw pulses are current measured through each channel, which is related to the number of phonons being absorbed. Figure 4 shows an example of such a data pulse. After some time phonons have diffused uniformly throughout the detector. At this point phonons must slowly leak out, leading to a long decay tail in the pulse that will be seen in all eight of the channels. The lower plot shows these same pulses but are all scaled so that the slow decay tails match up. Note that Figure 1 contains a diagram of the channel regions: one is located on the bottom and the other is located on the top of the detector. Also, note that the regions on top are orthogonal to the regions on the bottom which gives us more information on the position of events. See Figure 5 for a diagram of the channel geometry.

The data and simulation pulses are then analyzed. The preliminary analysis includes determining, for each event, the decay time, the rise time, the amount of energy deposited

into each channel, etc. These parameters are then plotted in a histogram so data and simulation can be directly compared. The histograms are normalized so that all their areas are unity. Observing differences at this level serves as a gauge of how well we understand our detector and can help determine the most important input parameters for the simulation.

I will focus on three parameters. The first is called the 10-40% Rise Time. This is the time between the points when the phonon pulse is 10 and 40% of its maximum height. This piece of data gives us information of phonon transportation, particularly the Luke phonons since they reach the detector surface first. This also serves to discriminate between event types. Surface events vary in recoil energy and ionization energy, therefore they can easily be misinterpreted as nuclear or electron recoil events. However, surface events are also accompanied by fast rise times, while bulk recoils tend to have slow rise times. Surface events tend to associate with faster risetimes because phonons produced close to the surface may not have a chance to down convert before being absorbed into the QET. This means that high energy phonons are being absorbed. These phonons are able to break several cooper pairs instead of one, which in turn produces a faster rise time.

The second parameter is the decay time. This is the time it takes for the pulse to decay to a factor of $e$ of its maximum height; this is a typical convention for any given exponential decay. The intrinsic phonons undergo anharmonic decay and eventually become ballistic. In this mode they are unlikely to down convert and will travel more readily to a surface. Therefore, the phonon pulse will decay faster as more and more phonons enter the ballistic regime. The decay time then allows us to see how long it takes before phonons become ballistic and if the down conversion process is properly modeled. This also tells us if our absorption rate into the QET is correct.

The third is known as the time to position independence. This is the amount of time before we can no longer tell where an event occurred by looking at the pulses. In other words, at this time phonons have diffused uniformly throughout the detector. This again will tell us if the phonon transport processes have been modeled properly. The main factor

influencing position independence is the down conversion rate, that is the rate at which phonons undergo anharmonic decay.

The aforementioned simulation must account for many processes, including those related to transportation in the crystal. Other basic considerations comprise probability of phonon absorption into the QET and how much energy will be collected into each partition in the sensor. The main goal of this research is to construct a complete analysis and comparison between simulation and calibration data sets. We are mainly concerned with data sets involving Cd-109, which as previously stated produces surface events.

## RESULTS

The following are all based on phonon output from Cd-109 simulation and data runs. The 10-40% Rise Time Histogram is shown in Figure 6. The top plots the rise time for the fastest channel for each event, note that this may not be the same channel for every event. The bottom plots the slowest risetime for each event. The data is plotted in gray and the simulation in black dotted lines. In the data, the slowest channel has a mean of 6 $\mu$s and a standard deviation of 3 $\mu$s, while in the simulation gives a mean of 4 $\mu$s with a standard deviation of 2 $\mu$s. The fastest channel has a mean of 54 $\mu$s in the data with a standard deviation of 12 $\mu$s. For fastest channel in the simulation the mean is 48 $\mu$s and a standard deviation of 8 $\mu$s. Note that these values are approximate.

The Decay Time histogram is shown in Figure 7. The differences are very apparent here, as the data distribution is broader and its mean is smaller than that of simulation. The data appears to decay about 200 $\mu$s faster than the simulation. However, they do share the same functional form: both have very clean Gaussian distributions. Also, note the height difference between the two distributions, this is due to normalization.

The Time to Position Independence Histogram is shown in Figure 8. The simulation shows position independence being reached around 250 $\mu$s, while data shows it to most

likely occur around 400 $\mu$s. Additionally, note that their functional forms match as they are both Gaussian with longer tails to the right.

## DISCUSSION AND CONCLUSIONS

For both the fastest and slowest risetimes the simulation appears to be slightly faster than the data. This could imply that the simulation Luke phonons reach the detectors too late, in that they are measured too close in time with phonons that should be arriving later. This effect should be sensitive to anharmonic decay since we are looking at surface events, meaning the decay rate may be too high. Another contributing factor will be our model of charge transportation, since it is the motion of the charges that produces these Luke phonons.

The simulation predicts a longer decay time than measured, which could indicate a problem with the QET model. If the absorption rate into the QET is underestimated, then phonons will remain in the detector for a longer period of time. The long decay time could also be due to the rate intrinsic phonons enter the ballistic regime. If the simulation underestimates the rate at which phonons down convert, it will also take longer for the pulse to decay.

The simulation predicts the events to reach position independence sooner than measured. This could mean that simulation phonons are down converting at too high of a rate. A high down converting rate will result in more athermal phonons, so they should statistically distribute themselves faster, which means the detector will reach position independence sooner.

## FUTURE WORK

The differences in the three parameters seem to be consistent. The absorption into the QET's and the rate of anharmonic decay seem to be common themes. It is not completely

clear as to how the anharmonic decay rate needs to be changed, though it appears to be too high. The next step is to tune the parameters used in the simulation to see if a good match can be made. If this fails then we will need to return to the physics processes involved and see what can be improved or included to better match what is physically occurring.

Currently, a probability is assigned to determine if a phonon is absorbed when it reaches a QET. A model of the physics occurring at the detector surface could be implemented to form a more physically realistic representation. The charge model could also be further developed; this should improve agreement in the rise times between data and simulation. Currently, the phonon pulse output is the majority of the analysis. If the simulation for measuring charge were improved it could also be used in the analysis, and could at least help our understanding of Luke phonon production. Further analysis needs to be done to determine what is actually causing the differences between data and simulation.

The SLAC CDMS group now has more data and simulation analyzed. The program to do these comparisons is now fully functioning, therefore other data sets can be analyzed with minimal changes to the program code. Germanium is also not well understood at very low temperatures, so the data taken will help us to determine what changes to make to our model. Outside of the comparison, the simulation can also be used to test different detector geometries before they are made. Though this method is not perfect, it will be very useful to exclude certain geometries before the trouble is gone through to fabricate the detectors.

## ACKNOWLEDGMENTS

This work was conducted at SLAC National Accelerator Laboratory and was funded by the United States Department of Energy, through the SULI program. I would like to thank my mentor, Rudy Resch, for his guidance and taking the time to explain what I didn't understand. I would also like to thank Dr. Eduardo do Couto e Silva, for checking in on my progress and moving my project along near stumbling blocks. The whole CDMS

collaboration at SLAC has been very helpful and supportive of my project; I want to thank all of them. The SULI staff, who worked to make this program run smoothly, provided great lectures for us, and ensured we had a productive summer. Finally, I want to thank all of my fellow SULI students who made this summer exciting and more than just about research.

## REFERENCES

[1] F. Zwicky, "On the Masses of Nebulae and of Clusters of Nebulae," *Astrophysical Journal*, vol. 86, p. 217, October 1937.

[2] L. Volders, "Neutral Hydrogren in M 33 and M 101," *Bulletin of the Astronomical Institutes of the Netherlands*, vol. 14, pp. 323–334, 1959.

[3] R. Sanders and E. Noorfermeer, "Confrontation of MOND with the Rotation Curves of Early-type Disc Galaxies," *Mon.Not.Roy.Astron.Soc*, p. 9, February 2008.

[4] C. N. Bailey, "The Cryogenic Dark Matter Search: First 5-Tower Data and Improved Understanding of Ionization Collection," Ph.D. dissertation, Case Western Reserve University, Cleveland, January 2010. [Online]. Available: http://cdms.berkeley.edu/Dissertations/cnbailey_thesis.pdf

[5] J. Filippini, "A Search for WIMP Dark Matter Using the First Five-Tower Run of the Cryogenic Dark Matter Search," Ph.D. dissertation, University of California, Berkeley, Berkeley, December 2008. [Online]. Available: http://cdms.berkeley.edu/Dissertations/filippini.pdf

[6] S. Leman, "Development of Phonon-Mediated Transition-Edge-Sensor X-ray Detectors for Use in Astronomy," Ph.D. dissertation, Stanford University, Palo Alto, September 2006. [Online]. Available: http://proquest.umi.com/pqdlink?vinst=PROD&attempt=1&fmt=6&startpage=-1&ver=1&vname=PQD&RQT=309&did=1221714061&exp=08-08-2015&scaling=FULL&vtype=PQD&rqt=309&TS=1281375994&clientId=83448

[7] Z. Ahmed *et al.*, "Analysis of the Low-Energy Electron-Recoil Spectrum of the CDMS Experiment," *Physical Review D*, vol. 81, p. 4, July 2009.

# FIGURES

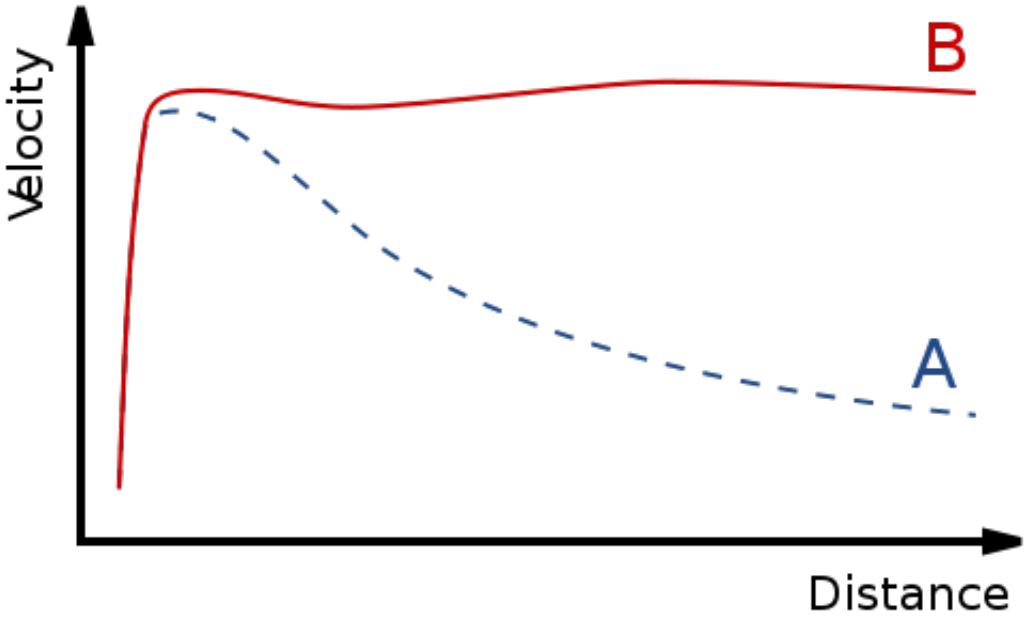


Figure 1: An example of a galaxy curve, note that distance is measured radially from the center of a galaxy. With Newtonian Dynamics we expect curve A, however we observe curve B.

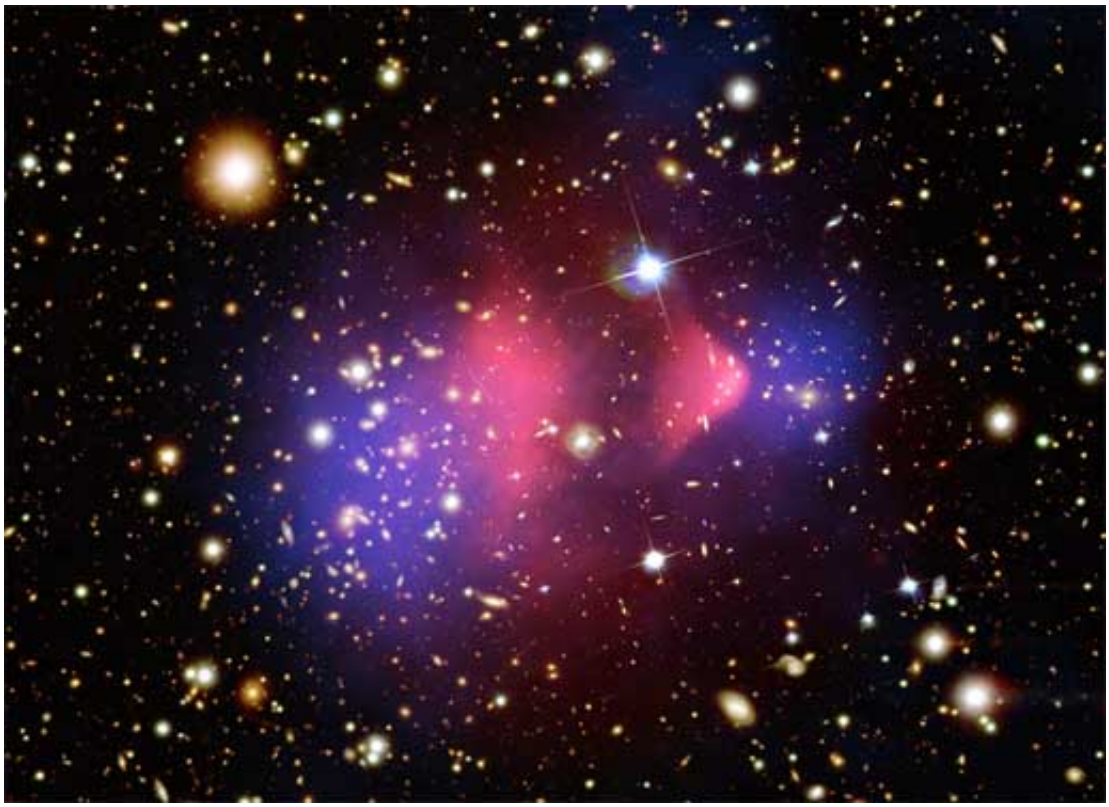

Figure 2: This is an x-ray and gravitational map of the Bullet Cluster. The pink at the center represents the x-ray image of the interstellar gas, while the blue is the dark matter that been separated from the rest of the cluster. The dark matter here was mapped using gravitational lensing.

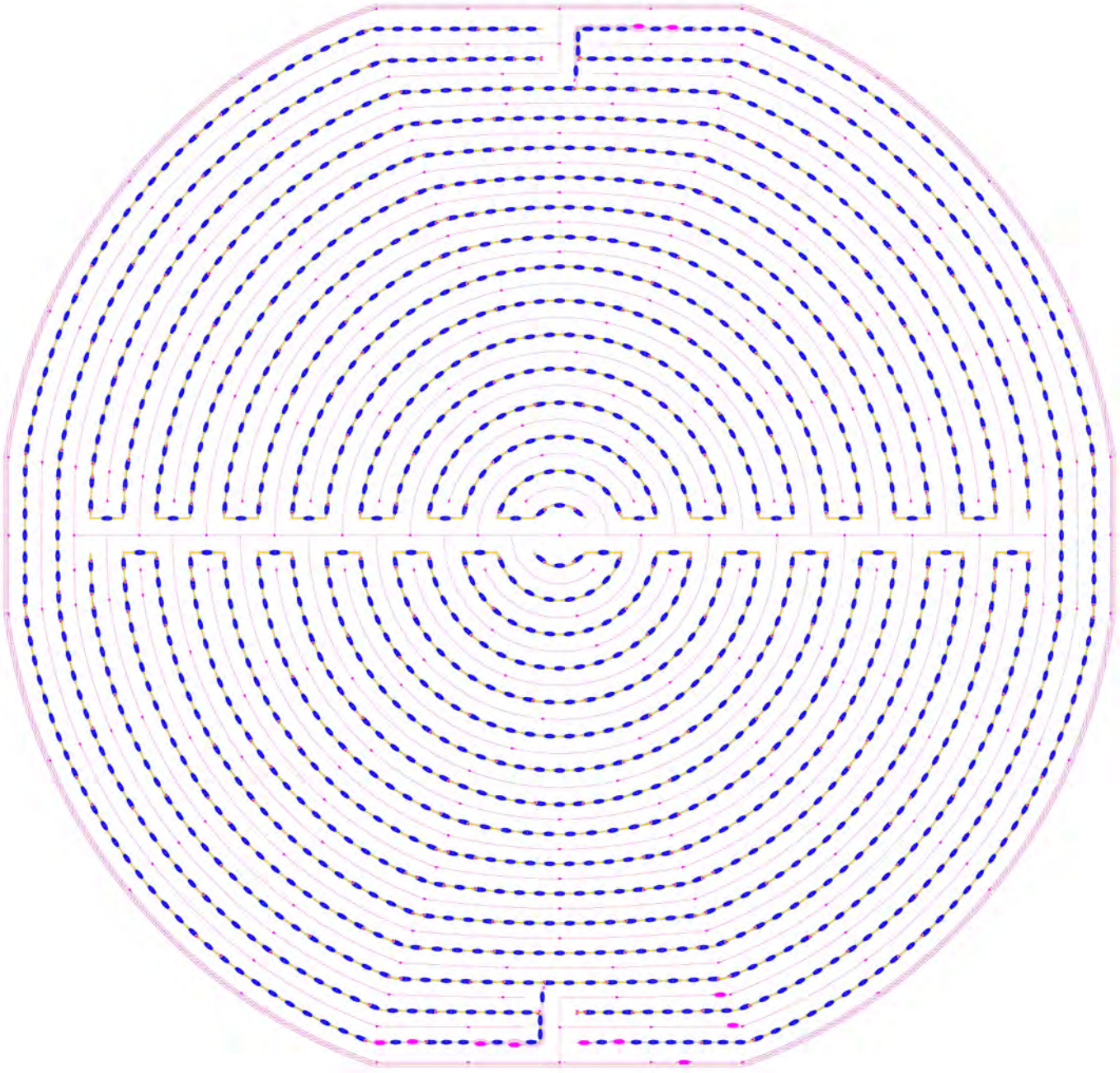

Figure 3: This is an image of the sensor geometry placed on the top of the detector. The blue sensors are the QET's, which contain the TES's. The pink sensors collect the charge. There are four separate sets of QET's on this side, all QET's that are connected are part of the same channel.

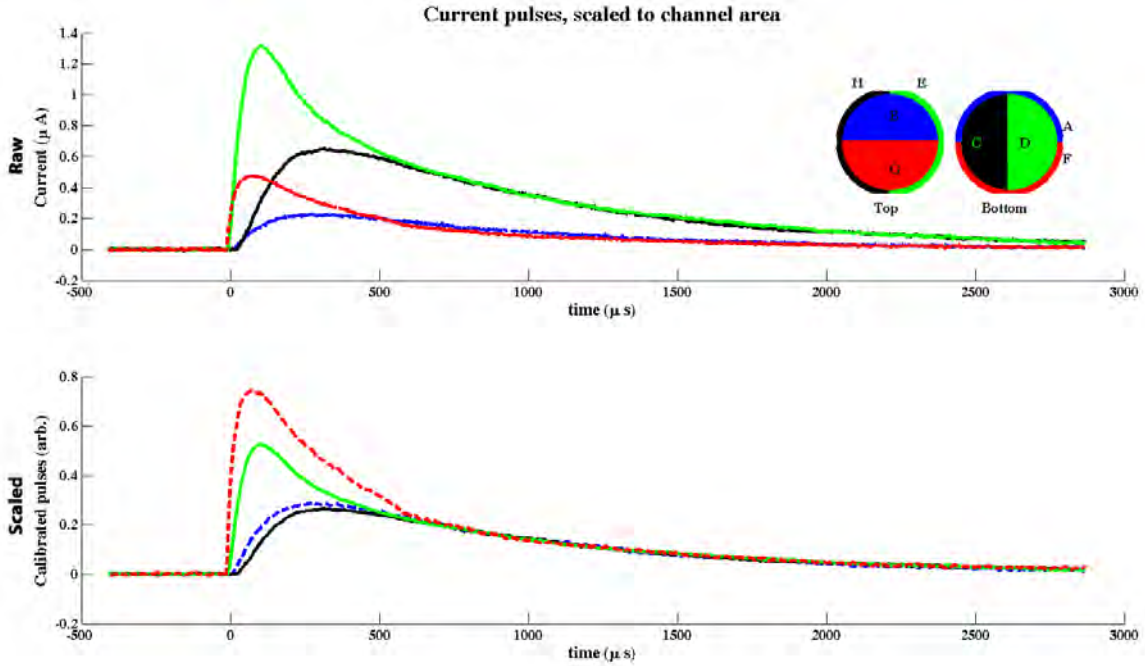


Figure 4: A typical plot of the phonon pulse. The top contains the raw data pulses, the bottom pulses are scaled. A diagram of the sensor regions on the detectors are located in the upper right corner. Note that only the bottom four channels have been plotted for simplicity. The dotted lines denotes data from an outer channel.

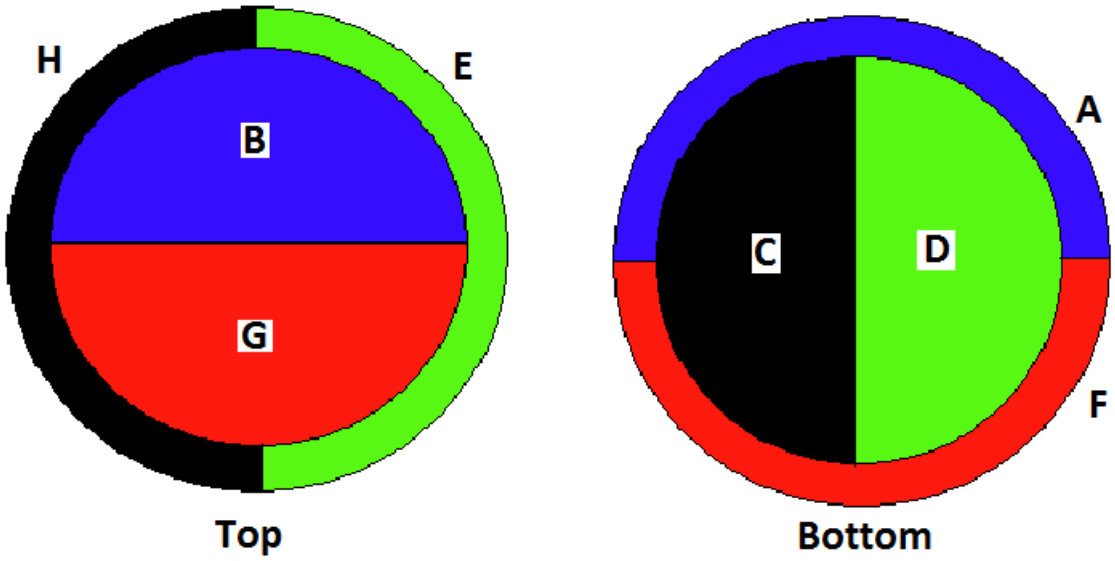


Figure 5: A diagram of the eight channels, which are located on the top and bottom of the detector. Channels labeled A, E, F, and H are called outer channels, while those labeled B, C, D, and G are known as inner channels. The top and bottom surfaces are oriented so that their geometries are orthogonal. A separate pulse is attained from each of the eight.

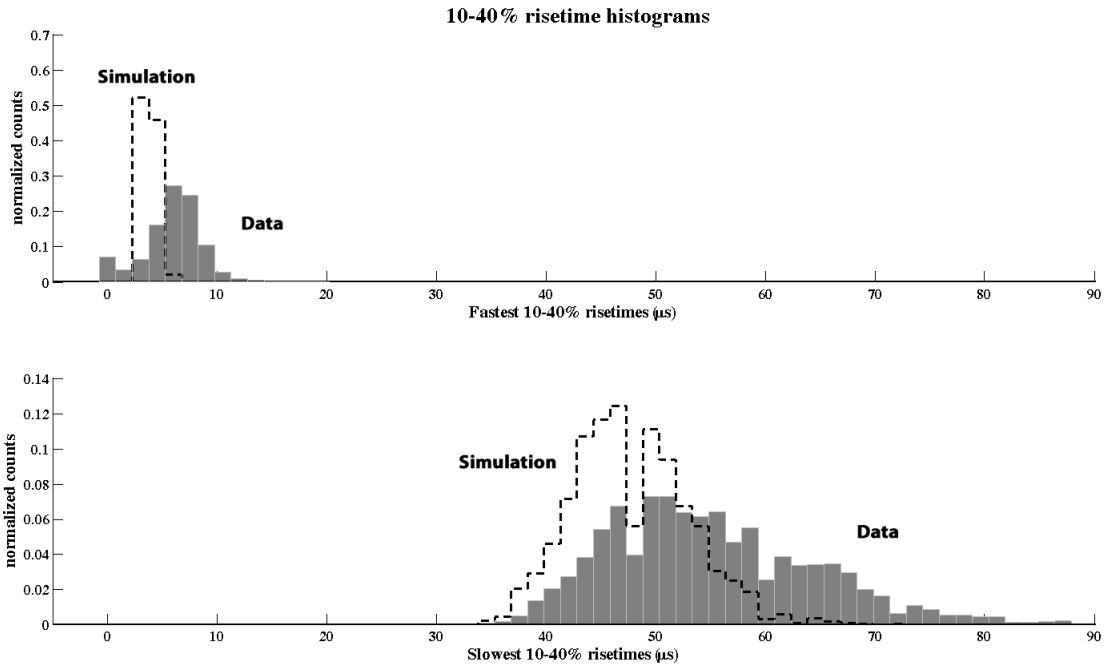


Figure 6: A plot of the slowest(top) and fastest(bottom) risetime for each event. Data is in gray and simulation is outlined in black dotted lines. The data for each has a similar range and distribution.

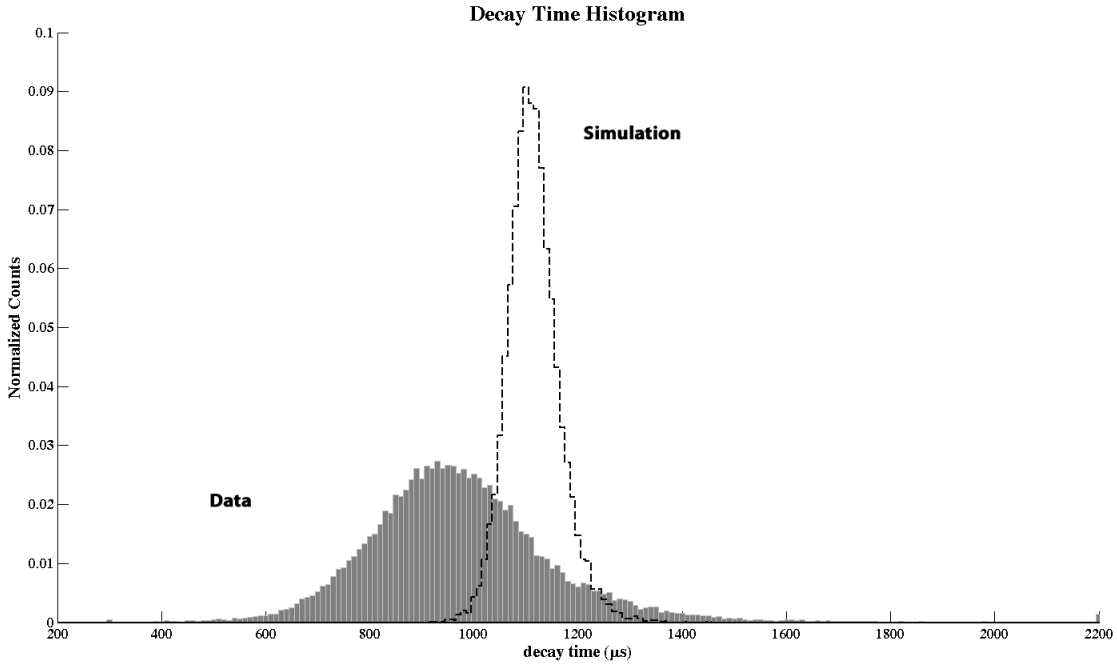


Figure 7: The distribution of the decay times for data and simulation. The simulation has a longer decay time and a thiner distribution, however both share a Gaussian functional form.

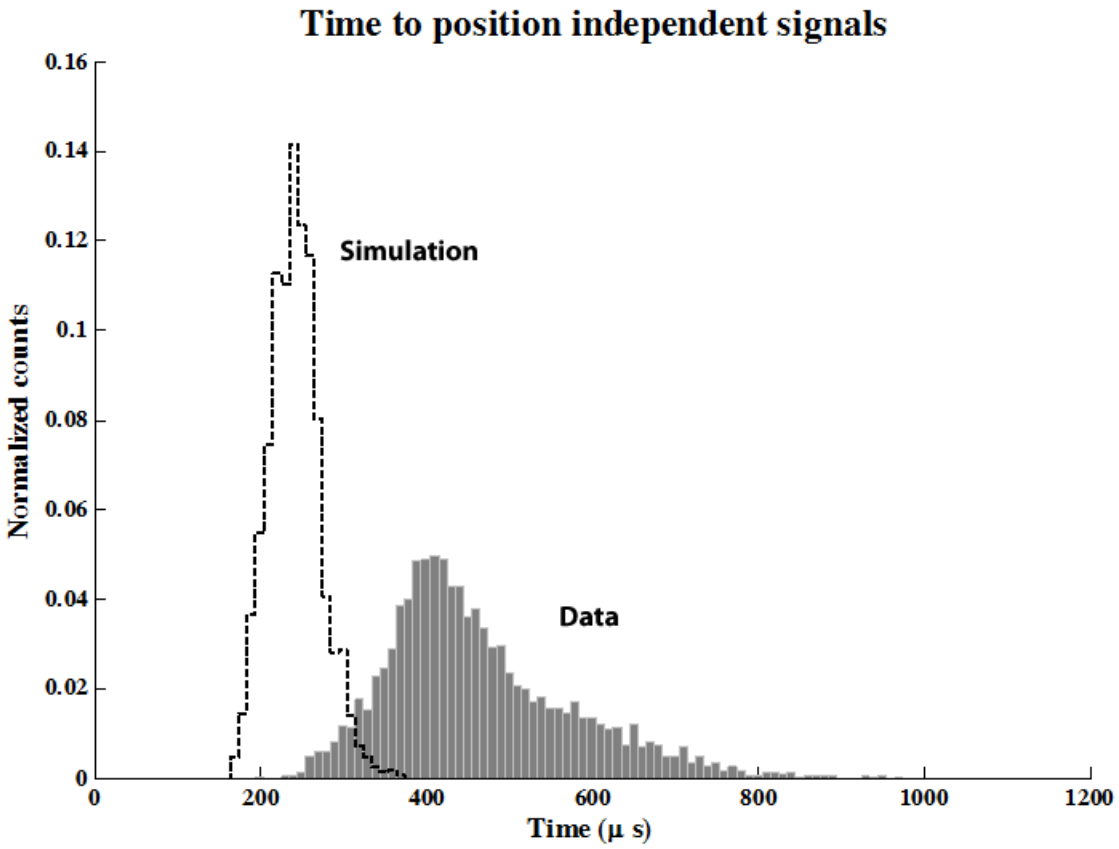


Figure 8: The time to position independence distributions. Note that they both have longer tails to the right.

SLAC-TN-11-005

# PyDecay/GraphPhys: A Unified Language and Storage System for Particle Decay Process Descriptions

Jesse N. Dunietz

Office of Science, Science Undergraduate Laboratory Internship (SULI)

Massachusetts Institute of Technology

Stanford Linear Accelerator Center

Stanford, CA

August 20, 2010

Prepared in partial fulfillment of the requirements of the Office of Science, Department of Energy's Science Undergraduate Laboratory Internship under the direction of Matthew Bellis with the BaBar team at the SLAC National Accelerator Laboratory.

Participant: _____

Signature

Research Advisor: _____

Signature

Work supported in part by US Department of Energy contract DE-AC02-76SF00515.

# TABLE OF CONTENTS

# ABSTRACT

PyDecay/GraphPhys: A Unified Language and Storage System for Particle Decay Process Descriptions. JESSE N. DUNIETZ (Massachusetts Institute of Technology, Cambridge, MA 02139) MATTHEW BELLIS (BaBar team at the SLAC National Accelerator Laboratory, Stanford, CA 94025)

To ease the tasks of Monte Carlo (MC) simulation and event reconstruction (i.e. inferring particle-decay events from experimental data) for long-term BaBar data preservation and analysis, the following software components have been designed: a language ("GraphPhys") for specifying decay processes, common to both simulation and data analysis, allowing arbitrary parameters on particles, decays, and entire processes; an automated visualization tool to show graphically what decays have been specified; and a searchable database storage mechanism for decay specifications. Unlike HepML, a proposed XML standard for HEP metadata, the specification language is designed not for data interchange between computer systems, but rather for direct manipulation by human beings as well as computers. The components are interoperable: the information parsed from files in the specification language can easily be rendered as an image by the visualization package, and conversion between decay repesentations was implemented. Several proof-of-concept command-line tools were built based on this framework. Applications include building easier and more efficient interfaces to existing analysis tools for current projects (e.g. BaBar/BESII), providing a framework for analyses in future experimental settings (e.g. LHC/SuperB), and outreach programs that involve giving students access to BaBar data and analysis tools to give them a hands-on feel for scientific analysis.

# INTRODUCTION

When physicists want to analyze data from a collider experiment such as BaBar, they generally do so in two steps. First, they must simulate the decay reactions they are looking for so they know what current theories predict, and second, they must analyze the collider data so that they can compare actual results with theoretical predictions. For the first step, they need to specify the decay processes to simulate and the parameters – branching fractions, angular distributions, etc. – under which these processes should be simulated. For the second, they need to specify various parameters describing which events to search for amidst the petabytes of experimental data, which algorithms to use for reconstructing particle decays from detector data, which particle attributes to extract from the detector data, etc.

Currently these are specified in custom textfile formats, with the simulation and data-extraction formats sharing nothing. These configuration file formats are not very user-friendly, and can be so time-consuming to learn that anyone who wants to write such a file generally simply copies an old one and modifies it. It is also often difficult to read out from such a file what decay it is actually analyzing; if that information is directly and clearly present, it is only in comments. Automated visualization of the decay is certainly not possible.

This arrangement is not ideal for a number of reasons. First, there is a decent chance that what an analyst has specified in a configuration file is not actually what he or she intended, and there is no way short of running the analysis or simulation to determine that. Additionally, it is difficult to introduce new collaborators to the project, since the learning curve for using the configuration files is so high. This is particularly problematic given that the SuperB collider, if it becomes a reality, will want to leverage BaBar's tools, but the SLAC researchers currently working with these obscure tools may no longer be available to explain the system at that point. There is also no easy way to search these files for particular decay

processes, and thus no easy way to know that the process one is examining has not been examined already. In fact, some of the configuration files are not even stored in a central, publicly available location. This lack of centrality and searchability can lead to duplication of effort. Finally, some BaBar team members have been advocating releasing some BaBar data to the public for use in classrooms, so that students can acquire a sense of what it is like to work with real physics data, and hopefully increase their excitement about and sense of participation in genuine physics. This of course requires that the tools for analyzing the BaBar data be intuitive and accessible to people outside the laboratory.

To address these problems, it was determined that a new system for specifying and storing decay information was necessary. The system would need to allow simple, intuitive input of decay information, without strange or obscure format features, to eliminate the high learning curve of the current system; easy visualization of the contents of such a configuration file, to allow ensuring the correctness of the input; and a searchable long-term storage system to allow collaborative sharing of and searching for decay descriptions. A system with all of these capabilities and characteristics was implemented in the course of this project.

## SYSTEM IMPLEMENTATION

The entire system was implemented in Python. Each of the functionalities listed above was implemented in a separate module. All components of the system assume that the physical processes under study can be characterized as a tree of particles, where the root of the tree is the initial particle and the children of each particle-node are the decay products of that particle. This model is somewhat complicated by the probabilistic nature of decays, as discussed below.

### *Decay Process Internal Representation*

A set of Python classes was created to represent physical decay processes and groups of such processes. In terms of the tree model described above, every node (particle) in the tree has a type, a list of parameters – arbitrary name-value pairs – and a set of associated decays. These decays are essentially lists of product particles, along with associated parameters – again, merely name-value pairs. There is also a class representing a group of unrelated particles, i.e. a forest of such particle-decay trees, which can also contain general parameters pertaining to the whole simulation/reconstruction analysis.

The probabilistic nature of decays complicates the tree representation somewhat. For instance, if a $K^0$ can decay to either two $\pi^0$ particles or a $\pi^+/\pi^-$ pair, this effectively means there are two alternative trees for that $K^0$ particle. This is generally represented as alternative child-node sets for the particle object. For example, $D^+ \to K^*\pi, K^* \to \pi\pi$ internally has only one object representing the $K$ particle, with two alternative subtrees. However, it is sometimes useful, particularly for visualization, to have a single unambiguous tree with no probabilistic alternatives. For this purpose methods have been implemented to "flatten" the alternative trees into a set of full decay path trees. Thus, in the above example, this flattening would produce two trees, as illustrated in Figure 1. A noteworthy feature of this flattening is that, if the database (see below) contains branching fraction information for the decays under examination, the product branching fraction – that is, the probability of the entire flattened decay tree – can be computed in the processes of flattening the tree.

In many cases an analyst would like to specify that a particle should be allowed to decay "generically" – that is, it should decay according to the standard tables of decays and associated probabilities. A decay with no products is used to indicate such a generic decay.

These Python objects are the basis for the other components, which all use this object-based representation of decays. The objects can of course be created directly in Python code, but it is often easier obtain them from a database or "GraphPhys" representation.

### *GraphPhys Decay Description Language*

A decay description language, christened "GraphPhys", was created to allow specification of decays with various parameters to be written down in a simple, easily readable form. GraphPhys is essentially a subset of the Graphviz DOT graph description language. The abstract grammar for GraphPhys can be found in Figure 2.

Terminals are given here as single-quoted strings. Elements in brackets are optional; parentheses indicate grouping. Much as in Dot, whitespace is always ignored, and an ID is one of the following:

- Any string of alphabetic (`[a-zA-Z\200-\377]`) characters, underscores ('_') or digits (`[0-9]`) (unlike in Dot, an ID **may** begin with a digit);
- A numeral (`[\-]?(.[0-9]+ | [0-9]+(.[0-9]*)? )`);
- Any double-quoted string (`"..."`) possibly containing escaped quotes (`\"`)

Unlike Dot, GraphPhys does **not** allow HTML strings as IDs.

In GraphPhys, one particle decaying to another set of particles is represented by the name of the initial particle and an arrow, followed by a curly-brace-enclosed list of decay products. Figure 3 demonstrates this syntax with a sample GraphPhys file that describes the aforementioned $D^+$ decay with some additional parameters. The `simulator=JETSET` line is an example of setting a default parameter for all decays; the same can be done for particles. The `fraction` parameter, though not demonstrated in this example, is a special parameter used to indicate decay branching fractions: the simulator could explicitly told the probabilities for the $K^* \to \pi^+\pi^-$ and $K^* \to \pi^0\pi^0$, although these probabilities could alternatively be fetched from the database (see below). This is one of the few parameters whose meaning is fixed by the GraphPhys system. The `ChargeConj=True` line demonstrates how global parameters can be configured for the entire set of decays described in the file.

### *Database Structure and Implementation*

In addition to the internal Python-object representation, a database representation was designed and implemented for storing decay specification information in a searchable, scalable database. The hope is that researchers in a group or students in a school will be able to create local databases of stored decay specifications so that they can see what others have looked at. This is in part motivated by a desire to replace the current `.DEC` and `.tcl` files, used for configuring BaBar's MC simulation and reconstruction software, respectively. These files tend to be stored by the thousands alongside each other, sometimes under a user's home directory rather than in some shared location. Their filenames often reflect their contents, but they are still far from easy to search.

The Object-Relational Mapper (ORM) component of the Django web application framework [1] was used to define the structure of the database (though this structure can of course be dumped as generic SQL) and to manipulate it programmatically. This abstraction layer makes migration between database engines trivial and makes querying the database far easier.

The database was initially designed only to store the information contained by GraphPhys files, but it quickly became clear that it would be useful to store generic known particle/decay information as well. Broadly speaking, then, the database design can be split into two sets of tables:

1. **Particle/Decay Types:** The tables for storing the names and properties of known particles and decays. These tables exist to encapsulate some of the information contained in the publications of the Particle Data Group (PDG), the premier publisher of particle and decay data, in a computer-readable, searchable format that is also well-integrated with the other half of the database. The tables in this group are:

    - `pydecaydb_particlebasetype`: Contains the masses, charges, PDG ID numbers,

etc. of various types of "base" particle types, i.e. type information excluding information about charge conjugation.

- `pydecaydb_particletype`: Contains actual particle types, referencing base types and including charge-conjugated names. This table and the previous onecan be automatically populated from the PDG's CSV file [2] of particle data.
- `pydecaydb_decaymode`: Identifies standard known decay modes. The table itself stores only the initial particle type foreign key and the branching fraction of the decay mode.
- `pydecaydb_productsetmembership`: Associates particle types with decay modes. Each particle type/product set association also records a count of how many particles of that type are present in that product set.

2. **Particle/Decay Instances:** These tables store information pertaining to specific particles or decays that users have input using the PyDecay system – perhaps through GraphPhys, perhaps by direct Python object creation. Every time a user specifies that there is, for instance, a $\pi^+$ particle somewhere in his or her decay tree, this can be thought of as declaring a new $\pi^+$ instance, and it will be recorded as such if the decay tree is stored in the database. The tables in this set are:

   - `pydecaydb_particleinstance`: Stores the foreign keys for the type, parent particle (if any), and instance group (see below) of each particle instance. Because charged types are stored sign-independently, the entries in this table also indicate whether the particle is positively or negatively charged.
   - `pydecaydb_decayinstance`: Stores the foreign key for the initial particle of each decay instance. Products can be inferred by looking for particles whose parent is the initial particle. The decay mode can be inferred from initial instance type, product types, and intermediate angular momentum (if specified).

- `pydecaydb_instancegroup`: Provides group ID's for particles to identify themselves with. Each group ID indicates a group of unrelated particles – for example, a set of unrelated root particles from a single GraphPhys file.

Each of these tables also has an associated table for storing instance parameters as name-value string pairs.

Various functions for searching for and manipulating entries in the database in an object-oriented manner have been implemented in Python using the Django system.

While these tables constitute the primary database system in the PyDecay framework, a need was also recognized for allowing use of the framework without the heavyweight requirements of Django and a relational database system. To that end, an abstract interface to the particle type/decay mode segment of the database was created to allow alternative implementations for storing/fetching such data. Two alternative implementations are provided besides the Django implementation: a null implementation that always returns no results when retrieving particle/decay data, and a system that uses Python dictionaries to specify particle/decay information. A library-global settings file is used to specify which database implementation to use.

### *Visualization/Conversion Tools*

A visualization/conversion package was created for converting between various representation formats. The following representations of a decay tree are interchangeable, i.e. any one of them can be converted in to any other one (via PyDecay objects, in some cases):

1. **GraphPhys** – a string of text conforming to the GraphPhys language specification.
2. **PyDecay objects** – Python objects from the PyDecay library discussed above.
3. **Database instances** – rows from the second class of database tables described above, represented in code by Django Python objects.

4. **Database types** – rows from the first class of database tables described above; converting to this representation is primarily useful for inserting new decays into the decay modes table.

In addition, any of the above representations can be converted via PyDecay objects into any of the following alternative representations, though the reverse conversion is not possible:

1. **GraphViz diagram** – a visualization of decay trees illustrating decays as arrows between boxes that contain particle names and parameters and decay parameters. The visualization is generated by the GraphViz diagram-layout system [3] via the Pydot Python package [4].

2. **PyFeyn diagram** – a visualization of decay trees as "cartoon" decay diagrams, rendered using the PyFeyn Feynman diagram-drawing package [5]. Unlike the GraphViz visualizer, this visualizer does the layout internally, since PyFeyn does not do it automatically.

3. **tcl file** – a `.tcl` file in the same format as those used to configure BtaTupleMaker, the BaBar reconstruction software. This converter is a proof-of-concept to show that the PyDecay libraries can be used to create tools as powerful as the current ones but which can be used much more easily.

The conversion framework was designed to be sufficiently generic that conversion to new formats can easily be integrated. Conversion is performed by "converter" objects which all support the same conversion API. This would even allow building a system in which the precise type to be converted to was specified in a config file via the qualified name of the converter class to use.

## DISCUSSION AND CONCLUSIONS

PyDecay is a set of libraries for use in the creation of analysis tools. While it does not itself perform the analysis, the functionality it provides should make the creation of such tools almost trivial, thus accomplishing the major goals of the project.

As a proof of concept, a minimal Monte Carlo decay simulator was modified to use GraphPhys files as its input format. A kinematics checker was also implemented for checking that a decay specified in the GraphPhys format is kinematically possible. This latter functionality is particularly useful given that currently this type of check is typically done painstakingly by hand. The checker works with very minimal GraphPhys files, since the masses of the particle types can be loaded from the database.

The niche filled by PyDecay is, as far as we know, unique. There have been attempts to create a common XML dialect for HEP decay information, called HepML, which appears to be a similar concept to GraphPhys. This specification, however, appears to be for data *interchange* between software packages [6], e.g. for passing configuration parameters around between two Monte Carlo simulators in the same toolchain or in different projects. As an interchange format, HepML's requirements are fairly different from GraphPhys's. GraphPhys is meant to be an input format: GraphPhys files are human-editable textfiles which easily yield their meaning to another human on inspection, as well as being computer-readable. As anyone who as written XML by hand knows, XML files are neither easily writable nor easily readable by humans. In fact, the PyDecay converter framework could easily be used to write a converter between PyDecay objects and HepML strings.

As far as the database component, we know of no other HEP project that has created a similar searchable database of researchers' past decay specifications, nor even one that allows searching for known general particle/decay data. There are existing databases of such general data, most notably the PDG; unfortunately, the PDG does not make this database

available for public access. The Durham HepData project [7] allows searching for decay process information by inputting a text string describing the decay, but the information returned cannot be manipulated programmatically; the system simply returns a list of links to publications containing relevant information. PyDecay's database module is much more flexible, allowing queries such as "What are all the decay modes with any initial state and a final state of exactly 3 pions?"

The PyDecay suite has been demonstrated to several groups of potential users, generally getting a positive response. All the potential users who examined it have indicated that they would likely find it useful, and some indicated an interest even in just the minimal proof-of-concept tools that have been implemented so far.

Some work still remains to be done, however. Most notably, it is not currently possible to represent a certain type of decay specification that is sometimes useful to analysts. The problem occurs when analysts would like to specify a decay such as "X decays to Y, Z, and some other unspecified particles which are not of interest." Currently there is no way in any of the decay tree representations to capture the idea of "other unspecified particles." The feedback we have received indicates that this is something that analysts do often want to specify, making this functionality gap a potentially serious deficiency. On a similar note, the PDG lists several "inclusive modes" – modes including unspecified particles as described above. Thus, such underspecified decays may be present not just in an analysis but even in PDG standard data. These cannot currently be represented in the database, though some preliminary work has been done on figuring out how they could be. A few minor issues have also been identified with the GraphPhys syntax.

Despite these shortcomings, we feel that the functionality provided by PyDecay is sufficiently compelling that the system will be adopted in both experimental and outreach settings. We have made the tools and code publicly available, thus enabling adoption and improvement in any setting in which the libraries might prove useful.

## ACKNOWLEDGMENTS

I would like to thank Matt Bellis, my mentor, for all his passionate support, guidance, and teaching. He gave the project direction and enabled it to go as far as it did. I would also like to thank Steve Rock, the SLAC SULI Program Director, and the other SLAC SULI administrators who made the program run smoothly. Additional thanks to the SLAC National Accelerator Laboratory, the Office of Science, and the Department of Energy for running the SULI program. Special thanks to all those BaBarians who listened to our ideas, tested out the software, and gave us feedback.

## REFERENCES

[1] (2010, May) Django: The Web framework for perfectionists with deadlines. [Online]. Available: http://www.djangoproject.com/

[2] (2008) Masses, Widths, Quantum Numbers (IGJPC) and MC ID Numbers from 2008 Edition of RPP. [Online]. Available: http://pdg.lbl.gov/2010/mcdata/mass_width_2008.csv

[3] (2008, Apr.) Graphviz – Graph Visualization Software. [Online]. Available: http://graphviz.org/

[4] (2007, Oct.) Pydot. [Online]. Available: http://dkbza.org/pydot.html

[5] (2007, Sept.) PyFeyn. HepForge. [Online]. Available: http://projects.hepforge.org/pyfeyn/

[6] (2008, Mar.) HepML. HepForge. [Online]. Available: http://projects.hepforge.org/hepml/

[7] Durham Reaction Database. The Durham HepData Project. [Online]. Available: http://hepdata.cedar.ac.uk/reaction

[8] (2008, Aug.) The DOT Language. [Online]. Available: http://www.graphviz.org/doc/info/lang.html

# FIGURES

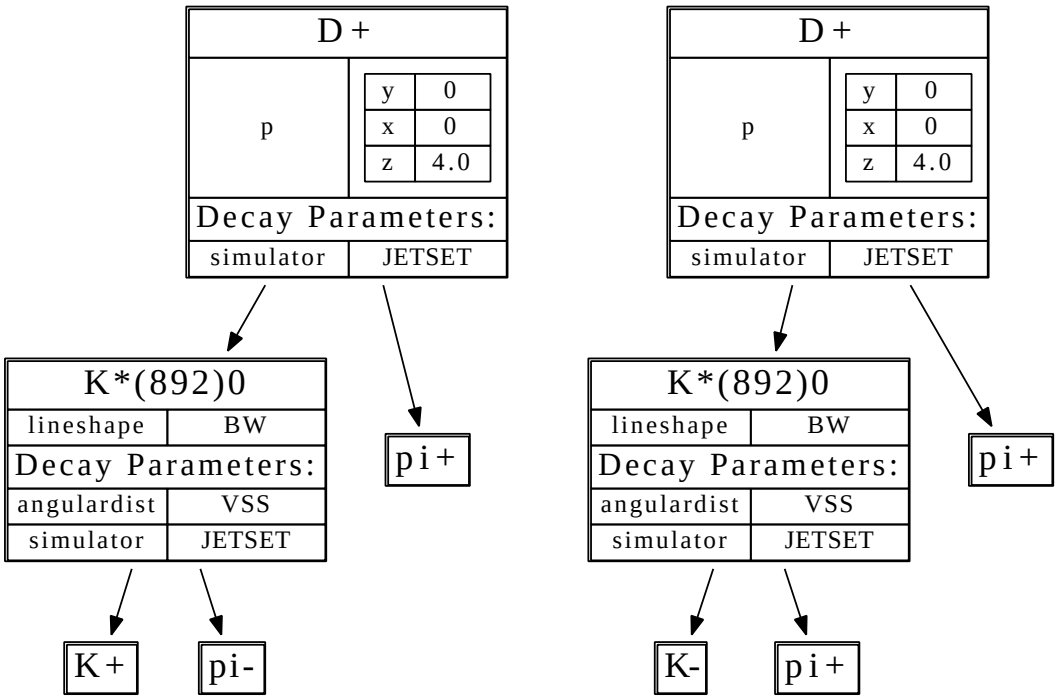


**Figure 1:** An example of how one decay tree with alternatives can be split into several distinct trees, (produced using the PyDecay Dot visualization package).

```
stmt_list      : [ stmt ';' [ stmt_list ] ]
stmt           : node_stmt
                     |       edge_stmt
                     |       default_stmt
                     |       param_stmt
default_stmt   : ('particle' | 'decay' ) param_list # Like 'node' and 'edge' in Dot
param_list     : '[' [ param_sequence ] ']'
param_sequence : ID [ '=' param_val ] [ ',' ] [ param_sequence ]
param_val      : ID | param_list | float_number
edge_stmt      : ID edgeRHS [ param_list ]
edgeRHS        : edgeop node_set
node_stmt      : ID [ param_list ]
node_set       : '{' id_list '}'
id_list        : ID [id_list]
param_stmt     : ID '=' param_val
```

**Figure 2:** The GraphPhys abstraction grammar. This is a simplified and slightly modified version of the standard DOT grammar[8].

```
decay [simulator=JETSET];
ChargeConj=True;

"D+" [p=[x=0, y=0, z=4.0]];
PiPlus1 [type="pi+"];
PiPlus2 [type="pi+"];
"K*(892)0" [lineshape=BW];

"D+" -> {"K*(892)0" PiPlus1};
"K*(892)0" -> {"K+" "pi-"} [angulardist=VSS];
"K*(892)0" -> {"K-" PiPlus2} [angulardist=VSS];
```

**Figure 3:** A sample GraphPhys file describing two possible decay paths for a $D^+$, with some additional parameters for simulation.

# Assessing Potential Acidification of Marine Archaeological Wood Based on Concentration of Sulfur Species

Sara Goldman

Office of Science, Science Undergraduate Laboratory Internship (SULI)

University of Colorado at Colorado Springs

Stanford Synchrotron Radiation Lightsource

Stanford, CA

August 20, 2010

Prepared in partial fulfillment of the requirements of the Office of Science, Department of Energy's Science Undergraduate Laboratory Internship under the direction of Dr. Apurva Mehta, Stanford Synchrotron Radiation Lightsource.

Participant: _____

Signature

Research Advisor: _____

Signature

Work supported in part by US Department of Energy contract DE-AC02-76SF00515.

## TABLE OF CONTENTS

## ABSTRACT

Assessing Potential Acidification of Marine Archaeological Wood Based on Concentration of Sulfur Species. SARA M. GOLDMAN (University of Colorado at Colorado Springs, CO 80918) APURVA MEHTA (Stanford Synchrotron Radiation Lightsource, Menlo Park, CA 94025)

The presence of sulfur in marine archaeological wood presents a challenge to conservation. Upon exposure to oxygen, sulfur compounds in waterlogged wooden artifacts are being oxidized, producing sulfuric acid. This speeds the degradation of the wood, potentially damaging specimens beyond repair. Sulfur K-edge x-ray absorption spectroscopy was used to identify the species of sulfur present in samples from the timbers of the *Mary Rose*, a preserved 16$^{th}$ century warship known to undergo degradation through acidification. The results presented here show that sulfur content varied significantly on a local scale. Only certain species of sulfur have the potential to produce sulfuric acid by contact with oxygen and seawater *in situ*, such as iron sulfides and elemental sulfur. Organic sulfurs, such as the amino acids cysteine and methionine, may produce acid but are integral parts of the wood's structure and may not be released from the organic matrix. The sulfur species contained in the sample reflect the exposure to oxygen while submerged, and this exposure can differ greatly over time and position. A better understanding of the species' pathway to acidifications required, along with its location, in order to suggest a more customized and effective preservation strategy.

## 1.0 INTRODUCTION

Waterlogged archaeological wood, frequently in the form of shipwrecks, is being excavated for historical purposes in many countries around the world. Even after extensive efforts towards preservation, scientists are discovering that accumulation of sulfate salts results in acidic conditions on the surfaces of the artifacts. Sulfuric acid degrades structural fibers in the wood by acid hydrolysis of cellulose, accelerating the decomposition of the ship timbers [1]. Determining the sulfur content of waterlogged wood is now of great importance in maritime archaeology. Artifact preservation is often more time consuming and expensive than the original excavation; but it is key to the availability of objects for future study as well as maintaining the integrity of historical data and preserving the value of museum pieces [2].

Sulfur occurs in a wide number of oxidation states from -2 to +6, and appears in numerous organic and inorganic compounds in nature. However, it is a very minor component of wood. Sulfur K-edge x-ray absorption spectroscopy (XAS) is a valuable technique because it has the ability to detect very low concentrations of sulfur in the specimen. XAS is also sensitive to differences in oxidation states, as well as long and short range order in molecules.

## 2.0 MATERIALS AND METHODS

### *2.1 Sample Preparation*

The sample of waterlogged archaeological wood used in the S K-edge XAS study was from the *Mary Rose,* currently in Portsmouth, England. The piece was cut from the oak stem post, which was excavated in 2003, and had not been treated with any preservation chemicals or any conservation methods other than drying. The sample was approximately 3cm by 4cm by ½ cm. Fifteen spectra were collected at different locations on the sample piece.

*2.2 S K-edge XAS Data Collection*

Sulfur K-edge x-ray absorption spectra were collected on a 20-pole 2.0 Tesla wiggler unfocussed beamline 4-3 at the Stanford Synchrotron Radiation Lightsource (SSRL) under standard ring operating condition of 3 GeV and ~200 mA ring current. X-ray energy was varied using a Si(111) double-crystal monochrometer with a non-fixed exit slit. Other upstream optics included a Ni-coated vertically collimating and harmonic rejection mirror. The sample chamber contained a helium atmosphere. The area of the X-ray beam was 1mm by 2mm. The sample was stored and handled at room temperature. The emitted X-ray fluorescence was measured at an angle of 0° using a Lytle detector. Thin double-stick sulfur-free Mylar tape was used to affix the sample piece to the sample holder. Energy calibration was achieved using $Na_2S_2O_3 \cdot 5H_2O$ as the calibrant, which was run before and after sample scans. The first peak of the $Na_2S_2O_3 \cdot 5H_2O$ spectrum was fixed at 2472.02 eV for calibration purposes [3].

S K-edge XAS data on reference compounds used in this study were previously measured on beamline 4-3 by Dr. Ritimukta Sarangi.

*2.3 Data Analysis*

The data were individually viewed in Sixpack, and any faulty or incomplete scans were removed [4]. The scans were calibrated and averaged in EXAFSPAK [5]. A second-order polynomial was fit to the pre-edge region and subtracted from the entire spectra as background. The data were normalized using the Pyspline program by subtracting a cubic spline and assigning the edge jump to 1.0 [6]. The area under the pre-edge peaks was fit using IFEFFIT in Sixpack, as well as the EDG_FIT subroutine in EXAFSPAK [7].

The absorption edge jump on XAS spectra corresponds to the total amount of the element present. It is determined by assigning a linear fit to the original pre-edge and post-edge data and calculating the distance between them (Figure 1). The edge jump of the data sets collected on different areas on the wood sample was calculated with Sixpack.

Due to the thickness of the sample (±1/2 cm), the resulting spectra were observed to be self-absorbed. Self-absorption correction was achieved using the FLUO program assuming infinite thickness [8].

## 3.0 RESULTS

The edge jumps calculated from the XAS spectra fluctuated from a low of 0.1915 to a high of 0.6897, indicating that the total sulfur content varied by up to three times on a local level (Table 1).

Although the spectra varied in total sulfur amount and species, two prominent peaks were observed in all of them (Figure 2). The first peak occurred at 2472.96 eV. The second larger peak occurred at 2482.60 eV.

Data were fitted with spectra using a library of sulfur reference compounds (Figure 3). Multiple fitting combinations were attempted in order to achieve the most accurate fit. The cysteine ($C_3H_7NO_2S$) and methionine ($C_5H_{11}NO_2S$) references produced similar results, and could be used interchangeably. Methionine was selected to act individually rather than including both references. A minor but quantifiable feature appeared between the first and second peak on all fifteen spectra (Figure 2). The sulfoxide reference was adjusted by -0.25 eV in order to better fit this area. This suggests that either the sulfoxide reference was slightly shifted, or an unidentified alternative compound with an oxidation state very similar to sulfoxide was present in the sample.

After eliminating reference compounds that did not appear in sufficient amounts (less than $1/100^{th}$ of a percent), the samples were fit with five primary components: methionine ($C_5H_{11}NO_2S$), sulfoxide (R-S(=O)-R', adjusted), sulfonate ($RSO_2O^-$), elemental sulfur ($S_8$), and sulfate ($SO_4^{2-}$). The fit fractions were calculated to be within 1-2% standard deviation. Total sums and R-values (the scaled error in the fit) were recorded (Table 1).

We observed the sum of the component fit fractions did not total to one (100%) for any of the samples. This difference could partially fall within standard deviation, but it is more likely that the sulfate content of the samples was underestimated due to self-absorption. Requiring the fit fractions to sum to one (100%) in the Sixpack program did not substantially alter the fit percentages, but did increase the error (R-value). It was decided that the analysis would continue without forcing the sum to one to maintain minimal error. It was assumed that the sulfate content was underestimated and the self-absorption correction performed was not entirely sufficient.

The fit data were normalized by multiplying the edge jump (total sulfur) by the fit fraction to get the species amount proportional to the total amount of sulfur present. The first peak at 2472.96eV is composed of elemental sulfur and methionine/cysteine. The second peak at 2482.60eV is composed primarily of sulfate, and to a lesser extent, sulfonate (Table 2). The features beyond the peak at 2482 eV indicate the presence of an unidentified ordered sulfate (Figure 2).

## 4.0 DISCUSSION

The sample piece did not receive excessive handling or any conservation chemicals after excavation in 2003. Because of this, we assumed that the components of the sample had not changed extensively in the intervening years, and represented the contents as if the piece had been newly salvaged.

The fit identified five components, discussed here in order of smallest average fit fraction to largest:

*4.3 Sulfonate*

Sulfonate is the salt of sulfonic acid, which is similar to sulfuric acid in structure. Sulfonic acid can be produced through the slow oxidation of organic sulfur (methionine/cysteine) with prolonged exposure to $O_2$ and water. The surviving timbers of the *Mary Rose* were embedded in clay and buried with silt, resting in an anaerobic environment *in situ* [9]. The presence of sulfonate suggests that during its 450 year burial period our sample must have come into contact with dissolved oxygen for an extended period of time. The gradual formation of sulfonate from organic compounds suggests that it is a natural consequence of wood spending a very lengthy time in contact with $O_2$ and water, and does not represent an immediate threat to the conservation of the wood. Our component analysis shows that thirteen of the fifteen samples contain small amounts of sulfonate, and the amount does not change greatly based on the total sulfur content.

*4.2 Sulfoxide (adjusted)*

Sulfoxides are oxidized sulfides, but sulfides to not naturally occur in oak. This suggests that sulfoxides are an indicator of an external source of sulfide. Previous studies have identified the activity of anaerobic bacteria in the wood [10]. The bacterial breakdown of organic matter produces hydrogen sulfide ($H_2S$). The presence of sulfoxides suggests that the ship's environment was either an ideal balance of sufficiently low oxygen to accommodate anaerobic

bacteria and enough oxygen to oxidize the $H_2S$ they produced; or some event occurred beneath the ocean to expose the area to more aerobic conditions. It is reasonable to suggest that a current of sufficient strength could change the silt coverage and thus the wood's exposure to dissolved oxygen. This process of burial and exposure could have happened many times over 450 years under water.

*4.1 Methionine/cysteine*

Sulfur occurs naturally in wood. Trees get the sulfur they require from the soil they grow in by taking up inorganic sulfate, reducing it, and incorporating it into amino acids such as methionine or cysteine [11]. The intensity of the organic sulfur methionine/cysteine peak varied 2.7 times between the least intense to the most intense spectrum. We observed that the intensity of XAS features was sensitive to the concentration of the sulfur species. The variation of the peak intensities for methionine/cysteine would depend on the cell structure of the wood and the underwater exposure it received. The sample with the largest amount of methionine/cysteine made up less than one fifth of its total sulfur content. We observed that the sulfurs in the amino acids were a minor component and did not fluctuate greatly based on the total sulfur content.

*4.4 Elemental Sulfur*

Inorganic elemental sulfur was present in all fifteen spectra as the primary component of the first peak observed at 2472.96eV. Elemental sulfur does not occur naturally in wood. The presence of elemental sulfur in the sample is primarily attributed to the $H_2S$-producing anaerobic bacteria. $H_2S$ can react with free sulfates in the water to produce elemental sulfur. Elemental sulfur combined with seawater and oxygen can produce sulfuric acid. The fact that $S_8$ is a required component of the fit indicates that it was lacking sufficient oxygen while under water to totally acidify. Rather, enough $O_2$ was present in the water to contribute to the formation of elemental sulfur, but not enough to oxidize it entirely.

*4.5 Sulfate*

Sulfate is the salt of sulfuric acid, and appears as the primary component of the total sulfur in all the samples. In fact, the increase in total sulfur content was primarily a result of increasing sulfate in the sample (Figure 4). Wood does not naturally contain sulfate, all of it had to come from an external source.

There are several pathways to producing sulfate, each beginning with the presence of the hydrogen sulfide produced by anaerobic bacteria. Hydrogen sulfide can form sulfuric acid by reacting with oxygen and seawater:

$$H_2S + O_2 + 2H_2O \rightarrow 6H^+ + SO_4^{2-}$$

Additionally, $H_2S$ can form elemental sulfur if $SO_4^{2-}$ is present in the water, and that $S_8$ can form more sulfuric acid with water and oxygen.

Previous studies have identified iron sulfides as a potential sulfur component in the wood [12]. The ship contained thousands of iron nails and fixtures, which over time would likely release ferric ions into the water. Hydrogen sulfide reacting with these ferric ions can produce iron sulfides such as pyrite ($FeS_2$) and pyrrhotite (FeS). These iron sulfides can produce sulfuric acid upon contact with air and seawater:

$$2FeS_2 + 7O_2 + 2H_2O \rightarrow 2Fe^{2+} + 4SO_4^{2-} + H^+$$

Iron sulfides can also form elemental sulfur and iron hydroxide if acid and other metal oxides are already present:

$$FeS + 1.5MnO_2 + 3H^+ \rightarrow Fe(OH)_3 + S^0 + 1.5Mn^{2+} \qquad [13].$$

Our sample spectra could not establish the presence of any form of iron sulfides. This indicates three possibilities. First, our sample did not have sufficient access to ferric ions and thus never contained iron oxides; second, if iron oxides formed, there was enough $O_2$ present to oxidize them immediately (either underwater or upon excavation); and third, the $H_2S$ reacted with any $O_2$ present to form sulfuric acid, rather than the $H_2S$ reacting with ferric ions to form iron sulfides.

Considering the extensive time under water and varied exposure to oxygen, combinations of these scenarios could occur as well.

The features on the XAS spectra beyond the second peak at 2482.60eV indicate the presence of an unidentified ordered sulfate (Figure 2). The more level (and less abundant) features beyond the second peak indicate a disordered free sulfate. The presence of a large amount of bound sulfates indicates that ordered insoluble metal sulfates have formed, meaning direct contact with metal ions has occurred. There is a small likelihood that the free cations were in the container holding the sample after excavation, or perhaps transferred during handling. The more likely explanation is that the sulfates came into contact with metal ions while still submerged. Seawater is known to contain many dissolved salts, and the most probable cations are sodium, magnesium, calcium, potassium, and strontium.

## 5.0 CONCLUSIONS

All of the sulfur species capable of becoming sulfuric acid upon contact with air and seawater were introduced as a result of the activities of anaerobic bacteria. The sulfur-bearing amino acids which naturally occur in the wood have the capability of producing minor amounts of sulfonic acid rather than sulfuric acid. However, all of these reactions hinge on the presence of oxygen.

In order for sulfate, sulfonate, sulfoxide, and elemental sulfur to be formed in our sample, oxygen had to be present over an extended period of time while submerged. A method to determine the oxygen exposure under water could assist in identifying how much sulfur is present with the immanent potential to acidify upon excavation.

Further XAS data analysis and comparison to reference compounds is required to identify the cation of the ordered sulfate. This would help us determine if the sulfates are reacting primarily under water, or if the sample is being contaminated during excavation and handling.

Also, if it is determined that the sulfate produced while under water has completely reacted while submerged, then any additional free sulfates identified later would have been formed after excavation by contacting atmospheric oxygen.

Additional references are required to ascertain whether or not sulfoxide is actually present or if a similarly structured compound is there instead.

Even though self-absorption correction was applied, it did not sufficiently adjust the sulfate amount. Further XAS spectra should be taken focusing on the issue of self-absorption in order to reduce the error in reference fitting.

## 6.0 ACKNOWLEDGEMENTS

I would like to thank Dr. Apurva Mehta for mentoring me on this project, and for dispensing exceptional advice and encouragement. I would also like to thank Dr. Ritimukta Sarangi for her generous support and guidance, and for contributing the additional S K-edge references used. Thank you to Dr. Eleanor Schofield, for the providing the sample and sharing beam time. Additionally, thanks to Dr. Steven Rock for his direction of the SULI program at SLAC. This research was funded by the U.S. Department of Energy, and the Stanford Synchrotron Radiation Lightsource.

## REFERENCES


[1] J. Gillon, " Marine archaeology: Acid attack," Nature, vol. 415, no. 21 Feb, pp. 847, 2002.

[2] D.L. Hamilton, Methods of Conserving Archaeological Material from Underwater Sites, 1 ed. , College Station, TX: Texas A&M University, 1999.

[3] R. Sarangi, J.T. York, M.E. Helton, K. Fujisawa, K.D. Karlin, W.B. Tolman, K.O. Hodgson, B. Hedman, E.I. Solomon, " X-Ray absorption spectroscopic and theoretical studies on (L)2[Cu2(S2)n]2+ complexes: Disulfide versus disulfide(1-) bonding," Journal of the American Chemical Society, vol. 130, pp. 676-686, 2008.

[4] S. Webb, Sixpack, version 0.67, 2010.

[5] G.N. George, EXAFSPAK and EDG_FIT, 2001.

[6] A. Tenderholt, PySpline: A program of processing XAS data, version 1.1, 2006.

[7] M. Newville, IFEFFIT, version 1.2.10, 2010.

[8] D. Haskel, FLUO, 1999.

[9] M. Sandström, F. Jalilehvand, E. Damian, Y. Fors, U. Gelius, M. Jones, M. Salome, " Sulfur accumulation in the timbers of King Henry VIII's warship Mary Rose: A pathway in the sulfur cycle of conservation concern," PNAS, Proceedings of the National Academy of Sciences, vol. 102, no. 40, pp. 14165-14170, 2005.

[10] K.M. Wetherall, R.M. Moss, A.M. Jones, A.D. Smith, T. Skinner, K.M. Pickup, S.W. Goatham, A.V. Chadwick, R.J. Newport, " Sulfur and iron speciation in recently recovered timbers of the *Mary Rose* revealed via X-ray absorption spectroscopy," Journal of Archaeological Science, vol. 35, pp. 1317-1328, 2008.

[11] S. Kopriva, T. Hartmann, G. Massaro, P. Hönicke, H. Rennenberg, " Regulation of sulfate assimilation by nitrogen and sulfur nutrition in poplar trees ," Trees - Structure and Function, vol. 18, no. 3, May, pp. 320-326, 2004.

[12] M Sandström, F. Jalilehvand, I. Persson, U. Gelius, P. Frank, I. Hall-Roth, " Deterioration of the seventeenth-century warship Vasa by internal formation of sulphuric acid," Nature, vol. 415, no. 21 Feb, pp. 893-897, 2002.

[13] B.B. Jørgensen, D.C. Nelson, " Sulfide Oxidation in marine sediments: Geochemistry meets microbiology," Geological Society of America Special Papers, vol. 379, pp. 63-81, 2004.

## FIGURES

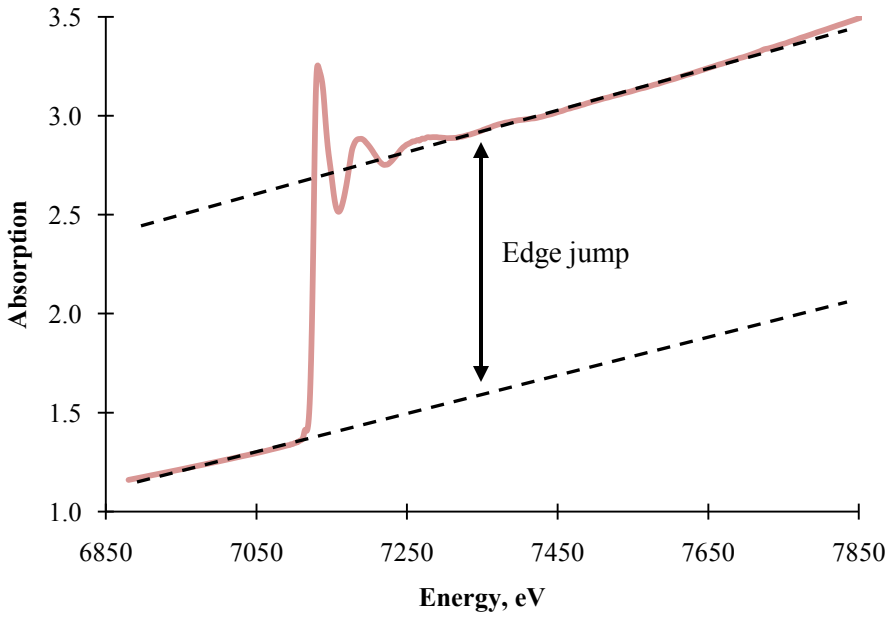


Figure 1: The edge jump corresponds to the total amount of the element present over the energy range selected. It is determined by assigning a pre-edge and post-edge line (on non-normalized data) and calculating the distance between them.

Table 1: The component fit fractions are rounded up to half a percent, and are within 1-2% standard deviation. Total sum and R value are calculated for each location.

| Sample | Edge Jump | Methionine $C_5H_{11}NO_2S$ | Elemental Sulfur $S_8$ | Sulfoxide (adj) R-S(=O)-R' | Sulfonate $RSO_2O^-$ | Sulfate $SO_4^{2-}$ | Sum | R-value |
|---|---|---|---|---|---|---|---|---|
| A | 0.661 | 0.029 | 0.070 | 0.011 | 0.019 | 0.800 | 0.929 | 0.0113 |
| B | 0.690 | 0.025 | 0.083 | 0.021 | 0.061 | 0.715 | 0.905 | 0.0077 |
| C | 0.483 | 0.062 | 0.158 | 0.036 | — | 0.639 | 0.895 | 0.0067 |
| D | 0.299 | 0.118 | 0.297 | 0.068 | — | 0.435 | 0.918 | 0.0028 |
| E | 0.256 | 0.162 | 0.283 | 0.096 | 0.160 | 0.251 | 0.952 | 0.0016 |
| F | 0.192 | 0.184 | 0.420 | 0.114 | 0.039 | 0.185 | 0.941 | 0.0008 |
| G | 0.263 | 0.192 | 0.420 | 0.120 | 0.063 | 0.152 | 0.947 | 0.0013 |
| H | 0.363 | 0.091 | 0.279 | 0.067 | 0.064 | 0.398 | 0.899 | 0.0035 |
| I | 0.389 | 0.059 | 0.283 | 0.077 | 0.117 | 0.355 | 0.890 | 0.0087 |
| J | 0.322 | 0.134 | 0.468 | 0.118 | 0.053 | 0.169 | 0.942 | 0.0010 |
| K | 0.260 | 0.148 | 0.435 | 0.121 | 0.052 | 0.174 | 0.930 | 0.0014 |
| L | 0.665 | 0.028 | 0.093 | 0.025 | 0.080 | 0.727 | 0.952 | 0.0077 |
| M | 0.322 | 0.057 | 0.272 | 0.071 | 0.144 | 0.339 | 0.883 | 0.0044 |
| N | 0.534 | 0.037 | 0.126 | 0.028 | 0.007 | 0.700 | 0.899 | 0.0067 |
| O | 0.478 | 0.039 | 0.175 | 0.037 | 0.063 | 0.615 | 0.929 | 0.0060 |

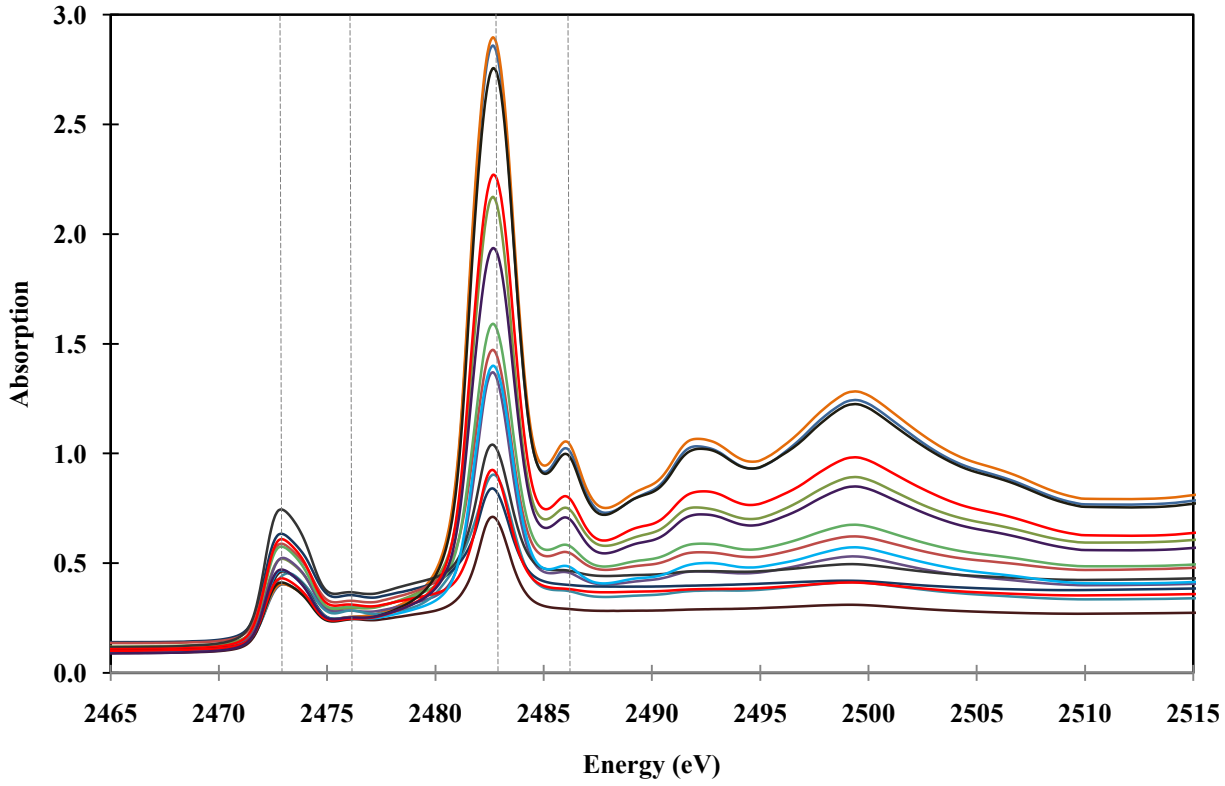


Figure 2: The fifteen XAS (absorption vs energy) spectra overlay. This data has not been normalized. The first peak occurs at 2472.96 eV, the second larger peak occurs at 2482.60 eV. Between them is a small feature near the oxidation state of sulfoxide. The features at energies greater than the peak at 2482 eV indicate the presence of an ordered sulfate.

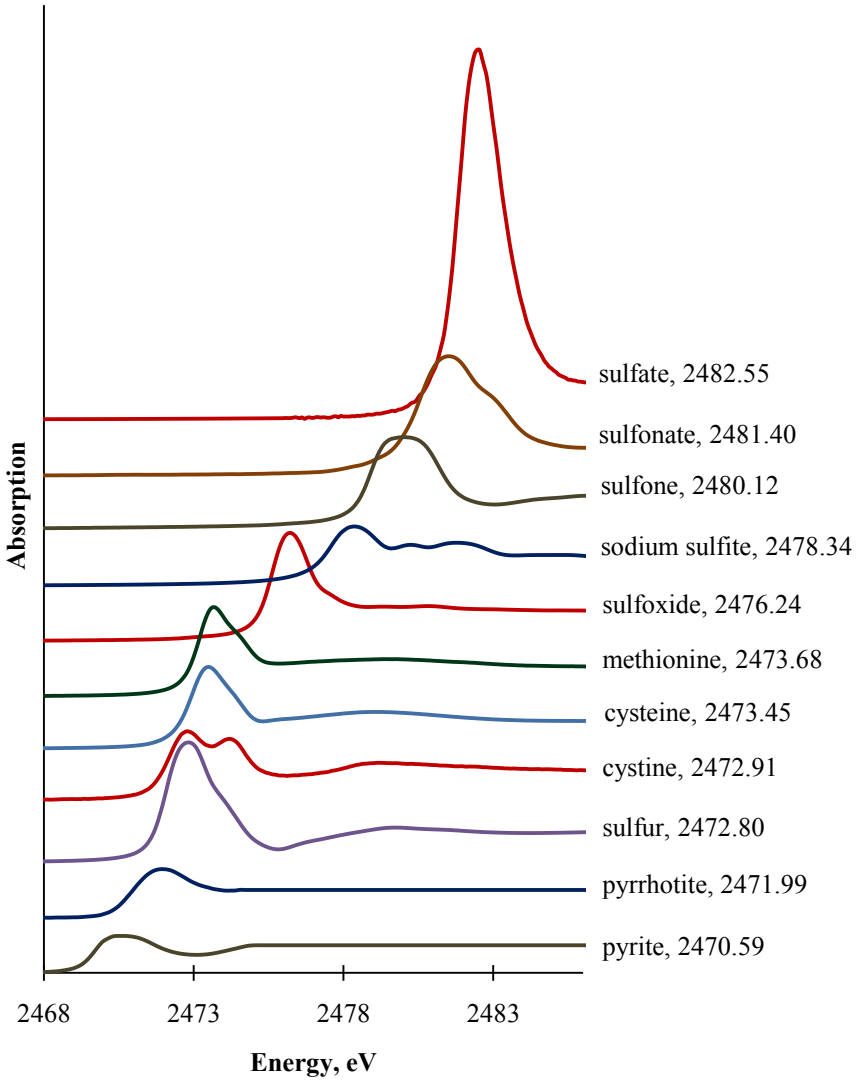


Figure 3: The library of reference spectra. These spectra were staggered vertically to better observe the peak energy differences.

Table 2: The normalized proportions of sulfur species at each location calculated by multiplying the fit fraction of each species by the total amount of sulfur (edge jump).

| Sample | Methionine $C_5H_{11}NO_2S$ | Elemental Sulfur $S_8$ | Sulfoxide R-S(=O)-R' | Sulfonate $RSO_2O^-$ | Sulfate $SO_4^{2-}$ |
|---|---|---|---|---|---|
| A | 0.0189 | 0.0461 | 0.0073 | 0.0127 | 0.5287 |
| B | 0.0172 | 0.0574 | 0.0146 | 0.0419 | 0.4931 |
| C | 0.0300 | 0.0764 | 0.0174 | — | 0.3088 |
| D | 0.0352 | 0.0888 | 0.0203 | — | 0.1301 |
| E | 0.0415 | 0.0723 | 0.0247 | 0.0409 | 0.0641 |
| F | 0.0352 | 0.0804 | 0.0218 | 0.0074 | 0.0354 |
| G | 0.0505 | 0.1105 | 0.0314 | 0.0165 | 0.0400 |
| H | 0.0331 | 0.1011 | 0.0244 | 0.0233 | 0.1442 |
| I | 0.0231 | 0.1100 | 0.0300 | 0.0454 | 0.1379 |
| J | 0.0432 | 0.1507 | 0.0382 | 0.0170 | 0.0545 |
| K | 0.0383 | 0.1129 | 0.0315 | 0.0134 | 0.0453 |
| L | 0.0184 | 0.0616 | 0.0169 | 0.0531 | 0.4829 |
| M | 0.0184 | 0.0876 | 0.0230 | 0.0463 | 0.1091 |
| N | 0.0198 | 0.0675 | 0.0152 | 0.0037 | 0.3737 |
| O | 0.0184 | 0.0838 | 0.0178 | 0.0301 | 0.2940 |

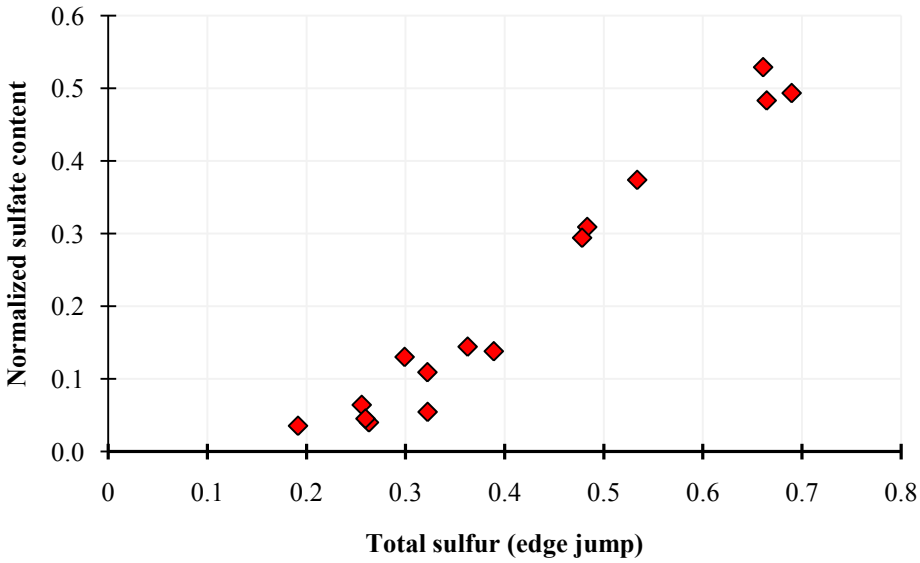


Figure 4: The normalized sulfate content compared to the overall sulfur content. As total sulfur increases, the sulfate content is observed to increase as well.

# Data Acquisition in a High Harmonic Generation Lab and at LCLS

Takako Hirokawa

Office of Science, Science Undergraduate Laboratory Internship (SULI)

University of Colorado–Boulder

SLAC National Accelerator Laboratory

Menlo Park, CA

August 20, 2010

Prepared in partial fulfillment of the requirements of the Office of Science, Department of Energy's Science Undergraduate Laboratory Internship under the direction of Markus Gühr & Brian K. McFarland at the Stanford PULSE Institute, SLAC National Accelerator Laboratory.

Participant: _____

Signature

Research Advisor: _____

Signature

Work supported in part by US Department of Energy contract DE-AC02-76SF00515.

# TABLE OF CONTENTS

# ABSTRACT

Data Acquisition in a High Harmonic Generation Lab and at LCLS. TAKAKO HIROKAWA (University of Colorado–Boulder, Boulder, CO 80310) MARKUS GÜHR & BRIAN K. MCFARLAND (Stanford PULSE Institute, SLAC National Accelerator Laboratory, Stanford, CA 94025)

In this paper, we examine data acquisition in a high harmonic generation (HHG) lab and preliminary data analysis with the *Cyclohexadiene Collaboration* at the Linac Coherent Lightsource (LCLS) at SLAC National Accelerator Laboratory. HHG experiments have a large number of parameters that need to be monitored constantly. In particular, the pressure of the target is critical to HHG yield. However, this pressure can fluctuate wildly and without a tool to monitor it, it is difficult to analyze the correlation between HHG yield and the pressure. I used the Arduino microcontroller board and created a complementary MATLAB graphical user interface (GUI), thereby enhancing the ease with which users can acquire time-stamped parameter data. Using the Arduino, it is much easier to match the pressure to the corresponding HHG yield. Collecting data by using the Arduino and the GUI is flexible, user-friendly, and cost-effective. In the future, we hope to be able to control and monitor parts of the lab with the Arduino alone. While more parameter information is needed in the HHG lab, we needed to reduce the amount of data during the cyclohexadiene collaboration. This was achieved by sorting the data into bins and filtering out unnecessary details. This method was highly effective in that it minimized the amount of data without losing any valuable information. This effective preliminary data analysis technique will continue to be used to decrease the size of the collected data.

# INTRODUCTION

Data acquisition is an integral part of any experiment. Without a tool to collect data, the experiment cannot produce results. This tool should be straight forward so that one can maximize use of one's time on tasks such as the data analysis. Each experiment has particular requirements for the data acquisition system. Though experiments in a high harmonic generation (HHG) lab and experiments using the Linac Coherent Lightsource (LCLS) X-ray free electron laser (FEL) at SLAC National Accelerator Laboratory revolve around the same general principle — using light pulses of extremely short wavelength and duration — the specifications of the data acquisition systems can differ vastly.

## *Motivation*

Laser pulses of femtosecond ($10^{-15}$ seconds) to attosecond ($10^{-18}$ seconds) duration and extremely short wavelength are used to study molecular electronic structure and dynamics. One way to produce these short laser pulses is to use a free electron laser (FEL) for X-rays that generates wavelengths at the atomic scale, as demonstrated with the LCLS. However, an FEL requires an enormous amount of equipment, room, and therefore funding to generate these X-ray beams. These requirements have reduced the amount of available user time. Alternatively, the so-called high harmonic generation (HHG) can be used to create short soft X-ray laser pulses that are much weaker in energy than FEL pulses. This second technology is widely used and is available in many laser labs in a table-top setting.

### *HHG Background*

HHG is achieved by ionizing atoms and letting their electrons recombine within several hundred attoseconds. This is accomplished by sending very short, strong infrared (IR) light pulses into a gas jet. Semi-classically speaking, [1, 2, 3] if the pulse's electric field is of the

same magnitude as that between an electron and the nucleus, the electric field bends the Coulomb potential such that one side of the potential well slopes up slightly while the other side slopes down (Fig. 1a). As a result, the electron tunnels out of the potential well and accelerate away from the ion. Since the laser field is oscillating very quickly, the potential flips rapidly so that the electron accelerates back into the center of the well, thereby gaining kinetic energy (Fig. 1b). When the it recombines with the atom, the electron emits its excess kinetic energy in the form of a photon (Fig. 1c). This recombination process takes a few hundred attoseconds, so the photons are released in an attosecond light pulse. The harmonic generation process repeats coherently on every half cycle of the strong driving laser field, and a train of attosecond pulses emerges. In the spectral domain, this series of pulses will appear as a discretization in the form of odd harmonics.

An experimental setup for a typical HHG experiment consists of many components. Figure 2 shows the sketch of a laboratory setup [4]. The harmonics are produced during the IR laser's interaction with the gas jet. They propagate through vacuum because they would be absorbed by air. The harmonic spectrum is dispersed by a grating spectrometer and detected by a soft x-ray CCD camera. These parts of the acquisition system have existed in the laboratory prior to this summer. I set up a new acquisition system that continuously logs crucial parameters of the experiment such as laser intensity and gas jet pressure. Since the gas jet pressure can fluctuate wildly and correlates with HHG yield, being able to monitor this parameter is extremely critical. The data acquisition system hard- and software had to be extremely flexible and needed to interface with MATLAB.

### *Cyclohexadiene Collaboration at LCLS*

During my stay at SLAC, I was part of the data acquisition subgroup in a user team at the LCLS. At this facility, femtosecond X-ray pulses are created by accelerating electrons

to high kinetic energies before they are injected into the undulators. Undulators consist of alternating magnetic structures that bend the electrons' path (Fig. 3). As the electrons change direction, they emit radiation in the form of X-ray photons. After they travel past the undulators, the electrons are sent to an electron dump, while the X-ray beam continues to propagate to be used for experiments.

The experiment conducted by the cyclohexadiene collaboration group at LCLS this summer investigated the opening of the cyclohexadiene ring-molecule after ultraviolet (UV) radiation. This was done by exciting the molecule with an ultrashort UV pulse and then probing it with a time delayed pulse of the LCLS to ionize and Coulomb explode the molecule. An electric field is imposed on the interaction region so that after the x-ray hits the cyclohexadiene, the ions and electrons from the shattered molecule are directed onto detectors. One can monitor the velocity, as well as the momentum, of the ions through velocity map imaging (VMI). An ion time of flight (iTOF) spectrometer is used to identify the mass-to-charge ratio of the fragments. The ions are accelerated onto an ion sensitive detector capable of detecting *single* ions (see VMI in Fig. 4). By documenting the iTOF and the VMI, one can reconstruct the transient configuration of the molecule on a femtosecond time scale. [5, 6]

# MATERIALS AND METHODS

## *Materials and Methods in the HHG Lab*

### *The Arduino*

The Arduino reads in sensor data and relays these values to the computer to which it is connected. The computer logs and plots the data. The Arduino has six analog inputs, 14 digital input and output pins, and a USB connection (Fig. 5). The analog inputs take DC voltage signals between 0 and 5 V and digitize them with 10 bit resolution. The Arduino is

currently housed in a box that includes a small breadboard for signal preconditioning. Figure 6 shows the Arduino and the breadboard in the box. Sensors that measure the parameters of the lab such as the pressure in the vacuum chamber or the laser power can be connected to the Arduino directly via shielded BNC connectors. Oftentimes, the sensors output a voltage range that exceeds the 0-5V range that the Arduino can accept. As a result, the signal has to be conditioned. In the case of the pressure gauge, a voltage divider is used to condition the signal such that its 0-10V range is limited to a 0-5V range. The Arduino has a clock speed of 16 MHz. The chip on the Arduino has flash memory of up to 16 KB onto which one can store a program as firmware [7]. This program is executed by the Atmel microcontroller chip on the Arduino board. [8]

The Arduino developers have created a programming environment that facilitates programming the microcontroller. Instead of using an assembly language, a convenient simple Java dialect is implemented [9]. For this project, I wrote a sketch onto the Arduino that allows it to recognize a signal from the computer that is transmitted via the serial port. The Arduino responds by sending a conditioned sensor value back to the computer via the same serial port. The following is an example of the sketch stored on the Arduino:

```
if (incomingByte == 'H')
      {digitalWrite(ledPin, HIGH) //led ON
      sensorValue = analogRead(sensorPin0);
      Serial.println(sensorValue);
      digitalWrite(ledPin, LOW); /*led OFF*/}
end
```

In this code example, `incomingByte` is the letter that the computer sends to the Arduino. In the second line of the loop, the Arduino reads analog input 0 and in the third

line, it sends that value to the computer. The first and fourth lines turn an LED on the Arduino board on and off, respectively.

### *MATLAB GUI*

I used MATLAB to control the Arduino and to extract and manipulate the raw data so that it can be easily analyzed. The Arduino performs several different measurements at once and the computer to which the Arduino is connected sends these measurements to a file, which can be used later for further analysis.

The MATLAB code I developed has a graphical user interface (GUI), as shown in Figure 7, which allows the users to label and change the parameters and their units. As soon as the GUI starts collecting data, the parameter information is written to a documentation file. In addition, the users can run the code in two modes. One mode continuously plots the nearly instantaneous values (there is some time delay between the Arduino getting a sensor value and the computer receiving the value from the Arduino) while the other mode collects data up for a user-specified duration and plots the average. When the GUI updates the plot, it displays the mean value of each of the measured parameters. When the Arduino has collected a data point from a particular input and has converted it to a meaningful value, the MATLAB code writes the value to a file with a time stamp.

## ***Methods used in the Cyclohexadiene Collaboration***

A velocity map imaging (VMI) spectrometer was used to detect the ions of the Coulomb exploded cyclohexadiene ring, as well as to record their time of flight. The VMI consists of two oppositely charged plates above and below the interaction region called the repeller and the extractor, respectively. To detect the positive ions, the repeller is positively charged while the extractor is negatively charged. The ions are accelerated through a hole in the

extractor plate and past a lens system and a drift tube before they hit a micro-channel plate (MCP)[10]. Because the signal of a single ion is too weak to be detected, it is amplified by the MCP. The MCP has a number of small channels through which electrons can travel. When an ion hits the MCP, an electron is emitted and multiplied by repeatedly being accelerated and hitting the channel wall. The electron shower has ample charge to generate a fluorescence on the phosphorous screen behind the MCP. Though the phosphorous screen is showing electrons, it is recording where the ions have hit. A camera records images of the screen at the repetition rate of the LCLS.

Since this repetition rate is around 100 Hz, a minute of the experiment will generate about 60,000 images. A single image is a relatively large file, so if one runs the experiment for many hours over several days, one amasses enormous amounts of data. The amount of data needs to be reduced in order to maximize data analysis efficiency.

The camera images are stored as very large .xtc files. To reduce the amount of collected data, a C program finds the x- and y-positions of the ion hits and stores them as smaller .dat files. We wrote a MATLAB script that takes these .dat files, picks out ions and sorts these ion hits by a variety of parameters such as the delay between the UV and the LCLS pulses or the energy of the LCLS pulse that produced the ion hits. This is necessary because the delay and pulse energy as well as other parameters fluctuate at LCLS on a shot to shot basis. Binning is accomplished by splitting the difference between the highest and lowest recorded time delay between the UV and LCLS pulses into a certain number of segments of equal size. Each of these time delays segments represent a bin. Any single shot with a time delay that falls within a particular bin range is sorted into that bin. For example, if a shot has an associated time delay of 210 femtoseconds, the ions recorded in this shot are sorted into the 200-250 femtosecond bin. When the code is finished binning, the data is reduced to time delays and the number of ion hits now associated with these time delays. This

sorting technique minimizes the amount of data taken during the LCLS run. In addition to fluctuating time delay, the LCLS pulse energy also fluctuates, so the data is further reduced by filtering out the ion hits that were produced with a pulse energy below a particular level.

# RESULTS

### *Pressure vs. HHG Yield*

As previously mentioned, the gas pressure in the chamber fluctuates and the HHG yield depends on the pressure. Since the Arduino-GUI system can read in and log sensor values with satisfactory speed, we can monitor the fluctuating pressure more closely. The HHG intensity is detected by a camera. The resulting measurement is time-stamped. Having a time-stamp on the pressure measurements collected by the Arduino enables us to match HHG yield with the corresponding pressure with considerably less difficulty. Figure 8 shows a graph of the pressure versus HHG yield.

### *Results in Ion Binning*

The MATLAB code we wrote was able to pick out the ions successfully. In particular, binning by time delay has helped reduce the amount of data. We are able to provide results from further analysis that have utilized our code. Figure 9 shows that the C-code was indeed able to pick out single ion hits. This shows that the first stage in the data reduction worked. Then, these ion hits from the single shots were binned according to the time delay between UV and X-ray pulse. An image of the binned shots is shown in Figure 10.

# DISCUSSION AND CONCLUSIONS

## *A Better Data Acquisition System*

Replacing the old data acquisition infrastructure with an Arduino board has improved data collection significantly, as data acquisition has become more flexible, user-friendly, and cost effective. The old code, which plotted the pressures with respect to time was not very user-friendly; however with the GUI, it is much easier to stop and restart data acquisition without having to close the GUI window or restart MATLAB. An additional benefit is that the Arduino chip is a very reasonably priced microcontroller that has several useful applications for data acquisition, some of which have yet to be exploited.

### *Controlling Components using the Arduino*

Given the versatile functionality of the Arduino, it will be able to control instruments in the lab or sound alarms based on the values being measured, in order to protect components like vacuum pumps from high pressure and other hazardous conditions. For this application, the Arduino would not necessarily be connected to the computer. Therefore, the code should be written onto the Atmel chip as before, but the Arduino would not interact with a computer-controlled program. The code should be able to take the different undesirable scenarios into account and control different components of the experiment accordingly.

## *Further Work in the Cyclohexadiene Collaboration*

The MATLAB code we wrote kept the more important pieces of information related to the time delays and the higher pulse energies, while eliminating enormous amounts of excess data, proving that this binning technique we utilized was every efficient. Due to promising preliminary results using the MATLAB code, it will be implemented to sort with different parameters and reduce the amount of unnecessary data.

## ACKNOWLEDGMENTS

I would like to thank my mentors Markus Gühr and Brian McFarland as well as Joe Farrell, Max Chalfin, and the rest of the Bucksbaum group for their guidance and support during my summer. In addition, I would like to thank SLAC and the DOE for providing the funding that made this amazing opportunity possible. Finally, I would like to thank my fellow SULI interns for a wonderful summer.

## REFERENCES

[1] P. B. Corkum, "Plasma perspective on strong field multiphoton ionization," *Phys. Rev. Lett.*, vol. 71, pp. 1994–1997, 1993.

[2] K. J. Schafer, B. Yang, L. F. DiMauro, and K. C. Kulander, "Above threshold ionization beyond the high harmonic cutoff," *Phys. Rev. Lett.*, vol. 70, pp. 1599–1602, 1993.

[3] J. L. Krause, K. J. Schafer, and K. C. Kulander, "High-order harmonic generation from atoms and ions in the high intensity regime." *Phys. Rev. Lett.*, vol. 68, no. 24, pp. 3535 – 8, 1992.

[4] B. McFarland, J. Farrell, P. Bucksbaum, and M. Gühr, "High harmonic generation from multiple orbitals in $N_2$," *Science*, vol. 322, p. 1232, 2008.

[5] A. Eppink and D. Parker, "Velocity map imaging of ions and electrons using electrostatic lenses: Application in photoelectron and photofragment ion imaging of molecular oxygen," *Rev. of Sci. Instrum.*, vol. 68, pp. 3477–3484, 1997.

[6] J. Feldhaus and B. Sonntag, "Free-electron lasers high-intensity x-ray sources," in *Strong Field Laser Physics*, ser. Springer Series in Optical Sciences, T. Brabec, Ed. Springer Berlin / Heidelberg, 2008, vol. 134, pp. 91–107.

[7] doc8161.pdf. [Online]. Available: http://www.atmel.com/dyn/resources/prod_documents/doc8161.pdf

[8] Arduino - ArduinoBoardDuemilanove. [Online]. Available: http://arduino.cc/en/Main/ArduinoBoardDuemilanove

[9] "Arduino - Introduction," http://arduino.cc/en/Guide/Introduction.

[10] D. Rolles, Z. Pesic, M. Perri, R. Bilodeau, G. Ackerman, B. Rude, A. Kilcoyne, J. Bozek, and N. Berrah, "A velocity map imaging spectrometer for electron-ion and ion-ion coincidence experiments with synchrotron radiation," *Nuclear Instruments and Methods in Physics Research Section B: Beam Interactions with Materials and Atoms*, vol. 261, pp. 170 – 174, 2007.

[11] H. Frank, "File: FEL principle.png - Wikipedia, the free encyclopedia," http://en.wikipedia.org/wiki/File:FEL_principle.png.

# FIGURES

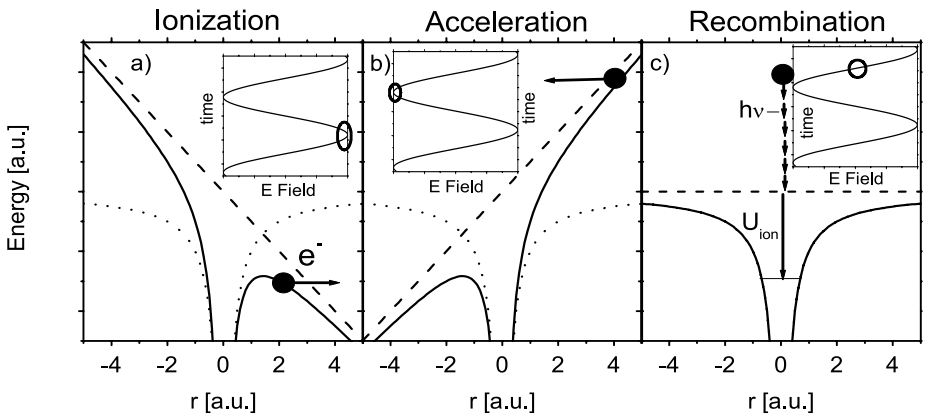


Figure 1: The dashed line represents the electric field potential, while the dotted line represents the Coulomb potential of an atom. The sum of the two potentials is represented by the solid line. The inset shows where the atom is with respect to the electric field phase. For more explanation see text.

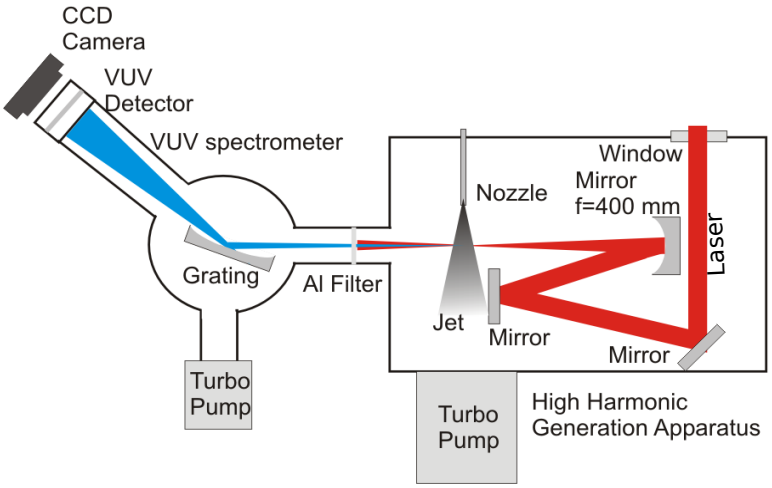


Figure 2: General set up for the experiment. The laser system is omitted and only the vacuum chambers containing the harmonic generation and the spectrometer are shown. The parameters that we can monitor with the Arduino are the laser power and the pressure of the gas in the jet before it enters the chamber.

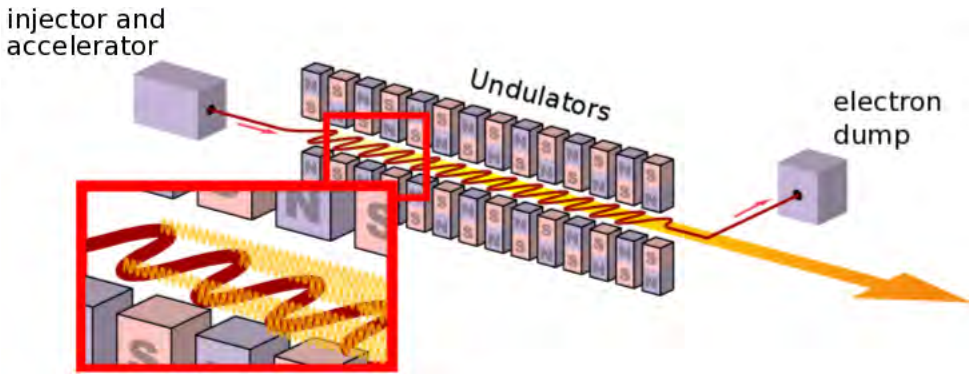


Figure 3: A layout [11] of the x-ray free electron laser at LCLS. Electrons are accelerated into the undulators where x-ray radiation is emitted whenever an electron changes direction. After they pass through the undulators, the electrons are sent to the electron dump while the x-rays continue to the experimental halls to be used.

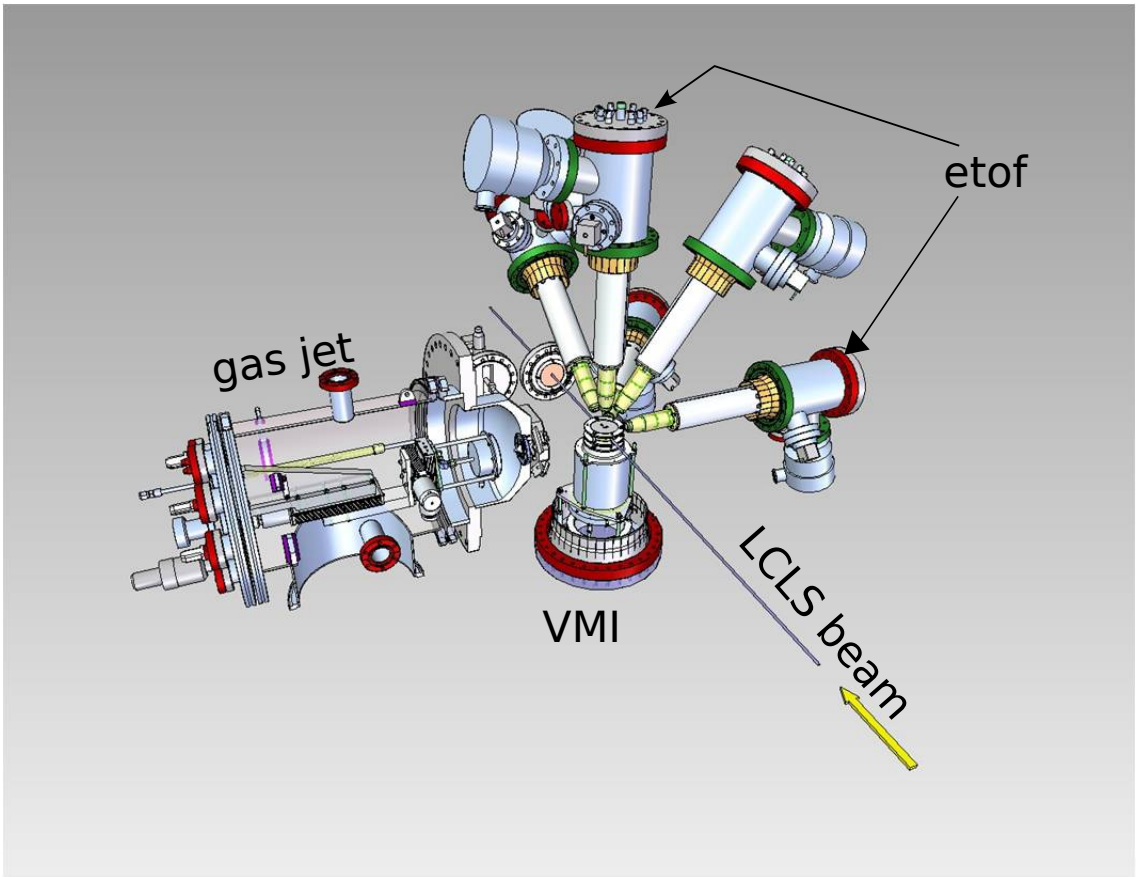


Figure 4: General setup of the AMO end station at LCLS. When the gas jet and the LCLS beam interact, the information about the ions are collected by the velocity map imaging (VMI) spectrometer. (Picture see John Bozek)

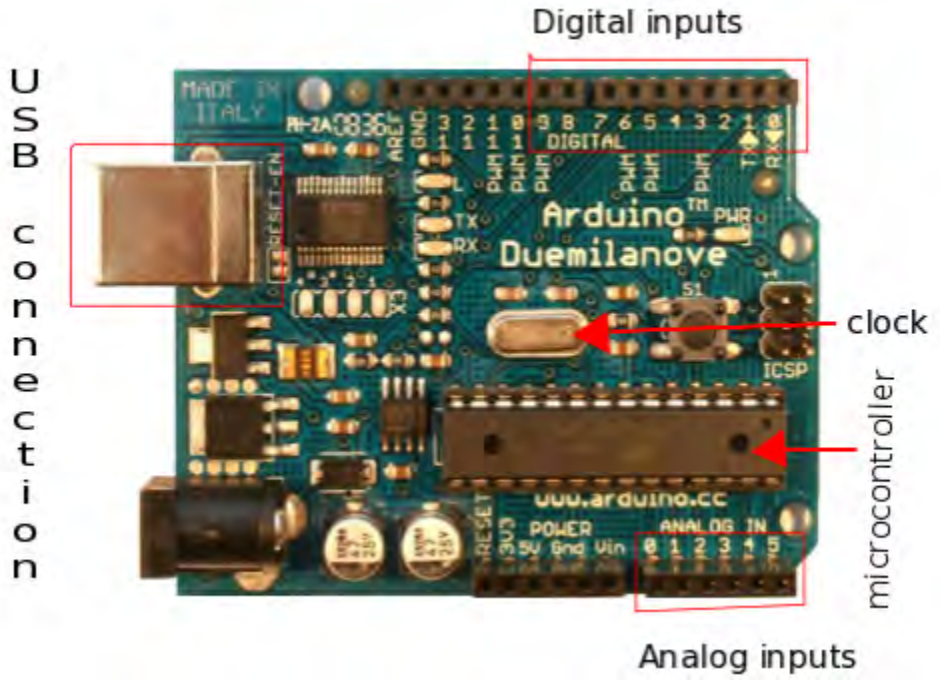


Figure 5: The Arduino Duemilanove has 6 analog inputs and 14 digital inputs.

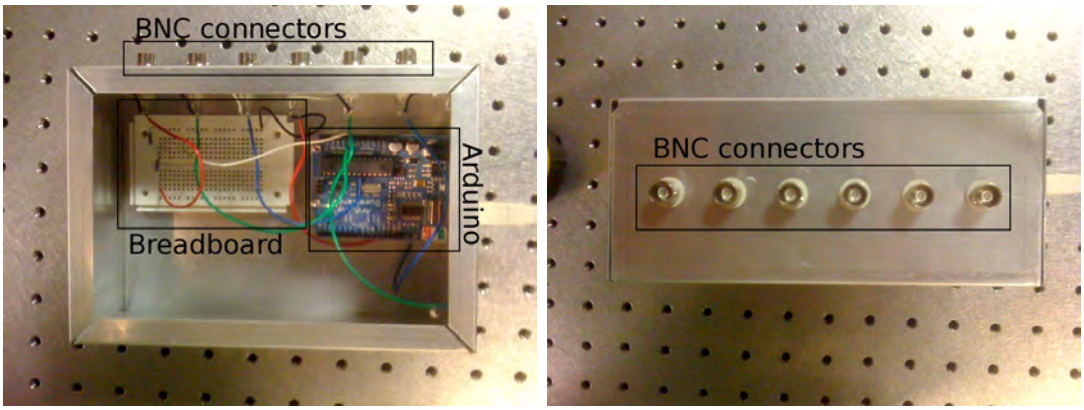


Figure 6: The photo on the left shows the Arduino and a little breadboard in the compartment. The breadboard is used to hold circuits to precondition the incoming voltage signal. The Arduino is on stands so that the bottom does not touch metal box. The photo on the right shows the box from the side to show the 6 BNC connectors.

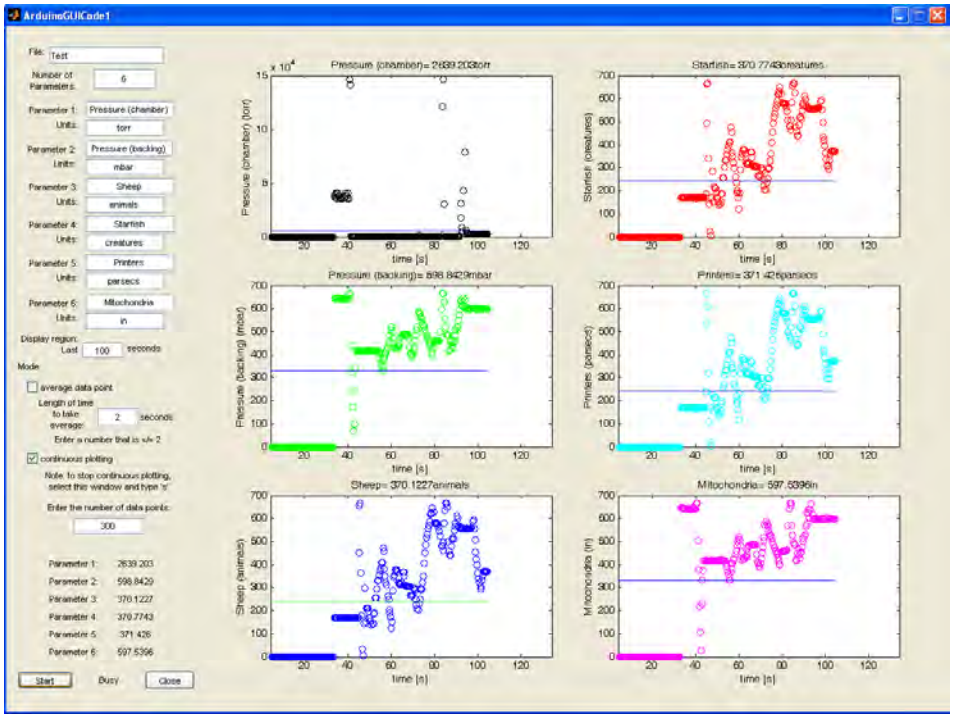


Figure 7: The GUI above is in continuous plotting mode and is monitoring six inputs.

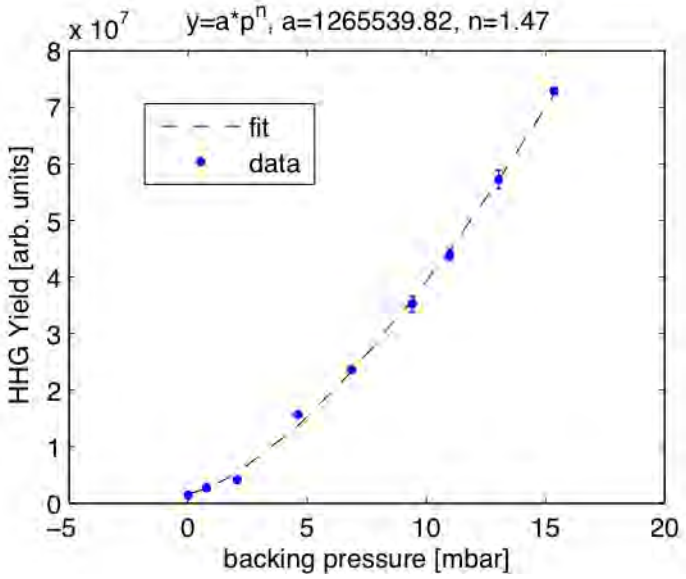


Figure 8: Pressure versus HHG Yield. In an ideal case of perfect phase matching, n would be 2, meaning the signal would increase quadratically with pressure.

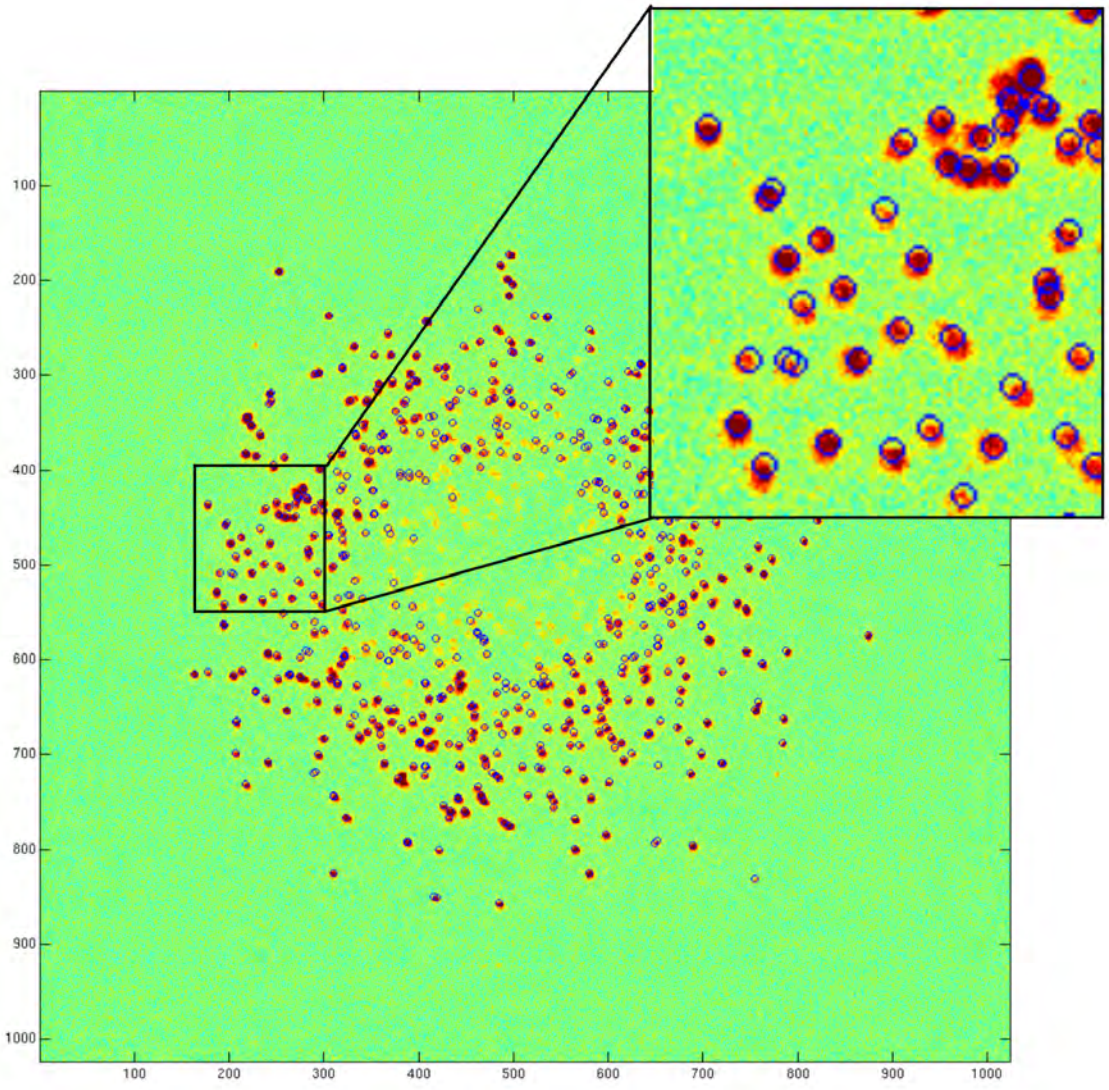


Figure 9: Image processed by C to pick out the ions hitting the VMI (blue circles). One can see that spots of signal intensity are treated as single ion hits. MATLAB is used to superimpose the image and the ions picks from the C code.

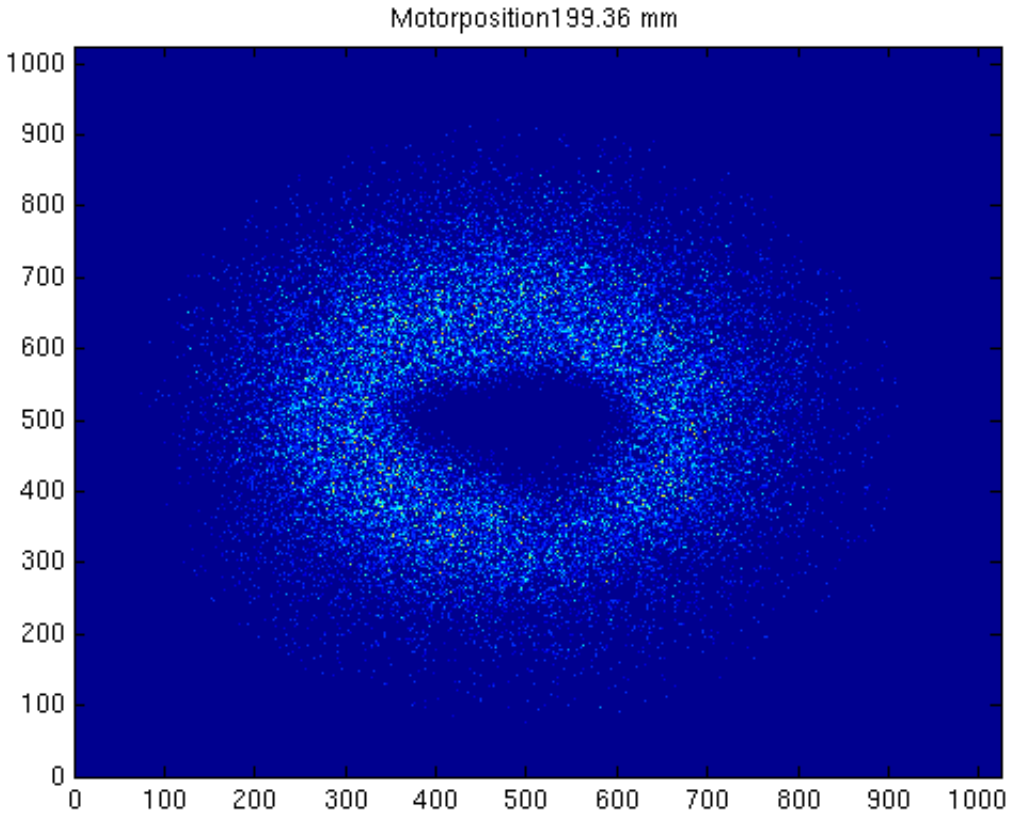


Figure 10: Ion hits of a particular time delay. The Motorposition defines the delay between the UV and the LCLS pulses.

# Calibration analyses and Efficiency Studies for the Anti Coincidence Detector on the Fermi Gamma Ray Space Telescope

Chris Kachulis

Office of Science, Science Undergraduate Laboratory Internship (SULI)

Yale University

Stanford Linear Accelerator Center

Stanford, CA

August 13, 2010

Prepared in partial fulfillment of the requirements of the Office of Science, Department of Energy's Science Undergraduate Laboratory Internship under the direction of Eric Charles at the Kavli Institute for Particle Astrophysics and Cosmology, Stanford Linear Accelerator Center.

Participant: _____

Signature

Research Advisor: _____

Signature

Work supported in part by US Department of Energy contract DE-AC02-76SF00515.

# TABLE OF CONTENTS

# ABSTRACT

Calibration analyses and Efficiency Studies for the Anti Coincidence Detector on the Fermi Gamma Ray Space Telescope. CHRIS KACHULIS (Yale University, New Haven, CT 06520) ERIC CHARLES (Kavli Institute for Particle Astrophysics and Cosmology, Stanford Linear Accelerator Center, Stanford, CA 94025)

The Anti Coincidence Detector (ACD) on the Fermi Gamma Ray Space Telescope provides charged particle rejection for the Large Area Telescope (LAT). We use two calibrations used by the ACD to conduct three studies on the performance of the ACD. We examine the trending of the calibrations to search for damage and find a timescale over which the calibrations can be considered reliable. We also calculated the number of photoelectrons counted by a PMT on the ACD from a normal proton. Third, we calculated the veto efficiencies of the ACD for two different veto settings. The trends of the calibrations exhibited no signs of damage, and indicated timescales of reliability for the calibrations of one to two years. The number of photoelectrons calculated ranged from 5 to 25. Large errors in the effect of the energy spectrum of the charged particles caused these values to have very large errors of around 60 percent. Finally, the veto efficiencies were found to be very high at both veto values, both for charged particles and for the lower energy backsplash spectrum.

# 1 INTRODUCTION

The Anti Coincidence Detector (ACD) on the Fermi Gamma Ray Space Telescope is a detector system built around the silicon strip tracker on the Large Area Telescope (LAT). The purpose of the ACD is to provide charged particle rejection for the LAT. To do this, the ACD must be calibrated correctly in flight, and must be able to efficiently veto charged particle events while minimizing false vetoes due to "backsplash" from photons in the calorimeter [1]. There are eleven calibrations used by the ACD. In this paper, we discuss the use of two of these calibrations to preform three studies on the performance of the ACD. The first study examines trending of the calibrations to check for possible hardware degradation. The second study uses the calibrations to explore the efficiency of an on-board hardware veto. The third study uses the calibrations to calculate the number of photoelectrons seen by each PMT when a minimum ionizing particle is detected, which is a useful value for performing simulations.

# 2 MATERIALS AND METHODS

## *2.1 Detector and Calibrations*

The ACD is composed of eighty-nine 10 mm and 12 mm thick plastic scintillator tiles, which cover the top and four sides of the tracker. The top tiles are arranged in a five by five square, while the four sides have three rows of five tiles each above one large rectangular tile. The gaps between tiles are covered by eight 1.5 mm wide fiber scintillating ribbons. The ACD is shown from the side in Figure 1 [2]. Each tile is optically linked to two separate photo multiplier tubes (PMTs) by wavelength shifting fibers. Scintillation in the tiles from charged particles emits photons which are detected by the PMT's. The voltage readout from the PMT is then converted to a digital signal, called a Pulse Height Analysis (PHA) [1].

We wrote calibration programs in Python using the CERN data analysis package Py-

ROOT [3]. For this paper we are interested particularly in two calibrations; the Pedestal and MIP Peak calibrations. The Pedestal calibration finds the PHA base signal for each PMT. The circuitry of the PMT increases the base voltage from zero, so even when there are no particles passing through the tiles, the voltage output is not zero, and so the PHA signal is also nonzero. Thus, the Pedestal calibration is finds the PHA signal that corresponds to no physics. This is done by taking measurements of the PHA on a periodic trigger at a rate of 2 Hz. Since there is usually no physics in a particular tile, the resulting histogram will have a peak at the pedestal value which is nicely fit by a Gaussian. The mean of the Gaussian is then the value of the pedestal. We can deal with the small number of events where there are particles in the detector by confining the range over which the Gaussian is fitted. A typical pedestal fit is shown in Figure 2. As can be seen in Figure 2, the fitted pedestal value has a very low error, since the peak is very sharp. Typical values for the width of the Gaussian are around 3 PHA counts.

The MIP peak calibration finds the PHA signal of a minimum ionizing particle, which is known to correspond to about 1.9 MeV at normal incidence in the 10 mm tiles. It is important to clarify what we mean when we refer to a MIP. Usually the term MIP refers to a particle at the minimum of the Bethe-Bloch curve. For protons passing through the ACD, this minimum corresponds to a proton energy of 3.19 GeV. However, as can be seen in Figure 3, the geomagnetic cutoff ranges from about 6 GeV to about 14 GeV in Fermi's orbit. This means that lower energy particles, including protons that are usually called MIPs, will be swept away by the earth's magnetic field and will not reach the ACD. So when we refer to a MIP, we are referring to protons right around these geomagnetic cutoffs, since this are the protons that will deposit the lowest energy in the ACD. Because of the shallow rise in the Bethe-Bloch curve above minimum ionizing energies, the spread in the proton energies actually causes a very small spread in the mean energies deposited in the ACD, as shown in Figure 4. This spread is further diminished by the fact that the cosmic ray proton spectrum

falls off very sharply as energy increases. So most of the particles measured by the ACD will deposit about the same mean energy. To find this peak, we select events where a track points to a tile. We then normalize for the angle of incidence and the width of the tile. Histograms of these normalized events contain two peaks, one at the MIP peak, and another backsplash peak, as shown in Figure 5.

The backsplash peak is actually due to three components, backsplash X-rays from the calorimeter, cosmic X-rays, and residual signal from previous events. We call this peak backsplash because the backsplash is the component of this spectrum which is important to this paper since backsplash is the component associated with physics events. The backsplash peak fits very well to an exponential decay.

The MIP peak (assuming a single mean energy value for incoming particles) is in theory a Landau distribution of the energy lost by a MIP in the tile convolved with a Poisson distribution of the PMT counts which has been stretched to account for the conversion from photoelectron counts to PHA counts (for further discussion see section 3.2, specifically Eq.5). However, since fitting a convolution is impractical, we must use other methods. We use three separate fits on the MIP peak, all of which give very consistent MIP peak values. The first fit is a Poisson distribution added to a decaying exponential to account for the backsplash. Since the Landau distribution is significantly thinner than the distribution of the MIP peak (see section 2.3 for calculation) a simple Poisson distribution works quite well. The Poisson distribution works particularly well at low PHA values, which makes it very useful for efficiency calculations since the vetoes we study are at low PHA values. The Poisson-Exponential fit is shown in Figure 6.

The second fit is a Gaussian, again added to a decaying exponential to account for the backsplash. This is a reasonable fit because when the expected value of a Poisson distribution is large it becomes similar to a Gaussian. As will be seen in section 3.2, the number of photoelectrons seen by the PMT's ranges 5 to 25, which is right in the area

where it becomes reasonable to estimate a Poisson distribution with a Gaussian. For this reason, the Gaussian cannot be trusted at low PHA, which is where it diverges most from the Poisson-Landau convolution, and thus where the Poisson distribution is necessary. However, the width and mean of the Gaussian are still trustworthy, which is important. The Gaussian has an advantage over the Poisson because the Gaussian's width is not defined as the (scaled ) square root of its mean. Thus the Gaussian can allow for the combination of the spread from the counting statistics of the PMTs, the Landau distribution, and the particle energy spectrum. This allows us to separate the different contributions, which is important when calculating the number of photoelectrons counted by each PMT. The Gaussian-Exponential fit is shown in Figure 7.

The final fit is a double Gaussian. This fit is used to fit higher PHA values than the other two fits. At higher PHA values the Poisson-Landau convolution falls below the histogram because of contamination from higher energy particles. The double Gaussian allows us to extend our fit to higher values and the calculate more accurate values for the total number of charged particle events, which we need to know to calculate veto efficiencies. Above the range of the double Gaussian we simply add up the number of events in the histogram. The double Gaussian fit is shown in Figure 8

### *2.2 Trending*

We check for possible signs of degrading due to radiation damage that is a danger for any detector in space by examining the trends of MIP peak and Pedestal calibrations. We would expect degrading of the tiles or the optical connections to cause systematic downward trending in MIP peak values, while leaving Pedestal values unchanged. Degrading of the PMT and Analog to Digital Converter (ADC) circuitry could cause a the Pedestal values to trend either up or down, depending on the manner in which the circuitry is degrading. To examine this trending, we sampled data from once every four weeks between weeks 28 and

108 of the mission. We then plotted Pedestal and MIP peak values versus time, and fit a straight line to the data. The slope of that line indicates the trend of the calibration.

### *2.3 Photoelectron Calculation*

We use the Exponential-Gaussian fit to calculate the number of photons seen by each PMT. The spread of the MIP peak is due to three sources; the counting statistics which follow a Poisson distribution with standard deviation $\sqrt{N}$ where $N$ is the number of counts, the Landau distribution of the energy lost by a particle in the scintillator, and the particle energy spectrum. The Landau distribution has been well studied, and it is known that the full-width-at-half-maximum of the Landau distribution is $4\xi$ where:

$$\xi = \frac{K}{2N_A}\frac{n_e w}{\beta^2} \tag{1}$$

for K=0.307075 MeV cm$^2$ mol$^{-1}$, $N_A$ Avogadro's number, $n_e$ the electron density of the absorber, and $w$ the width of the absorber[4]. We normalized our events to a tile width of 1 cm, and the ACD tiles are EJ-200 Plastic Scintillators manufactured by Eljen Technology [5]. The electron density of the scintillators is specified as $n_e = 3.33 \times 10^{23}$ electrons/cm$^3$ [6]. Our particle spectrum is dominated by particles right around the geomagnetic cutoff, which ranges from about 8 GeV to about 16 GeV over the path of the satellite. These correspond to beta values for protons of $\beta = 0.993$ and $\beta = 0.998$. Plugging everything in and using the average of our two $\beta$s, we find that $\xi = 0.0857$ MeV. This indicates a f.w.h.m. of the Landau distribution of 0.344 MeV. The f.w.h.m. of the MIP peak is generally around 1.5 MeV, thus indicating that the spread of the Gaussian is due mainly to the Poisson counting statistics. This explains why the Exponential-Poisson fit works well. The contribution from the particle energy spectrum has not been well studied. To get a very rough estimate we assume that this spread contributes a spread of 12 percent of the MIP peak. It should be noted that this

is an extremely rough estimate. The energy loss spectrum is likely not particularly Gaussian, so it's effect on the spread will need to be very well studied to be correctly accounted for. We then subtract both this spread and the spread due to the Landau from the Gaussian spread in quadrature.

$$\sigma_C = \sqrt{\sigma^2 - \sigma_L^2 - \sigma_E^2} \tag{2}$$

where $\sigma_C$ is the standard deviation due to counting statistics, $\sigma_L$ is from the Landau distribution, $\sigma_E$ is from the particle energy spectrum and $\sigma$ is the original standard deviation of the fit. Then, from the square root law, we know that:

$$\frac{\mu}{\sigma_C} = \frac{N}{\sqrt{N}} = \sqrt{N} \tag{3}$$

where $\mu$ is the mean of the Gaussian. Finally, since the PHAs are normalized for the path length of the particle through the ACD, we divide our calculated number of photoelectrons by the average path length factor (defined as the path length divided by 10 cm) to find the number of photoelectrons counted by each PMT for a MIP at normal incidence.

One complication that must be accounted for is that because of the asymmetry of the Landau distribution, the convolution of the Landau with the Poisson shifts the peak about 5 percent higher. So in practice we use the formula:

$$\frac{0.95\mu}{\sigma_C} = \frac{N}{\sqrt{N}} = \sqrt{N} \tag{4}$$

### *2.4 Veto Efficiency*

We used the Exponential-Poisson distribution to study the efficiency of the onboard hardware veto. As explained above in sections 2.1, the exponential in this fit accounts for the backsplash peak. One of the objectives of the ACD is to avoid falsely vetoing backsplash events, which is one of the three components of the backsplash peak [5]. The Poisson distribution

accounts for the charged particles we want to veto. We can thus separate the histogram into these two components, and analyze the respective fraction of charged particles and backsplash rejected by a particular veto setting.

We also use the Double Gaussian fit when measuring the efficiency. The Exponential-Poisson fit allows us to separate the different components around the first dip, where they both have noticeable effects. The Double Gaussian is used at higher PHA to allow us to extend the fit farther than the reasonable range of the Exponential-Poisson fit, and more closely match the higher energy particle contamination. These two fits are stitched together just above the peak, as shown in Figure 9. Beyond the range of the Double Gaussian a simple count of the number of entries in the histogram is used. It is important to note that the histograms cut off around 2000 PHA. Around 15 percent of the total events are generally above 2000 PHA, so the total number of charged particles must be multiplied by 1.15 before being used for efficiency calculations.

# 3 RESULTS

## *3.1 Trending*

Neither the MIP peak nor the Pedestal trends exhibit any evidence of systematic drift. Histograms of these trends are shown in Figure 10 and Figure 11. As can be seen from these histograms there is no systematic drift in either calibration. Since the MIP peak values would be expected to trend downward if tile or optical connection damage were beginning to affect them, the Gaussian distribution of the MIP peak trend indicates that the possible trends of individual PMTs are more likely statistical noise than actual degrading of individual tiles or PMT optical connections. This indicates there is not yet a noticeable effect from radiation damage to the tiles or optical connections.

The same logic cannot be applied to the Pedestal trends, since these would be expected

to trend both up and down, depending on the particular damage in each PMTs respective circuitry. However, the sharpness of the Pedestal trend peak around zero indicates that the Pedestal values have been remaining very stable, and thus give no indication of any degrading of the circuitry.

The stability of the calibrations indicates that at current rates the calibrations can be trusted for at least a couple of years. For the pedestal calibration, a two sigma tile calibration will be within 5 percent of correct for 3.74 years. For the MIP peak calibration, it will be within 5 percent for 1.80 years. This does not mean that current calibrations should be taken as correct for the next two years, since future damage to the instrument could greatly change calibrations. It only indicates that no significant damage has yet occurred, and that calibrations from a few years ago can still be considered reasonably valid.

### *3.2 Photoelectron Calculations*

The number of photoelectrons counted by each PMT from a MIP at normal incidence was calculated for run 0299978033. The run number indicates that the data run began at 23:13:53 UTC on July 4, 2010. Figure 12 shows a histogram of the number of photoelectrons counted by each PMT. Two PMTs (PMT A on tile 220 and PMT A on tile 423) are not included in the histogram because they have poor optical connections which cause their event histograms to be too skewed to make reliable fits. The number of photoelectrons ranges from just above around 5 to around 26 photoelectrons, with a mean of 11.87 photoelectrons. The errors on these values are very large (around 60 percent) because of the large uncertainty of the particle energy spectrum effect. In order to make more reliable calculations, the effect of the particle energy spectrum must be further studied and well understood.

We can use our photon calculations to calculate the theoretical distribution of PHA values that they should result in and compare it to the actual histogram of events. In doing this, we ignored the effects of the particle energy spectrum since we do not understand it very well.

The Landau distribution is computed easily in ROOT from the MIP peak value (multiplied 0.95 to account for the shift caused by the convolution) and the value of $\xi$ calculated above. We normalized this distribution empirically for the number of particles in the histogram which are MIPs (not backsplash peak or higher energy contamination). The calculated photoelectron value gives us a photoelectron PHA ratio, $\rho_p = \frac{\mu}{N_p}$. The distribution is then calculated point by point as:

$$D(x) = \int_{-\infty}^{\infty} P_{\rho_p, \frac{x'}{\rho_p}}(x) L(x')\, dx' \tag{5}$$

where $P_{\rho_p, \frac{x'}{\rho_p}}$ is the Poisson distribution with mean $\frac{x'}{\rho_p}$ stretched by a factor of $\rho_p$. This Poisson distribution is thus a PHA version of the regular Poisson distribution with a mean of x'. We calculated the Poisson-Landau distribution D(x) as a discrete sum with step size 1 and limits $x \pm 1000$. Figure 13 shows the resulting distribution in red along with the corresponding histogram of events. As can be seen in Figure 13, the Poisson-Landau fits very well to the histogram of events. This may indicate that the particle energy spectrum effect is rather small, although further study is needed to draw any real conclusions.

Figure 14 compares the Poisson-Landau distribution to the Exponential-Poisson and Exponential-Gaussian fits in the low PHA range where the vetoes are studied. As can be seen in Figure 14 the Exponential-Poisson matches the actual Poisson-Landau distribution much better than the Exponential Gaussian in this range. This is the reason we use the Exponential-Poisson fit when studying the veto efficiency.

### *3.3 Veto Efficiency*

We calculated the charged particle and backsplash efficiencies for run 0299978033 for different vetoes ranging from 0.2 MIPs to 0.6 MIPs. For the charged particles, efficiency was defined as the fraction of events rejected by a particular veto, while for the backsplash efficiency was

defined as the fraction of events allowed through by a particular veto. So, for both elements higher efficiencies are better.

Because of the setup of of the ACD cuts, we are particularly interested in the veto efficiencies at 0.22 MIPs and 0.44 MIPs. In the LAT photon selection process there is one cut which examines the ratio of the energy in the ACD to the energy in the calorimeter and rejects the event if this ratio is greater than 0.008. Thus this cut will reject a 100 MeV event if any tile records over 0.44 MIPs. There is a tighter cut at 0.22 MIPs when a track points directly to within 16 mm of the ACD tile where energy is recorded, since such an event is less likely to be backsplash.

Histograms of the charged particle and backsplash efficiencies for a veto of 0.44 MIPs are shown in Figures 15 and 16. Again the two bad PMTs are not included. As can be seen in Figure 15, the average charged particle efficiency at 0.44 MIPs is 0.988 with a standard deviation is 0.00765. The average backsplash efficiency is slightly lower, at 0.9438. The backsplash efficiencies have a wider spread than the charged particle efficiencies, with a standard deviation of 0.02002. This is partly due to the fact that since the charged particle efficiencies are closer to 1, the spread, particularly on the high side, gets squeezed together more simply by the fact that the efficiency cannot be greater than 1. This effect is also responsible for the fact that the backsplash distribution is more symmetric than the charged particle distribution.

Since an event with a track pointing all the way to the ACD is less likely to be backsplash, we are more concerned with the charged particle efficiency for the 0.22 MIP cut than with the backsplash efficiency. A histogram of the charged particle efficiency for the 0.22 MIP cut is shown in Figure 17. As can be seen the mean efficiency is 0.9992, with a standard deviation of 0.001352.

# 4 CONCLUSION

We used the pedestal and MIP peak calibrations for the ACD on the Fermi LAT to conduct three studies. In the first study, an examination of the trends of the calibrations revealed no indication of degrading hardware on the LAT. We calculated timescales over which the pedestal and MIP peak calibrations would remain reliable. The pedestal calibration remains reliable for a timescale of about 3.74 years, while the MIP peak calibration remains reliable for a timescale of about 1.8 years. In the second study we measured the efficiencies of different veto thresholds, with particular interest in the efficiencies at 0.44 MIPs and 0.22 MIPs. The charged particle efficiency was found to be on average 0.9992 at 0.22 MIPs and 0.988 at 0.44 MIPs while the backsplash efficiency was found to be 0.9438 at 0.44 MIPs. These high efficiencies indicate that the choices of those setting for ACD veto cuts are good decisions. Finally we made rough estimates of the number of photons seen by a PMT from a MIP at normal incidence. The mean of this calculation was 11.87 photons, although the large uncertainties of the effects of particle energy spectrum cause large uncertainties of around 60 percent in these photon calculations. In order calculate more precise values for the number of photons, the particle energy spectrum will need to be closely studied.

# 5 ACKNOWLEDGMENTS

I would like to thank my mentor Eric Charles for his guidance and support. I would also like to thank the U.S. Department of Energy and their financial support, SLAC for hosting the SULI program, and everyone involved in running the SULI program at SLAC for making the program run so smoothly.

# REFERENCES


[1] A. Moiseev *et al.*, "The anti-coincidence detector for the glast large area telescope," *Astroparticle Physics*, vol. 27, pp. 339–358, 2007.

[2] http://fermi.gsfc.nasa.gov/acd/images/djt/ACD_June4.html, August 2010.

[3] "How to use the python pyroot interpreter?" http://root.cern.ch/drupal/content/how-use-use-python-pyroot-interpreter, August 2010.

[4] C. Amsler *et al.*, "Review of particle physics," *Physics Letters*, vol. B667, pp. 1+, 2008.

[5] A. Moiseev *et al.*, "High efficiency plastic scintillator detector with wavelength-shifting fiber readout for the glast large area telescope," *Nuclear Instruments and Methods in Physics Research A*, vol. 583, pp. 372–382, 2007.

[6] *EJ-200 PLASTIC SCINTILLATOR*, Eljen Technology.

# FIGURES


Figure 1: The ACD seen from the side.

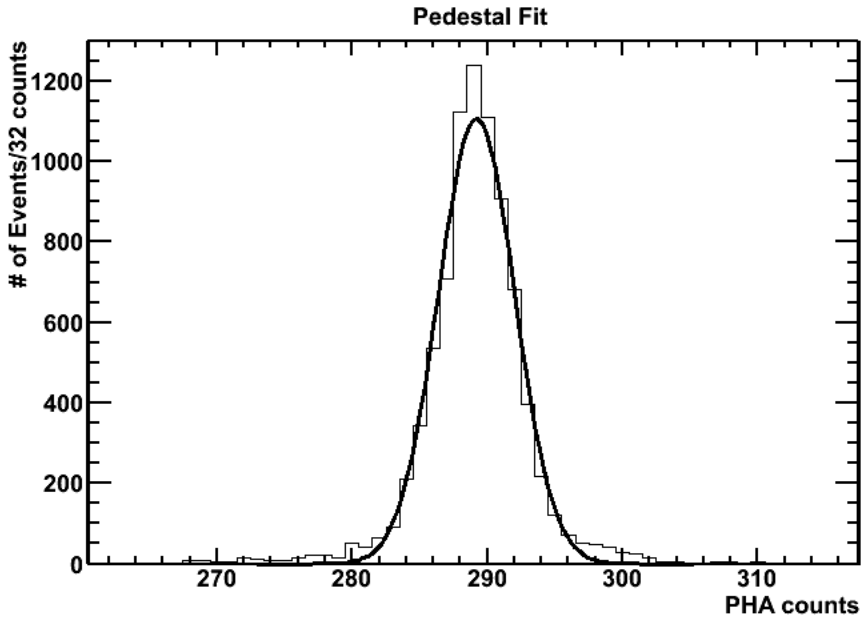


Figure 2: Typical Pedestal Fit

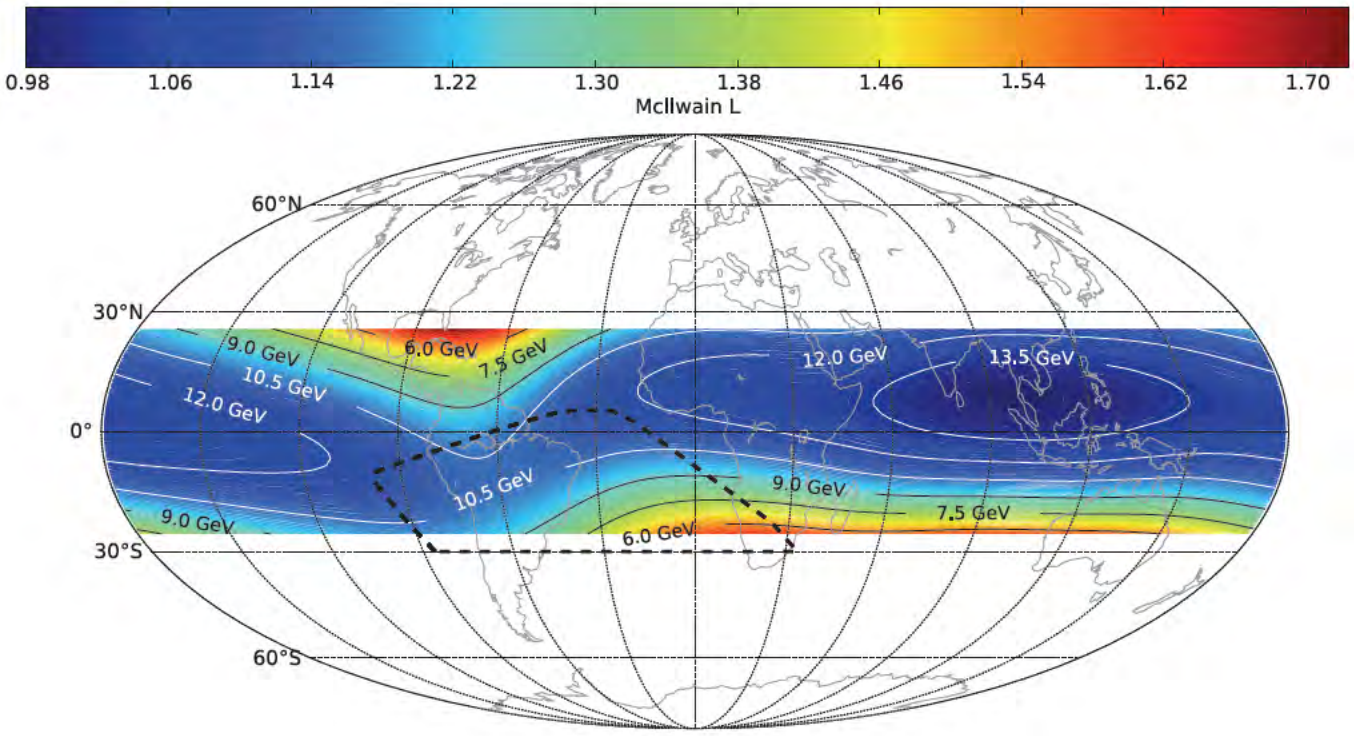


Figure 3: The geomagnetic cutoff in the orbit of Fermi, at Fermi's altitude.

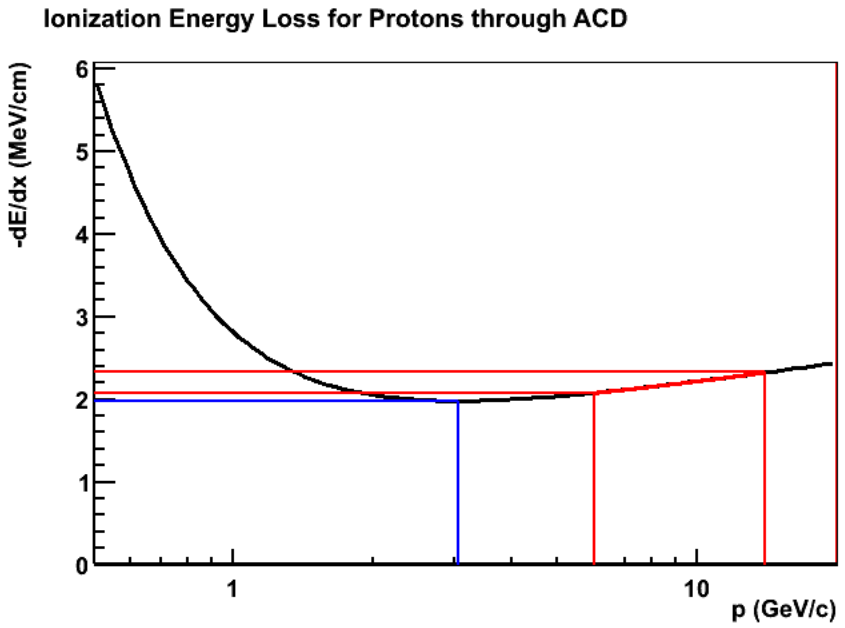


Figure 4: The Bethe-Bloch curve for particles in the ACD. The blue lines indicate a true "minimum ionizing particle." The red lines indicate the geomagnetic cutoff range over the orbit of Fermi.

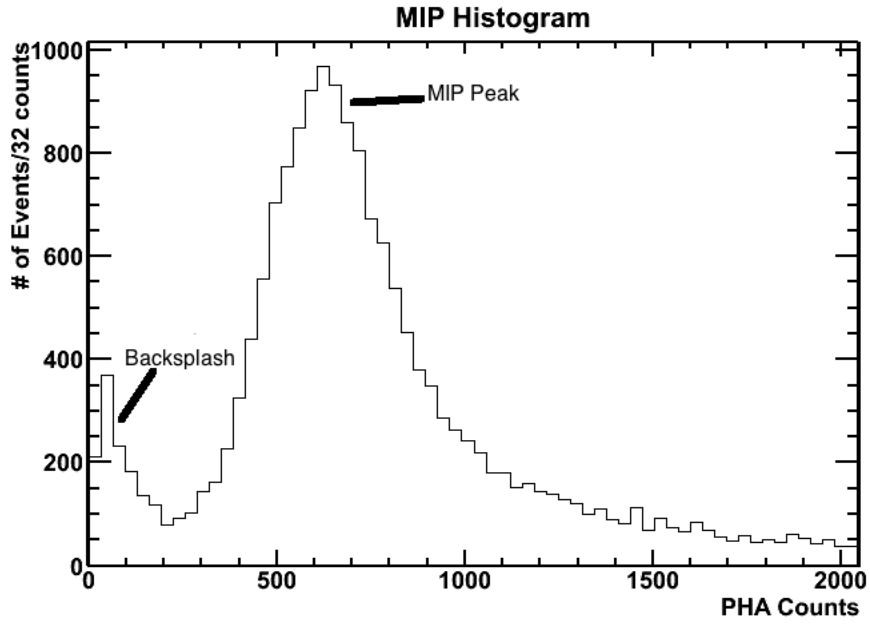


Figure 5: The two peaks of a MIP peak histogram

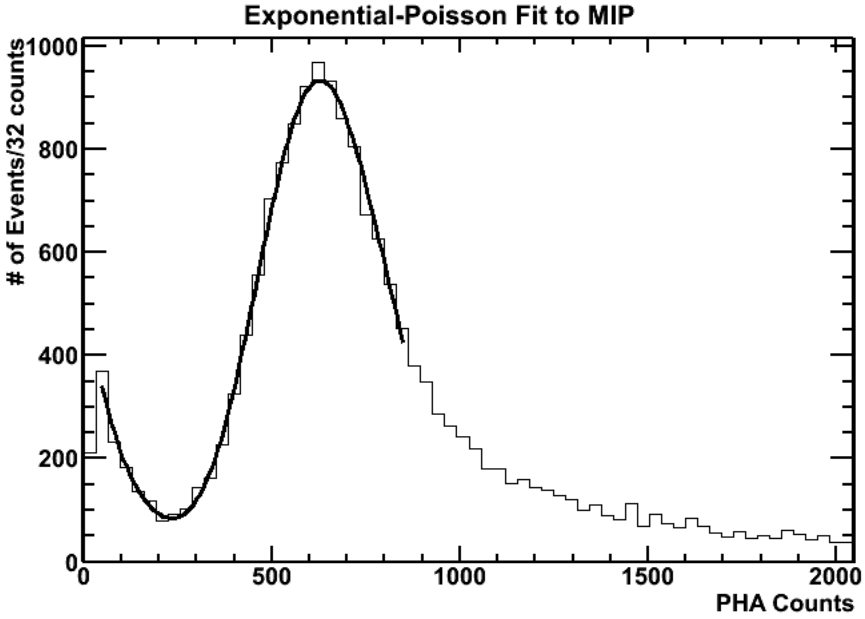


Figure 6: Exponential-Poisson fit to MIP peak.

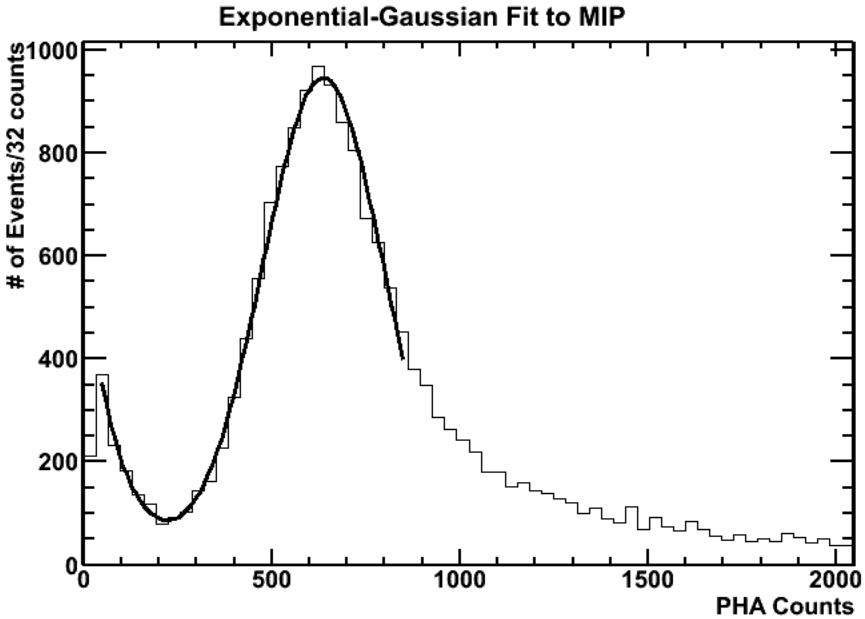


Figure 7: Exponential-Gaussian fit to MIP peak.

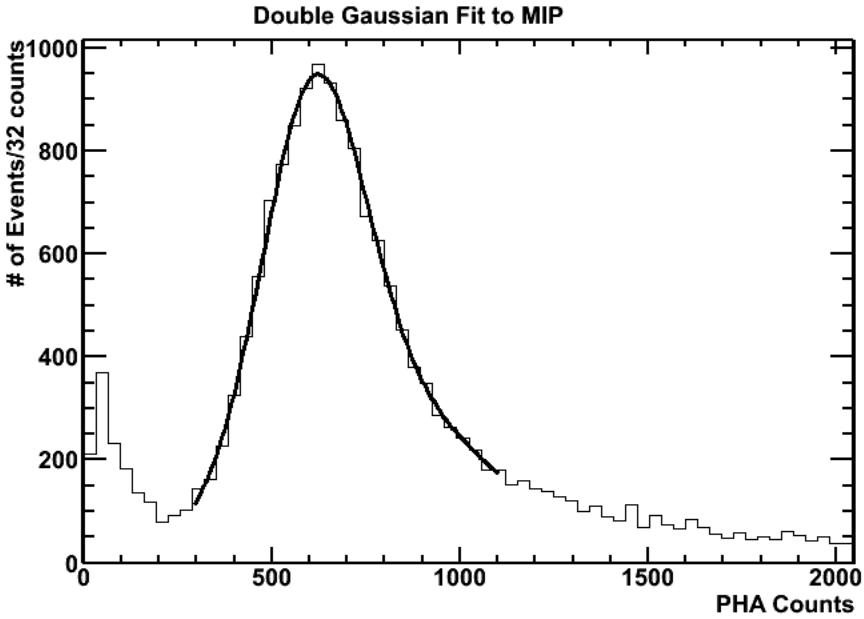


Figure 8: Double Gaussian fit to MIP peak.

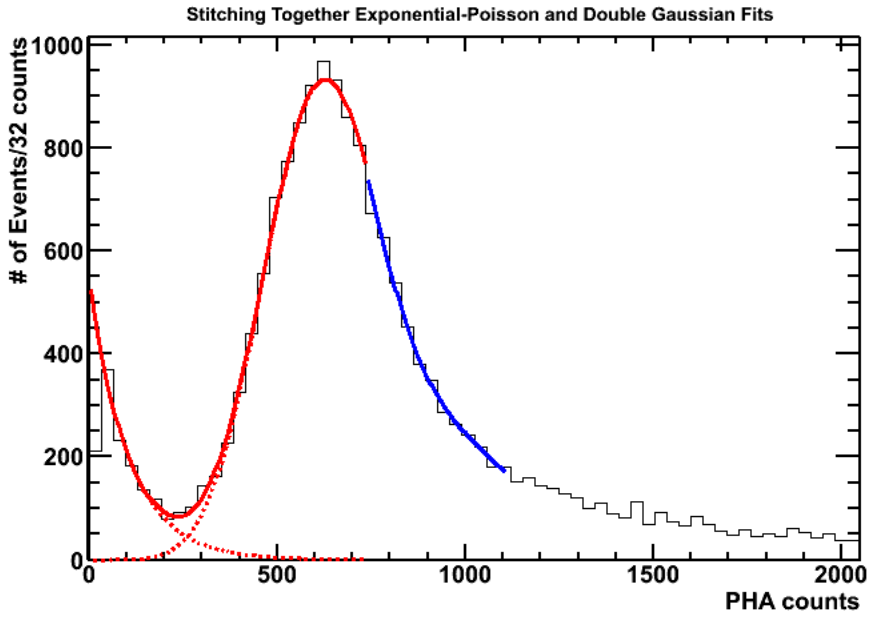


Figure 9: Stitching together the Exponential-Poisson and Double Gaussian fits. The red is the Exponential-Poisson fit, the blue is the Double Gaussian fit. The dotted red lines show how the histograms are separated into backsplash and charged particle components.

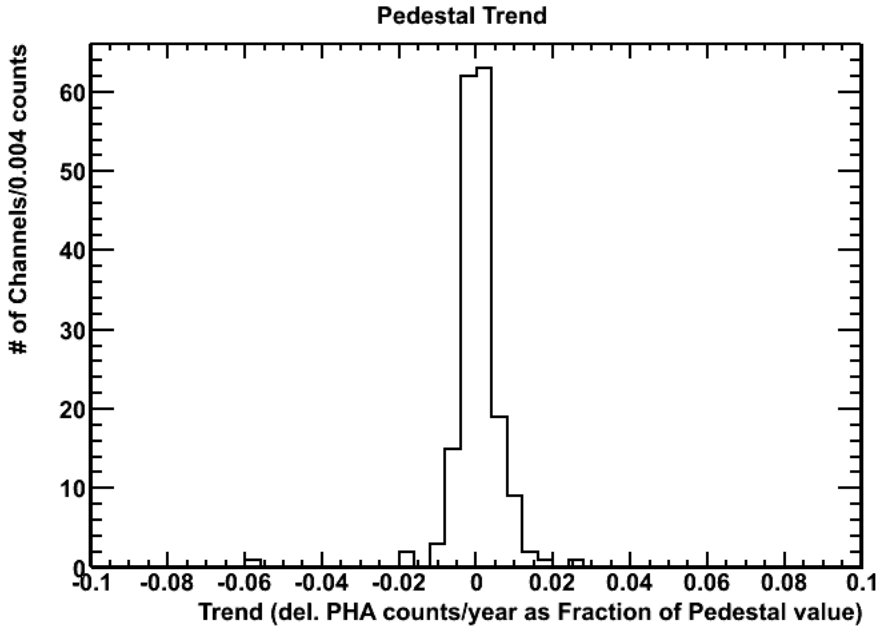


Figure 10: Histogram of Pedestal Trend

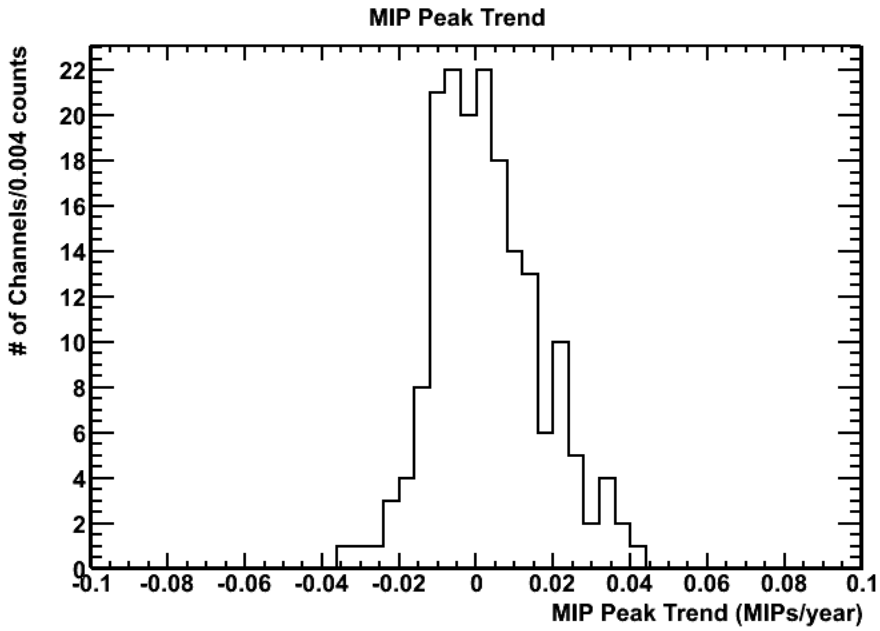


Figure 11: Histogram of MIP Peak Trend

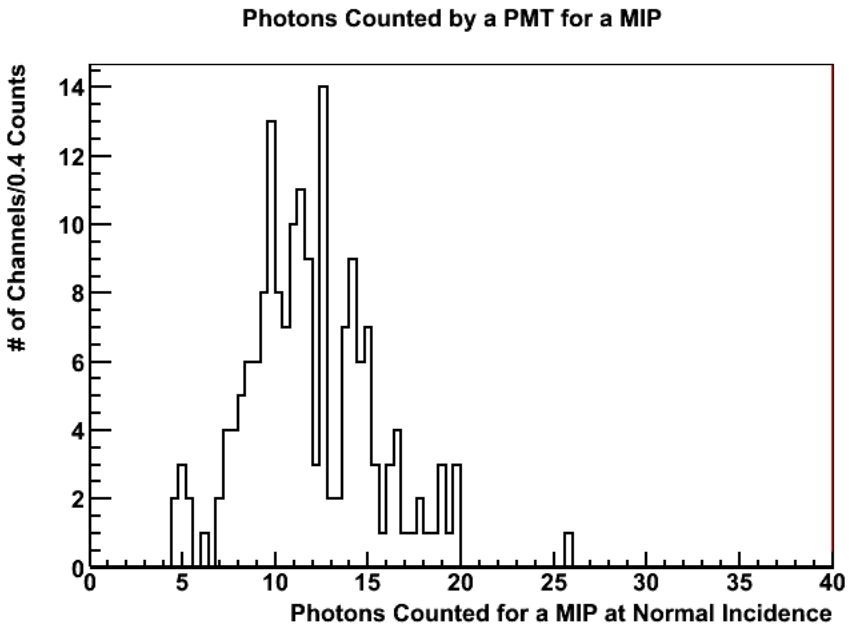


Figure 12: Photons seen for a MIP.

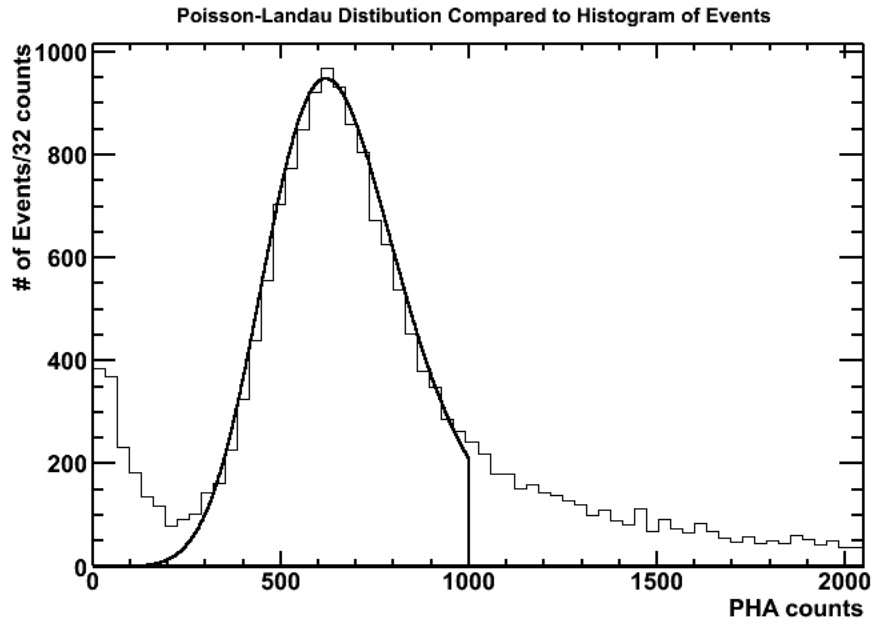


Figure 13: Comparison to Poisson-Landau distribution to histogram of events.

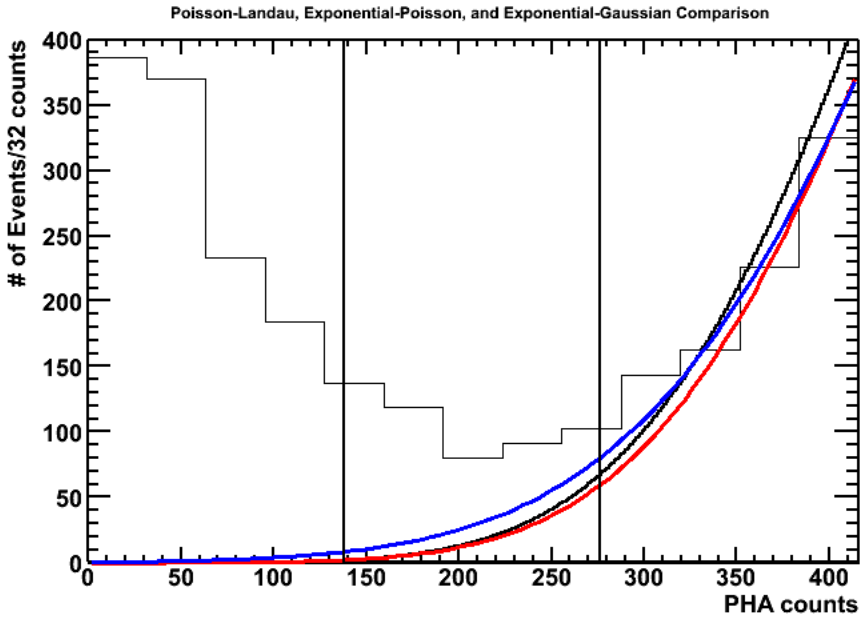


Figure 14: Comparison of Poisson-Landau convolution to Exponential-Poisson and Exponential Gaussian fits. The Poisson-Landau is black, the Exponential-Poisson blue, and the Exponential-Gaussian is red. The two vertical lines are at 0.22 MIPs and 0.44 MIPs.

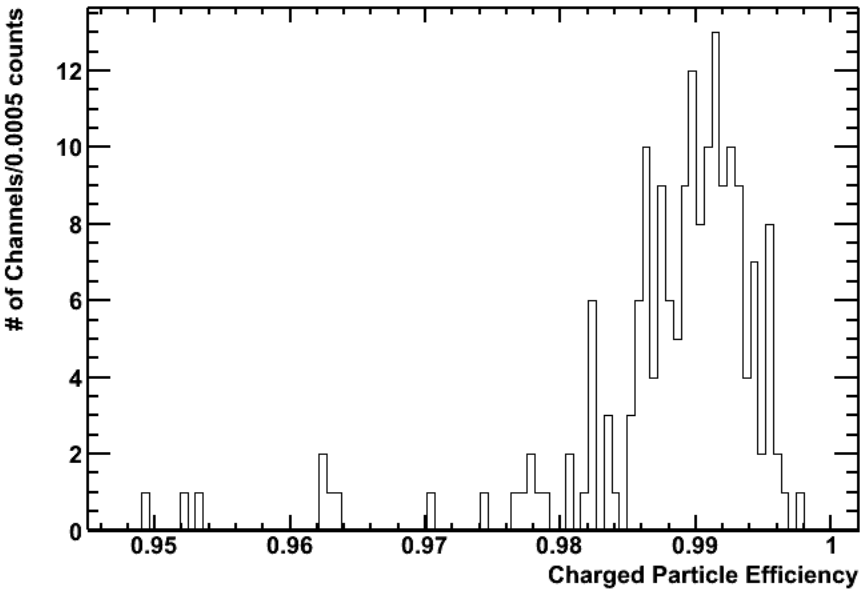


Figure 15: Histogram of charged particle veto efficiency at 0.44 MIPs

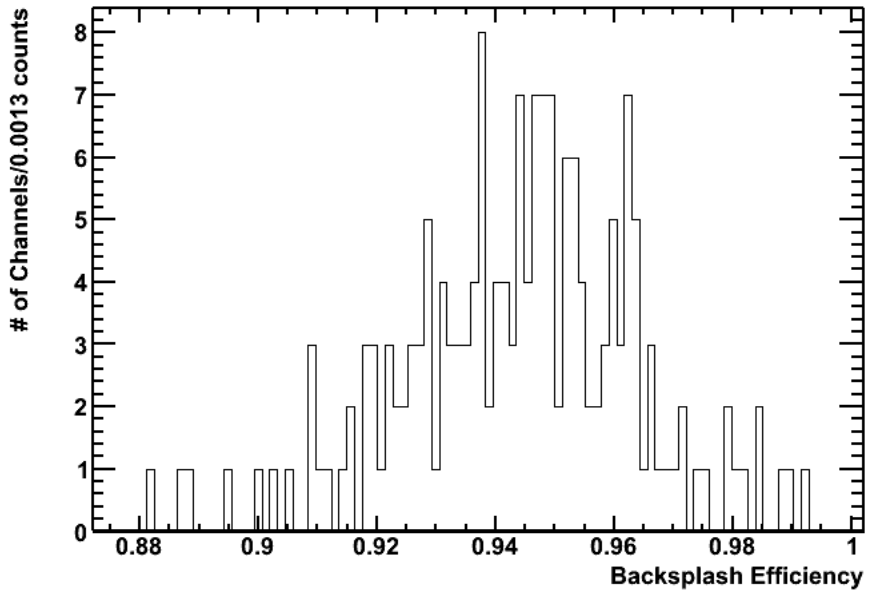


Figure 16: Histogram of backsplash veto efficiency at 0.44 MIPs

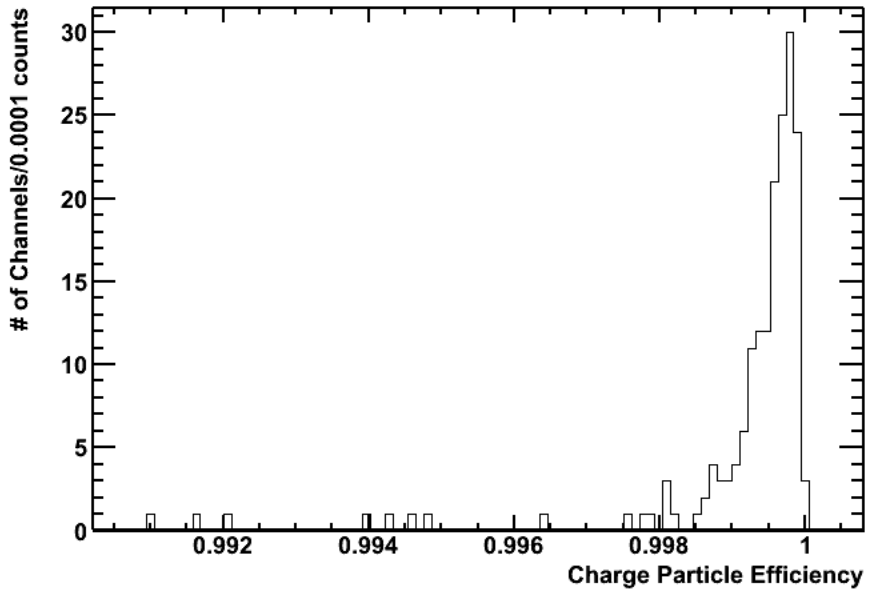


Figure 17: Histogram of charged particle veto efficiency at 0.22 MIPs

# Parallelizing AT with MatlabMPI

Evan Y. Li

Office of Science, Science Undergraduate Laboratory Internship (SULI)

Brown University

SLAC National Accelerator Laboratory

Menlo Park, CA

August 20, 2010

Prepared in partial fulfillment of the requirements of the Office of Science, Department of Energy's Science Undergraduate Laboratory Internship under the direction of Xiaobiao Huang at the Stanford Synchrotron Radiation Lightsource (SSRL).

Participant: _____

Signature

Research Advisor: _____

Signature

Work supported in part by US Department of Energy contract DE-AC02-76SF00515.

# TABLE OF CONTENTS

# ABSTRACT

Parallelizing AT with MatlabMPI. EVAN Y. LI (Brown University, Providence, RI 02912) XIAOBIAO HUANG (Stanford Synchrotron Radiation Lightsource (SSRL), Menlo Park, CA)

The Accelerator Toolbox (AT) is a high-level collection of tools and scripts specifically oriented toward solving problems dealing with computational accelerator physics. It is integrated into the MATLAB environment, which provides an accessible, intuitive interface for accelerator physicists, allowing researchers to focus the majority of their efforts on simulations and calculations, rather than programming and debugging difficulties. Efforts toward parallelization of AT have been put in place to upgrade its performance to modern standards of computing. We utilized the packages MatlabMPI and pMatlab, which were developed by MIT Lincoln Laboratory, to set up a message-passing environment that could be called within MATLAB, which set up the necessary pre-requisites for multithread processing capabilities. On local quad-core CPUs, we were able to demonstrate processor efficiencies of roughly 95% and speed increases of nearly 380%.

# INTRODUCTION

As the field of accelerator physics continues to grow, so too does the need for faster, more efficient methods of beam simulation in computationally intensive tracking functions. The Accelerator Toolbox (AT) for MATLAB, which has been in development at the Stanford Synchrotron Radiation Lightsource (SSRL), has grown increasingly popular throughout the scientific community in recent years. This is due to its ability to combine the efficacy of modern-day, industry-standard tracking algorithms with the flexibility, intuitiveness, and efficiency of the MATLAB working environment, making it the modeling code of choice in SLAC projects such as the SPEAR3 Synchrotron Light Source [1].

Though it functions as a powerful tool, AT's methods and implementations for particle simulation still show room for further development. A number of the most difficult tasks in storage ring simulation, particularly processes such as lattice design optimization and dynamic aperture tracking, require highly computation-intensive algorithms. With plans to upgrade the performance of the SPEAR3 storage ring, SSRL now requires even more powerful calculations to be implemented for optimization processes. This drastically increases the amount of time and processing power needed to produce satisfactorily accurate models of particle beam motion. While AT's current methods are presently capable of performing these tasks, code can take a sizable amount of time to run to completion, detracting from the efficiency that AT strives to provide for its users.

Our goal is to upgrade AT's functionality with the efficiency standards of modern computing. We have worked to implement design changes to our computing models by transitioning the passmethods from their original serial-code construction to a generalized parallel-computing structure, allowing these functions to take advantage of both the symmetric multiprocessing capabilities of most modern-day computers and the overwhelming computational power of supercomputing clusters present in large-scale research facilities. It should be noted

that parallel computing has proven to be one of the most straightforward and promising approaches toward hastening the computing speed in accelerator physics, as the main source of bottlenecks in AT's performance stems from heavily reiterative calls of particle tracking functions which are largely independent of each other. In addition, tests in computational accelerator physics have demonstrated promising values for processor efficiencies [2], allowing us to reduce computing times by hundreds of factors with the use of a large computer cluster.

The first revisions we implemented were conducted using OpenMP specifications for C/C++ compilers (OpenMP has emerged as the standardized model for shared memory computing). By exploiting the multi-core processing capabilities of common workstations, we were instantly able to observe runtime speed increases to nearly 400% of their original values. Once we were able to successfully demonstrate the efficacy of parallel computing on a local machine, we then worked to implement parallelization adhering to a distributed memory model by using the MatlabMPI implementations of the standardized Message Passing Interface (MPI), which allowed us to run AT on multi-CPU setups and supercomputing clusters. By introducing these modifications, we were able to demonstrate enormous upgrades in AT's computational abilities, and can potentially reduce processing times to less than 1% of those associated with the previous implementations.

## DYNAMIC APERTURE DETERMINATION

The dynamic aperture is a property of accelerator structures which describes certain boundary conditions, inside of which a particle can continue to exhibit a stable orbit as it passes repeatedly through the electromagnetic fields of the apparatus. Conversely, particles located outside of the dynamic aperture will tend to exhibit chaotic orbits, causing their transverse displacements from the axis of the beam to amplify, resulting in collisions with the physical

aperture of the machine. This chaotic behavior is a highly problematic experimental factor, as it results in low injection efficiency, beam loss, and increased radiation hazards. To ensure a successful design, the dynamic aperture must be calculated repeatedly and the beam optics adjusted many times to maximize the stability of the beam.

In the particle accelerator design process, tasks of calculating the dynamic aperture and finding the optimal lattice design have proven to be some of the most computationally intensive problems that accelerator physicists face, with optimization algorithms demonstrating runtimes on the order of several hours, days, or even weeks. Currently, there is promising evidence to suggest that these are the algorithms that will benefit most from implementations of parallel computing. Our project will focus on `ringpass`, which defines the function that AT uses to carry out this computing procedure and thus will be the focus of our parallelization efforts.

## DISCUSSING `RINGPASS`

AT models accelerator particle motion by representing the electromagnetic properties of the fields in the lattice as passmethod functions, M, which act upon the vector representation of the particle to produce the evolved trajectory vector:

$$\vec{X}(n) = M_n M_{n-1} \cdots M_2 M_1 \vec{X}_0$$

Calls to `ringpass` will evolve the particle trajectories as the script is run. Each function call receives three input arguments, which correspond to the following variables: the particle accelerator's lattice of beam optics, the particle beam's initial coordinates, and the number of turns for which the beam should be tracked. Instances of `ringpass` often involve millions of reiterative calls to the AT library functions and passmethods. Although intensive and seemingly inefficient, these are calculations that must be executed due to the chaotic, non-

linear behavior of high-order magnets. This behavior results in beam motion that cannot be analytically described, thus calling for heavily taxing numerical calculations to obtain an accurate visualization of the beam's behavior.

## PARALLELIZATION STRATEGY

Parallel computation has become an increasingly universal method for performing large-scale computations in an efficient manner. The parallel model allows jobs to be broken down into discrete sets of instructions, which can be executed simultaneously on multiple processors, allowing for dramatic increases in performance quality. Our methods focused primarily on the various approaches for making AT compatible with parallel processing.

As parallel computing has grown increasingly popular, a number of methods have emerged as the standardized systems for the varying forms of parallel computation (Figures 1, 2). Our first goal was to introduce OpenMP directives and routines to the existing AT source code, allowing the toolbox to be used on systems following a Uniform Memory Access (UMA) model. This is a straightforward procedure which requires only minor alterations to the code as the passmethods are written in C, for which OpenMP has a direct implementation that is compatible with MATLAB's MEX compiling function [3].

The shared memory model can be further improved upon by expanding and adhering the structure to a general distributed memory model. However, the transition toward a distributed memory model is less straightforward. While MathWorks has developed packages for cluster parallelization, standard versions of MATLAB do not currently support methods for message-passing between CPUs. We solve this issue by invoking MatlabMPI and pMatlab [4], which can be used by MATLAB as implementations of the Message Passing Interface (MPI), a library that has emerged as the universal standard for message-passing programs. pMatlab operates by adhering to a Single Instruction, Multiple Data (SIMD) computing

structure by using distributed array datatypes, which partition data amongst CPUs to be processed separately in accordance with a single, defined set of instructions.

Once we set up the distributed computing environment for MATLAB, we were able to combine our implementations of OpenMP and MPI by using the message-passing functions to distribute data to a cluster of multi-core machines. This allows us to utilize the shared memory computing interface for managing local task distribution for each of the individual CPUs, while functioning in a global distributed memory interface. To perform all of these tasks, we set up the MATLAB environment and AT toolbox on all of the machines in the cluster and utilize the MPI routines on the host machine to distribute partitions of the particle beam vector representation amongst each of the worker machines. At the end of the computing procedures, information from each CPU will be consolidated and processed, allowing us to receive outputs from beam tracking functions in a fraction of the original serial-code's runtime.

## INSTALLING AND RUNNING

### *Configuring pMatlab and MatlabMPI*

Our parallelized implementation of `ringpass` uses the packages MatlabMPI and pMatlab from MIT Lincoln Laboratory. It can be installed using the following instructions:

- The user must extract the pMatlab library to a directory which is visible to all CPUs in the communicator
- Each MATLAB startup.m file on individual nodes should be modified to run the scripts contained in the pMatlab/startup.m file
- PC users should also append `addpath .\MatMPI` to the startup file.

This should allow MATLAB to run pMatlab scripts from the home process. To address further difficulties, it would be helpful to consult the pMatlab/MatlabMPI documentation, located at http://www.ll.mit.edu/mission/isr/pmatlab/pmatlab.html

MatlabMPI sets up the necessary I/O communication processes to run MATLAB scripts on multiple computers, while pMatlab implements higher level functions to automate tasks such as data distribution and memory management. It is imperative that it is set up properly on the system before proceeding. They can be tested using the examples located in the pMatlab/examples and pMatlab/MatlabMPI/examples directory.

### *Testing parringpass*

We provide the functions `prpTest`, `prpTestLaunch`, and `samplePlot` to simulate a test run of AT's parallel capabilities. To run these files, the user should navigate the MATLAB working directory to the /examples folder and run the `prpTestLaunch` script. If the script completes, the `samplePlot` script can be run as well to obtain a picture of the phase space plots of each tracked particle (Figure 3).

### *Running parringpass*

The MATLAB script, `parringpass`, is designed to function as a parallelized version of AT's `ringpass` function. It should not be directly called from the command line, but rather from within the `parringpass`launch function, which specifies the settings corresponding to the communication directories and the number of threads/processors. For help setting up communications, consult both the pMatlab documentation and the MatlabMPI documentation, located within the pMatlab/MatlabMPI path.

Before the launch script is run, `parringpass` itself has a number of parameters that should be specified from within the function. This is due to the process by which pMatlab carries out its calculations. Parameter arguments cannot be directly passed into the func-

tions; they must be directly instantiated from within the script. The `parringpass` code provides example formats for declaring these variables, which should be changed according to the desired calculations:

```
% ARGUMENTS
SPEAR3; % Script which instantiates the corresponding version of the SPEAR3
  lattice.
numberParticles = 1024; % Specifies the number of particles to track
Rin = zeros(6,numberParticles); % Instantiates an array of zeros representing
  the initial coordinates
NT = 1024; % Integer specifying number of passes through ring
```

pMatlab uses distributed array computing to run its parallel processes. For this reason, arrays must be instantiated using the `zeros()`, `ones()`, or `rand()` functions, which are overloaded by the pMatlab libraries to be compatible with distributed matrix computing.

## RESULTS AND DISCUSSION

Though `parringpass` has yet to be tested on a multi-CPU cluster due to configuration issues, we were able to demonstrate enormous performance upgrades by taking advantage of parallel capabilities on a multi-core system and running it in a simulated multi-CPU environment with access to four discrete nodes. The resultant computation runtimes are demonstrated (Figure 4), as well as the processor performance graphs recorded using the Windows Task Manager (Figure 5).

From the test runs utilizing a quad-core processor in a simulated distributed memory environment, we observe a speed factor increase of 3.7, correspond to an approximate efficiency of 95% per processor, strikingly close to an ideal, linear speed increase for parallel computing applications. Studies in parallel computing and computational accelerator physics have demonstrated similarly high efficiencies on high-performance supercomputing clusters, predicting processor efficiencies for `parringpass` of over 80% [2], even with communications set up between hundreds of discrete nodes.

# CONCLUSIONS AND FUTURE WORK

By exploiting the efficacy of modern-day parallel computing, we were able to demonstrate incredibly efficient speed increments per processor in AT's beam-tracking functions. Extrapolating from prediction, we can expect to reduce week-long computation runtimes to less than 15 minutes. This is a huge performance improvement and has enormous implications for the future computing power of the accelerator physics group at SSRL. However, one of the downfalls of `parringpass` is its current lack of transparency; the pMatlab and MatlabMPI packages must first be well-understood by the user before the system can be configured to run the scripts. In addition, the instantiation of argument parameters requires internal modification of the source code. Thus, `parringpass`, cannot be directly run from the MATLAB command line, which detracts from its flexibility and user-friendliness. Future work in AT's parallelization will focus on development of external functions and scripts that can be called from within MATLAB and configured on multiple nodes, while expending minimal communication overhead with the integrated MATLAB library.

# ACKNOWLEDGMENTS

I would first like to acknowledge the U.S. Department of Energy and the Accelerator Physics Group at the Stanford Synchrotron Radiation Lightsource (SSRL), located at the SLAC National Accelerator Laboratory for their roles in funding and hosting the program. I would especially like to thank Xiaobiao Huang for his endless support since the project's inception, and all of his efforts in making this the best summer experience of my life. Special thanks to Eric Shuphert, Shannon Ferguson, and Steve Rock for organizing the SULI program, as well as all of the SULI interns, for making the internship such a rewarding nine weeks.

# REFERENCES


1. Terebilo, A. "Accelerator Toolbox for MATLAB." SLAC-PUB-8732 (2001).

2. Pelegant: A Parallel Accelerator Simulation Code for Electron Generation and Tracking Y. Wang and M. Borland, AIP Conf. Proc. 877, 241 (2006), DOI:10.1063/1.2409141

3. Barney, Blaise. "Introduction to Parallel Computing". Lawrence Livermore National Laboratory. 6/13/10 ¡https://computing.llnl.gov/tutorials/parallel_comp/¿.

4. Kepner, Jeremy. "MIT Lincoln Laboratory: MatlabMPI". Massachusetts Institute of Technology. 07/16/10 ¡http://www.ll.mit.edu/mission/isr/matlabmpi/matlabmpi.html¿.

5. Wille, Klaus. The Physics of Particle Accelerators. New York: Oxford University Press, 2000.

# FIGURES

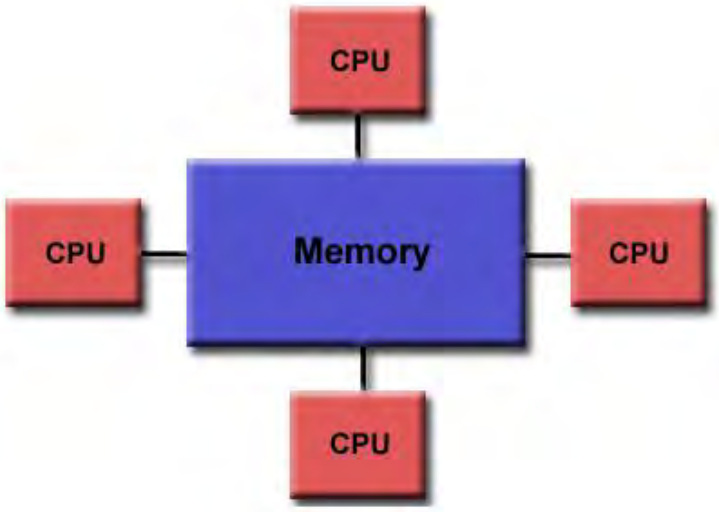


Figure 1: Shared Memory (UMA) Schematic: The image above demonstrates setup of a shared memory multiprocessing unit. All four processors run independently of one another, but have access to a universally distributed memory source. This setup will allow AT to run significantly faster even on low-cost workstations.

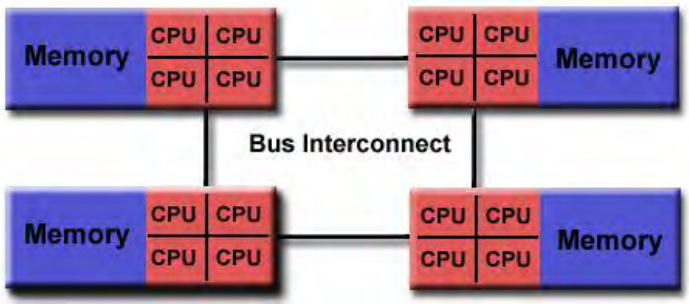


Figure 2: Distributed Memory (NUMA) Schematic: The image above demonstrates setup of a distributed memory multiprocessing unit. In this system, multiple machines run independently of one another with access only to a local memory source, but also implement connections for communications and passing of messages. By utilizing this setup, we can increase AT's processing power to over 100 times its current performance capabilities. Note that UMA systems may be embedded within a larger NUMA system.

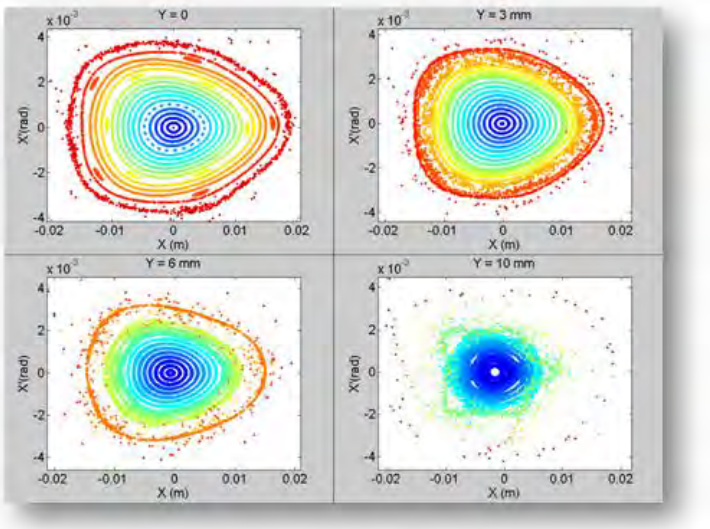


Figure 3: Phase Space Plots: The above plots show Poincare maps of particle trajectories as they are evolved through the SPEAR3 ring lattice. Each color corresponds to a discrete particle with a different set of initial conditions.

| Number of Processors | Single | Dual | Quad |
|---|---|---|---|
| Computation Time (s) | *78.2974* | *41.1318* | *21.1746* |
| Communication Time (s) | *0.0012* | *1.4272* | *1.5732* |
| Total Runtime (s) | *78.2986* | *42.5590* | *22.7478* |

Figure 4: Processor Runtimes: The above table demonstrates the decrease in processor times in a simulated Distributed Memory environment as the code is run on additional threads.


Figure 5: Processor Activity Recordings: These figures show the recorded processor activity on a quad-core processor in a simulated distributed-memory computing environment for one, two, and four processors, respectively. As the number of threads increases, we can note clear increases in processing activity and decreases in computing time.

# Creating an EPICS Based Test Stand Development System for a BPM Digitizer of the Linac Coherent Light Source

Farah Memon
Office of Science, Science Undergraduate Laboratory Internship Program

San Jose State University

SLAC National Accelerator Laboratory
Menlo Park, California

August 13, 2010

Prepared in partial fulfillment of the requirement of the Office of Science, Department of Energy"s Science Undergraduate Laboratory Internship under the direction of Shantha Condamoor in the Controls Department division at SLAC National Accelerator Center.

Participant: _____
Signature

Research Advisor: _____
Signature

Work supported in part by US Department of Energy contract DE-AC02-76SF00515.

## TABLE OF CONTENTS

## ABSTRACT

Creating an Improved Test Stand Development System for a BPM Digitizer of the Linac Coherent Light Source. Farah Memon (San Jose State University, San Jose CA 95192) SHANTHA COONDAMOOR (Controls Department, Stanford Linear Accelerator center, Menlo Park, CA 94025)

The Linac Coherent Light Source (LCLS) is required to deliver a high quality electron beam for producing coherent X-rays. As a result, high resolution beam position monitoring is required. The Beam Position Monitor (BPM) digitizer acquires analog signals from the beam line and digitizes them to obtain beam position data. Although Matlab is currently being used to test the BPM digitizer‟s functions and capability, the Controls Department at SLAC prefers to use Experimental Physics and Industrial Control Systems (EPICS). This paper discusses the transition of providing similar as well as enhanced functionalities, than those offered by Matlab, to test the digitizer. Altogether, the improved test stand development system can perform mathematical and statistical calculations with the waveform signals acquired from the digitizer and compute the fast Fourier transform (FFT) of the signals. Finally, logging of meaningful data into files has been added.

## INTRODUCTION

The Linac Coherent Light Source (LCLS) is a novel invention of SLAC National Accelerator Laboratory which aims to create movies of molecular activities by capturing images using powerful and high frequency x-ray pulses. Since the x-rays have a wavelength which is smaller than the dimensions of chemical molecules, 1.5 Angstroms to be exact, they are able to successfully provide insight regarding the structure of molecules and the properties of chemical reactions [1]. Not only are the x-ray pulses short in wavelength, giving them substantial energy, but they are also flashed once every 100 femtoseconds with energy ranging from 540eV to 9.0keV [2]. These features of the x-ray pulses make them an ideal source for offering accurate depictions about the movement, structure, and the arrangement of particles at the atomic level. Due to these advantageous properties, the LCLS can be used to provide monumental advances in the fields of medicine, chemistry, and materials science.

One device used to monitor the LCLS instrument is the Beam Position Monitor (BPM) digitizer. The Controls Department utilizes the BPM digitizer to scrutinize the trajectory of the electron beam in the LCLS due to the digitizer‟s capability of providing a method to derive the location and the length of the electron bunches in the undulators. Four unique analog signals are captured, one from each side of the beam as shown in Figure 1, and converted to low intermediate frequency (IF) signals [3]. These radio frequency signals are transformed into digital signals using analog-to-digital converters (ADCs). Data is acquired by the ADCs at each rising edge of the clock signal, which may be either external with a frequency of 119MHz or internal with a frequency of 125MHz. Once digitized, each analog signals is loaded into one of the four 16K by 18 bit buffers, depending on its input channel. The analog signals are comprised of multiple samples where each sample is 18 bits long, with the first 16 bits enclosing the raw

data. The input clock signals of the buffers (Clk1, Clk2, Clk3, and Clk4), generated by the four individual ADCs, trigger the release of the samples into the buffers. Apart from the raw sample data and the four clock signals, the buffers also need the acquisition gate signal, which defines the number of samples obtained in each cycle. The acquisition gate signal is generated by any of the two methods: internal triggering or external triggering. In the former case, the internal trigger generates the acquisition gate signal, while in the latter case, one of the two external triggers (Trig1 or Trig2) is responsible. This process is clearly demonstrated in Figure 2. Since the buffers have 16K locations, a maximum of 16384 samples can be passed to each buffer in one cycle [4]. In the case of this research project, for the purpose of limiting the scope of testing, 4096 samples can be passed altogether, corresponding to 1024 samples per channel. Once transferred to the buffers, the analog signals are digitized and in a format that allows mathematical calculations and digital processing to be computed.

The main components used to control the devices located on the periphery of the LCLS, such as the BPM Digitizer, are the Input and Output Controllers (IOCs) and operator interfaces (OPIs), which are both are connected via a local area network (LAN). While the IOCs are servers that are used to communicate to the device, perform mathematical calculations on its data, and monitor its internal registers, the OPIs are client computers utilized to view the device‟s information gathered from the IOC in a user-friendly way. As depicted in Figure 3, most of the IOC is devoted to running the Experimental Physics and Industrial Control System (EPICS) Core and the Application Database. The EPICS Core is responsible for transferring data between the IOC and the OPI while the Application Database is essential for keeping an accurate track of the captured data in an organized database fashion [5]. In the case of the BPM digitizer, the IOC is a VME 64x crate with a Motorola microprocessor VME6100 that uses the Real-Time Executive

for Multiprocessor Systems (RTEMS) operating system (OS) while the OPI is a Dell computer with Linux as its OS.

The Application Database is a collection of records, or macros, necessary to obtain data from the device or perform operations on data which has already been collected. Records contain a list of subroutines that are activated each time the record is required to process and obtain useful information. There exist multiple fields in the records, called Process Variables (PVs). While some fields are inputs and defined by the user, other fields are outputs of the record [5]. On the other hand, the EPICS Core consists of Channel Access which is fundamentally a path of communication between the IOC, also known as the server, and the OPI, also called the client. Through its path of communication, Channel Access successfully provides access to the contents of PVs, located in the IOC, to the OPI, thus permitting the user to observe the contents of the record fields [6].

Currently, Matlab is being utilized to test the BPM digitizer. The Matlab scripts provide results to the computer through Matlab Guide. However, it is preferable to use EPICS, as an integrated test tool as well, due to its reliability, community support, and tractability. Many national laboratories are in the process of using EPICS, which is a set of software libraries and applications, for controlling large scientific instruments. This paper thoroughly explains the process of providing the required functionalities for testing the digitizer using EPICS.

## MATERIALS AND METHOD

*Equipments and Project Problem*

In order to provide an effective test stand development system that accurately tests the BPM digitizer before it goes into the production stage, several equipments were utilized. These include the following:

1. Cisco Systems Catalyst 3750 Series Switch
2. Digi Port Server TS 16 serial port
3. Power-One Hybricon VME 64x crate
4. HP Signal Generator (Model 8648C)
5. Stanford Research Systems Digital Delay Generator (Model DG645).
6. The VME 64100 microcontroller in the VME 64x crate‟s Slot 1.
7. BPM Digitizer (Model 114-045-1) in the VME 64x crate‟s Slot 4.

The primary goal of the digitizer, as seen earlier, is to provide a digital representation of the four different analog signals acquired from the electron‟s trajectory in the LCLS. The driver for the BPM digitizer was derived from the driver that is part of the production BPM Application Code.

The Matlab scripts, which currently test the digitizer, compute the DC offset, minimum, maximum, peak-to-peak, and the fast Fourier transform (FFT) of the four individual signals. As Figure 4 illustrates, the results of all the mathematical operations are clearly displayed on Matlab Guide graphical user interface (GUI). Although the Matlab scripts offer a suitable test stand configuration system, similar and even advanced functionalities need to be provided through EPICS to accurately examine the digitizer. Currently the EPICS driver code only permits the

user to precisely view the four waveform signals as one whole signal on the EDM panel, which is the GUI for EPICS.

*Configuration and Setup of the Devices*

The first step to develop the test stand development system using EPICS is to configure the IOC properly with the OPI. To accomplish this task, the VME 64x crate containing the microprocessor and the digitizer was connected to the Linux computer over a local area network (LAN) using a Cisco Systems Catalyst 3750 Series Switch. A Digi Port Server TS 16 serial port is also used for local or remote debugging of the IOC, as displayed in Figure 5. The HP Signal Generator, shown in Figure 6, provides the input waveform signals, 40MHz at 0dB on first two channels, which are close to the actual analog signals which the digitizer may acquire. To obtain and process the data, the digitizer needs to be clocked and triggered, both of which can be either external or internal. For testing purposes, the internal clock with a frequency of 125MHz is employed. A Digital Delay Generator, illustrated in Figure 7 is used to externally trigger the signal at a rate of 10Hz although the input waveform signals can also be triggered internally through software.

After configuring the hardware devices, the IOC application for the BPM digitizer was built using EPICS environment, tools, and packages. Once the IOC application is built using the make command in Linux, the following directories are created in the IOC Application folder: bin, db, dbd, and, lib. The application is built against RTEMS 4.9.1 RTOS and the output object file is placed in the bin directory as the result of the „make" command. The dbd directory consists of the definitions of all the records the user can generate while the db directory contains the list of all the records which have been created in the specific IOC application. Additionally, the

configure directory sets up the environment variables needed to process the IOC. Finally, there is a startup script for setting up the IOC appropriately after booting.

The next step consisted of running the latest driver code. A subset of R5-3-0 of BPM Application Code was used for this project. The simulation related portions of the driver code were disabled as this had dependencies on other code which were not needed for this project. All the test application software was built on top of this driver code to test the basic functionalities on the IOC. The rudimentary functionalities of the driver code allow the four waveform signals to be properly obtained from the digitizer and be accurately displayed on the EDM panel as one cumulative signal. Additionally, the driver code provides some low-level functions for exposing specific parameters of the digitizer, such as serial, firmware, and crate number, which the test application software presented in the EPICS GUI. The iocConsole is another tool used to control the IOC by providing a unique pathway of communication between the IOC and the Linux computer. Due to its ability to directly communicate, via serial communication, with the IOC, it is used to issue commands and debug. One of the useful commands that is issued from the iocConsole software, includes bsp_reset(), which allows the IOC to reset during during development.

*Implementing the Advanced Functionalities*

The test application extended the driver to support new features. These advanced operations consist of illustration of all four input signals as independent waveforms, mathematical calculations, fast Fourier transforms, and logging of data.

Illustration of the Input Signals

In order to separate the combined input signal into four different waveforms, the genSub record was used. The genSub record, when processed, invokes a subroutine in the source code,

which is essentially a C function. This specific record can access up to 21 PVs as inputs, whether they are in scalar or array format, and perform complex calculations using the input parameters. The genSub record is passed as a pointer of a structure (*psub) to the subroutine and the different fields of the genSub record, such as the input and the output fields, are all elements of the structure and accessed using the pointer [7]. For the separation of the waveform signal, a genSub record called *showWaveform* was created. This record accepted the combined signal as well as the four distinct signals to the four input channels. When invoked, it divided the combined signal, holding 4096 elements, into four waveforms, each comprising 1024 samples. After executing the division, the subroutine uses a database access routine, *dbPutField*, to change the contents of the four input fields that correspond to the waveforms of the four channels. These four waveform signals are displayed in the original EDM panel.

Waveform Analysis

To perform the calculations on the four waveform signals, the wavePro*c* module, which is a set of functions that interfaces with the existing source code, was used. This specific module is available from EPICS and serves as a tool that interacts with waveform records and performs mathematical and statistical operations on them [8]. After incorporating the waveProc module, four instances of the waveAnl record were created. Each record pertains to the waveform on each channel. The waveAnl record accepts the raw waveform as its input, performs calculations, and outputs the answers of the calculations in different PVs which are presented in an EDM panel. To effectively expose all the data, separate EDM screens for each channel and the combined waveform were created that clearly displays all the meaningful and useful data for that particular channel in a well structured manner. These five new EDM screens, called the Waveform Analysis Record Panels, are linked to the original EDM screen via a button.

## FFT Processing

The FFT is computed on the waveform signals of the four channels using Matlab *labCA*. This test program allows a Matlab client to interface via Channel Access to the IOC and have access to all the published PVs. As a result, Matlab script was written that captured the digitized waveform signals, stored them as variables, performed FFT, computed the power spectrum, and calculated the fundamental frequency. The power spectrum and the fundamental frequencies of the four channels were linked to separate PVs, which were exposed on the FFT EDM panel. This specific panel is linked to the main EDM panel via the „FFT Button".

## Logging of Data

The application added a new feature to store the results of a test along with the data collected from the waveform signals and the digitizer into a log file. The log files are created on demand and stored with file names that have time stamp of the test time. All of the log files are saved in the nfs directory specified by the following path:

/nfs/slac/g/lcls/epics/ioc/data/ioc-b34-cd16/output

Six different types of log files are created: four log files corresponding to the four input waveforms, one log file for the combined waveform, and one generic log file for hardware-specific information, i.e, serial, firmware, and hardware revision number. To create the five log files that record all the mathematical data relating to the waveform signals, a function was implemented in the waveAnl record. This function was called upon the click of a button in each wave Analysis Record EDM Panel. Moreover, to produce the generic log file, a subroutine record named *genericLog* was created. This subroutine captured the hardware specific parameters and when processed upon the click of a button on the main EDM panel, created a log file that adequately and neatly stored all the information relevant to the digitizer.

## GRAPHICAL USER INTERFACE AND PRESENTATION OF RESULTS

After compiling the code and linking all the EDM panels, the test development system prototype was built. As portrayed in Figure 8, the main EDM panel displays the four waveforms, each corresponding to a different channel. The graphs possess the zoom-in capability such that the user may be able to concentrate and carefully observe a particular area of a waveform. The combined signal can be viewed by clicking upon the button, „VMEADC03-All". This button brings up an EDM panel that demonstrates a graph of the combined waveform signal, as illustrated in Figure 9. Besides the four graphs, five buttons are on the main panel that link to the Wave Analysis Record EDM panels. Four of the five buttons correspond to panels of the four individual waveforms („VMEADC03-1", „VMEADC03-2", „VMEADC03-3", „VMEADC03-4") and one of the buttons links to the wave analysis record panel of the combined signal („VMEADC03").

Each of the Waveform Analysis Record panel exhibits important parameters of the waveAnl record. Displayed in Figure 10, these include the maximum (MAX), minimum (MIN), peak-to-peak (PEAK), variance (VAR), standard deviation (STDEV), and mean (MEAN). The maximum is the maximum sample point in the waveform signal, the minimum is the minimum sample point in the signal, and the peak-to-peak is the difference between the maximum and the minimum. The variance and the standard deviation are a measure of the spread of the sample points in the waveform. Lastly, the mean corresponds to the dc offset pertaining to the input signal. Apart from these mathematical values, the panel depicts a more diminutive version of the graph. Most importantly, the panel has a button called „Process". Corresponding to a PV of the waveAnl record, upon clicking this button, the record processes, and the values on the panel are updated. Another significant button includes „Logger"; this button triggers the creation of a log

file that stores the mathematical values of the signal in a method displayed in Figure 11. The name of the log file is in the following format: *chNlog_MM-DD-YY_HH:MM:SS.dat*. The letter N corresponds to the channel number. It spans from 0 to 4 where 0 indicates the combined signal and 1-4 are relevant to the signals of Channels 1 to Channel 4. On the main EDM panel exists a button labeled „Genric Log", used to activate the *genericLog* subroutine. Upon clicking this button, the generic log file is created with the name generic.dat. This file, as displayed in Figure 12, stores hardware-specific parameters of the digitizer.

Lastly, the power spectrum and the fundamental frequencies of the four waveforms are displayed on the FFT EDM panel, as shown in Figure 13. This specific EDM panel is linked to the main EDM panel via the „FFT" button. In order to dynamically view the power spectrum, the Matlab script needs to be running in the background and can be stopped by pressing the „Stop FFT" button on the FFT EDM panel.

## DISCUSSION AND CONCLUSION

Currently, the improved test stand development system is running effectively to monitor the BPM digitizer. It can divide the combined waveform acquired from the device into four separate waveforms, with one corresponding to each channel. Additionally, mathematical and statistical values relevant to the waveforms are computed using the waveAnl record from the waveProc module. The FFT and the logging functionalities have also been incorporated.

To further improve the test stand development system, a few additional functionalities need to be inserted. These include adding buttons on the main EDM panel that open up PDF documents discussing ways to configure the digitizer. This feature will assist the user in setting up the test stand system if he or she is not familiar with the steps. Furthermore, the capability of changing engineering units needs to be provided; the user should be able to change between the

units of samples and volts with a click of a button. Changing units should change the scale of the graphs and the values of the mathematical operations. In conclusion, the test stand system created as a result of this project, can be used as a guide to generate improved EPICS based test stand systems for other digitizers including the Phase and Amplitude (PAD) digitizer.

## ACKNOWLEDGEMENTS

I would like to thank the Department of Energy (DOE) for providing a beneficial and rewarding research experience through the Summer Undergraduate Laboratory Internship (SULI) program. The research was effectively held at the Controls Department of the Stanford Linear Accelerator Center (SLAC). Most importantly, I would like to thank my mentor, Shantha Condamoor, for guiding me through my internship experience and providing constructive feedback for my project. Lastly, I am also appreciative towards Sonya Hoobler, Matt Boyes, David Earl Anderson, and Ernest Williams for their assistance during my internship program.

## REFERENCES


[1] J. Frisch et al. *Beam Position in LCLS* [Online]. Available: http://www.als.lbl.gov/biw08/papers-final/MOIOTIO02.pdf

[2] *LCLS FAQ* [Online]. Available: https://slacportal.slac.stanford.edu/sites/lclscore_public/Lists/LCLS_FAQ/FAQ.aspx

[3] R. Lill et al. *Design and Performance of the LCLS Cavity BPM System*[Online]. Available: http://accelconf.web.cern.ch/accelconf/p07/PAPERS/FRPMN111.PDF

[4] W. Ross, "SLAC BPM Digitizing Module 144-045-1 Programming Module"

[5] (2008, March 10). *EPICS I*[Online]. Available: https://confluence.slac.stanford.edu/download/attachments/67503315/LCLS-EPICS-Intro.pdf?version=1&modificationDate=1257093082000

[6] B. Dalesio. (1999). *Channel Access Concepts* [Online]. Available: http://www.slac.stanford.edu/comp/unix/package/epics/training/documents/02_CA_Concepts.pdf

[7] A. Foster. (2003, March 12). *The EPICS genSub Record Reference Manual* [Online]. Available: http://www.slac.stanford.edu/grp/ssrl/spear/epics/site/genSub/genSubManual.pdf

[8] E. Norum. *WaveProc* [Online]. Available: http://www.aps.anl.gov/epics/modules/soft/waveProc/index.html

[9] E. A. Medvedko et al. *LCLS Stripline BPM System Commissioning* [Online]. Available: http://trshare.triumf.ca/~pac09proc/Proceedings/papers/th6rep036.pdf

**FIGURES**

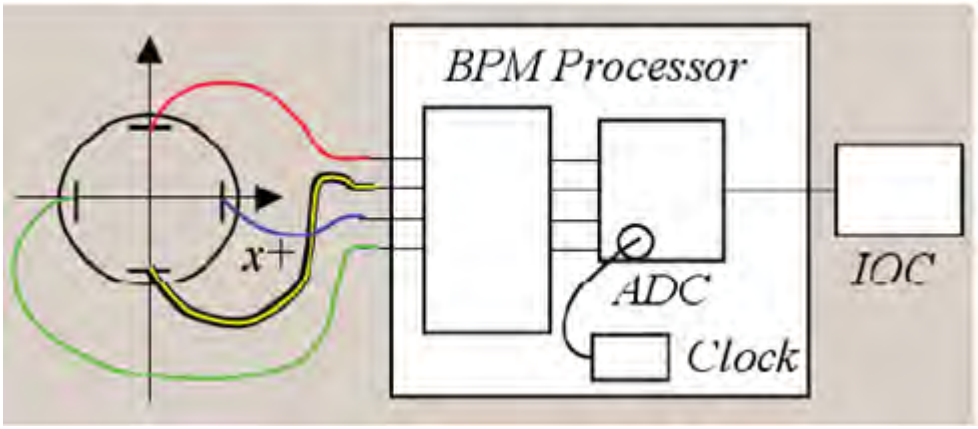


Figure 1: The BPM digitizer acquires four analog signals from the four different edges of the beam line near the undulators [9].

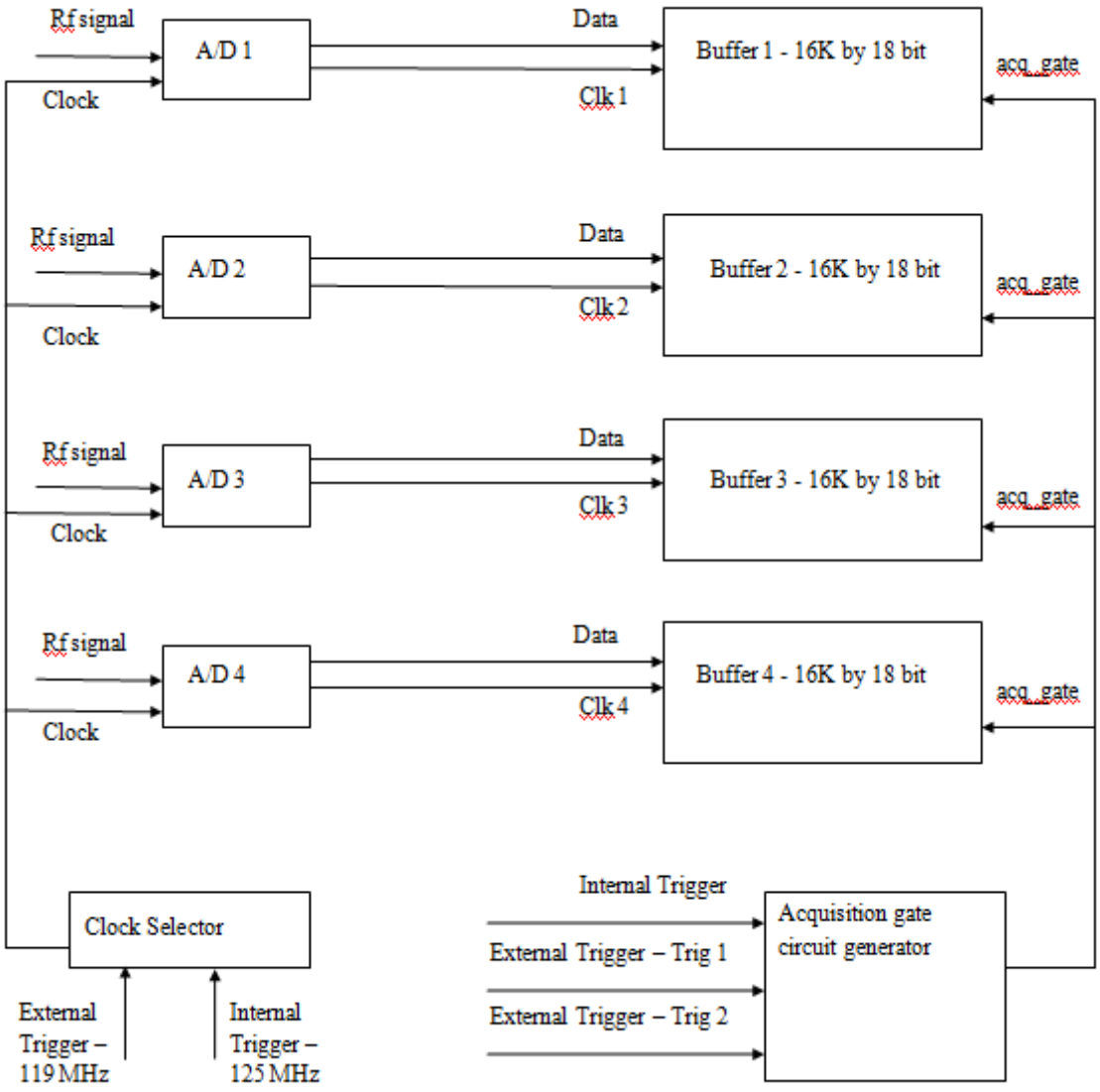


Figure 2: The process of converting the RF signals into digitized samples and storing them into the buffers.

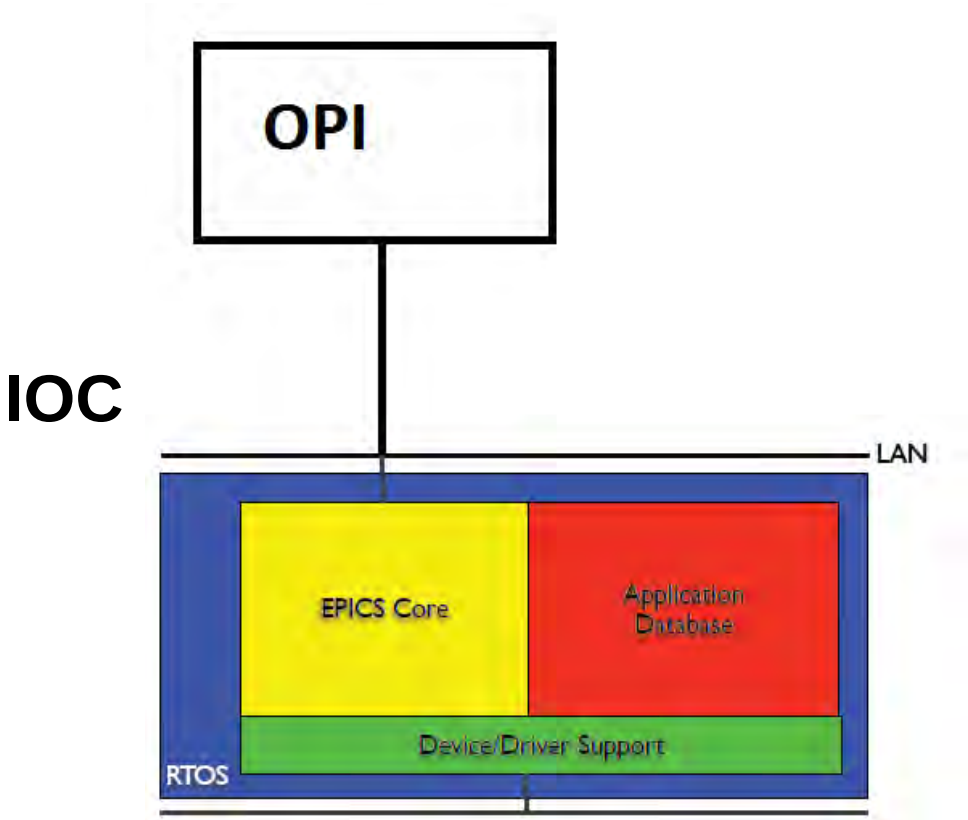


Figure 3: The IOC, consisting of the EPICS Core, the Application Database, and the Device/Driver Support is connected to the OPI through LAN.

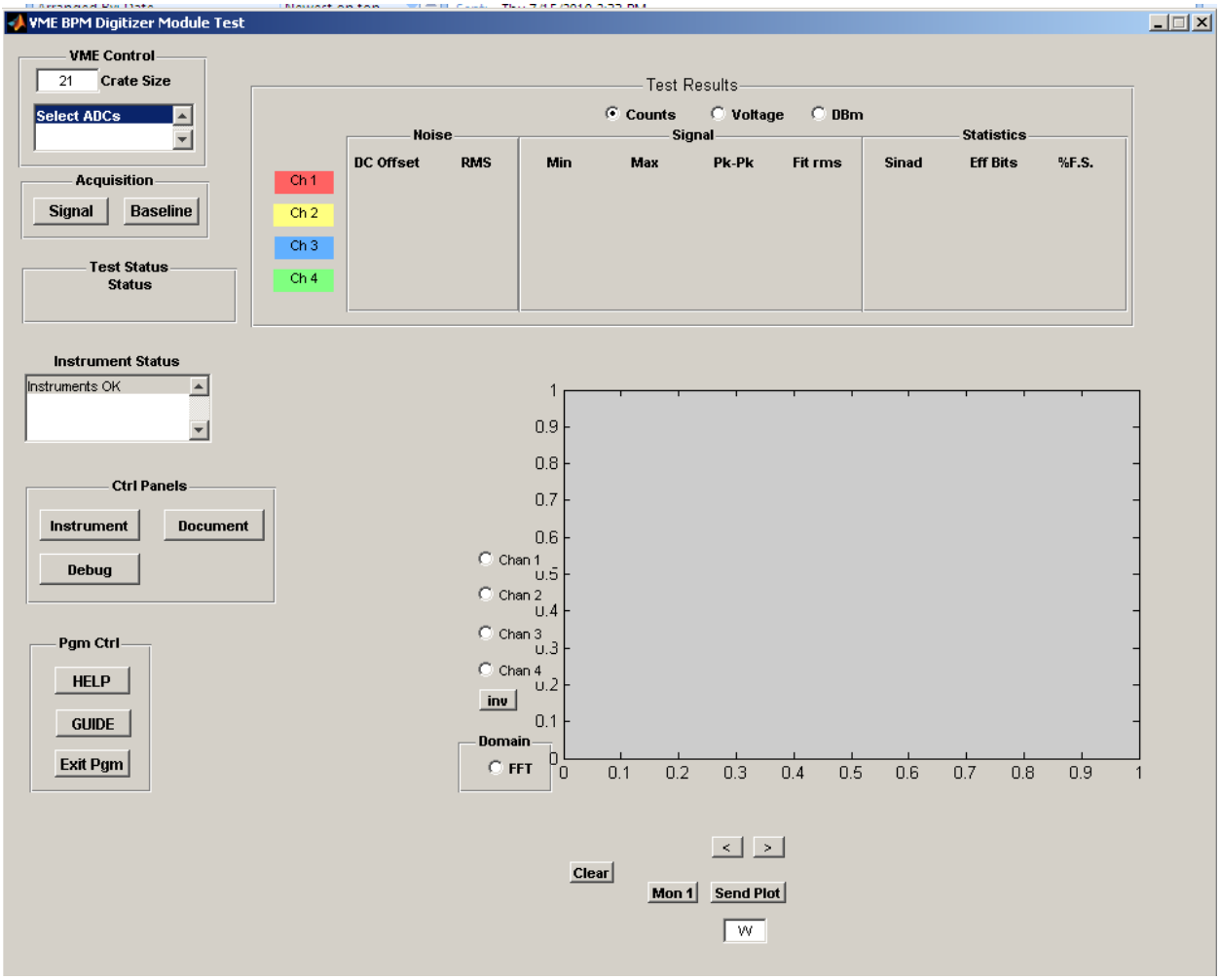


Figure 4: The existing functionalities provided by the Matlab Scripts on Matlab Guide.

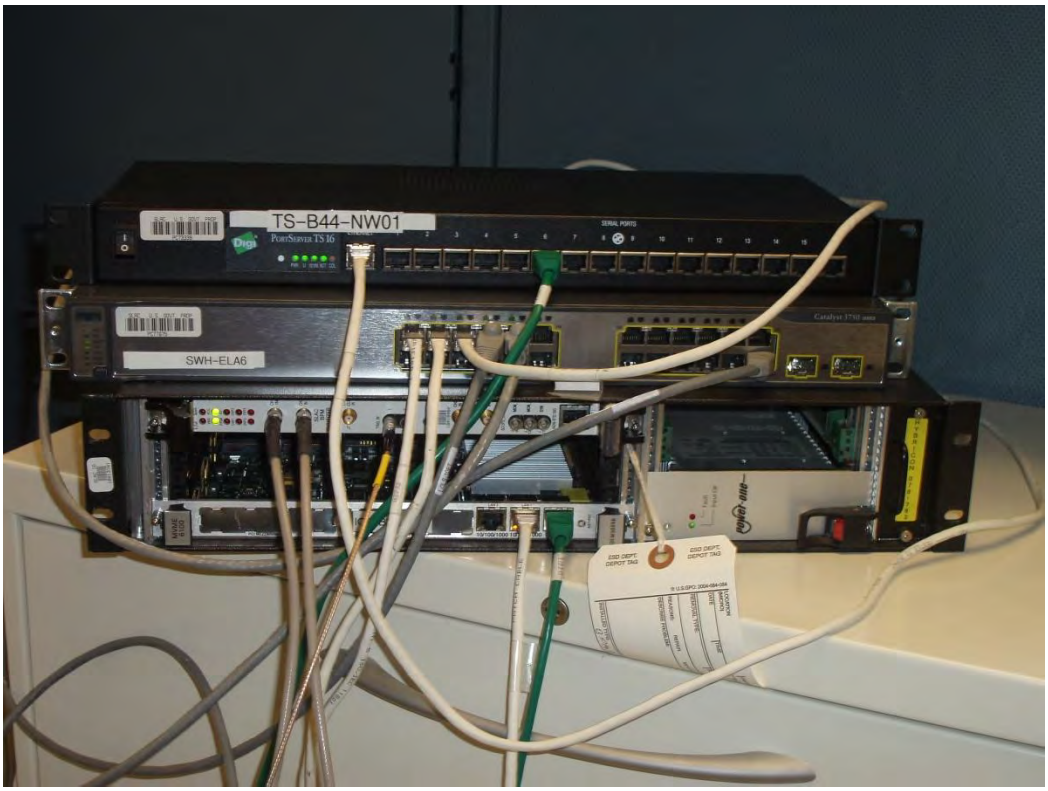


Figure 5: (From Top to Botton) Digi Port Server TS 16 serial port, Cisco Systems Catalyst 3750 Series Swithc, and Power-One Hybricon VME 64x crate.


Figure 6: An HP Signal Generator (Model 8648C)


Figure 7: Stanford Research Systems Digital Delay Generator (Model DG645).

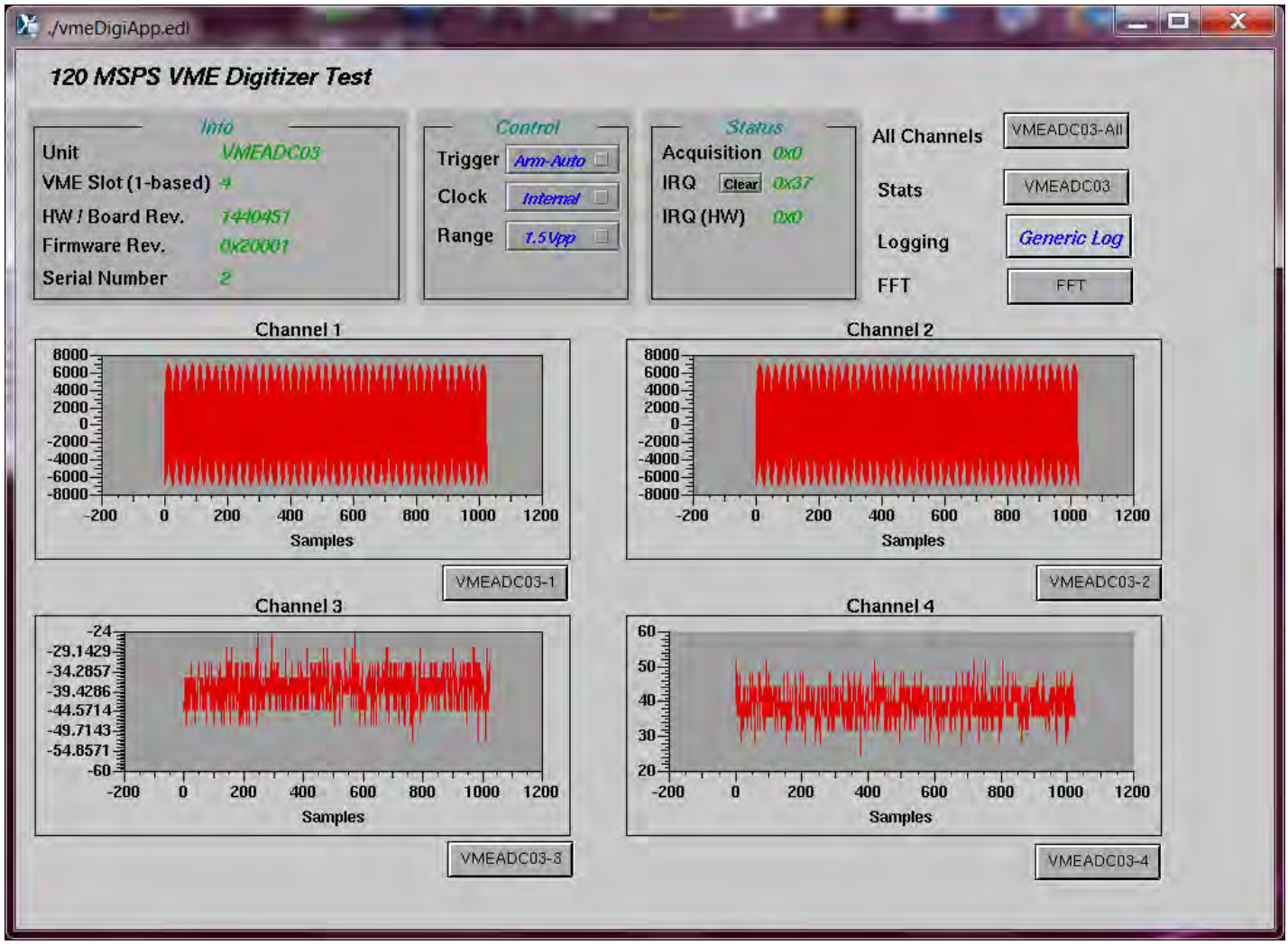


Figure 8: The main EDM panel with the four waveform signals along with the buttons („VMEADC03", „VMEADC03-1", „VMEADC03-2", „VMEADC03-3", „VMEADC03-4") to display each Waveform Analysis Record panel. The combined waveform signal is displayed via „VMEADC03-All" button while the generic log file is created through „Generic Log" button.

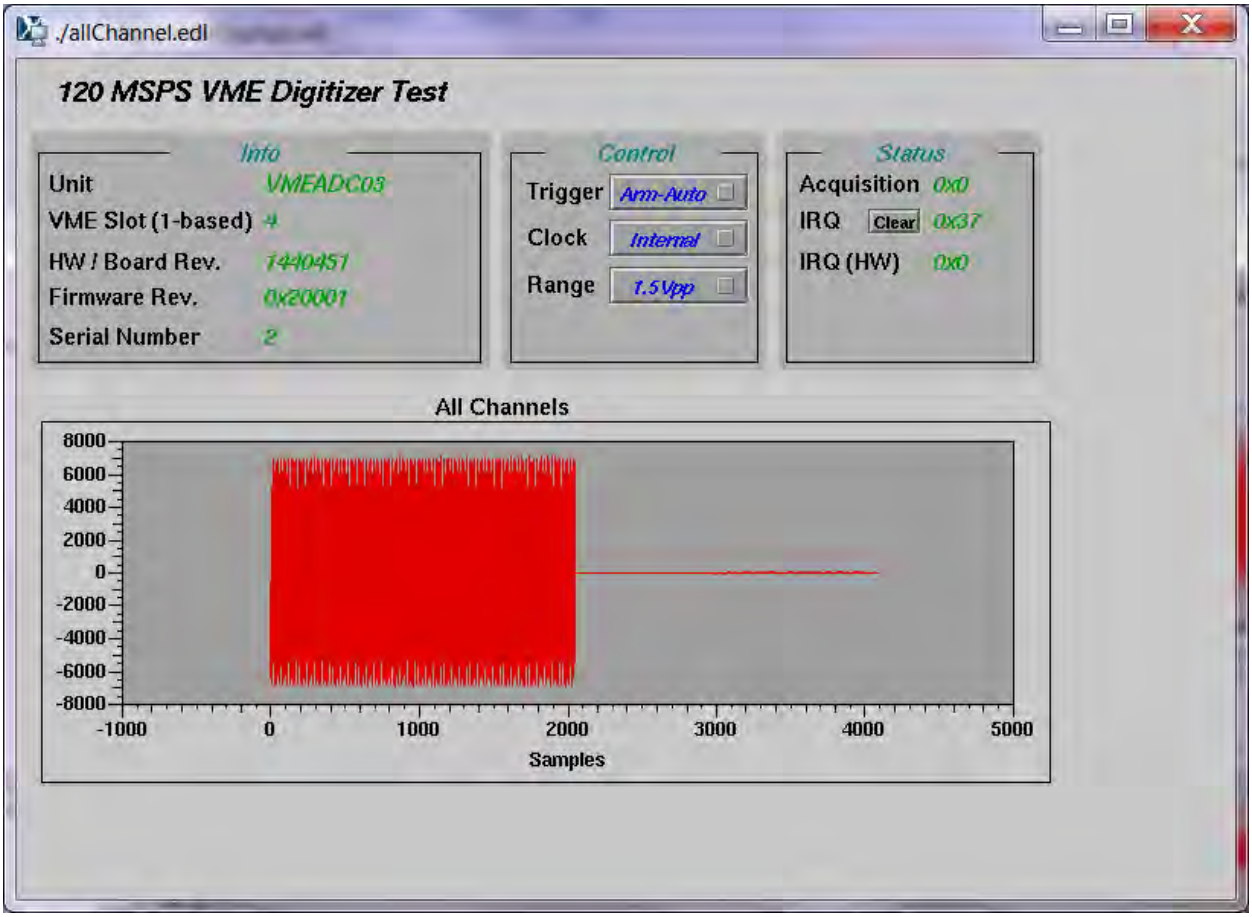


Figure 9: The EDM panel displaying the combined waveform signal. It is brought up upon the click of the „VMEADC03-All" button on the main EDM panel.

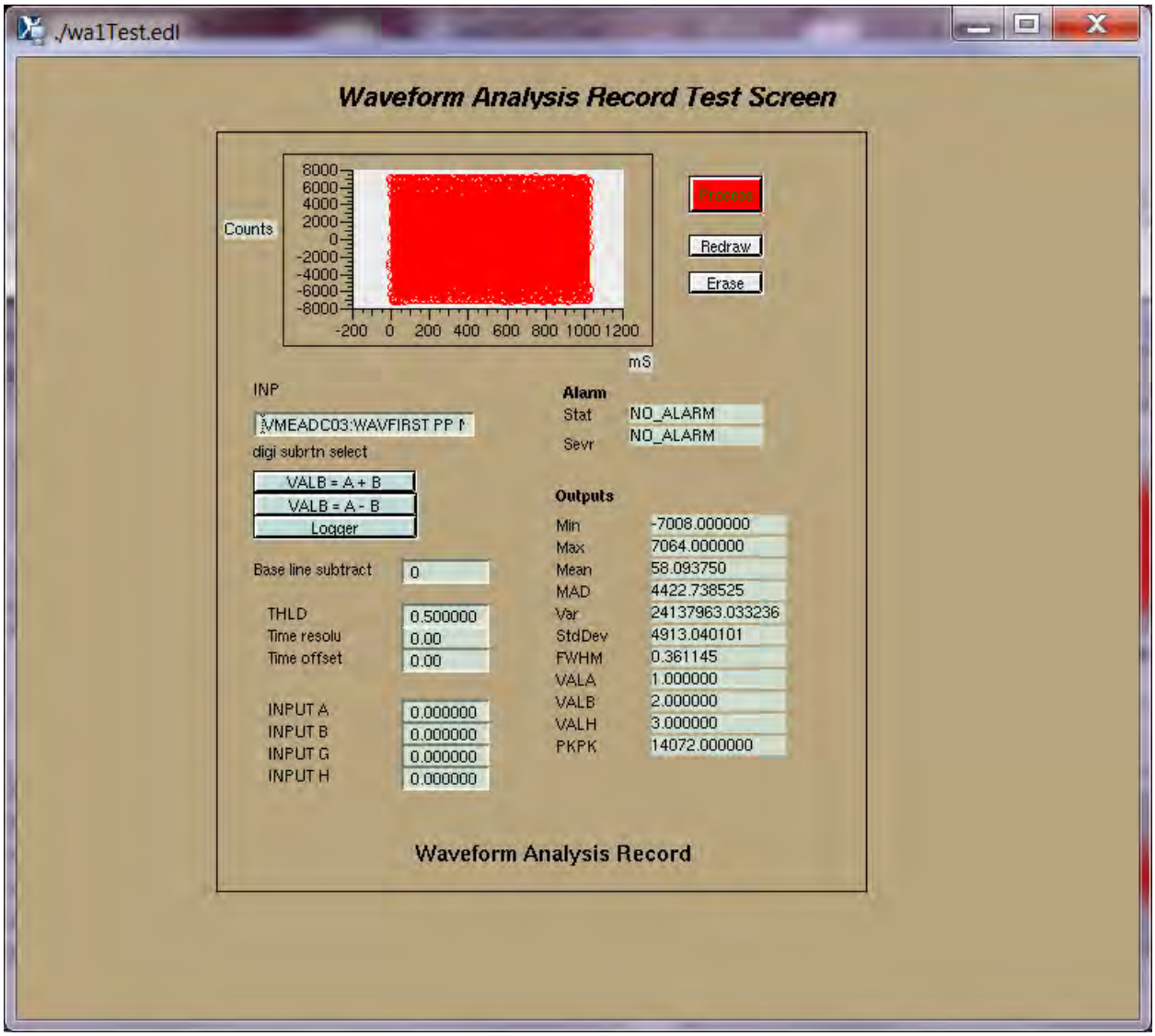


Figure 10: The Waveform Analysis Record EDM panel displays the waveform and the mathematical and statistical data relating to the waveform. All the elements on the EDM panel are process variables of the waveAnl record.

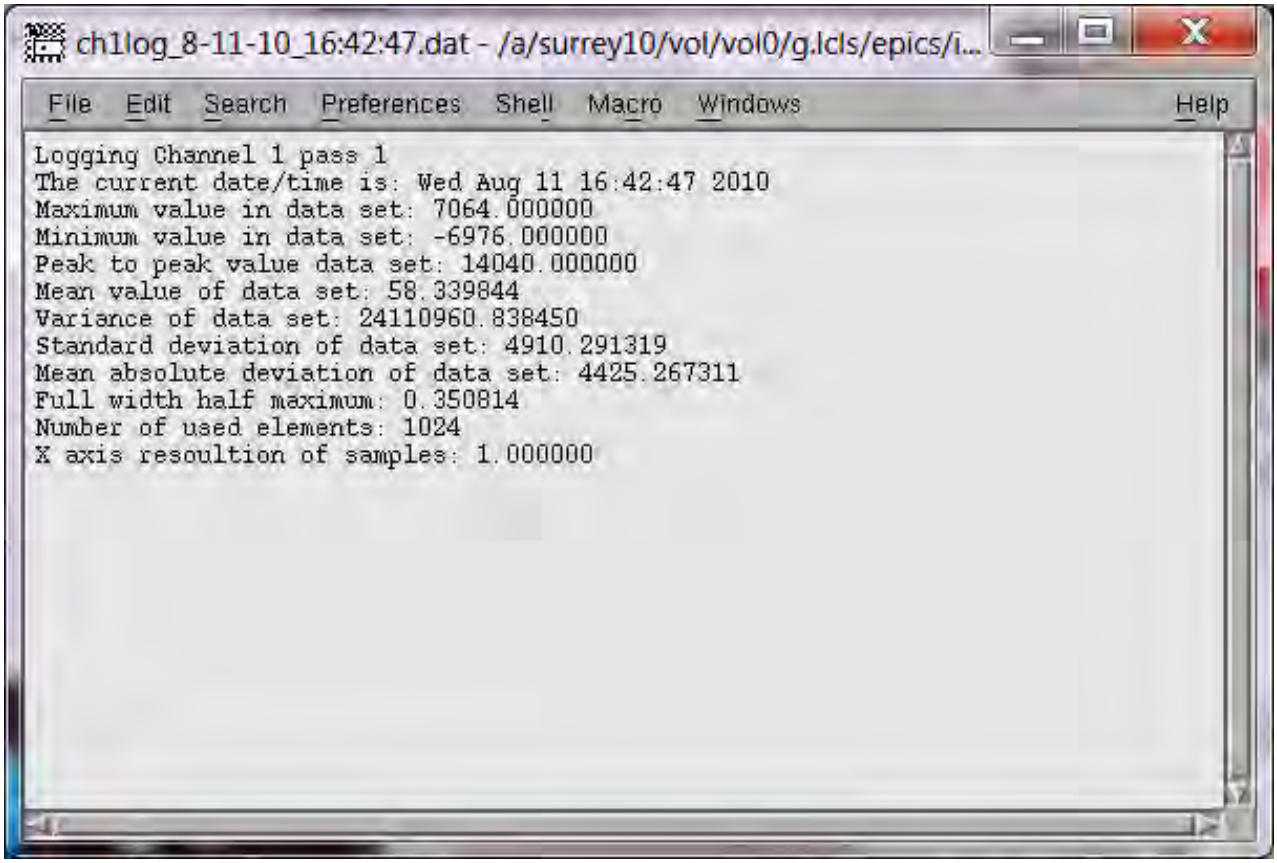


Figure 11: The channel log file consisting of the mathematical data pertaining to the waveform. It is created by pressing the “Logger” and the “Process” buttons on the Waveform Analysis Record panels.

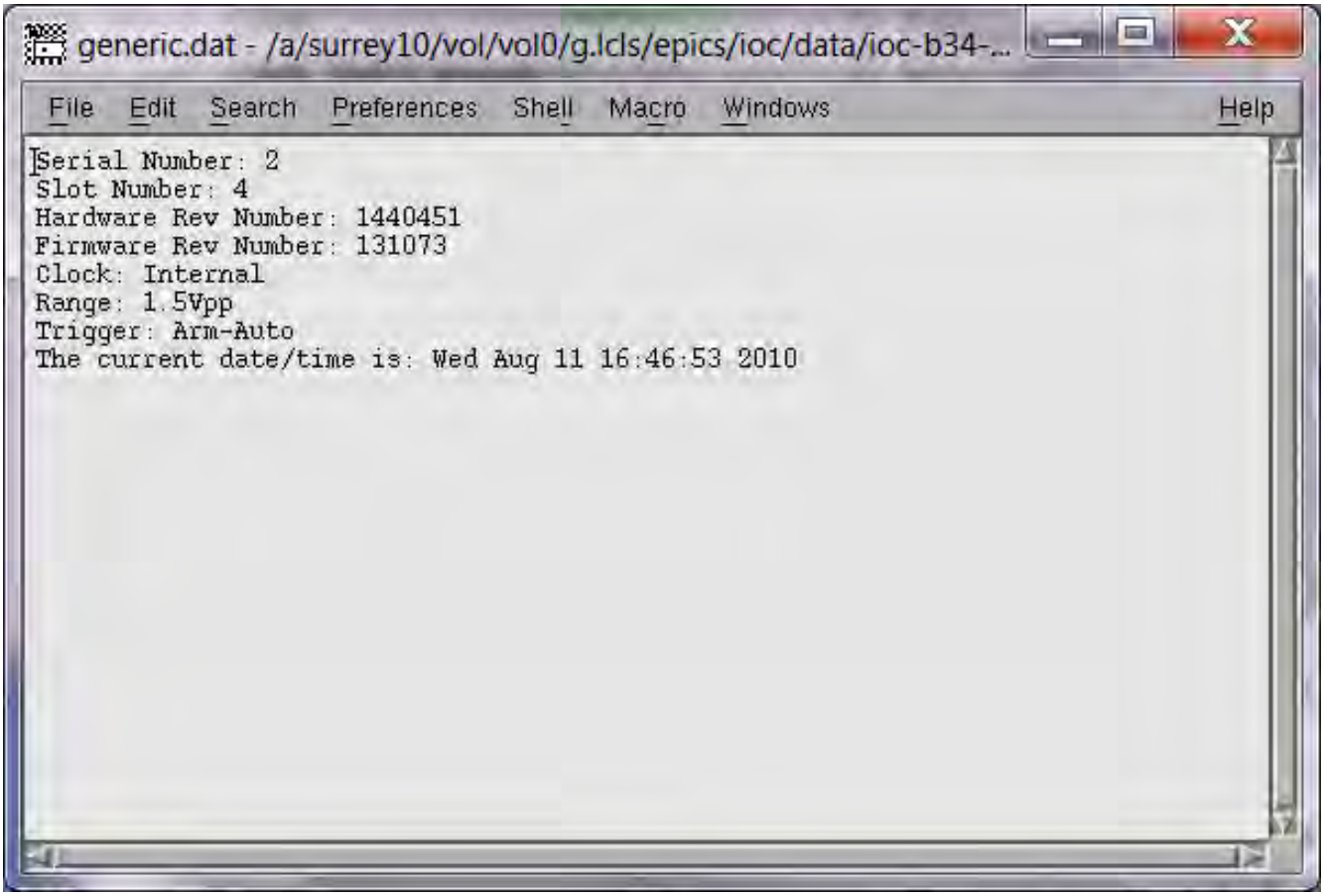


Figure 12: The generic log file carries the parameters that are specific to the digitizer. It is created upon the click of the “Generic Log” button on the main EDM panel.

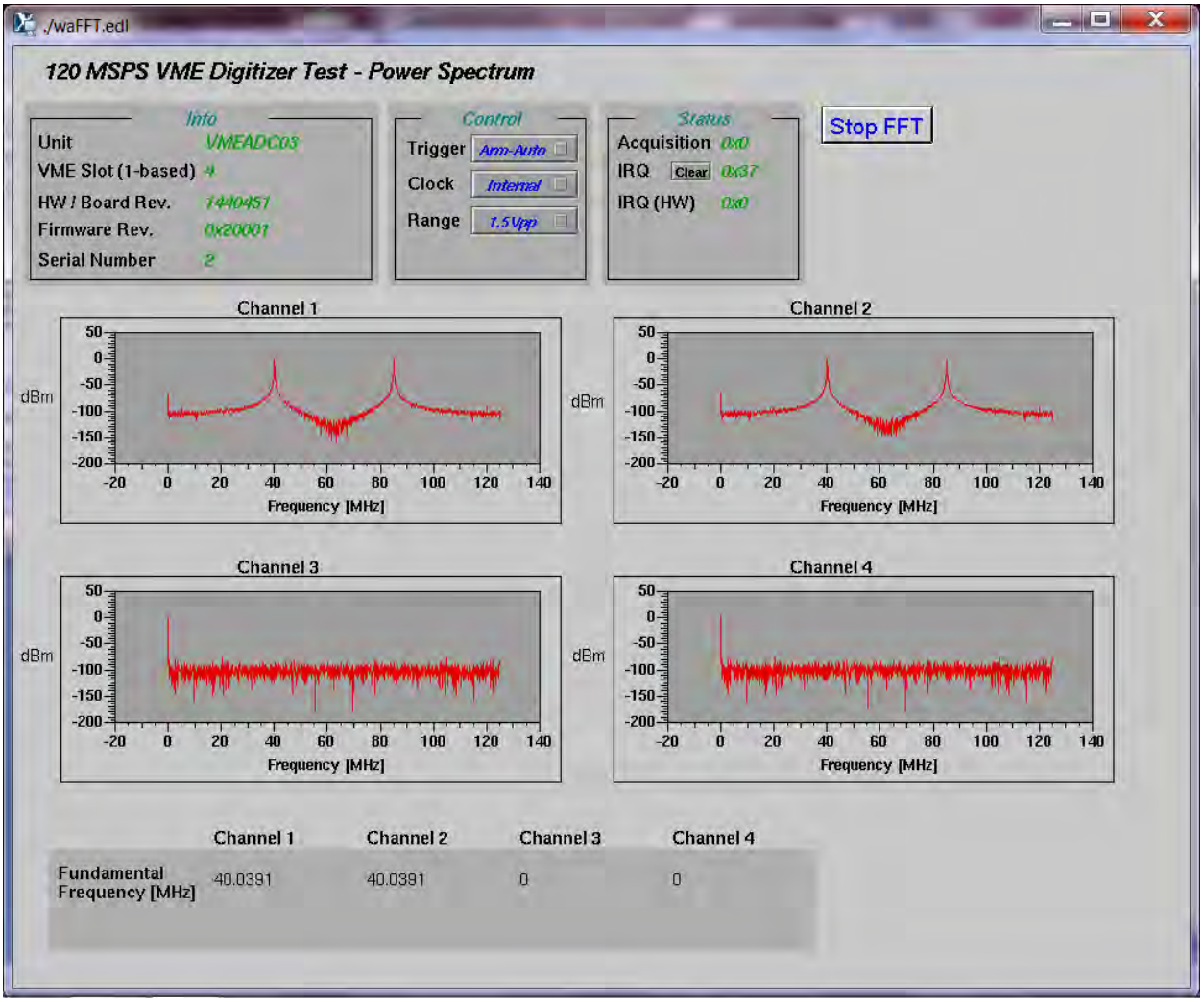


Figure 13: The FFT EDM Panel displays the power spectrum and the fundamental frequencies for the four RF signals. It is invoked upon clicking the „FFT" button on the main EDM panel.

# New Technique for Speciation of Uranium in Sediments Following Acetate-Stimulated Bioremediation

Nikki Peck
Office of Science, Science Undergraduate Laboratory
Internship Program

Harvey Mudd College

Stanford Linear Accelerator Center National Accelerator Laboratory
Menlo Park, CA

August 13, 2010

Prepared in partial fulfillment of the requirement of the Office of Science, Department of Energy's Science Undergraduate Laboratory Internship under the direction of John Bargar in the Molecular and Environmental Interface Science department at the Stanford Linear Accelerator Center.

Participant: _____
Signature

Research Advisor: _____
Signature

Work supported in part by US Department of Energy contract DE-AC02-76SF00515.

## TABLE OF CONTENTS

**ABSTRACT**
New Technique for Speciation of Uranium in Sediments Following Acetate-Stimulated Bioremediation, NIKKI PECK (Harvey Mudd College, Claremont, CA 91711) JOHN BARGAR (SLAC National Accelerator Laboratory, Menlo Park, CA 94025)

Acetate-stimulated bioremediation is a promising new technique for sequestering toxic uranium contamination from groundwater. The speciation of uranium in sediments after such bioremediation attempts remains unknown as a result of low uranium concentration, and is important to analyzing the stability of sequestered uranium. A new technique was developed for investigating the oxidation state and local molecular structure of uranium from field site sediments using X-Ray Absorption Spectroscopy (XAS), and was implemented at the site of a former uranium mill in Rifle, CO. Glass columns filled with bioactive Rifle sediments were deployed in wells in the contaminated Rifle aquifer and amended with a hexavalent uranium (U(VI)) stock solution to increase uranium concentration while maintaining field conditions. This sediment was harvested and XAS was utilized to analyze the oxidation state and local molecular structure of the uranium in sediment samples. Extended X-Ray Absorption Fine Structure (EXAFS) data was collected and compared to known uranium spectra to determine the local molecular structure of the uranium in the sediment. Fitting was used to determine that the field site sediments did not contain uraninite ($UO_2$), indicating that models based on bioreduction using pure bacterial cultures are not accurate for bioremediation in the field. Stability tests on the monomeric tetravalent uranium (U(IV)) produced by bioremediation are needed in order to assess the efficacy of acetate-stimulation bioremediation

## 1. INTRODUCTION

The production of uranium (U) for power generation and defense has led to contamination at many locations across the country [1]. One of the proposed methods for remediating contaminated groundwater hinges on the use of microbes to reduce soluble metallic ions into insoluble forms. Of particular interest is the reduction of hexavalent U (U(VI)) into tetravalent U (U(IV)). U(VI) is very toxic and very soluble, while U(IV) is much less soluble and thus less mobile in ground water [2]. Current models assume that this reduction results in the production of biogenic uraninite, $UO_{2+x}$, $0 \leq X \leq .25$ [3]. Due to its relative stability and insolubility, uraninite is thought to have great potential as a means of sequestering subsurface U contamination [4]. However, the actual speciation; that is, the chemical and physical form, oxidation state and local molecular structure of bioremediated uranium at contaminated sites remain unknown as a result of its complex biogeochemistry. Identifying this speciation is vital to understanding the stability of the reduced uranium and thus analyzing the efficacy of bioremediation attempts. Uranium speciation as a result of acetate-stimulated bioremediation, as well as its variation through time, was investigated through *in situ* U(VI) reduction in field tests at a former uranium mill in Rifle, CO.

Typical bioremediation techniques rely on the reduction of U(VI) into U(IV) by microbes like *Geobacter* species [5]. Electron donor molecules like acetate or ethanol are injected into the ground water source to generate anoxia and thus create optimal reducing conditions [3]. Microbes then mediate the reduction of electron receptors like $NO_3^-$, Fe(III), $SO_4^{2-}$ and, most notably, U(VI). Microbial reduction at the field site can be thought of as proceeding in two main stages: iron and sulfate reduction. Reduction of U(VI) has been found to decrease dramatically upon the transition from iron to sulfate reduction, inspiring a need for investigation of how uranium speciation varies through these stages.

The field site used for this experiment is located in Rifle, CO, at the site of a former uranium mill. As a result of the Uranium Mill Tailings Remedial Act, contaminated soil was removed and disposed of, but up to 0.17 mg/L uranium [6] remains in the alluvial aquifer below the site. Acetate, $CH_3COO^-$, has been injected in the groundwater at the Rifle site to serve as an electron donor for microbial bioremediation as per the following expected reaction:

$$0.125\ CH_3COO^- + 0.775\ UO_2^{++} + 0.3538\ H_2O + 0.0113\ NH_4^+ = 0.0113\ BM{-}\_iron + 0.775\ UO_2(s) + 0.855\ H^+ + 0.1938\ HCO_3^-\ [3]$$

This research focuses on determining what form of uranium is produced by acetate stimulated bioremediation at the Rifle site. Though models predict that bioremediation will produce uraninite as a final product, the products of bioremediation in the field remain unknown as a result of the extremely low concentrations of uranium in treated sediments. Background uranium concentration in sediments is approximately five parts per million, while the Extended X-ray Absorption Fine Structure detection limits is approximately fifty parts per million. However, the use of novel in-well sediment columns allows for investigation of the products of microbial metal reduction in various conditions by permitting the addition of uranium and other influent solutions without fear of harm to the environment.

The in-well reactor column setup used at the Rifle, CO site operates by pulling groundwater through a glass column full of bioactive sediment from the Rifle site, as shown in Figure 2. Uranium is amended into the influent groundwater, eliminating the previous issue regarding uranium concentration in sediments being too low for analysis using spectroscopic methods. In August 2010, we deployed twenty-two in-well columns in two different wells at the Rifle site, wells CD-04 and CD-11. Figure 1 illustrates the flow cell and well setup at the Rifle site. The CD-11 columns were also subject to a bicarbonate injection, to investigate the effect of bicarbonate on uranium speciation as well. Once sediment had been harvested, X-ray Absorption

Spectroscopy (XAS) was used to discern both the local and compound-scale structure of the reduced uranium from the columns, and thus to answer the overarching question of what is produced during acetate stimulated bioremediation. In particular, this experiment is concerned with the products of stimulated sediment bioremediation during iron and sulfate reduction.

## 2. MATERIALS AND METHODS

*i. Experimental Apparatus*

The experimental apparatus consists of a number of glass columns (Kontes chromatography columns) affixed to a PVC pipe and inserted into a well at the Rifle site. Two peristaltic pumps (Ismatec) are also utilized in the column setup. One pump draws effluent groundwater out of the column at 0.2 mL/min, while the other amends uranium stock solution into the groundwater flowing through a column at .02 mL/min to provide an approximate ten to one dilution. The uranium stock solution consisted of 200 uM U(VI), as well as some additional acetate to ensure that microbial stimulation is achieved. The columns themselves, shown in Figure 1, are filled with sediment and contain a single inlet line on the bottom of the column and an outlet line on top. Fourteen of these columns are affixed to a PVC pipe via cable ties and submerged in Rifle well CD-04 at depths from 22 to 16 feet below ground level, while another eight of these columns are similarly submerged in Rifle well CD-11. At the outlet of each column, a length of polyethylene (PE) tubing connects to the outlet and travels up the well to approximately one foot below the water line, where it then connects to approximately 16 feet of stainless steel tubing. 1/8 inch stainless steel tubing is used above the water line because of its low oxygen diffusivity. The stainless steel tubing then connects to the effluent peristaltic pump outside of the well. Tubing from the influent pump connects to stainless steel and PE tubing just as with the effluent pump. Once at the column itself, the influent tubing is connected to a tee,

which in turn connects to a length of PE tubing drawing groundwater from 17 feet below ground level through a one way valve, and two feet of PE tubing connecting to the inlet of a column. The two feet of PE tubing provides sufficient length to allow for mixing of groundwater with the amended uranium via diffusion. The one way valve prevents the uranium amendment from leaking into the groundwater. In order to enforce anoxia, the influent peristaltic pump is sealed inside of a glove bag inflated with a gas mixture of nitrogen and 5% carbon dioxide, and bottles containing influent solution were filled with the same gas mixture. The gas mixture was divided between two glove bags and three bottles of influent solution via stainless steel tees, and several plug valves were used as flow control devices.

*ii. Experimental Setup and Procedure*

Setup of this experiment consisted of three main steps: assembly of the in-well reactors, column packing, and tube priming. Assembly of the in-well reactors involved connecting different tubing types, putting together the columns themselves, and attaching columns and their associated tubing to a ¾ inch PVC pipe. Connections between different pieces of 1/8 inch tubing were made using a slightly larger piece of soft tubing, specifically 3/32 inch inner diameter Tygon tubing. A small piece of such tubing, when stretched over 1/8 inch outer diameter polyethylene or stainless steel tubing, was able to effectively connect the two tubing types without fear of leakage or air incursion. The columns themselves were assembled as per the instructions provided by their manufacturer, with one small alteration. In order to prevent the flow of fine sediment particles through the column and into the tubing, the filters included in the columns were removed and replaced with a small circle of nylon organza. Upon assembly, the columns were attached to a 20 foot PVC pipe via 14 inch cable ties tied through holes drilled in the pipe. As a result of the four inch diameter of the wells, it was necessary for two columns to be affixed next to each other, and for each set of two columns to be in line with the set below, as

diagrammed in Figure 3. Column packing refers to the process by which the columns were filled with sediment. In order to assure even flow and to decrease the number of air bubbles present in the system, the columns need to be filled very thoroughly with as much sediment as possible. This was attained by creating a slurry of sediment and water, and gently tapping any air bubbles out of the column while pumping water through the filled column with one of the peristaltic pumps. Finally, every length of tubing used in the setup needed to be primed to ensure that as little air as possible was introduced to the system. The priming process involved first running water in both directions, through both the influent and the effluent lines using a large groundwater pump. Following this, groundwater was pumped through each influent line with an Ismatec peristaltic pump until water was seen dripping out the effluent line.

Upon deployment into the wells at the Rifle site, the in-well column setup was simply allowed to remain in the well with a constant flow of groundwater through each column. Different columns were harvested at different time points, to give a time-dependent view of uranium speciation under acetate stimulation. Table 1 demonstrates the nominal harvest time of each column, although these times are subject to change based on whether the occurrence of iron reduction or sulfate reduction is detected.

*iii. Sample Preparation*

Samples collected from the column reactors for analysis via XAS techniques are both highly oxygen sensitive and radioactive and, as a result, were handled with extreme care. The samples were shipped from the Rifle site in stainless steel vacuum containers, and all sample preparation occurred within an anaerobic glove box marked as a contamination area. Sediment samples were transferred into centrifuge tubes via pipette, and then centrifuged for several minutes to force the sediment to separate from any water in the sample. The sediment was then carefully transferred into aluminum sample holders and covered with kaptan tape to prevent any sediment from

escaping while minimizing x-ray intensity loss. Once loaded into the beam hutch, a liquid nitrogen cryostat was used to maintain a vacuum on the sample and prevent any incursion of oxygen.

*iv. X-ray Spectroscopy*

Analysis of these samples relies on x-ray spectroscopic techniques. In particular, x-ray absorption near edge spectroscopy (XANES) and x-ray absorption fine structure spectroscopy (EXAFS) are utilized to discern the oxidation state and local molecular structures of the reduced uranium in the samples. These well-known techniques [7] were combined to provide a view of the oxidation state and local atomic structure of the uranium in the samples. Analysis of the spectroscopic results was performed using SixPack to process the resulting spectra and fit the results to the most probable crystal configuration.

## 3. RESULTS

XAS was performed on sediment samples from experimentation in the summer of 2009 in wells P-101 and P-102. Figure 4a depicts the spectrum produced by XAS at beam line 11-2 at SSRL for sediment taken from the column from well P-101. Figure 4c shows the spectrum produced by sediment taken from the sediment from well P-102. Figures 4b and 4d shown the Fourier transformed spectra for the sediment samples, with fits from SixPack. The low concentration of uranium in the samples, even after amendment, limits the resolution of the data collected. Each of these spectra indicates the structure of the uranium complexes present in the columns after acetate-stimulated bioreduction.

## 4. DISCUSSION AND CONCLUSION

As illustrated in Figures 4a-4d, spectra from XAS on sediments from columns deployed in Rifle wells P-101 and P-102 in 2009 show clear resemblance to one another, implying that the speciation of uranium is independent of from which well the column sediment is harvested. Data analysis and fitting using SixPack, shown in Figures 4a-4d, also reveal that the reduced uranium products are not uraninite, the spectrum for which is illustrated in Figure 5. Indeed, the most probable fits suggest that these uranium products are bonded with calcium and phosphorus, or possibly adsorbed onto iron biomass. The implications of these results are quite significant to bioremediation attempts at sites like Rifle. Acetate-stimulated bioreduction of uranium has been modeled as producing uraninite, but these results clearly display that this is not the case in Rifle groundwater. Rather, U(IV) appears to form complex structures including phosphorus and possibly calcium or iron. With uraninite seemingly serving no role in this reduction process, it is clear that uraninite cannot be used as a means of sequestering uranium from contaminated groundwater.

Further study is needed to fully understand the bioreduced structure of uranium. Limited resolution as a result of low uranium concentration makes determining the exact identity and locations of the atoms bonded to uranium impossible; hence, the addition of further uranium is a necessary step for improvement. Sediment samples from the 22 columns deployed in August 2010 are intended to provide further information about uranium speciation after acetate stimulation, specifically during iron and sulfate reduction.

## 5. ACKNOWLEDGEMENTS

This work was made possible by the Stanford Synchrotron Radiation Light Source at the Stanford Linear Accelerator Center National Accelerator Laboratory, the Department of Energy, the United States Geological Study and the city of Rifle. I would like to thank my mentor, John

Bargar, as well as Patricia Fox, Jim Davis, Jose Cerrato, Carolyn Sheehan, Sung-Woo Lee, Mike Massey, Marc Michel, Joanne Stubbs, Juan Lezama, Cynthia Patty, and Carol Morris for their invaluable assistance.

## 6. REFERENCES

[1] Riley, R.G., Zachara, J.M., Wobber, F.J., "Chemical Contaminants on DOE Lands and Selection of Contaminant Mixtures for Subsurface Science Research," U.S. Department of Energy, 1992.

[2] Langmuir, D., "Uranium solution-mineral equilibria at low temperatures with applications to sedimentary ore deposits," Geochimica et Cosmochimica Acta, vol. 42, no. 6, pp. 547-569, 1978.

[3] Yabusaki, S.B., Fang, Y., Long, P.E., et al., "Uranium removal from groundwater via *in situ* biostimulation: Field-scale modeling of transport and biological processes," Journal of Contaminant Hydrology, vol. 93, no. 1-4, pp. 216-235, 2007.

[4] Bargar, J., Bernier-Latmani, R., Giammar, D., et al., "Biogenic Uraninite Nanoparticles and Their Importance for Uranium Remediation," Elements, vol. 4, pp. 407-412, 2008.

[5] Anderson, R., Vrionis, H., Ortiz-Bernad, I., et. al, "Stimulating the In Situ Activity of *Geobacter* Species To Remove Uranium from the Groundwater of a Uranium-Contaminated Aquifer," Applied Environmental Microbiology, vol. 69, no. 10, pp. 5884-5891, 2003.

[6] "Ground Water Compliance Action Plan for the Old Rifle, Colorado, UMTRA Project Site," U.S. Department of Energy, document no. U0066302, 2001.

[7] Kelly, S.D., Hesterberg, D., Ravel, B., "Analysis of Soils and Minerals Using X-ray Absorption Spectroscopy in Methods of Soil Analysis, Part 5 -Mineralogical Methods, Ulery and A.L., Drees, L.R., Eds., Madison, WI: Soil Science Society of America, 2008.

**FIGURES**

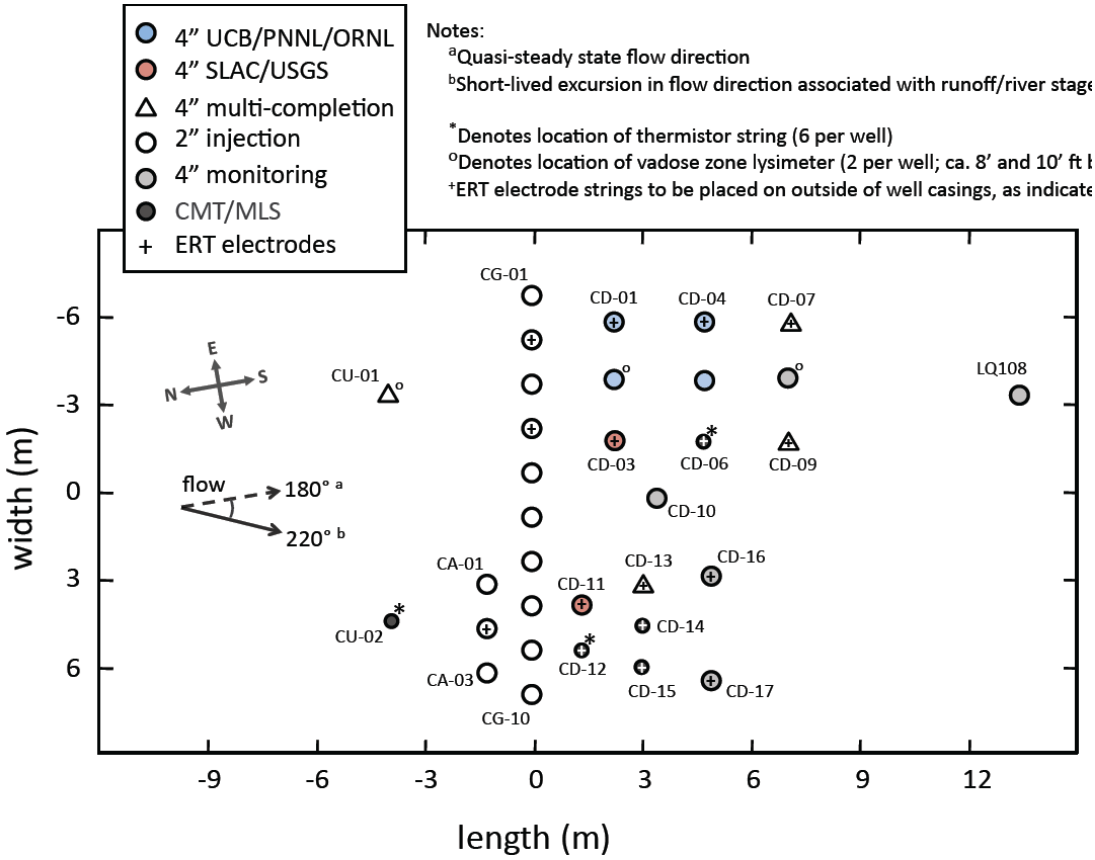


Figure 1: The flow cell and well setup at the Rifle site. The wells used in this experiment were wells CD-04 and CD-11. The designation "CD" refers to the location of the wells as being downstream of the injection sites ("D") and in experimental plot C.

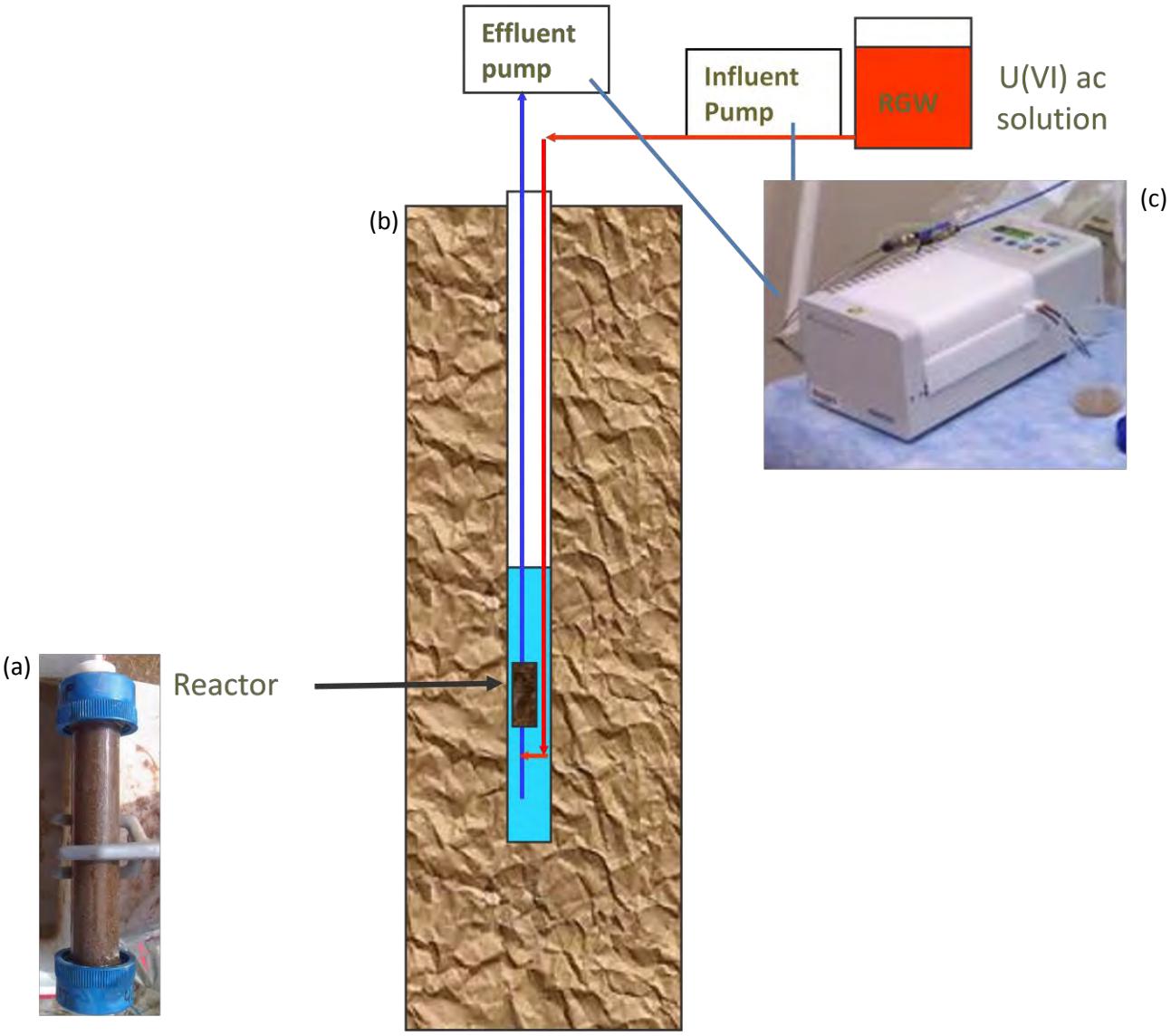


Figure 2: The *in situ* column setup. (a) One *in situ* column, filled with bioactive Rifle sediment. (b) A schematic of a Rifle well demonstrating the flow of U(VI) stock solution into the column and ground water out of the column. (c) One of the peristaltic pumps utilized in the setup.

Figure 3: The in-well column setup. The columns are the blue-capped cylinders and are shown filled with sediment. The blue tubing is polyethylene tubing.

(a)

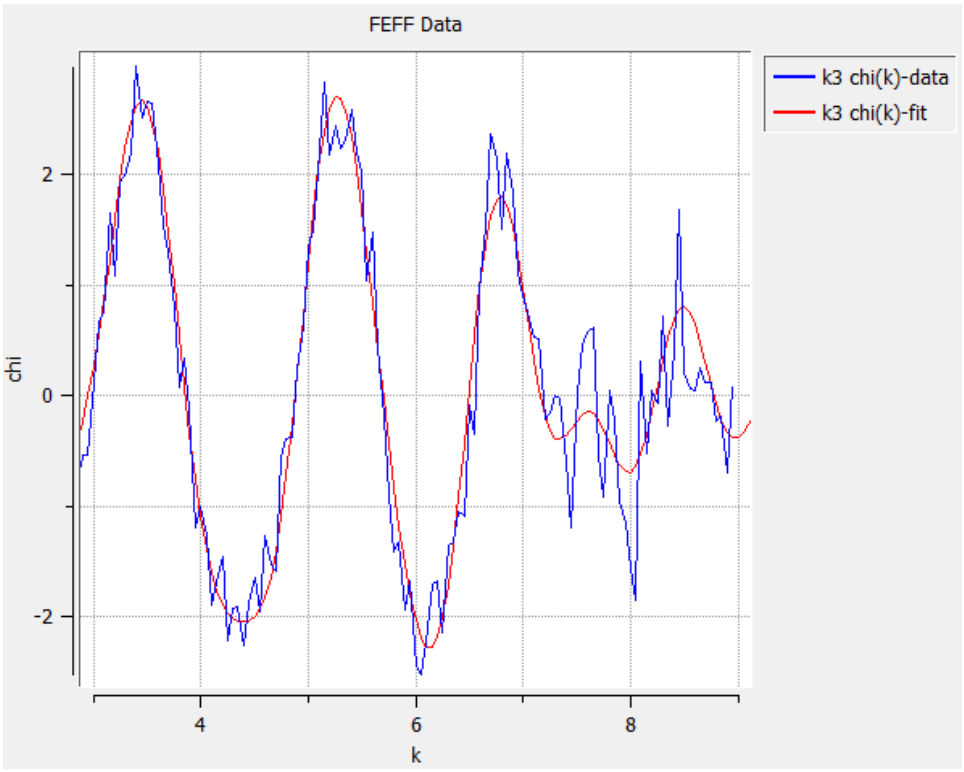
FEFF Data
k3 chi(k)-data
k3 chi(k)-fit
chi
2
0
-2
4
6
8
k

(b)

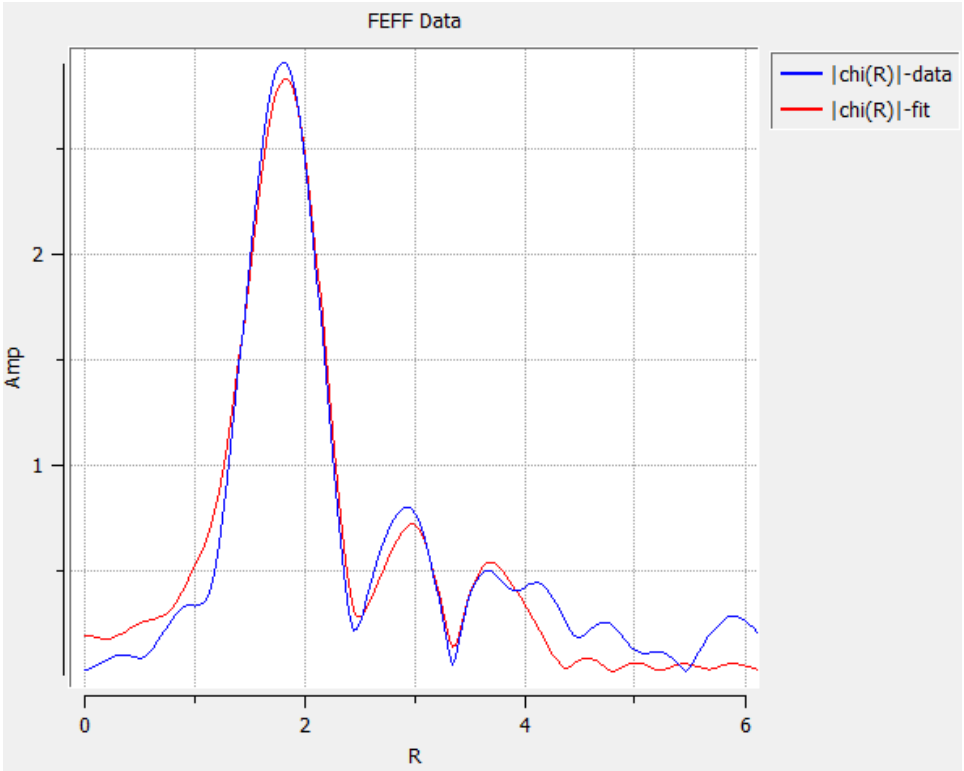
FEFF Data
|chi(R)|-data
|chi(R)|-fit
Amp
2
1
0
2
4
6
R

(c)

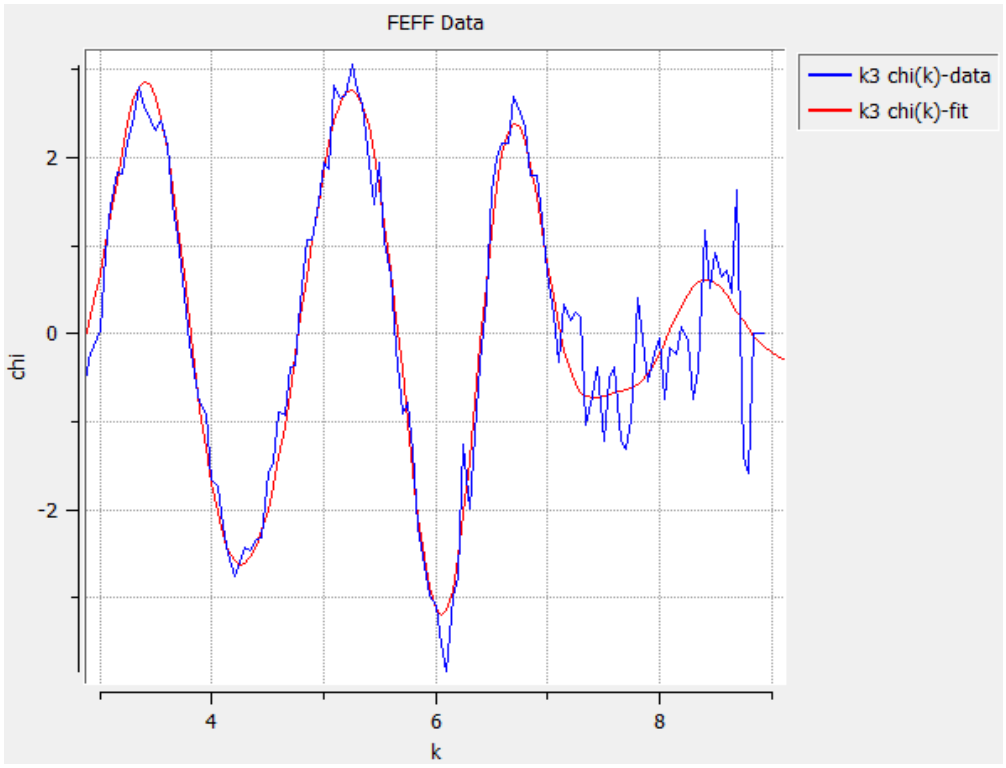


(d)

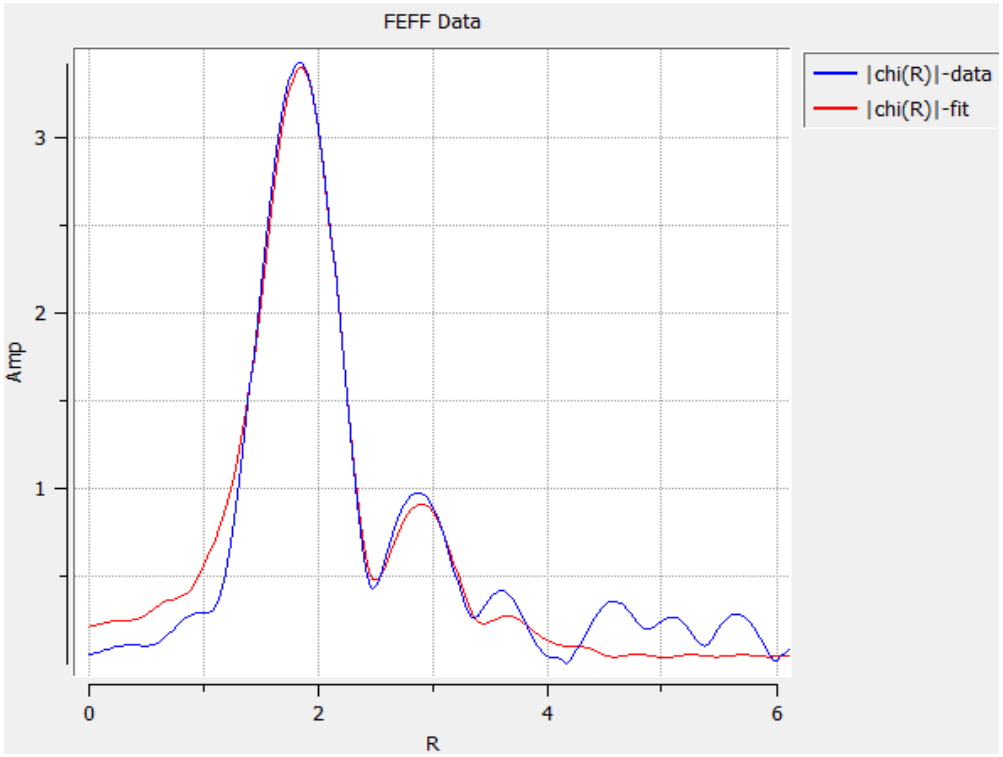


Figure 3: In all plots, Actual data is shown in blue, while a fit using bonds to oxygen, phosphorus and iron is shown in red. (a) P101 EXAFS chi vs. k data. (b) P101 EXAFS Fourier transformed data plotting amplitude versus bond distance in angstroms. (c) P102 EXAFS chi vs. k data. (d) P102 EXAFS Fourier transformed data plotting amplitude versus bond distance in angstroms.

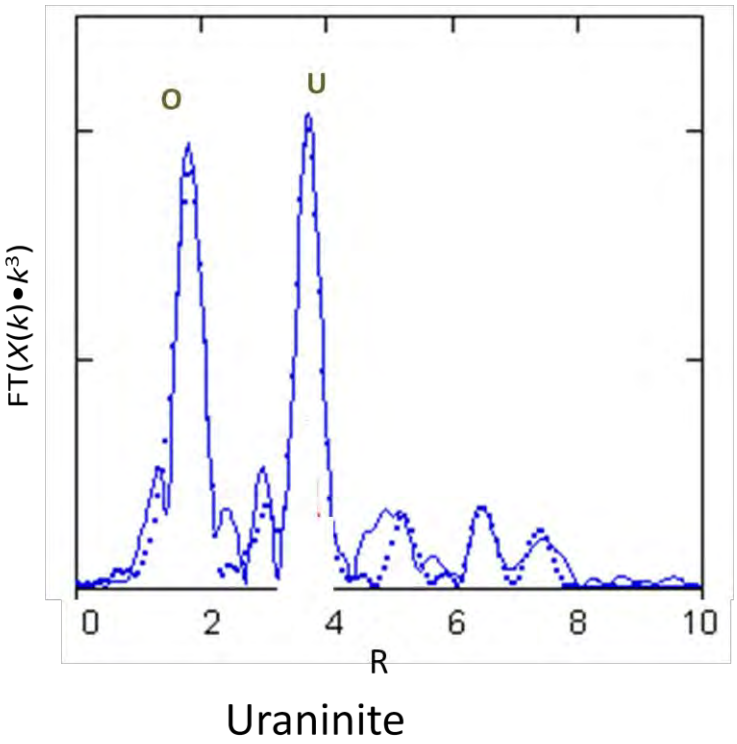


Figure 5: Uraninite EXAFS spectrum. Noticeable features include a large peak at 3.87 angstroms representing a uranium-uranium bond, as well as large peak at approximately 2 angstroms representing a uranium-oxygen bond.

# Improving Phase Measurement Procedures for Pump-Probe Experiments

Cara P. Perkins

Office of Science, Science Undergraduate Laboratory Internship Program

Merrimack College

SLAC National Accelerator Laboratory
Menlo Park, California

August 20, 2010

Prepared in partial fulfillment of the requirement of the Office of Science, Department of Energy's Science Undergraduate Laboratory Internship under the direction of Josef C. Frisch of the Linac Coherent Light Source group at SLAC National Accelerator Laboratory.

Participant: _____
Signature

Research Advisor: _____
Signature



Work supported in part by US Department of Energy contract DE-AC02-76SF00515.

## TABLE OF CONTENTS

Page

## ABSTRACT

Improving Phase Measurement Procedures for Pump-Probe Experiments.
CARA P. PERKINS (Merrimack College, North Andover, MA, 01845), JOE FRISCH (SLAC National Accelerator Laboratory, Menlo Park, CA 94025).

Pump-probe experiments use a visible laser to excite an atom or molecule, while an X-ray pulse measures its shape. The phases and pulse times of each beam are used to calculate the object's positing at a given time – a moving picture of the chemical reaction. Currently, the fastest X-ray pulses can travel a time-length of five femtoseconds. However, present-day phase measurements can only be done as quickly as 50 femtoseconds. The purpose of this research is to explore ways in which phase-timing measurements can be improved. Three experiments are undergone to find the key factors in phase-timing. Different frequency mixers, the radio frequency (RF) components used for phase measurement, are tested for the highest sensitivity. These same mixers are then tested using two different power splitters for the lowest noise-to-sensitivity ratio. Lastly, the temperature dependency of phase is explored by testing each component at a range of temperatures to see how the phase is affected. This research demonstrated that certain mixers were more sensitive than others; on average, one mixer performed the best with a sensitivity of 0.0230 V/ps. The results also showed that that same mixer combined with one splitter gave the best noise-to-sensitivity ratio overall with an average of 6.95E-04 fs/√(Hz). All the components tested exhibited a temperature-dependent phase change (ranging from 1.69 to 81.6 fs/ ˚C); the same mixer that performed at the highest sensitivity with the least noise had a significantly greater phase change than the other two. In conclusion, the experiments showed that a temperature-controlled environment is most appropriate for phase measurement. They also demonstrated that mixers are not significantly noisy and that certain types of mixers may perform better than others, which could be accounted for in their construction. The results of this research encourage further investigation into the study of different mixers and other RF components used in pump-probe experiments.

## INTRODUCTION

The Linac Coherent Light Source (LCLS) at the Stanford Linear Accelerator Center (SLAC) National Accelerator Laboratory is the fastest, shortest pulse, highest-energy X-ray laser in the world. The LCLS shoots a beam of electrons through a specific type of magnets called undulators that create an X-ray. Initially, all the electrons begin traveling at different times. The electrons exhibit energy changes according to the effect that the electric field has on them. Those with higher energies move faster than those with lower energies. Eventually, the electrons "bunch" together at X-ray wavelengths, forming the shortest X-ray pulses yet. These fast, short X-ray pulses are used to carry out a pump-probe experiment. A pump-probe experiment triggers molecules with a visible laser and then uses the X-ray laser pulse to measure them a very short time later. Each laser beam travels through a resonance cavity that gives off a radio frequency (RF) signal containing the beam's phase information. As the beams pass through the experimental target, they trigger the detection system that measures their respective timing. By measuring the beams' phases and times relative to a reference point, the time dependence of the way the molecules move can be found, creating a movie of the chemical reaction.

This system of keeping the beams in time with respect to phase works for pulse times of about 50 femtoseconds. The LCLS can generate X-ray pulses as quickly as five femtoseconds, and it is believed that one can generate a visible beam of the same time-length [1]. These super fast lasers, however, are of no good if their phase and time measurements are not synchronized.

The purpose of this investigation is to improve the accuracy and speed with which phase is measured. A series of tests is undergone using signal generators, RF components, an oscilloscope, a voltmeter, and a spectrum analyzer. The ideal phase measurement setup has the lowest possible ratio of frequency noise to sensitivity and the least amount of phase drift. The

sensitivity is simply a reading of the average voltage out of the system per unit of time. Frequency noise is defined as fluctuations in a signal reading due to disturbances such as vibrations [2], while phase drift is defined as the variation in phase with time due to changes in the environment, mainly temperature.

## MATERIALS AND METHODS

### Sensitivity

The first experiment in this project tests three different frequency mixers, the components used for phase measurement in pump-probe experiments, at a variety of RF and local oscillator, LO, power levels to determine the sensitivity, or the voltage per time, of the electronic configuration using an oscilloscope. A mixer takes the two waveforms from the RF and LO inputs and outputs the intermediate frequency (IF) signal, carrying the sum and difference frequencies:

$$\boldsymbol{Output_{IF}} = 2\text{Cos}\,(\boldsymbol{\omega_{LO}}t\,) \cdot \text{Cos}(\boldsymbol{\omega_{RF}}t\,).$$

$$= \text{Cos}\,((\boldsymbol{\omega_{LO}} - \boldsymbol{\omega_{RF}}\,)t\,) + \text{Cos}\,((\boldsymbol{\omega_{LO}} + \boldsymbol{\omega_{RF}}\,)t\,) \quad [4]. \qquad (1)$$

Two of the mixers tested are Level 17 and the last is Level 10. The optimal power settings designated by the manufacturers for Level 17 and Level 10 mixers are 17 dBm LO and 10 dBm RF, and 10 dBm LO and 5 dBm RF, respectively [3]. For the purpose of this paper, the Mini-Circuits® Level 17 frequency mixer (model ZX05-1HW+), the Mini-Circuits® Level 17 frequency mixer (model ZFM-4H-S+), and the Mini-Circuits® Level 10 frequency mixer (model ZFM-150) will be referred to as the first, second, and third mixers, respectively. The mixers are tested at ranges of 5 to 20 dBm LO and 0 to 15 dBm RF inputs. (The third mixer is also tested at an LO input of 0 dBm since it is speculated to operate at lower power settings.)

Two signal generators at slightly different frequencies provide the RF (at 476 MHz) and LO (at 476.01 MHz) power inputs to the mixer. Early measurements indicated that the two signal generators could not achieve power levels higher than 15 dBm. To obtain the higher power levels, a 20 dBm gain RF amplifier (Mini-Circuits® ZHL-2010+) is added after each signal generator, followed by a 470 MHz low pass filter (Mini-Circuits® VLFX-470). This filter blocks the high frequency harmonics generated by the components themselves, but is not strong enough to eliminate the 476 MHz signal. The output of the mixer travels through a 98 MHz low pass filter (Mini-Circuits® SLP-100+) before the oscilloscope. This low pass filter ensures that the frequency read off the oscilloscope is a reading of the difference in frequencies of the RF and LO signals only (which should be 10 kHz in this case) (Figure 1). The signal creates a sine wave in the screen of the oscilloscope (Figure 2). The slope of the waveform taken at the zero-crossing (Volts/picoseconds) and the frequency of the incoming signal (the difference frequency) are read off the oscilloscope (Figure 3). The inverse of the difference frequency multiplied by the slope gives the number of volts per period of the waveform. Multiplying this by the frequency of the RF signal, gives a value in volts per picoseconds – the power sensitivity (S) and the difference between the RF and LO inputs:

$$\textbf{\textit{Volts per Period}}\ [\mathrm{V}] = (\ 1/f_{diff}\ )\ [\mathrm{ps}^{-1}] \cdot \textbf{\textit{Slope}}\ [\mathrm{V/ps}]. \qquad (2)$$

$$\boldsymbol{S}\ [\mathrm{V/ps}] = \textbf{\textit{Volts per Period}}\ [\mathrm{V}] \cdot f_{RF}\ [\mathrm{ps}^{-1}]. \qquad (3)$$

**Noise**

Another electronic configuration is used to find the noise of the RF components using a spectrum analyzer (Figure 4). A single signal generator is followed by the same RF amplifier and 470 MHz low pass filter (for the same reasons as before), and a power splitter to provide the LO and RF inputs to the mixer. A phase shifter allows the user to adjust the phase of the RF signal

going into the mixer. Again, the mixer output travels through the 98 MHz low pass before reaching the spectrum analyzer. Before taking measurements from the spectrum analyzer, the mixer power inputs are chosen to compare closely with those for the sensitivity measurements to calculate the noise-to-sensitivity ratios later. Also, the phase of the RF signal must be fixed at 90°; it is necessary to have the waveforms 90° out of phase with one another because the highest phase sensitivity occurs at 90°. This is done by plugging the mixer output (after the 98 MHz filter) into the voltmeter and adjusting the phase shifter until the voltage reading is 0 V (since the sensitivity readings were also taken at the zero-crossing).

The spectrum analyzer displays a sharply decreasing curve that levels off and becomes mostly flat (Figure 5). At any point on this plot a measurement of voltage at a given resolution bandwidth (RBW), ranging from 100 Hz to 100 kHz, may be taken. These measurements are used to find the noise level, NL (volts per root Hertz), of the electronic setup. Several voltage measurements taken at the same bandwidth, but different points along the curve can be used to try to find the 1/f noise, or pink noise, of the electronic setup. When referring to electronic devices, 1/f noise is often called pink or flicker noise and is caused by impurities in the circuitry. The more flicker noise produced using a given frequency mixer or power splitter indicates a greater amount of impurities [5].

Next, the noise-to-sensitivity ratio is calculated. Utilizing the data already gathered for the sensitivity of the mixers at given RF and LO inputs allows for the calculation of the picoseconds per root Hertz of the configuration – a noise-to-sensitivity ratio, NSR:

$$\boldsymbol{NSR}\ [\text{ps} / \sqrt{(\text{Hz})}] = \boldsymbol{NL}\ [\text{V}/\sqrt{(\text{Hz})}] \,/\, \boldsymbol{S}\ [\text{V/ps}]. \qquad (4)$$

These tests, carried out at the same LO and RF power ranges as the sensitivity tests, use the same three frequency mixers as before, and also two different splitters. The first splitter is a

coaxial power splitter (Mini-Circuits® model ZFSC-2-1W+) which is made of transformers and other electronic devices that, presumably, have the potential to add extra noise. The second, Anaren® model (no. 40263), is made of a printed circuit (PC) board – a much simpler design.

**Phase Drift**

The timing system in the LCLS can easily change phase conditions; phase drift may be caused by instable temperature. For this reason, it is necessary to check for phase temperature dependencies of the RF components. This part of the project uses the same electronic setup as the noise experiment, but with one of the RF components on a temperature regulated plate (Figure 6).

At this point in the project, the sensitivity and noise measurements provide a decent understanding of what the optimal RF and LO power settings are for each mixer. This part of the experiment uses these optimal settings so that only the temperature is varying. Starting at the highest temperature reached by the temperature regulation machine, the signal is sent to the voltmeter. (The temperature regulation machine has a range of 10 to 35 ˚C. According to the manufacturers, all the RF components used in this experiment should operate properly in this range.) As with noise measurements, the phase is fixed at 90° at this high temperature. As the temperature-controlled RF component cools, the voltage reading on the voltmeter is noted at each degree Celsius. This process continues until the temperature has reached the minimum. Then, the system is warmed up to its original temperature while the voltage reading is periodically recorded. If the phase drift of the component is temperature-dependent, the voltage reading should move away from zero as the component cools and then return to zero as it heats up to its starting temperature. This experiment is carried out for a total of eight times; the two splitters, three mixers, amplifier, and phase shifter each have a turn on the temperature-regulated

plate. The eighth experiment tests a 10 ft. cable coil between the phase shifter and the RF input to the mixer.

Each reading off the voltmeter provides a change in voltage per degree Celsius. Taking the average change in voltage per degree Celsius and dividing it by the sensitivity gives the change in phase time per degree Celsius, or the phase drift:

$$\textit{Phase Drift}\ [\text{fs}/^{\circ}\text{C}] = (\Delta V/^{\circ}C)_{avg} / S\ [\text{V/fs}]. \quad (5)$$

## RESULTS

### Sensitivity

The sensitivity experiment gave 20 sensitivity measurements, corresponding with different RF and LO inputs, for each mixer. The best sensitivity measurement, 0.056 20 V/ps, was taken using the first mixer at 20 dBm LO input and 15 dBm RF input, while the worst sensitivity reading, 0.004 21 V/ps, was taken using the third mixer at 17 dBm LO and 0 dBm RF. On average, the first mixer was the most sensitive at about 0.023 00 V/ps, followed by the second at 0.018 60 V/ps, then the third at 0.005 96 V/ps (Table 1).

### Noise

Six sets of data resulted from the noise experiment. Each of the three mixers was tested for noise using each of the two splitters. Using one splitter versus another did not seem to have a great effect on the noise. While taking the data, it became clear that the plot shown on the spectrum analyzer was not actually displaying flicker noise. Although the plot looked like a 1/f plot (Figure 5), it was determined that the steep decline in noise voltage was simply a result of the averaging of lower-frequency harmonics, not eliminated by the low pass filters. This discovery led to the decision to neglect searching for the 1/f plot and deal specifically with the

noise-to-sensitivity ratio. The readings off the spectrum analyzer were taken from the regions of the plot that were mostly level. Taking the average ratios for each combination showed that the first mixer combined with the first splitter had the least amount of noise with a noise-to-sensitivity ratio of 6.95E-04 fs/√(Hz), followed by the second mixer with the second splitter at 7.47E-04 fs/√(Hz), the first mixer with the second splitter with a ratio of 7.56E-04 fs/√(Hz), the second mixer with the first splitter at 9.00E-04 fs/√(Hz), the third mixer with the first splitter at 1.62E-03 fs/√(Hz), and finally the third mixer with the second splitter at 1.70E-03 fs/√(Hz), (Table 2). For the purpose of further investigation, a second RF amplifier, followed by enough attenuation so that no power was added to the system, was inserted before the RF input of the mixer to see if the noise increased at all. The noise floor and, thus, the noise-to-sensitivity ratio did not increase with the additional amplifier.

**Phase Drift**

The phase drift experiment provided eight phase drift measurements – one for each of the items tested on the temperature-regulated plate. The RF component with the least amount of phase drift, 1.86 fs/˚C, was the second mixer, while the 10 ft. cable coil had the greatest amount of phase drift at 81.6 fs/˚C. Falling between these two were the first splitter at 3.78 fs/˚C, the third mixer at 6.95 fs/˚C, the amplifier at 7.88 fs/˚C , the second splitter at 8.5 fs/˚C, the phase shifter at 24.6 fs/˚C, and the first mixer at 26.8 fs/˚C, respectively (Table 3).

## DISCUSSION

While reviewing the results of this project, certain things must be kept in mind. One is the fact that these experiments were done using only three mixers, while there are millions of different mixers in existence. The same is true for splitters. Also, the manufacturers of the RF

components used in this project only provide user specifications for general applications. Therefore, these results cannot be compared to other results since these components were not intended to be used with the fastest X-ray laser beam in the world.

## Sensitivity

The sensitivity graphs show that the output voltage of all three mixers increased with the RF power (Figures 7a-f). When looking at the graphs of the sensitivity as a function of the LO power (Figures 7b, d, f), one sees that once the mixers reach a certain LO power input, their outputs level off. In the case of all three mixers, the highest sensitivity occurred at the highest LO and RF power inputs tested, 20 dBm LO and 15 dBm RF. If a user is concerned solely with getting a maximum voltage out of a mixer, then these power levels are beneficial. However, the flat areas on the sensitivity versus LO power plots (Figures 7b, d, f) indicate regions where the power does not affect the overall sensitivity. Therefore, these settings may be better-suited for someone who is not using the mixers at very specific power levels. The results also showed that the Level 10 mixer was less sensitive than the Level 17 mixers by and order of 10. Therefore, it may be possible that all Level 17 mixers are more sensitive than Level 10 mixers.

## Noise

To better understand why these flat-lined plots are more significant, consider the noise graphs (Figures 8a-f). For example, the graphs of the first mixer noise levels show that a 10 dBm LO input consistently gives the lowest noise-to-sensitivity ratio, and this noise level does not change much between a 5 to 10 dBm RF input. Because the pump-probe experiment is so complicated, one cannot be very concerned with exact power levels while measuring phase. Therefore, having a range of power inputs where the noise-to-sensitivity measurement does not change significantly is very helpful. With respect to the second mixer, the lowest noise ratio is at

17 dBm LO with an RF range of 5 to 10 dBm. The third mixer gives the lowest noise-to-sensitivity ratio at 10 dBm LO and an RF range of 5 to 10 dBm. Two main points of interest are within these results. One is that this flat-line plot is most visible at the 100 Hz RBW for the Level 17 mixers, and at the 10 kHz RBW for the Level 10 mixer. It is also interesting that both the first and third mixers operate best at 10 dBm LO and 5 to 10 dBm RF, even though the former is a Level 17 mixer and the latter is a Level 10 mixer. This could have resulted from the way the mixers were built, with respect to both their mechanical blueprints and their materials – information that Mini-Circuits® has the right to withhold from customers (and *does* withhold from customers).

**Phase Drift**

The results of the phase drift experiment show that all the RF components tested have at least some temperature dependency, some greater than others (Table 3). These results imply that the easiest way to avoid phase drift in the LCLS system is to regulate temperature, eliminating most, if not all, of the phase drift in the RF components. Because the cable coil showed the highest phase drift as a function of temperature, limiting the amount of cable used would also help reduce phase drift. (There are other types of cables in existence that claim to have lower noise levels, but they have yet to be tested.) Why some components have more phase drift with temperature may have to do with the materials they are made of or how they are built. For example, the phase drift of the first mixer is greater than that of the other two mixers by an order of magnitude, even though this same mixer performed best during the sensitivity and noise experiments. Again, Mini-Circuits® does not reveal details of the construction of its components so there is no way to say one construction or one material is better than another.

## Conclusion

This project demonstrates one way to test frequency mixers, but it does not provide an answer for what type of mixer would be the "best"- especially considering how differently these mixers performed. There are too many unknowns with respect to the construction of frequency mixers to say that one design is better than another. Further research on this subject may provide a better understanding of the performance of mixers that would eliminate the need to test individual mixers for noise-to-sensitivity ratios.

But what do all these results mean for pump-probe experiments at the LCLS? Multiplying the square-root of the 200 kHz RBW, used by the LCLS system, by the noise-to-sensitivity results shows that the noise produced by the mixers affects the phase-time measurements by less than one femtosecond (Table 2). Therefore, neither mixers nor amplifiers (as noted earlier) are main contributors to noise, and will not significantly disrupt the RF signals of the pump and probe beams; other components have yet to be tested. Lastly, the phase drift measurements are on the femtosecond scale (Table 3). By maintaining a temperature within one-tenth of a degree Celsius, one can not only harness the phase drift of the system, but also keep the phase timing down at the LCLS's five-femtosecond scale.

**ACKNOWLEDGEMENTS**

I would like to express my greatest appreciation to the people responsible for the overall production and success of this project, completed at SLAC National Accelerator Laboratory during the months June through August, 2010. Thank you to the U.S. Department of Energy for funding the Science Undergraduate Laboratory Internships (SULI), and thank you to SLAC for organizing this SULI program. I would also like to thank Stanford University for its contribution to the program, including the provision of housing. I must also acknowledge my laboratory partner and fellow intern, Michael Whalen, and the laboratory technician, George Burgueno, for their assistance with this project. Lastly, a special thank you goes to Joe Frisch, the creator of this project and my mentor.

## REFERENCES


[1] A. Brachmann, C. Bostedt, J. Bozek, R. Coffee, F.J. Decker, Y. Ding, D. Dowell, P. Emma, J. Frisch, S. Gilevich, G. Haller, G. Hays, Ph. Hering, B. Hill, Z. Huang, R. Iverson, E. Kanter, B. Kraessig, H. Loos, A. Miahnahri, H.-D. Nuhn, A. Perazzo, M. Petree, D. Ratner, R. Santra, T. Smith, S. Southworth, J. Turner, J. Welch, W. White,, J. Wu, L. Young: SLAC National Laboratory, Stanford CA, USA, J. M. Byrd, G. Huang, R. Wilcox: LBNL, Berkley CA, USA, "Femtosecond Operation of the LCLS for User Experiments," accelconf.web.cern.ch/accelconf/IPAC10/papers/tupe066.pdf.

[2] "Noise (Electronics)," August 5, 2010, http://en.wikipedia.org/wiki/Noise_%28electronics%29.

[3] "Frequently asked questions about phase detectors (AN-41-001)," Mini-Circuits ®, July 17, 2010, https://www.minicircuits.com/pages/pdfs/an41001.pdf.

[4] F. Marci, C. Marci, "Mixer Basics Primer," http://webcache.googleusercontent.com/search?q=cache:VL2K6UX-jUUJ:www.markimicrowave.com/menus/appnotes/mixer_basics_primer.pdf+purpose+of+a+microwave+mixer&hl=en&gl=us.

[5] "Flicker Noise," July 10, 2010, http://en.wikipedia.org/wiki/Flicker_noise.

## TABLES AND FIGURES

**Average Sensitivity of the Mixers**

| Mixer Number | Sensitivity (V/ps) |
|---|---|
| 1 | 0.023 00 |
| 2 | 0.018 60 |
| 3 | 0.005 96 |

Table 1. This table displays the average power sensitivity of each of the three mixers.

**Average Noise of Mixer and Splitter Combinations**

| Combination | Noise-to-Sensitivity Ratio (fs/√(Hz)) | LCLS Timescale at 200 kHz RBW (fs) |
|---|---|---|
| #1 Mixer, #1 Splitter | 6.95E-04 | 0.311 |
| #1 Mixer, #2 Splitter | 7.56E-04 | 0.338 |
| #2 Mixer, #1 Splitter | 9.00E-04 | 0.402 |
| #2 Mixer, #2 Splitter | 7.47E-04 | 0.334 |
| #3 Mixer, #1 Splitter | 1.62E-03 | 0.724 |
| #3 Mixer, #2 Splitter | 1.70E-03 | 0.760 |

Table 2. Here are the average noise-to-sensitivity ratios of each mixer / splitter combination.

**Average Phase Drift of Different Components**

| RF Component | Phase Drift (fs/˚C) |
|---|---|
| #1 Mixer | 26.8 |
| #2 Mixer | 1.86 |
| #3 Mixer | 6.95 |
| #1 Splitter | 3.78 |
| #2 Splitter | 8.50 |
| RF Amplifier | 7.88 |
| Phase Shifter | 24.6 |
| 10 ft. Cable Coil | 81.6 |

Table 3. Table 3 shows the average change in phase time per degree Celsius for each RF component tested on the temperature regulation plate.

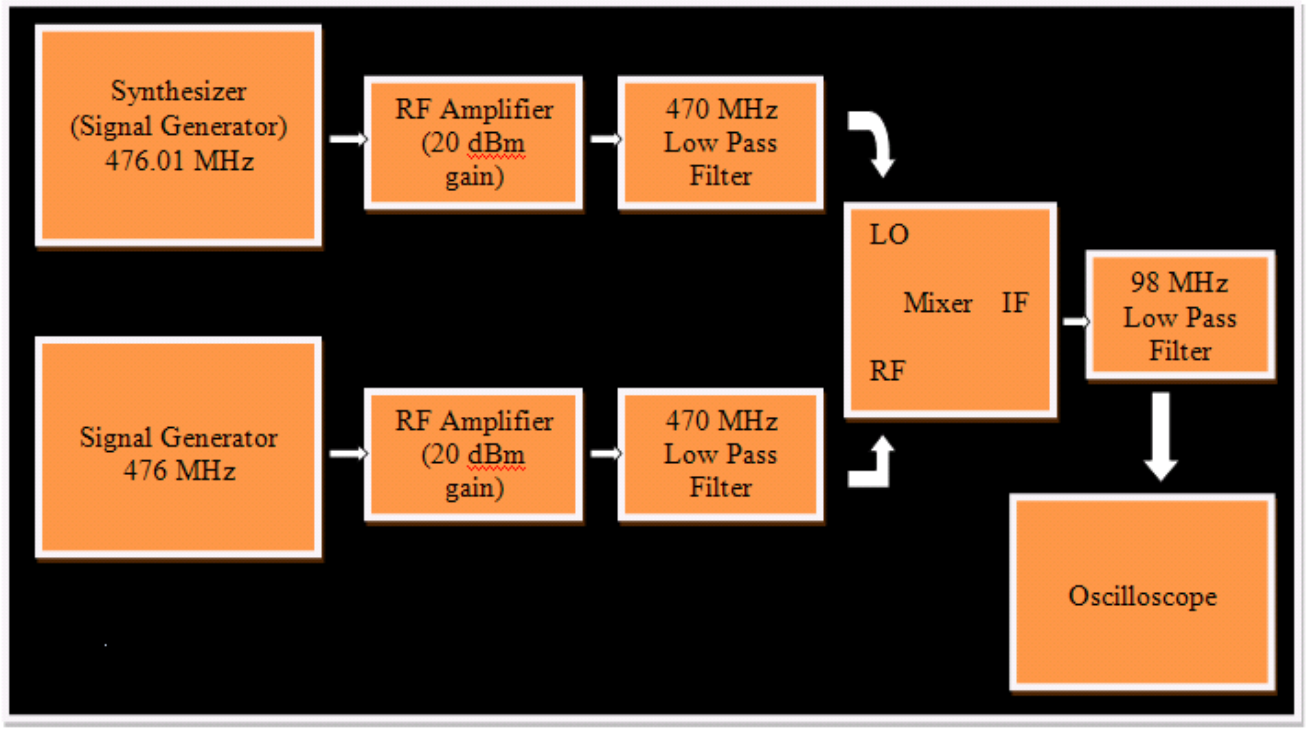


Figure 1. This is the electronic setup used to collect the power sensitivity data for each of the three frequency mixers.

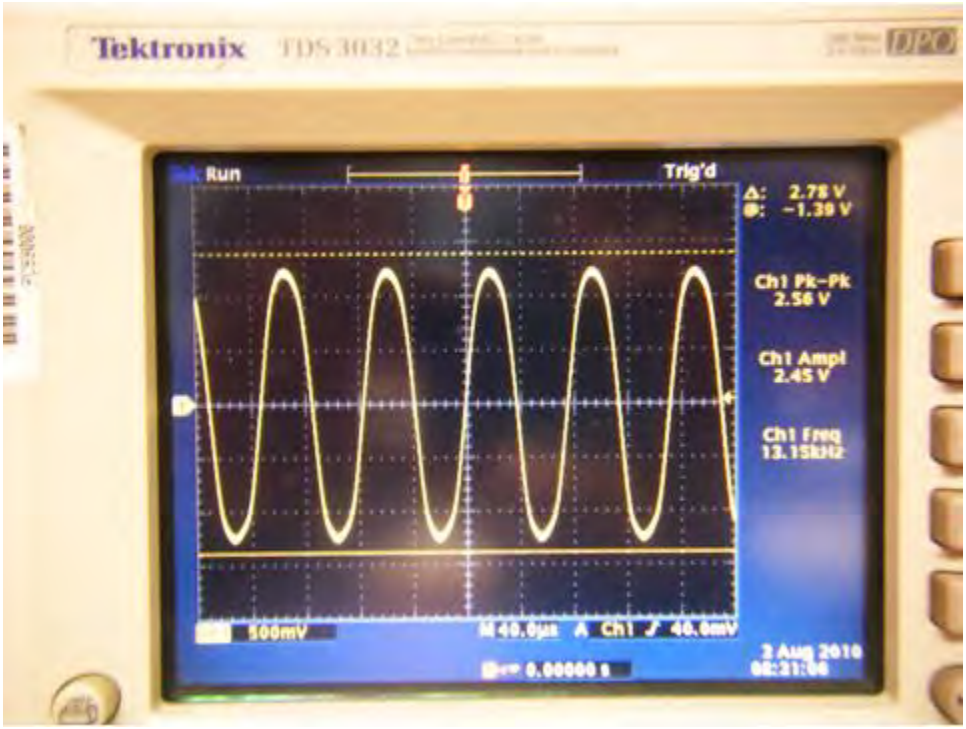

Figure 2. The signal from the IF of the mixer produces a sine waveform at the difference frequency on the oscilloscope.

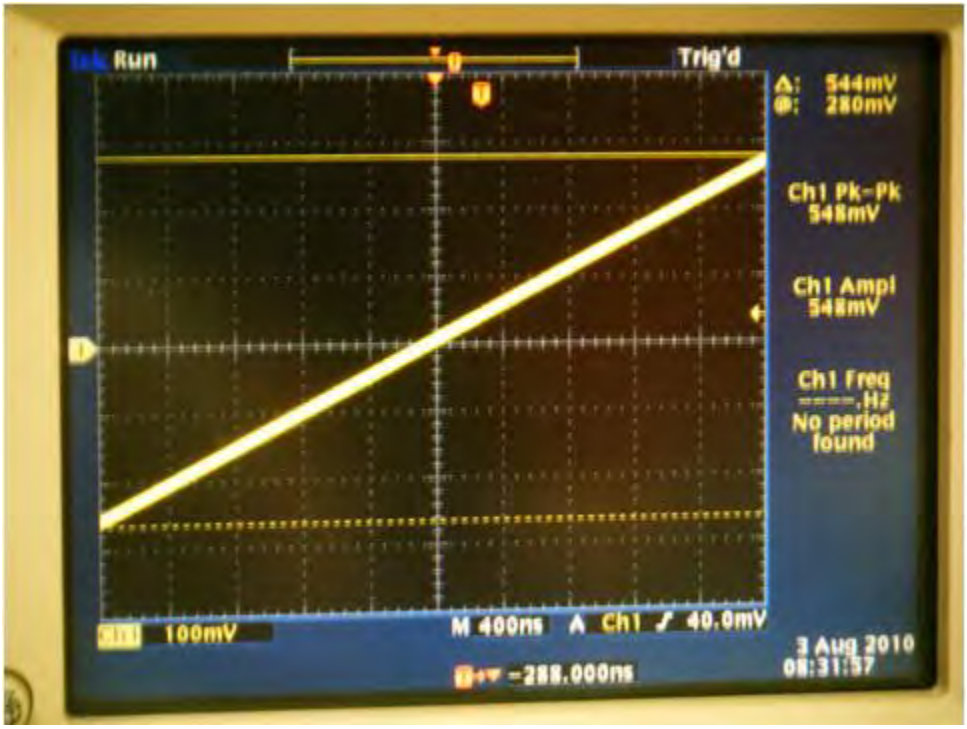

Figure 3. Zooming in at the zero-crossing gives a line with a slope of voltage per time.

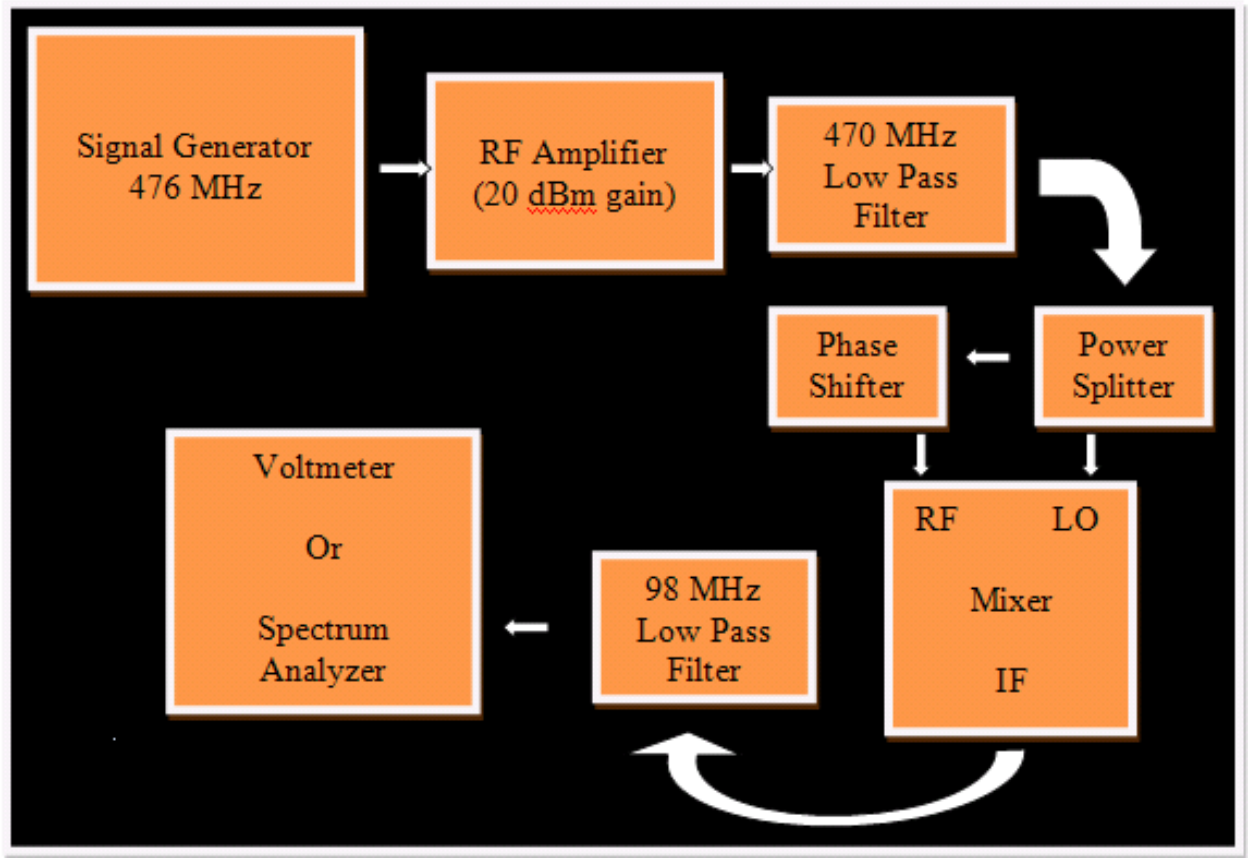


Figure 4. This is the setups used to measure the noise levels of the three mixers and two splitters.

Figure 5. The spectrum analyzer displays a noise plot that resembles a 1/f plot.

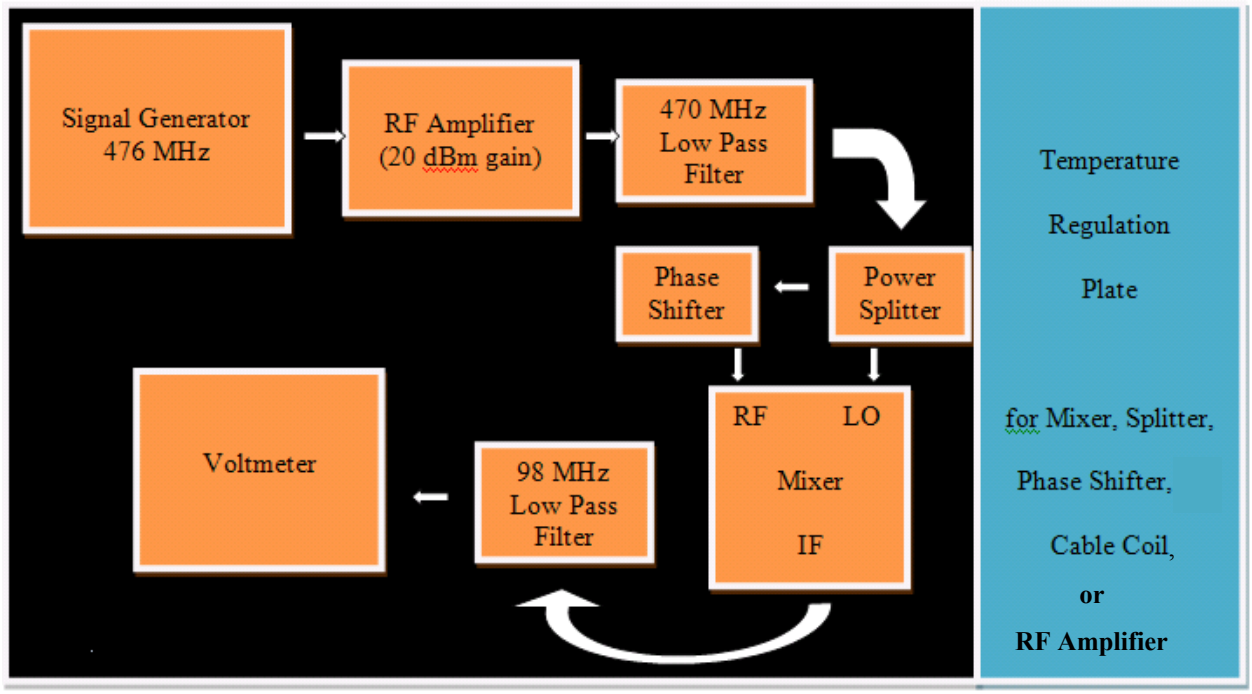

Figure 6. The phase drift setup is very similar to that of the noise experiment. Here, each of the eight components tested would take a turn on the temperature regulation plate, as shown.

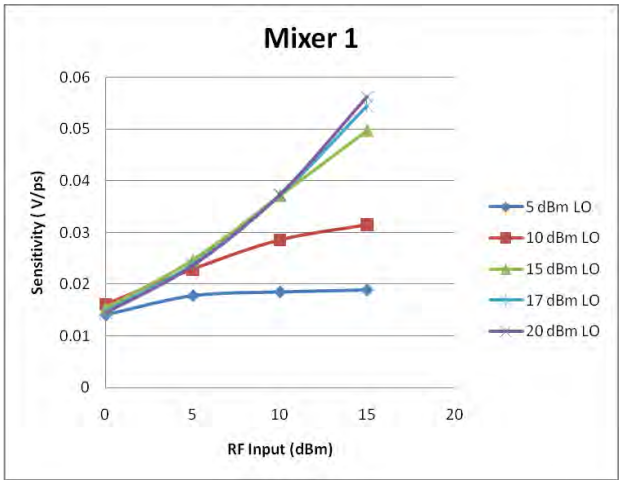


Figure 7a. Mixer 1's sensitivity vs. RF plot.

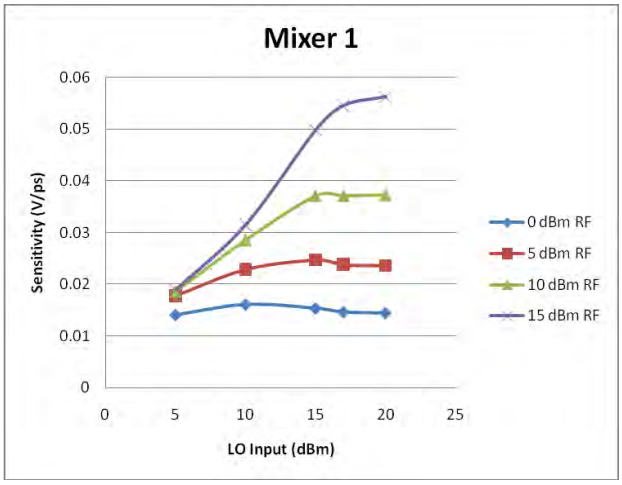


Figure 7b. Mixer 1's sensitivity vs. LO plot.

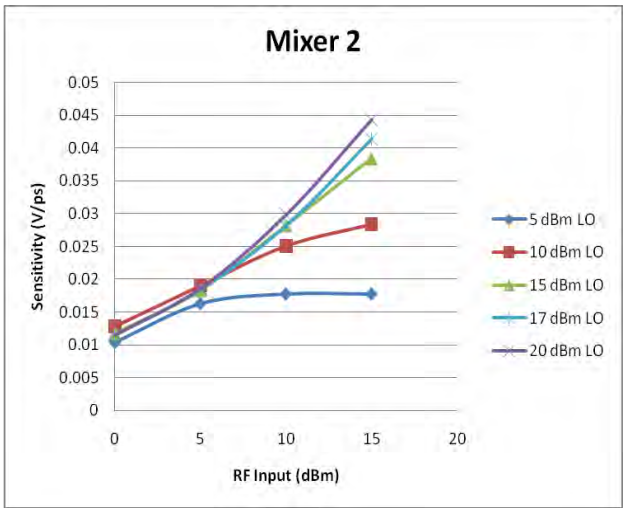


Figure 7c. Mixer 2's sensitivity vs. RF plot.

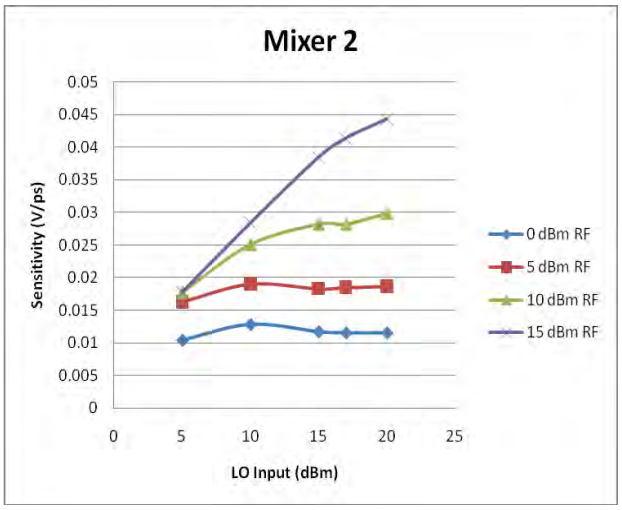


Figure 7d. Mixer 2's sensitivity vs. LO plot.

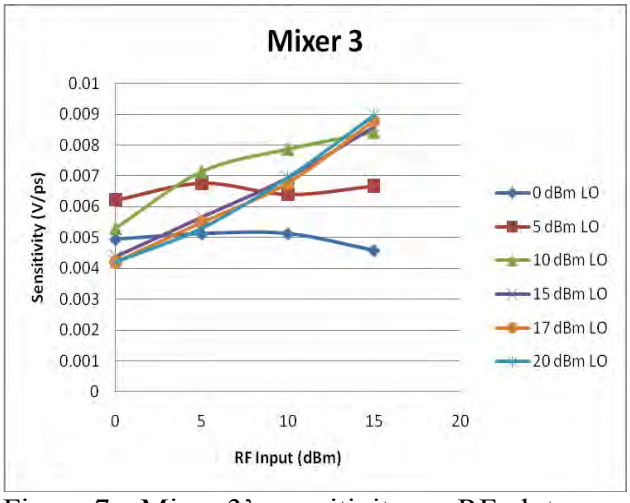


Figure 7e. Mixer 3's sensitivity vs. RF plot.

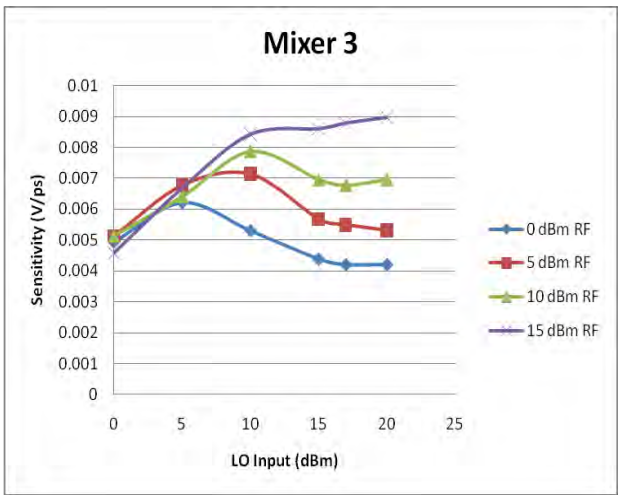


Figure 7f. Mixer 3's sensitivity vs. LO plot.

Figures 8a-f. These graphs show the noise-to-sensitivity ratio vs. the RF input for each of the six mixer / splitter combinations.

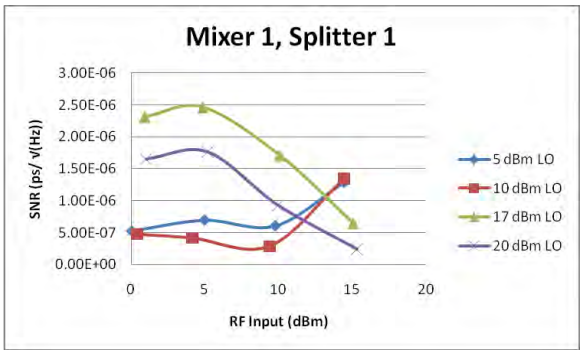


Figure 8a. Taken with a 100 Hz RBW

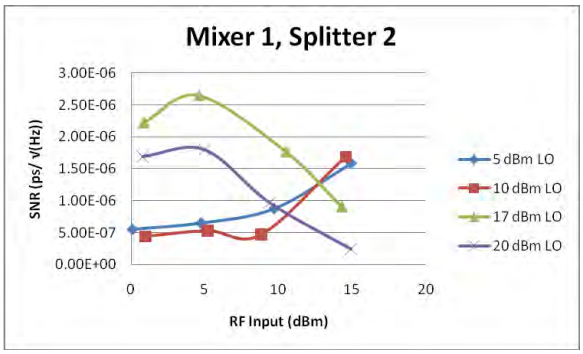


Figure 8b. Taken with a 100 Hz RBW

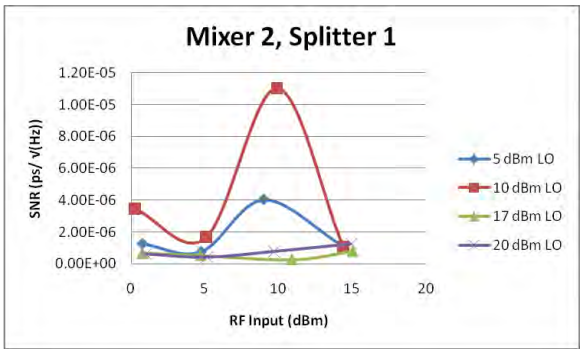


Figure 8c. Taken with a 100 Hz RBW

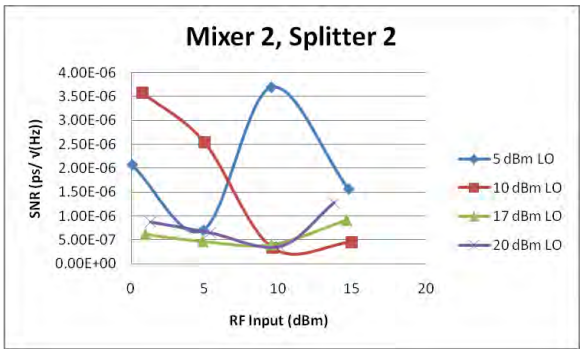


Figure 8d. Taken with a 100 Hz RBW

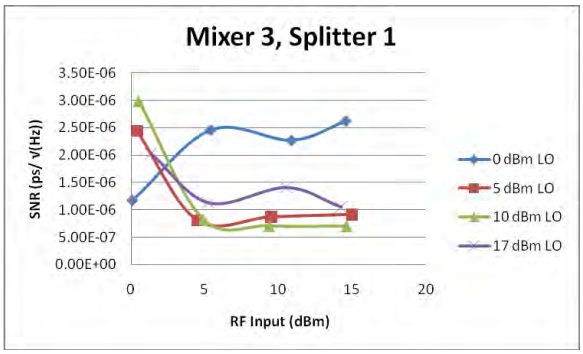


Figure 8e. Taken with a 10 kHz RBW

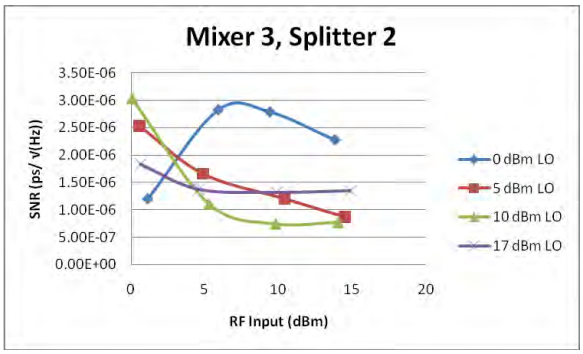


Figure 8f. Taken with a 10 kHz RBW

# Anomalous X-ray Diffraction Studies for Photovoltaic Applications

Grisel Rivera Batista
Department of Energy, Science Undergraduate Laboratory Internship Program

University of Puerto Rico, Río Piedras Campus
San Juan, Puerto Rico

SLAC National Accelerator Laboratory
Menlo Park, California

August 13, 2010

Prepared in partial fulfillment of the requirement of the Office of Science, Department of Energy's Science Undergraduate Laboratory Internship under the direction of Michael Toney, Sumohan Misra and Joanna Bettinger in the Stanford Synchrotron Radiation Lightsource at SLAC National Accelerator Laboratory.

Participant: _____
Signature

Research Advisor: _____
Signature

Research Advisor: _____
Signature

Research Advisor: _____
Signature

Work supported in part by US Department of Energy contract DE-AC02-76SF00515.

## TABLE OF CONTENTS

# ABSTRACT

Anomalous X-ray Diffraction Studies for Photovoltaics Applications – Solar Cells, GRISEL RIVERA BATISTA (University of Puerto Rico, Río Piedras Campus, San Juan, PR 00931-1907) MICHAEL TONEY, SUMOHAN MISRA, JOANNA BETTINGER (SLAC National Accelerator Laboratory, Menlo Park, CA 94025)

Anomalous X-ray Diffraction (AXRD) has become a useful technique in characterizing bulk and nanomaterials as it provides specific information about the crystal structure of materials. In this project we present the results of AXRD applied to materials for photovoltaic applications: ZnO loaded with Ga and $ZnCo_2O_4$ spinel. The X-ray diffraction data collected for various energies were plotted in Origin software. The peaks were fitted using different functions including Pseudo Voigt, Gaussian, and Lorentzian. This fitting provided the integrated intensity data (peaks area values), which when plotted as a function of X-ray energies determined the material structure. For the first analyzed sample, Ga was not incorporated into the ZnO crystal structure. For the $ZnCo_2O_4$ spinel Co was found in one or both tetrahedral and octahedral sites.

# INTRODUCTION

The use of anomalous X-ray diffraction (AXRD) provides element and site specific information for the crystal structure of a material. This technique lets us correlate the structure to the electronic properties of the materials as it allows us to probe precise locations of cations in the spinel structure. What makes it possible is that in AXRD the diffraction pattern is measured at a number of energies near an X-ray absorption edge of an element of interest. The atomic scattering strength of an element varies near its absorption edge and hence the total intensity of the diffraction peak changes by changing the X-ray energy. Thus AXRD provides element specific structural information. This method can be applied to both crystalline and liquid materials. One of the advantages of AXRD in crystallography experiments is its sensitivity to neighboring elements in the periodic tables. This method is also sensitive to specific crystallographic phases and to a specific site in a phase [1].

The main use of AXRD in this study is for transparent conductors (TCs) analysis. TCs are considered to be important materials because of their efficiency and low risk of environmental pollution. These materials are important to solar cells as a result of their remarkable combination of optical and electrical properties, including high electrical conductivity and high optical transparency in the spectrum of visible light [2][3]. TCs provide a transparent window, which allows sunlight to pass through while also allowing electricity to conduct out of the cell.

Spinel materials have the chemical form $AB_2O_4$, and are made of a face-centered cubic (FCC) lattice of oxygen anions and cations in specific interstitial sites (see Figure 1,2) [4] [5]. A normal spinel has all *A* cations on tetrahedral sites and *B* cations on octahedral sites. In contrast; an inverse spinel has the *A* and half of the *B* cations on octahedral sites and the other half of the *B* cations on tetrahedral sites; a mixed spinel lies between (see Figure 3). In the spinel structure, 8

of 64 possible tetrahedral sites and 16 of 32 possible octahedral sites are filled. Normal spinels have particularly high conduction as the linear octahedral chains of *B* cations likely serve as conduction paths [2].

In this paper we present how the data obtained with AXRD is used to analyze TCs properties as they apply to photovoltaic applications. One of the materials used for this analysis is zinc oxide. It has been loaded with 5% and 10% of Ga, which has an absorption edge of 10367 eV. The peak (100) was measured for the zinc oxide loaded with 10% Ga. In the case of 5% Ga, we measured peaks (100) and (101). With the information provided by the AXRD we can identify if Ga is being incorporated in the ZnO crystal structure. The analysis of 311 plane in the $ZnCo_2O_4$ spinel shows if Co is in tetrahedral or octahedral site.

## MATERIALS AND METHOD

### *Theoretical Model*

In a diffraction experiment, incident X-rays are directed toward a sample of interest, and are deflected by the atoms in the sample. The waves that are diffracted from different atoms can interfere with each other and consist of sharp interference maxima (peaks) with the same symmetry as in the distribution of atoms [4]. The atomic distance is an important fact in this analysis because it is directly related to the peaks in an X-ray diffraction patterns. For a given set of lattice planes with an inter-planar distance of *d*, the condition for a diffraction (peak) to occur can be simply written as which is known as the Bragg's law.

$$n\lambda = 2d\sin\theta \qquad (1)$$

In this equation, $\lambda$ is the wavelength of the X-ray, $\theta$ is the scattering angle, and $n$ is an integer representing the order of the diffraction peak (see Figure 4). It represents the scattering of radiation from two crystal planes of a crystal. These planes behave like half-reflecting mirrors. There is a difference of $2d\sin\theta$ in the pathlength travelled by the two beams of radiation where $d$ is the perpendicular distance between the planes (the path difference is marked in green and the expanded construction alongside makes the geometry more clear). As the angle of reflection is changed so does the difference in pathlength travelled by the two beams. When the path difference is equal to an integer number of wavelengths the two beams will reinforce one another and when it is an integral number of half wavelengths the two waves will interfere destructively with one another. The intensity of the total reflected radiation will vary sinusoidally with $\theta$ [6][7]. Understanding and application of Bragg's Law can provide much useful information about various samples. It can identify the lattice parameter and phase of the material. Proper understanding of the structure factor can yield more information, particularly when combined with X-ray absorption for AXRD measurements.

$$F_{(h,k,l)} = \sum_{n=1}^{atoms} f_n\left(E\right) e^{(2\pi i)(hx_n + ky_n + lz_n)} \tag{2}$$

$$f_n = f_0\left(Q\right) + f^{'}\left(E\right) + if^{"}\left(E\right) \tag{3}$$

In this equation $f_n$ represents the atomic scattering factor, $x_n$, $y_n$, *and* $z_n$ are the fractional positions of the $n^{th}$ atom, $f_0\,(Q)$ is the normal factor (E independent), $f'(E)$ is the anomalous (E dependent), and $f''(E)$ is the absorption (E dependent). The $f_n$ varies near X-ray absorption edge, producing a total intensity change. One fact to be considered about $f_n$ is that it depends on

oxidation state of the element [2]. Calculating the scattering factor let us know the intensity value since both are proportional.

$$I_{hkl} = \left| F_{hkl} \right|^2 \tag{4}$$

In this equation, the intensity, *I,* is equal to the square of the absolute value of the scattering factor. For this reason, if the X-ray energy near the absorption edge is varied, then total intensity change.

***Data Analysis***

The software used to develop the analysis was Origin. Once the data was collected at SSRL beamline 2-1, we used Origin to fit peaks and obtain their integrated intensity (peaks area). As peaks are a combination of Gaussian and Lorentzian functions, we used the Pseudo Voigt function for fitting. Compared with Gaussian and Lorentzian functions, Pseudo Voigt gave us the lowest standard errors in the fittingFor each data set we selected some scans to make an average of the $w_G$, $w_L$, and $m_\mu$. The reason we used the average values was to keep the peak shape constant for all X-ray energies.

When the peaks are fitted, we proceed to plot the obtained peak area values as a function of X-ray energies. If we see a feature at an energy corresponding to the absorption edge of a particular element, then that element is present at that particular crystallographic phase. In our case, we are looking for Ga in ZnO, which has an absorption edge at 10367 eV, and for Co in $ZnCo_2O_4$ spinel, which has an absorption edge at around 7709 eV. The presence of the cation in

the graph tells us about the material structure. We can determine if the atoms are in tetrahedral or octahedral site in the compound.

## RESULTS

The average values obtained using Pseudo Voigt function were 0.5835 for $w_G$, 1.2969 for $w_L$, and -0.0196 in $m_\mu$. In the case of the Gaussian and Lorentzian fitting, the average values for each $w$ were 0.4976 and 0.6196 respectively. For the ZnO loaded with Ga, the data obtained showed a smooth curve in the plot of area as a function of X-ray energies. It did not show any dip at the Ga-absorption edge (see Figures 5,6,7).

Figure 4 shows the fitting for the spinel $ZnCo_2O_4$ in 311 geometry. There is a big change around 7730 eV, which means that cobalt is present in the sample because its absorption edge is very close to that found in the fitting (7709 eV). The 311 plane probes both tetrahedral and octahedral sites in the spinel crystal structure, so the "dip" seen near the Co absorption edge means that Co is found in one or both of these sites (see Figures 8,9).

## DISCUSSION AND CONCLUSIONS

The absorption edge seen for $ZnCo_2O_4$ determined that Co is present in the sample in tetrahedral and octahedral structure. It means that we can find $Co^{2+}$ and $Co^{3+}$ in the plane 311. With the obtained results is clear that AXRD is a used technique for the determination of the structure of a material since we were able to obtain the needed data to identify whether the Ga and Co were in tetrahedral or octahedral sites. In the case of the fitting, we can conclude that diffracted peak intensity decreases depending on elements present on diffracting planes. As the energy is varied

through the absorption edge, there is a step function in diffracted intensity. In general, the structural information obtained via diffraction is combined with chemical information obtained via spectroscopy. At an absorption edge, there is a significant change in the atomic scattering factor, which in turn affects the structure factor. Thus by scanning energy while maintaining the Bragg condition for a particular atomic plane, it is possible to determine if certain elements are present based on changes in scattered intensity associated with each element's absorption edge.

## ACKNOWLEDGMENTS

This work was supported by the U.S. Department of Energy, Office of Science, through the Summer Undergraduate Laboratory Internship Program (SULI) and Stanford Synchrotron Radiation Lightsource (SSRL) at SLAC National Accelerator Laboratory. I would especially like to thank my mentors Michael Toney, Sumohan Misra, and Joanna Bettinger for their guidance during the realization of my project. I would also like to thank Yezhou Shi and Rodrigo Noriega for their help and explanations. Finally, I would also like to thank Stephen Rock and all the SULI staff at SLAC for give me the opportunity to work during this summer under their program.

## REFERENCES

[1] Bettinger, J., Misra, S. *Anomalous X-ray Diffraction (AXRD)*, California. 2010.

[2] Bettinger, J. *Probing the Effects of Dopants, Defects, and Crystal Structure in Spinel Transparent Conducting Oxides for Photovoltaic Applicationsi,* California.

[3] Granqvist, C. G., *Transparent conductors as solar energy materials: A panoramic review*, Department of Engineering Sciences, The Ångström Laboratory, Uppsala University, Uppsala, Sweeden. 2007.

[4] Pecharsky, V. K., Zavalij, P.Y., *Fundamentals of Powder Diffraction and Structural Characterization of Materials,* Page 146-152, Springer, New York. 2005.

[5] Thomas, R.K., *Simple Solids and their Surfaces* [Online]. Available: http://rkt.chem.ox.ac.uk/tutorials/surfaces/solids.html

[6] Introduction to X-ray Diffraction, Materials Research laboratory, University of California, Santa Barbara. 2010.

[7] Cullity, B.D., Stock, S.R., *Elements of X-Ray Diffraction*, Page 31-47, Prentice Hall, New Jersey. 2001.

# FIGURES

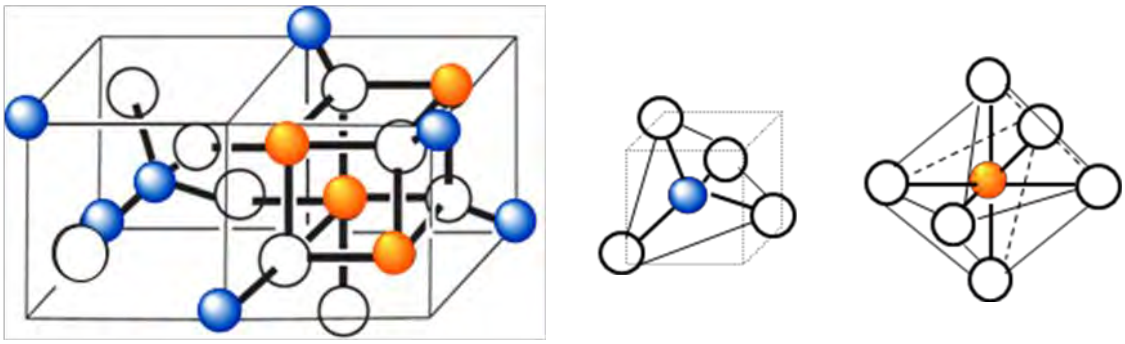

(a) (b) (c)

Figure 1: (a) Model of spinel $AB_2O_4$ structure (b) Model of tetrahedral sites in the spinel (c) Model of octahedral site in the spinel.

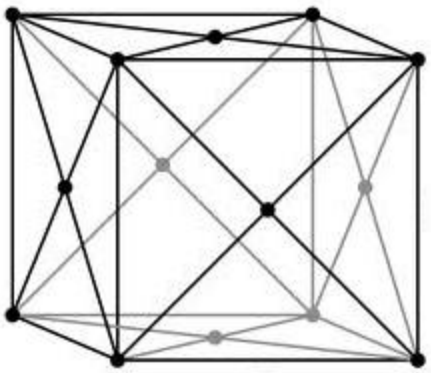

Figure 2: In a Face Centered Cubic (FCC) lattice the atoms are arranged at the corners and center of each cube face of the cell.

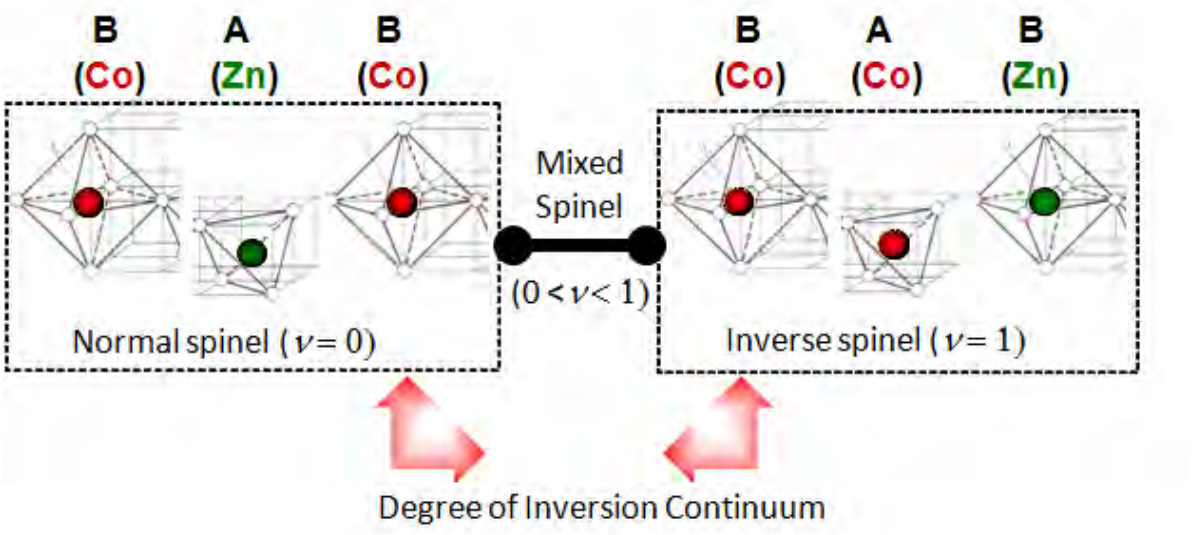


Figure 3: Representation of normal and inverse spinel of a $ZnCo_2O_4$. In the normal spinel Zn atom is in tetrahedral site and both Co atoms are in octahedral sites. For the inverse spinel, Zn is in octahedral site and atoms of Co are in tetrahedral and octahedral sites.

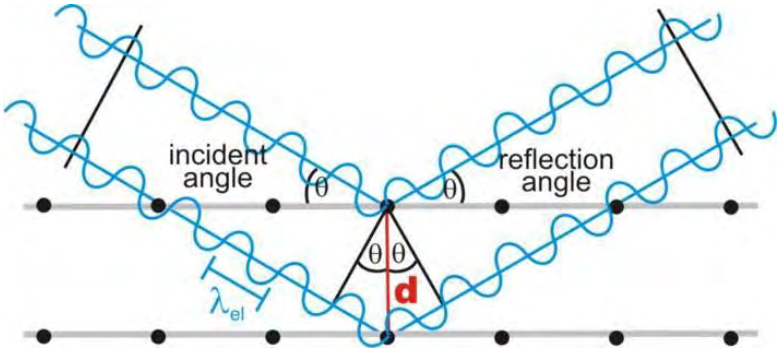


Figure 4: Model of Bragg's Law. Blue lines indicates the X-ray beamed and diffracted. θ is the angle formed by the diffraction, *d* is the distance between the atoms plate

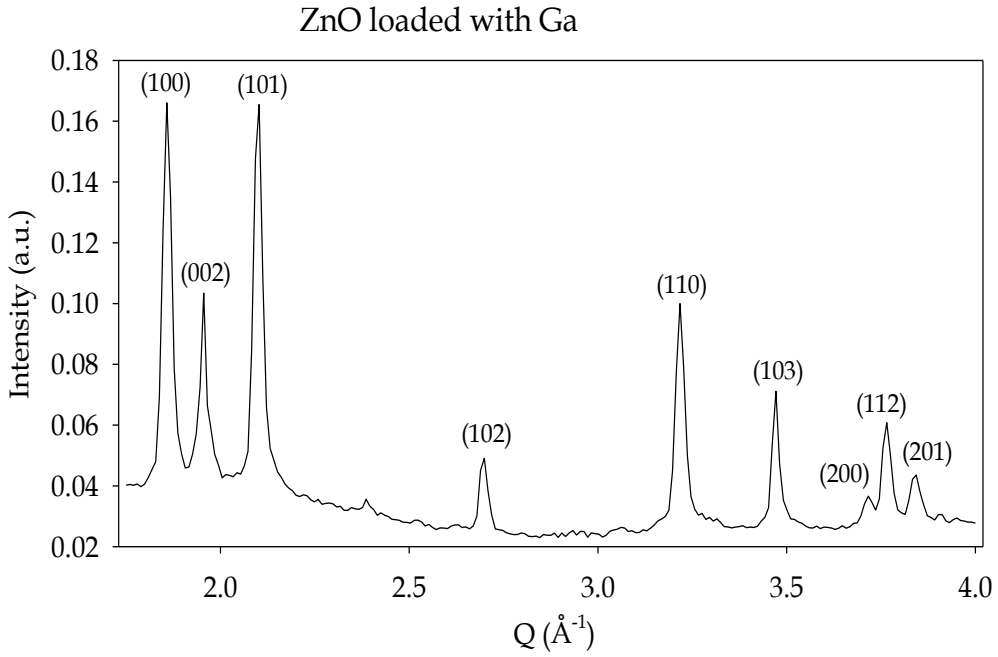


Figure 5: X-ray diffraction pattern for ZnO. The peak (100) is analyzed using Origin software.

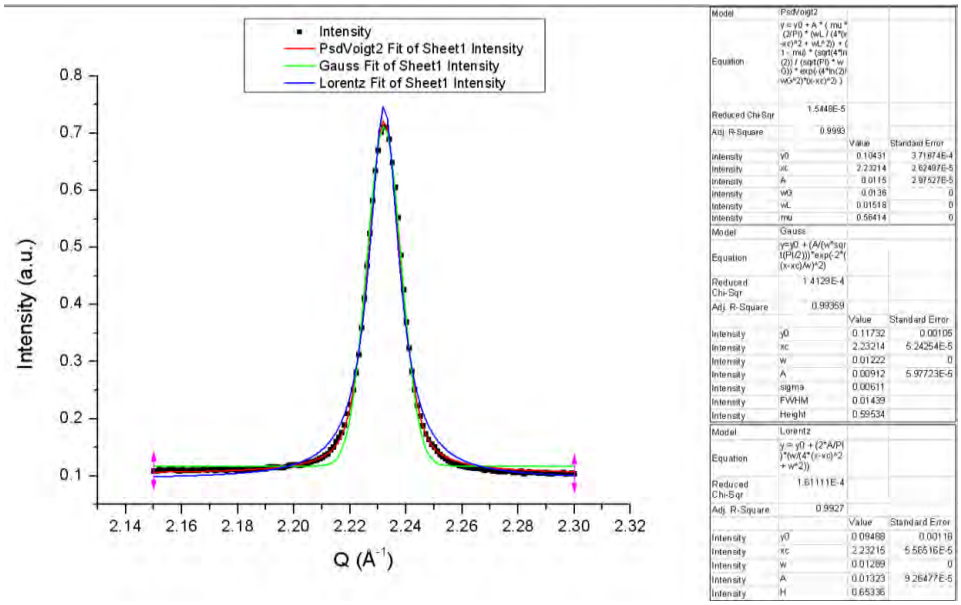


Figure 6: Fitting of peak (100) for scan 90 of ZnO. Red line indicate the fiiting using Pseudo Voigt function, green line indicates the fitting using Gauss function, and blue line indicate the fitting using Lorentz function.

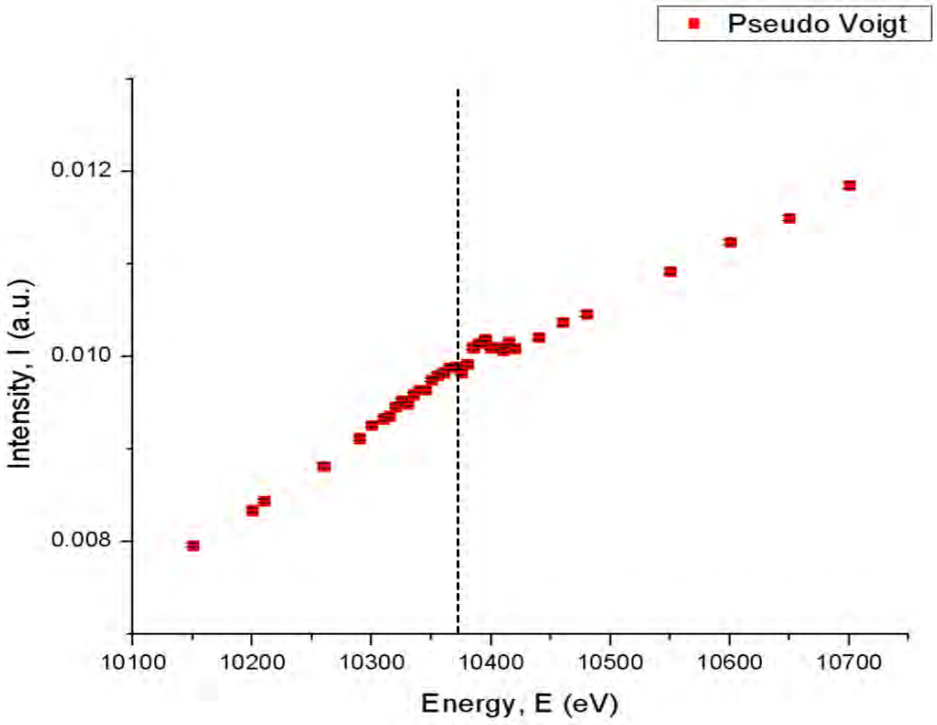


Figure 7: Graph of integrated intensity as a function of X-ray energy. Dashed line indicate Ga absorption edge at 10367 eV.

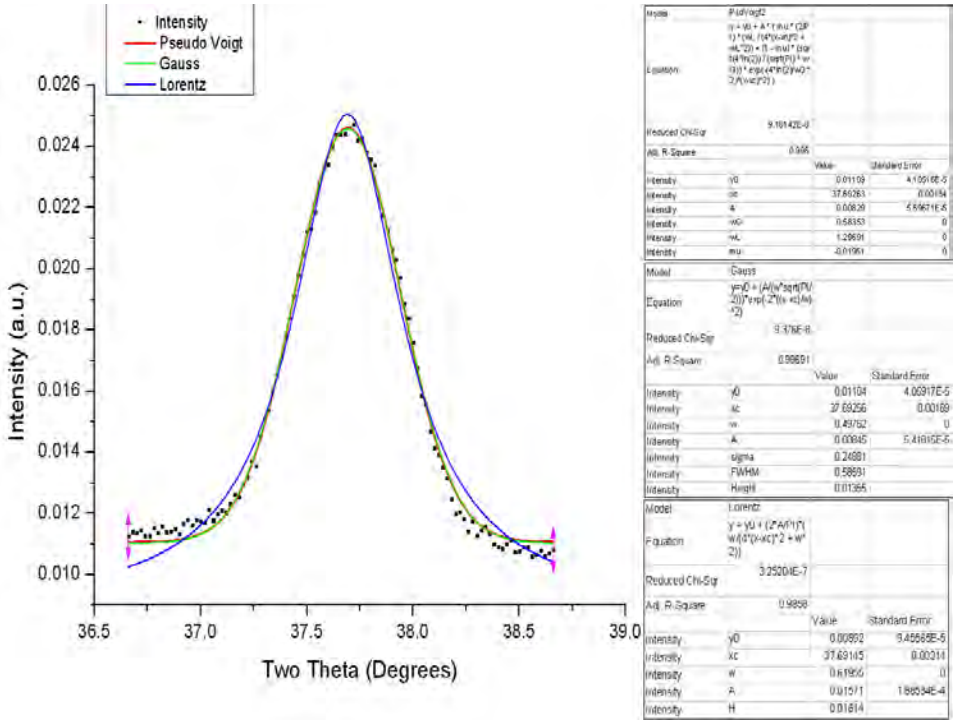


Figure 8: Fitting of peak (311) for scan 90 of $ZnCo_2O_4$ spinel. Red line indicate the fiiting using Pseudo Voigt function, green line indicates the fitting using Gauss function, and blue line indicate the fitting using Lorentz function.

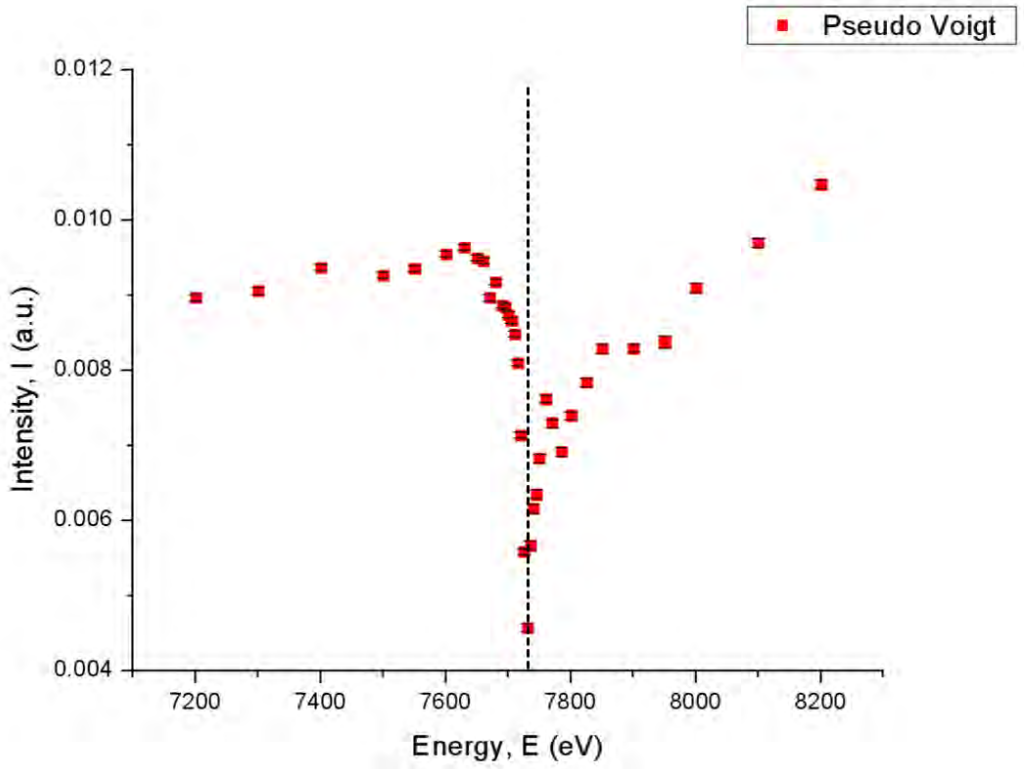


Figure 9: Graph of integrated intensity as a function of X-ray energy. Dashed line indicate Co absorption edge at 7709 eV.

# Investigation of novel decay $B^+ \rightarrow \psi(2S)\omega K^+$ at BaBar

Jacob Schalch

Office of Science, Science Undergraduate Laboratory Internship (SULI)
Oberlin College
SLAC National Accelerator Laboratory
Stanford, CA

August 18, 2010

Prepared in partial fulfillment of the requirements of the Office of Science, Department of Energy's Science Undergraduate Laboratory Internship under the supervision of Arafat Gabareen Mokhtar at the BaBar Collaboration, SLAC National Laboratory. I would like to thank the United States Department of Energy, the SLAC National Accelerator Laboratory, and the directors and administrators of the SULI internship program for making this research possible. I would also like to thank his mentor Arafat Mokhtar as well as the entire SULI community.

Participant:_____

Research Adviser:_____

Work supported in part by US Department of Energy contract DE-AC02-76SF00515.

# Table of Contents

## I. Abstract

We investigate the undocumented B meson decay, $B^+ \rightarrow \psi(2S)\omega K^+$. The data were collected with the BaBar detector at the SLAC PEP-II asymmetric-energy $e^+e^-$ collier operating at the $\gamma(4S)$ resonance, a center-of-mass energy of 10.58 GeV/$c^2$[1]. The $\gamma(4S)$ resonance primarily decays to pairs of B-mesons.

## II. Introduction

The BaBar collaboration at the PEP-II ring was located at the SLAC National Accelerator Laboratory and was designed to study the collisions of positrons and electrons. The $e^-$ $e^+$ pairs collide at asymmetric energies, resulting in a center of mass which is traveling at relativistic speeds. The resulting time dilation allows the decaying particles to travel large distances through the detector before undergoing their rapid decays, a process that occurs in the in the center of mass frame over extremely small distances. As they travel through silicon vertex trackers, a drift chamber, a Cerenkov radiation detector and finally an electromagnetic calorimeter, we measure the charge, energy, momentum, and particle identification in order to reconstruct the decays that have occurred.

While all well understood mesons currently fall into the qq model, the quark model has no a priori exclusion of higher configuration states such as qqqq which has led experimentalists and theorists alike to seek evidence supporting the existence of such states. Currently, there are hundreds of known decay modes of the B mesons cataloged by the Particle Data Group, but collectively they only account for approximately 60% of the B branching fraction and it is possible that many more exist [2].

In this note we attempt to establish evidence for a novel B meson decay mode $B^+ \rightarrow \psi(2S)\omega K^+$. We examine resonant features in the energy regimes of the B-meson itself (5.279 GeV/$c^2$), the ω-meson (0.782 GeV/$c^2$), and the ψ(2S)-meson (3.686 GeV/$c^2$). The ψ(2S) is reconstructed in this analysis in four decay modes: ψ(2S): $\psi(2S)\rightarrow e^+e^-$, $\psi(2S)\rightarrow \mu^+\mu^-$, $\psi(2S)\rightarrow J/\psi(\mu^+\mu^-)\pi^+\pi^-$, and $\psi(2S)\rightarrow J/\psi(e^+e^-)\pi^+\pi^-$

[3]. The first two have low branching fractions, (0.752±0.017% and 0.75±0.05% respectively). The latter two have significantly higher branching fractions, (both 1.93±0.06%)[3]. Note that in this analysis, the use of charge conjugated reactions is implied, so we analyze $B^- \rightarrow \psi(2S)\omega K^-$ along with $B^+ \rightarrow \psi(2S)\omega K^+$.

## III. Methods

Events were selected for the presence of significant signals at the B, ψ(2S) and ω resonances. Primarily we are searching for structure in the ψ(2S)ω mass range. While we are looking for a direct three body decays, structure in the ψ(2S)ω invariant mass would suggest that this is instead a two body decay, first decaying $B^+ \rightarrow XK^+$ and then $X \rightarrow \psi(2S)\omega$, where X represents an intermediate state. While we identify the Kaon (K), the $B^+$ , ψ(2S), and ω must be observed indirectly, through their decay products. To improve the $B^+$ mass resolution we use the energy substituted mass, $m_{ES}$, which uses the beam energy information to reconstruct the mass of the $B^+$ meson[4].

In order to quantitatively analyze these events, first attempt to determine an instrument resolution function as a function of energy and its most accurate parametrization. This enables us to determine which portion of our signal width is attributable to instrument resolution limitations, and which are actual signal. Furthermore, we perform additional fits to parametrize the background and measure the signal size in the resonant ranges of interest. We utilize ROOT, a robust, software package designed specifically for high energy physics data analysis.

The selection criterion for the B-signal is shown in Table 1. To extract the B-signal, we fit $m_{ES}$. For the background contamination, we use an Argus function while for the signal we use a single Gaussian function. The total number of B-candidates from the fit is 138±25. The fit of the $m_{ES}$ is shown in Figure 1, and a satisfactory fit is observed.

In order to examine ω events, we examine the 3π-mass distribution. The 3π-mass distribution is

fitted with a polynomial background function and a Breit Wigner function convolved with a Gaussian resolution function for the signal. The signal size is 240±45 events. Note that we assumed 10 MeV/$c^2$ resolution when fitting the 3π-mass distribution. The histogram and fit of the 3π-mass distribution is shown in figure 2.

The selection criterion for the ψ(2S)-meson are shown in Table 2. Figure 3 shows the mass of dileptons, and $J/\psi\pi^+\pi^-$, for the decays of the ψ(2S) meson. In all decays, clear ψ(2S)mass resonances are observed. A summed histogram of these contributions represents the total ψ(2S) signal and is shown in Figure 4.

**V. Results and Conclusion**

We performed fits for two histograms: one at the $m_{3\pi}$ invariant mass, and one in the energy substituted mass, $m_{ES.}$ We examine four histograms in the region of common decays of the ψ(2S) meson. There is a one-to-one correlation between the B-signal (i.e. $m_{ES}$ signal), ψ(2S)-signal, and ω-signal. As such, the number of signal events in all distributions should be similar[5].

We have searched for the decay of $B^+ \rightarrow \psi(2S)\omega K^+$ using the full BaBar data sample. Clear signal in $B^+$, ψ(2S), and ω-mesons were observed. Therefore, we found definite evidence for this novel decay mode. This result is new and will be added to the Particle Data Group list of B-meson decay modes. No new structure has been observed in the ψ(2S)ω mass distribution.

## VI. Tables and Figures

| Selection Category | Criterion |
|---|---|
| $J/\psi \to \mu^+\mu^-$ mass ( GeV/$c^2$) | $3.06 < m_{\mu\mu} < 3.14$ |
| $J/\psi \to e^+e^-$ mass ( GeV/$c^2$) | $2.95 < m_{ee} < 3.14$ |
| $K_S$ mass ( GeV/$c^2$) | $0.472 < m_{\pi\pi} < 0.522$ |
| $\pi^0$ mass ( GeV/$c^2$) | $0.115 < m_{\gamma\gamma} < 0.150$ |
| $\omega$ signal region ( GeV/$c^2$) ($B^+$) | $0.7695 < m_{3\pi} < 0.7965$ |
| $\omega$ signal region ( GeV/$c^2$) ($B^0$) | $0.7605 < m_{3\pi} < 0.8055$ |
| $\Delta E$ ( GeV) ($B^+$) | $\lvert\Delta E\rvert < 0.020$ |
| $\Delta E$ ( GeV) ($B^0$) | $\lvert\Delta E\rvert < 0.015$ |
| $m_{ES}$ ( GeV/$c^2$) | $5.274 < m_{ES} < 5.284$ |
| B helicity angle $\theta_B$ | $\lvert\cos\theta_B\rvert < 0.9$ |
| Photon helicity angle $\theta_\gamma$ | $\cos\theta_\gamma < 0.95$ |
| $\psi\,(2S)$ veto ( GeV/$c^2$) | $3.661 < M_{J/\psi\pi\pi} < 3.711$ |

Table 1. Principal criteria used to select B candidates [5]

| Selection Category | criterion |
|---|---|
| $\psi(2S) \to e^+e^-$ | $3.44 < m_{e^+e^-} < 3.74$ GeV/$c^2$ |
| $\psi(2S) \to \mu^+\mu^-$ | $3.655 < m_{\mu^+\mu^-} < 3.715$ GeV/$c^2$ |
| $\psi(2S) \to J/\psi(e^+e^-)\pi^+\pi^-$ | $3.64 < m_{J/\psi(e^+e^-)\pi^+\pi^-} < 3.74$ GeV/$c^2$ |
| $\psi(2S) \to J/\psi(\mu^+\mu^-)\pi^+\pi^-$ | $3.655 < m_{J/\psi(\mu^+\mu^-)\pi^+\pi^-} < 3.715$ GeV/$c^2$ |

Table 2. For decay modes with ψ(2S) in the final state, in addition to the selection criteria in table 1, we apply the mass requirements shown above in table 3[5].

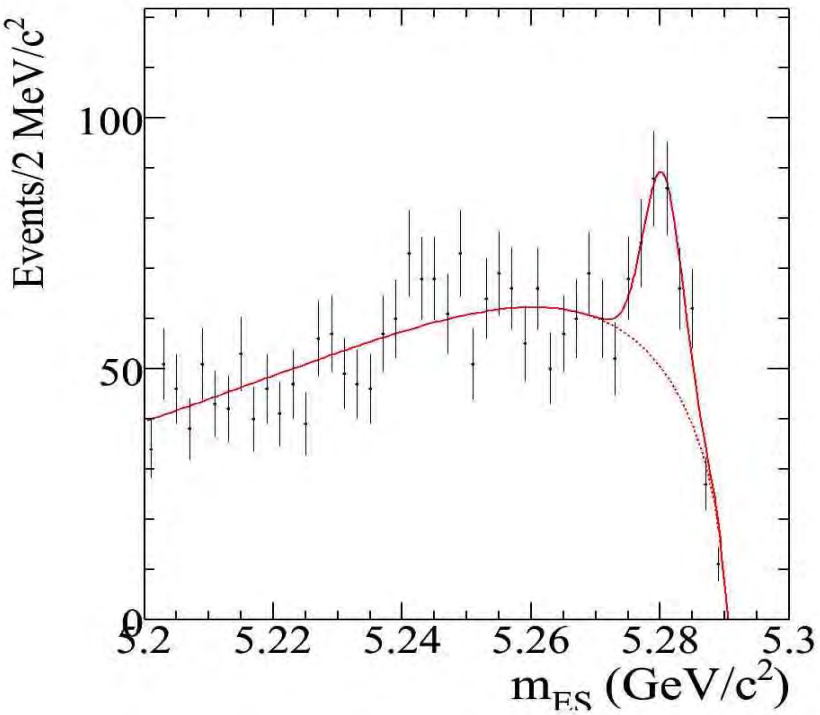


Figure 1. A fit of the B meson resonant feature near the kinematic limit. The data are shown by the filled circles and the solid (dotted) line shows the fit result of the fit (background).

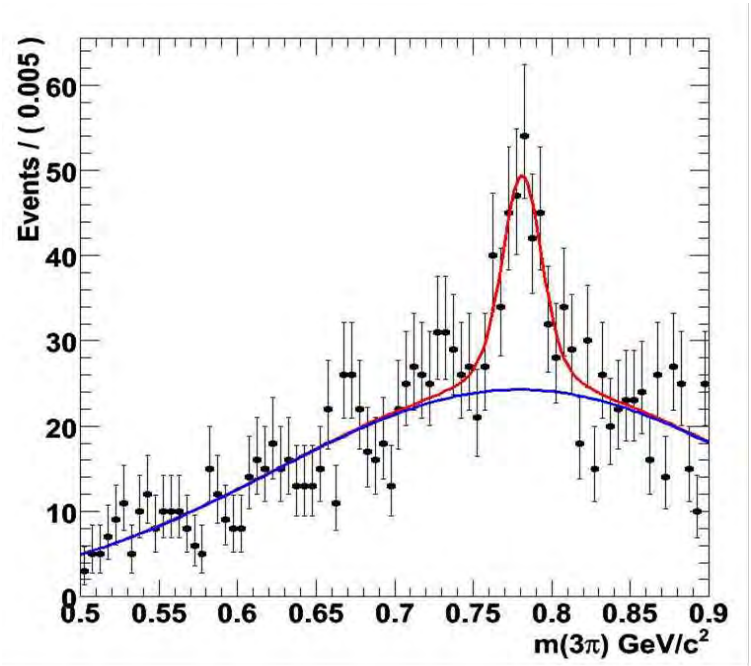


Figure 2. The 3π mass distribution for the events of $B^+ \to \psi(2S)\omega K^+$. The filled circles show the data points and the red curve stands for the fit result. The blue curve represents the background contamination in the fit.

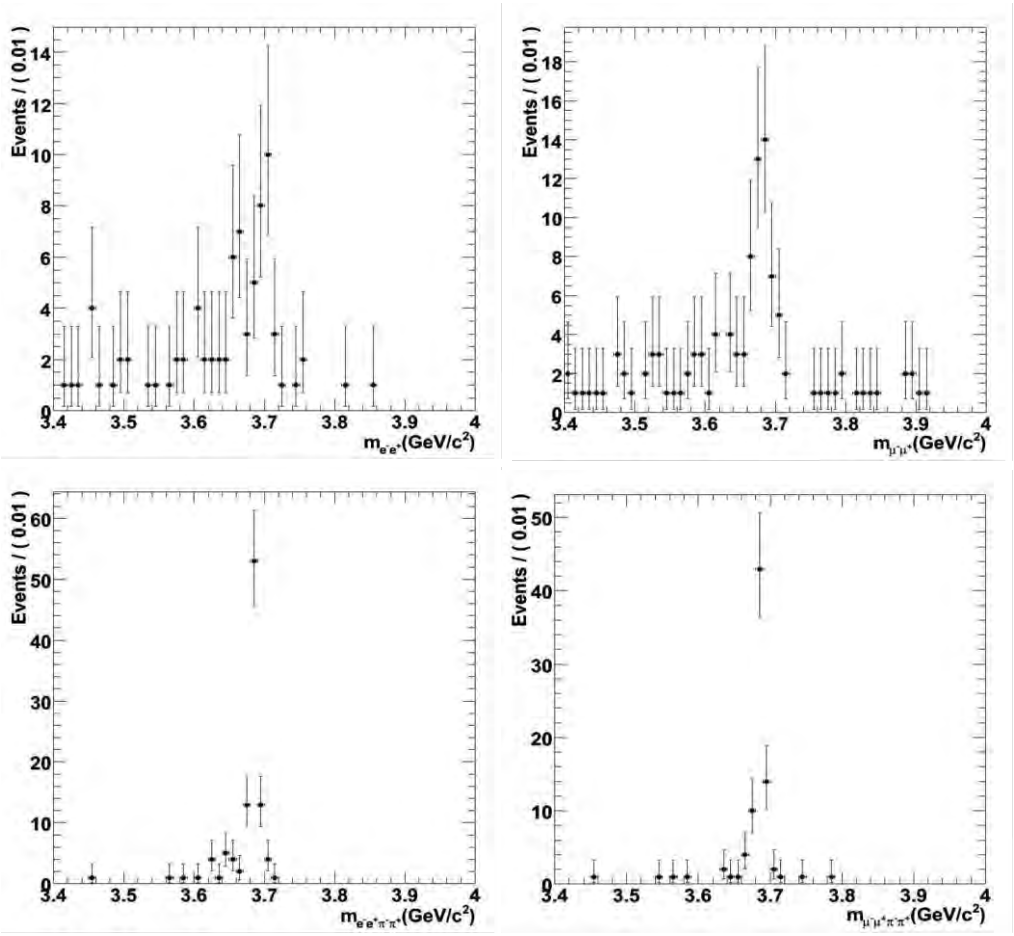


Figure 3. Histograms of the four measured contributions to the ψ(2S) resonance clockwise from the top left, the first histogram corresponds to $\psi(2S)\rightarrow e^+e^-$, the second to $\psi(2S)\rightarrow \mu^+\mu^-$, the third $\psi(2S)\rightarrow J/\psi(e^+e^-)\pi^+\pi^-$. and the last to $\psi(2S)\rightarrow J/\psi(\mu^+\mu^-)\pi^+\pi^-$.

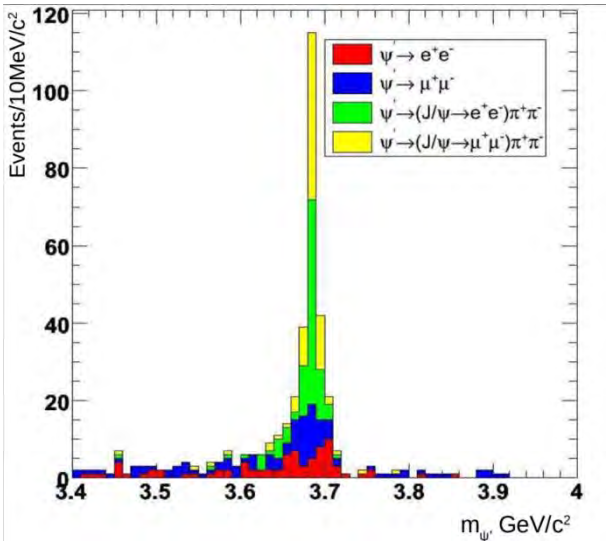


Figure 4. A summed histogram of events from four contributing ψ(2S) decay modes.

## VII. References


[1] B. Aubert, et al. Search for the $Z(4430)^-$ at BaBar. *Phys. Rev. D79*, 112001, 2009.

[2] P. del Amo Sanchez, et al. Evidence for the decay $X(3872) \rightarrow J/\psi\omega$. Hep-ex: 1005.5190, 1 Jun 2009.

[3] C. Amsler, et al. Review of particle physics. *Physics Letters* B. 667,1. 2008.

[4] S. Godfrey and N. Isgur. Mesons in relativized quark model with chromodynamics. *Phys. Rev. D.* 32:1, 1 July 1985.

[5] A. Mokhtar. Search for new X(3872) decay modes at BaBar. *BaBar Analysis Document.* 1978.5, 13 April, 2010. (internal document)

# Bi-Plasma Interactions on Femtosecond Time-Scales

Emily A. Sprague
Office of Science, Science Undergraduate Laboratory Internship Program

University of Illinois
Urbana-Champaign, IL

SLAC National Accelerator Laboratory
Menlo Park, CA

July 21, 2010

Prepared in partial fulfillment of the requirements of the Office of Science, Department of Energy's Science Undergraduate Laboratory Internship under the direction of Aaron Lindenberg at the PULSE Institute for Ultrafast Energy Science, Stanford Linear Accelerator Center.

Participant: _____
Signature

Research Advisor: _____
Signature

Work supported in part by US Department of Energy contract DE-AC02-76SF00515.

## TABLE OF CONTENTS

**ABSTRACT**

Bi-plasma interactions on femtosecond time-scales. EMILY SPRAGUE (University of Illinois, Urbana-Champaign, IL 61801) AARON LINDENBERG (PULSE Institute for Ultrafast Energy Science, Stanford Linear Accelerator Center, Stanford, CA 94025)

Ultrafast THz radiation has important applications in materials science studies, such as characterizing transport properties, studying the vibrational response of materials, and in recent years, controlling materials and elucidating their response in intense electromagnetic fields. THz fields can be generated in a lab setting using various plasma-based techniques. This study seeks to examine the interaction of two plasmas in order to better understand the fundamental physics associated with femtosecond filamentation processes and to achieve more efficient THz generation in a lab setting. The intensity of fluorescence in the region of overlap was measured as a function of polarization, power, and relative time delay of the two plasma-generating laser beams. Results of time dependent intensity studies indicate strikingly similar behaviors across polarizations and power levels; a sudden intensity spike was observed at time-zero, followed by a secondary maxima and subsequent decay to the initial plasma intensity. Dependence of the intensity on the power through either beam arm was also observed. Spectral studies of the enhanced emission were also carried out. Although this physical phenomenon is still not fully understood, future studies, including further spectral analysis of the fluorescence overlap, could yield new insight into the ultrafast processes occurring at the intersection of femtosecond filaments, and would provide a better understanding of the mechanisms for enhanced THz production.

## INTRODUCTION

Terahertz radiation comprises electro-magnetic waves with frequencies on the order of $10^{12}$ Hz. Their low photon energies (~25 meV) allow them to penetrate non-conducting material or objects. Additionally, THz fields, as a form of non-ionizing radiation, could potentially replace x-rays as a structural probe. Applications of this type of radiation extend to areas such as medical imaging, security, and atomic spectroscopy.

Researchers at SLAC National Accelerator Laboratory‟s PULSE Institute are currently working to produce intense half-cycle terahertz pulses which turn on and off in hundreds of femtoseconds. This radiation will potentially be used in all-optical studies of materials as it allows biasing in materials without the use of electrodes. This experiment examines the interaction of two plasmas generated by femtosecond pulses in order to better understand unexplored processes at the intersection of two femtosecond filaments, and how to make more efficient strong-field, intense, terahertz beams in a lab-scale situation.

### *i. Terahertz Production*

To date, there are four broad categories of plasma-based THz generation techniques [1]. The first technique utilizes the radial acceleration of ionized electrons in a radial intensity gradient produced by an optical beam. Due to the ponderomotive force, this results in a conical THz emission at a given angle to the pulse propagation. A second method uses focused few-cycle pulses with under 10 fs durations to generate THz emission [1].

Of all the techniques, most attention has been directed toward the AC-bias and DC-bias methods. A typical experimental setup for both the AC-bias and DC-bias method consists of an incoming beam that is then split by a beam-splitter into two beam arms. In the Auston switch

approach, a DC-bias is applied to the plasma which generates a transverse external polarization, which results in around an order-of-magnitude THz field increase. The AC-bias approach also produces a transverse polarization, but without electrodes. Instead, a superposition of fundamental and second-harmonic pulse fields is used in order to produce a time-dependent current in the plasma region. Mixing the fundamental and second-harmonic fields allows for efficient THz generation; because one of the laser frequencies is an integer multiple of the other one, the net current as a result does not vanish over an entire set of cycles [2]. Consequently, by utilizing a focused, short pulse and four-wave mixing of the fundamental and second harmonic waves, electric fields with higher amplitudes can be generated [3]. Our experiment grew out of observations we made while employing the AC-bias approach.

There are several factors that influence the optimization of THz generation in the AC-bias approach. In order for the second harmonic wave to produce a maximum polarization asymmetry, it must possess a certain phase shift relative to the fundamental harmonic wave. The exact temporal overlap of the two pulses also contributes to maximum THz generation. Additionally, the polarization of the fundamental and second-harmonic waves heavily impacts the strength and polarization of the resulting THz wave [1]. The amplitude and the polarization of the resulting electrical current depends directly on the relative phase between the fundamental and second harmonic waves [4].

*ii. Femtosecond Laser Pulses*

Ultrafast pulses are commonly created by using mode-locked oscillators and are used in the production of plasma. One of the most-widely used tunable femtosecond laser sources is the Ti:sapphire amplifier. The Ti:sapphire crystal lases between the wavelengths of

680 nm to 1130 nm, which is the largest tuning range of any laser in this class. The shape of each of those femtosecond pulses can be described using a Gaussian function.

Fourier analysis shows that femtosecond laser pulses can only be generated with a broad spectral bandwidth. The minimum "transform-limited" duration of a pulse can be calculated for a given spectrum and central wavelength. To optimize a femtosecond pulse, the bandwidth and chirp must be considered. Both minimal chirp and large bandwidth are considered ideal. The chirp of a pulse refers to its spectral content and the bandwidth refers to the range of frequency. In this experiment, we used 1 mJ pulses centered at 800 nm with a pulse duration measured to be 44 fs using single-shot autocorrelation.

*iii. Kerr Lens Mode-locking*

A free-running laser simultaneously oscillates over all of the resonant frequencies in a given cavity producing continuous wave radiation at a narrow wavelength. To create trains of very short and intense light pulse, the laser is mode-locked. Mode-locking forces all of the modes, which are a set of frequencies, to have equal phase by introducing a disturbance to the system. This results in the constructive interference of all the different frequency waves at one point, producing a very intense and extremely short spike or a „pulse". There are two methods of mode-locking femtosecond lasers: passive mode-locking and active mode-locking. Active mode-locking requires modulation of the laser that is generated from an external clock source; however, passive mode-locking does not require an external clock, instead it requires the movement of a non-linear device within the cavity (e.g. moving a prism in or out of the cavity).

*iv. Plasma Filamentation*

Plasma, considered to be the most abundant state of matter, comprises ionized gas particles. Due to the presence of an abundance of charge carriers, plasma interacts easily with surrounding electromagnetic fields. Plasma can be formed through photoionization where photons from an external source, such as a laser, are absorbed by a gas, such as air, resulting in cations and emitted electrons. The intensity of THz radiation generated from plasma formation is dependent on the length and density of the plasma. Additionally, the beam profile and divergence of the THz radiation depend on the focal length of the lenses used [1].

## MATERIALS AND METHODS

*i. Setup*

Figure 1 shows the setup used consisting of lenses, mirrors, and beam-splitters. The lab setup mirrors previous bi-plasma crossing experiments performed in our lab [5]. 44 fs, 800 nm laser pulses generated by a passively mode-locked Ti:sapphire laser were split by a polarizing beam-splitter, which produced a horizontally (or p) polarized beam down arm 1 and a vertically (or s) polarized beam down arm 2. One of the laser pulses was focused by a f=100 mm lens, which generated a short plasma (P1) in air. The other laser pulse was focused by a f=200 mm lens to create a longer orthogonal plasma (P2) that crosses the beam path of the first plasma. A delay stage controlled the relative distance and the time between the arrival of the two plasmas. A CCD camera, with a lens of working distance ~5mm, mounted about 1.5 inches above the intersection of the plasma, was used to image the bi-plasma fluorescence phenomenon. Additionally, ND filters were placed in between the plasma region and the camera lens in order to increase the contrast ratio and prevent camera saturation between the plasma and background pixels.

*ii. Studies*

Much of the fundamental physics regarding the processes that occur within this plasma intersection remain unclear. At the intersection, for at least 20 picoseconds after time-zero, the photons from the lagging laser beam interact with the preformed plasma from the earlier laser beam. When both incoming beams spatially and temporally overlap, also referred to as time -zero, the resulting interaction produces an increase of intensity, surprisingly. We hypothesize that this is due to one of two effects: scatter during the reflected plasma lifetime or enhanced tunneling ionization.

Several experiments were set up to better understand the plasma in this area of overlap. In all scans, the dependence of the intensity of the fluorescent light as a function of time was studied. We varied the relative angle of polarization of the two incoming beams. Three configurations were used: s-s polarized, s-p polarized, and p-p polarized, as shown in Figure 2. To change the polarization of a beam path from s to p polarized, or vise versa, a half-wave plate was used. In the s-s polarization tests, both beam 1 and beam 2 were polarized in two different horizontal directions within the plane of propagation. For the s-p polarization, only beam 1 was horizontally polarized while beam 2 was vertically polarized. The p-p polarization contained both vertically polarized beams.

Additionally, a separate study was conducted using a blue bandpass filter, which blocks 800 nm and surrounding wavelengths of light, in order to characterize the properties of the fluorescence in the region of overlap. Similar time dependent intensity tests were performed using this setup in an attempt to distinguish between two known effects: scattering or tunneling ionization.

*iii. Data Analysis*

Data in this experiment was acquired using a home-built setup. For time dependent intensity studies, the camera images of the plasmas were analyzed using image processing techniques with the programs ImageJ and Matlab. Peak intensity data were averaged over 400-500 pixels at the plasma intersection, where each pixel had a diameter of 2.6 um. Background noise was subtracted from each pixel in the plasma intersection. Intensities were plotted as a function of increasing time.

**RESULTS**

Plasma filamentation and the fluorescent area of bi-plasma intersection were observed in the lab (Figure 3). Figure 4 shows three primary events in this plasma-crossing experiment: before time-zero, at time-zero or the primary intensity maxima, after time-zero at the secondary intensity maxima. A sudden and very dramatic fluorescence was observed at time-zero when both plasmas intersected, as can be seen in Figure 4. This peak intensity in the overlap region at time-zero was followed by a secondary burst of intensity about 30 ps later. Figure 5 shows the time-resolved traces for the peak intensities of the s-s, s-p, and p-p polarization sets. Observing across polarization sets, the peak intensity and point of decay consistently occur at the same time values regardless of the polarization or power of the incoming beams: 135 counts for peak intensity and ~177 counts for decay. Additionally, the time required for the intensity of the second peak to decay to the initial intensity was constant across all polarizations (~50 steps). All power levels and polarization sets experienced a full decay back to the starting intensities. No valuable data was obtained below a power of 250 mW in either beam path. The peak intensity at a given power level was always strongest for s-p polarizations and weakest for p-p polarizations.

The data exhibits interesting trends that depend on the relative power of either beam path. For example, the slope of the decay seems to decrease with decreasing power in the stationary arm. Also, the ratio of the peak intensity to background level intensity seems to decrease with increasing power in the delay arm (beam 1). This trend can be seen in Figure 6 for both the s-p and p-p polarizations; however, when examining the data for the s-s polarization, we noticed a direct rather than an inverse relationship exists between the intensity ratio and the power through the delay arm. In addition, similar trends exist in the ratio of the intensity of the secondary maxima to the background level.

Studies concerning the spectral properties of the fluorescent overlap region yielded interesting results. As shown in Figure 7, the time dependent intensity traces for data taken, with and without a blue bandpass filter, appear to be very similar in both overall shape and absolute values. Figure 8 displays camera images taken without any filter (ND or bluepass). Interestingly, secondary plasmas can be seen along the corners of the overlapping region as indicated in red. These secondary plasmas produce the same intensity level as the region of bi-plasma overlap. Additional interesting behavior can be seen in Figure 9, in which the fluorescent region of overlap appears to rotate clockwise through time.

## CONCLUSIONS

Although the data in this experiment is still preliminary, we can still infer some interesting conclusions propose direction for future studies. The images in Figure 9 show a wavefront disturbance. The time dependent intensity trace displays identical general behavior regardless of polarization and power through either beam arm. Although relative intensities vary among tests, the data always exhibits a dramatic spike at time-zero, followed by a secondary maxima and subsequent decay back to the starting intensity. The origin of this unexpected spike in intensity at time-zero is still not fully understood; however, data from the blue bandpass filter tests indicate that the processes governing the bi-plasma overlap likely result from an enhanced tunneling ionization process as opposed to scattering. Because the two traces (representing data taken with a blue bandpass filter and that taken without a blue bandpass filter) are almost identical, we can infer that the spike in intensity is not primarily due to 800 nm light, as the blue bandpass filter acts to block wavelengths of around 800 nm. Additionally, images in Figure 8 indicate that the observed secondary plasmas are likely not due to fluorescence, as shown by the disappearance of these secondary plasmas upon the addition of a blue bandpass filter.

An alternate possibility that could account for this fluorescence is Raman scattering [6]. In this study, Zhao, Witt, and Gordon report energy transfer between two laser beams intersecting at an acute angle. They observe an angular dependence of the fluorescent plasma intersection and a disappearance of the effect when the two incoming beams are orthogonal. Although intriguing, this explanation does not quite fit with the results presented in our study.

Looking at the power dependent polarization data in Figure 6, the linear relationship is not quite understood. The unexpected behavior of the s-s polarization in comparison to the s-p

and p-p polarization plots could perhaps be, in part, due to the constructive interference of both incoming s-polarized fields. Of the three polarization sets, the s-s combination is the only set in which the two incoming fields interfere constructively, which could perhaps give rise to this trend reversal in Figure 6.

In conclusion, by crossing two laser-generated plasma filaments we are able to observe fluorescence in the region of overlap perhaps due to the tunneling ionization effect. This fluorescent behavior through time was consistent across all polarizations and power levels. Future studies will involve detailed spectral analysis of this region using a fiber-coupled spectrometer to obtain the exact distribution and composition of the fluorescent light. By understanding how multiple plasmas interact, we hope to not only better understand ultrafast filamentation processes but also develop more efficient plasma-based methods for generating THz fields in a lab situation.

**ACKNOWLEDGEMENTS**

I would like to thank my mentor Aaron Lindenberg for direction and support. I would also like to thank Dan Daranciang, whom I worked alongside, for his assistance and encouragement. Additionally I would like to thank Haidan Wen for his help. Special thanks to SLAC National Accelerator Laboratory and the United States Department of Energy for this research experience.

## REFERENCES

[1] Thomson, M.D., Kreß M., Loffler T., and Roskos H.G., Broadband THz emission from gas plasmas induced by femtosecond optical pulses: From fundamentals to applications, Laser and Photonics Reviews, **1**, No. 4, 349-368 (2007).

[2] Kim K.Y., Glownia J.H., Taylor A.J., and Rodriguez G., Terahertz emission from ultrafast ionizing air in symmetry-broken laser fields, Optics Express, **15**, No. 8, 4577 (2007).

[3] Bartel T., Gaal P., Reimann K., Woerner M., and Elsaesser T., Generation of single-cycle THz transients with high electric-field amplitudes, Optics Letters, **30**, No. 20, 2805 (2005).

[4] Kim K.Y., Taylor A.J., Glownia J.H., AND Rodriguez G., Coherent control of terahertz supercontinuum generation in ultrafast laser–gas interactions, Nature Photonics, **2**, 605 (2008).

[5] Wen H., Daranciang D., Lindenberg A.M., High-speed all-optical terahertz polarization switching by a transient plasma phase modular, Applied Physics Letters, **96**, 161103 (2010).

[6] Zhao Y., Witt T.E. , and Gordon R. J., Efficient Energy Transfer between Laser Beams by Stimulated Raman Scattering, Physical Review Letters, **103**, 173903 (2009).

**FIGURES**

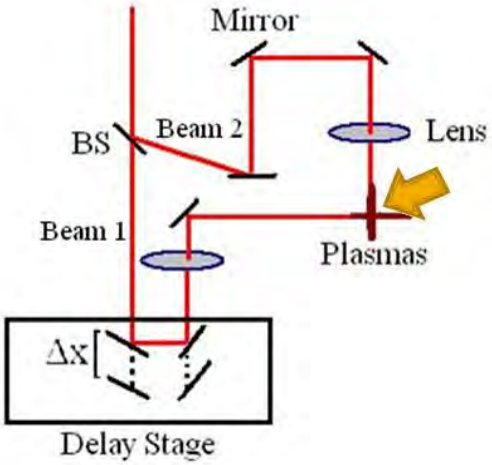


(a)

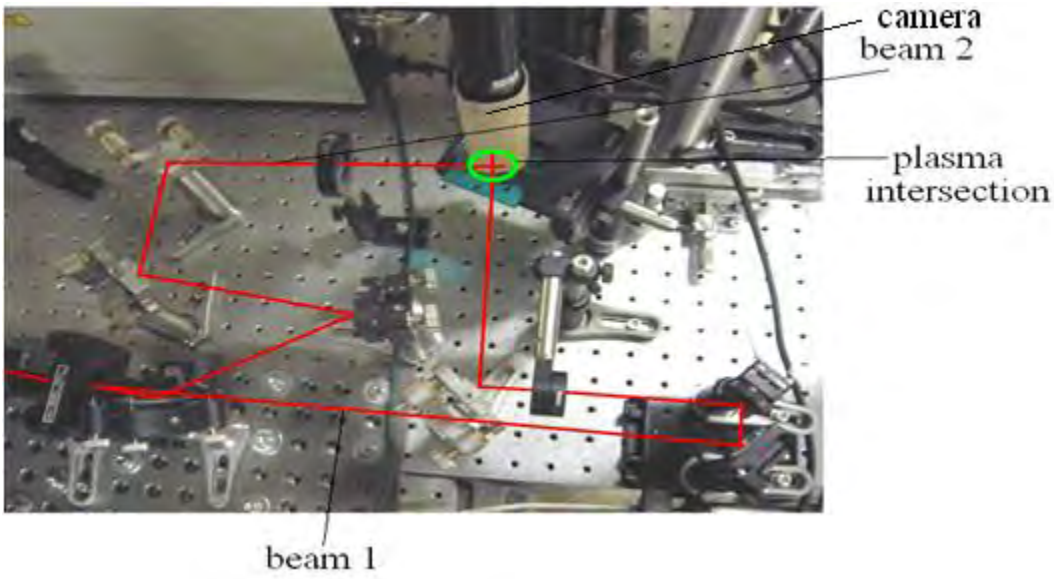


(b)

Figure 1. (a) Schematic of setup consisting of a polarizing beam-splitter, mirrors, lenses, and a delay stage. Yellow arrow indicates position at which bi-plasma phenomenon was observed and placement of CCD camera. (b) Photograph of lab setup with laser beam paths shown in red and plasma intersection in green.

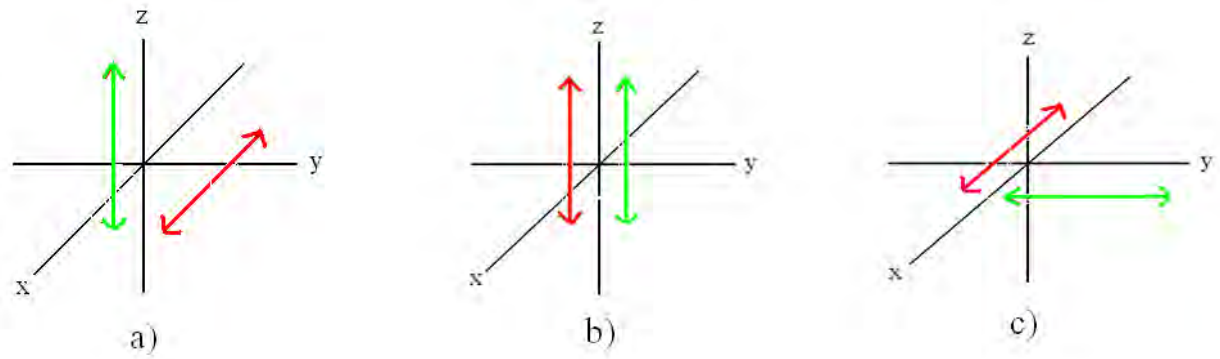


Figure 2. Visual representation of polarization sets for beam 1 and beam 2. a) s-p polarization with one beam vertically polarized and the other beam horizontally polarized. b) s-s polarization with both beams vertically polarized. c) p-p polarization with both beams horizontally polarized in different directions.

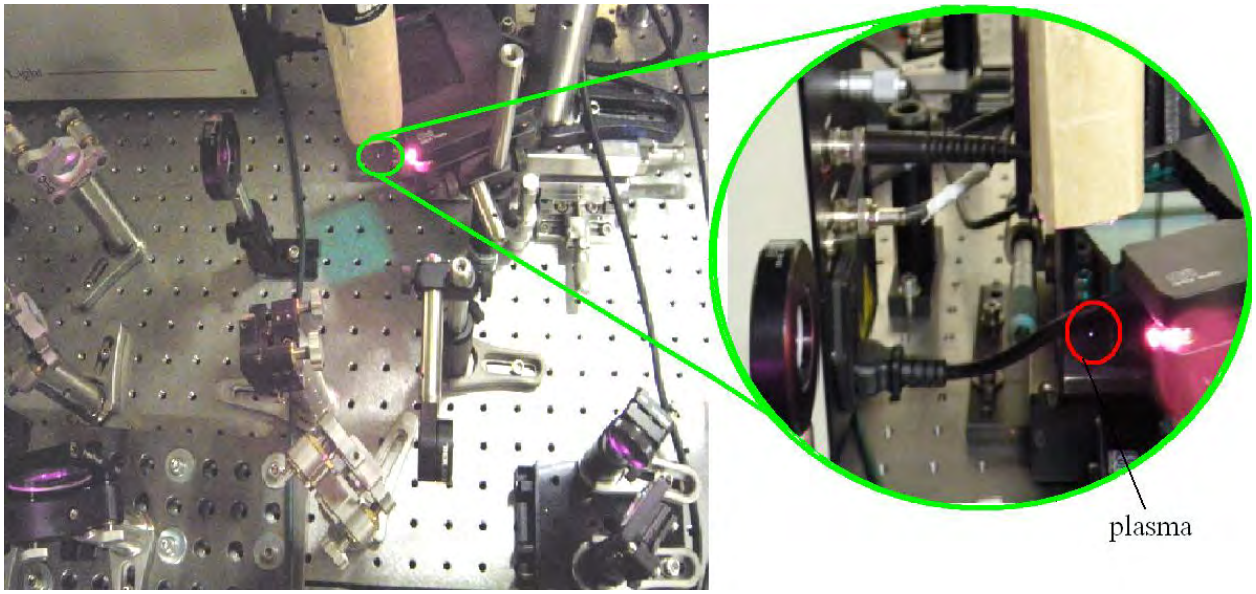


Figure 3. Photograph of plasma filamentation in the lab.

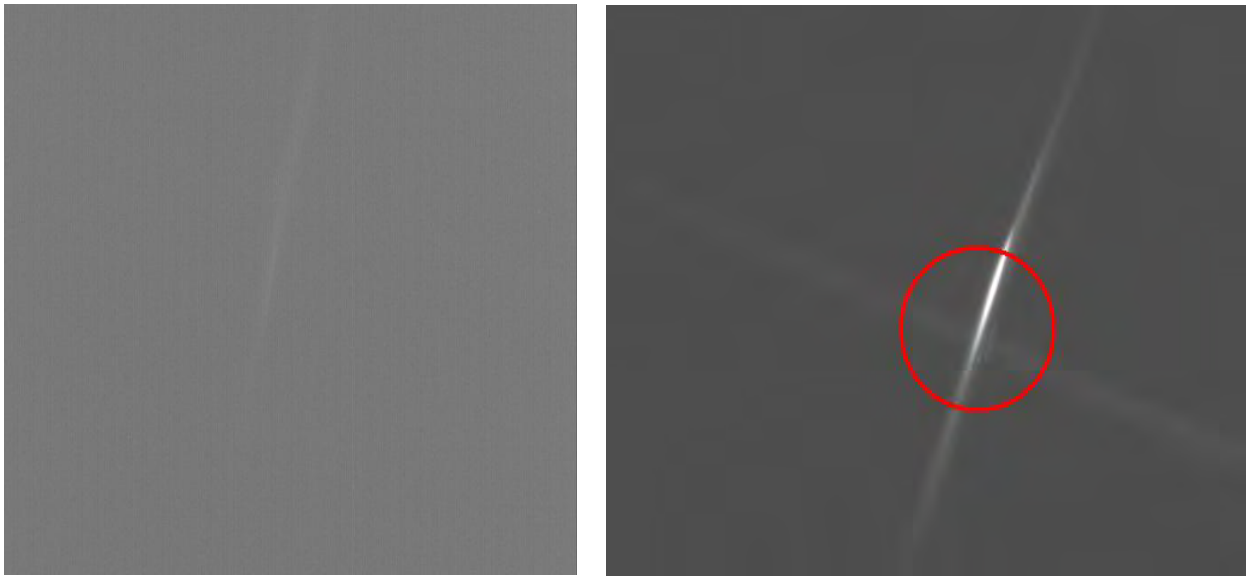

(a) (b)

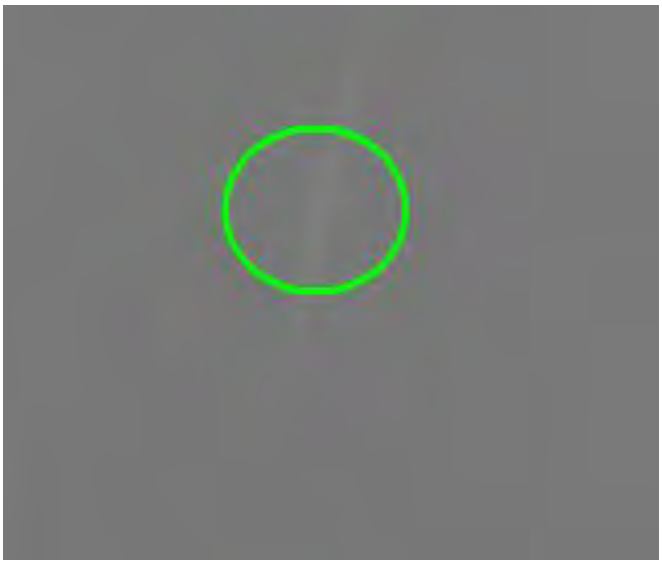

(c)

Figure 4: a) CCD camera image of plasma filaments before overlap. b) Image of plasma filaments intersecting at time-zero. Bright fluorescence is visible at region of overlap, as indicated in red. c) Image of plasma filaments at secondary maxima (after time-zero). Secondary fluorescence is indicated by green circle.

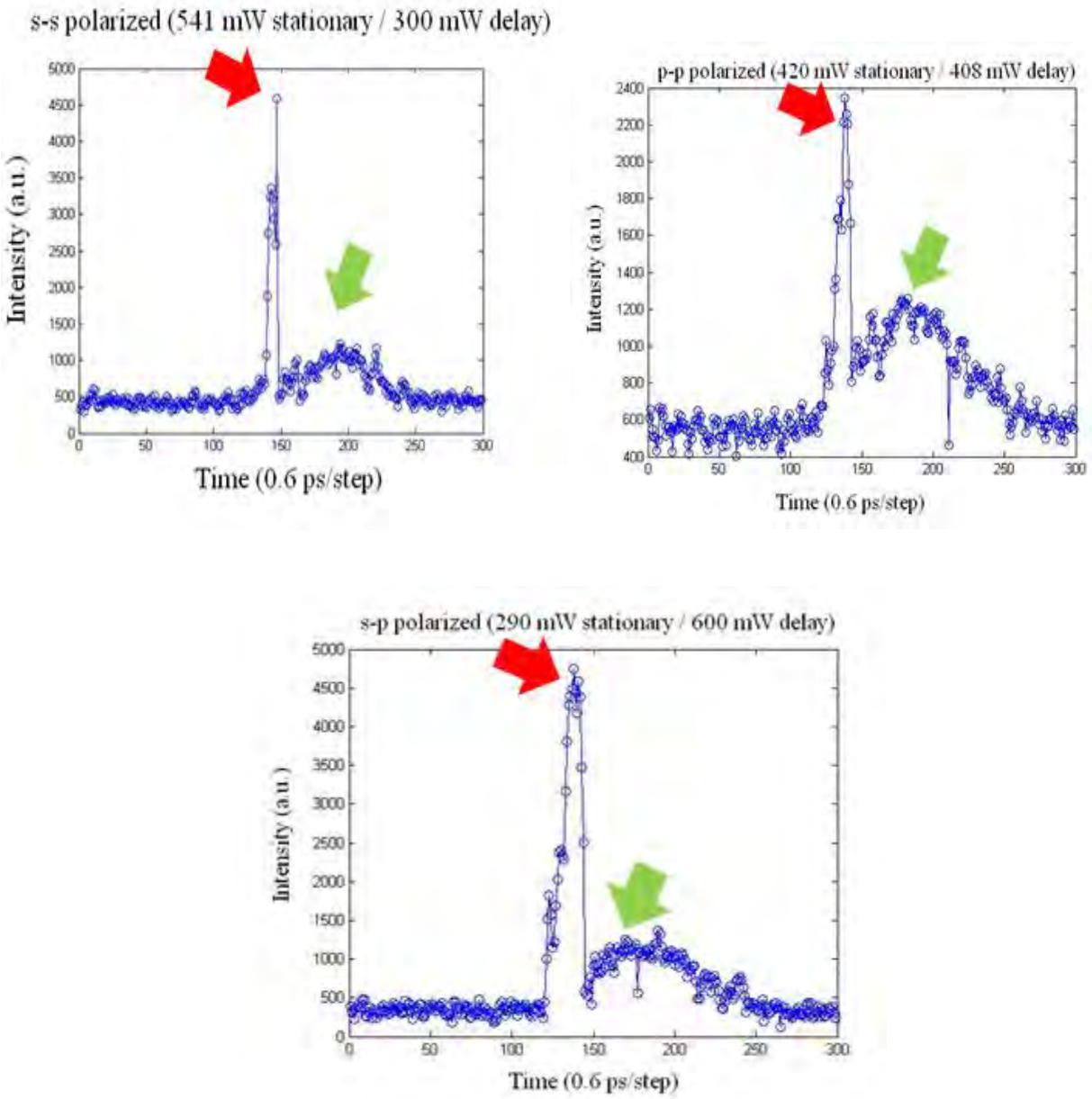


Figure 5. Peak Intensity vs. Time for three polarization sets. Peak intensity is indicated by the red arrow and secondary peak (also start of decay) is indicated by the green arrow. a) s-s polarization with 541 mW power in stationary arm (beam 2) and 300 mW power in delay arm (beam 1). b) p-p polarization with 420 mW power in stationary arm (beam 2) and 408 mW power in delay arm (beam 1). c) s-p polarization with 290 mW in stationary arm (beam 2) and 600 mW power in delay arm (beam

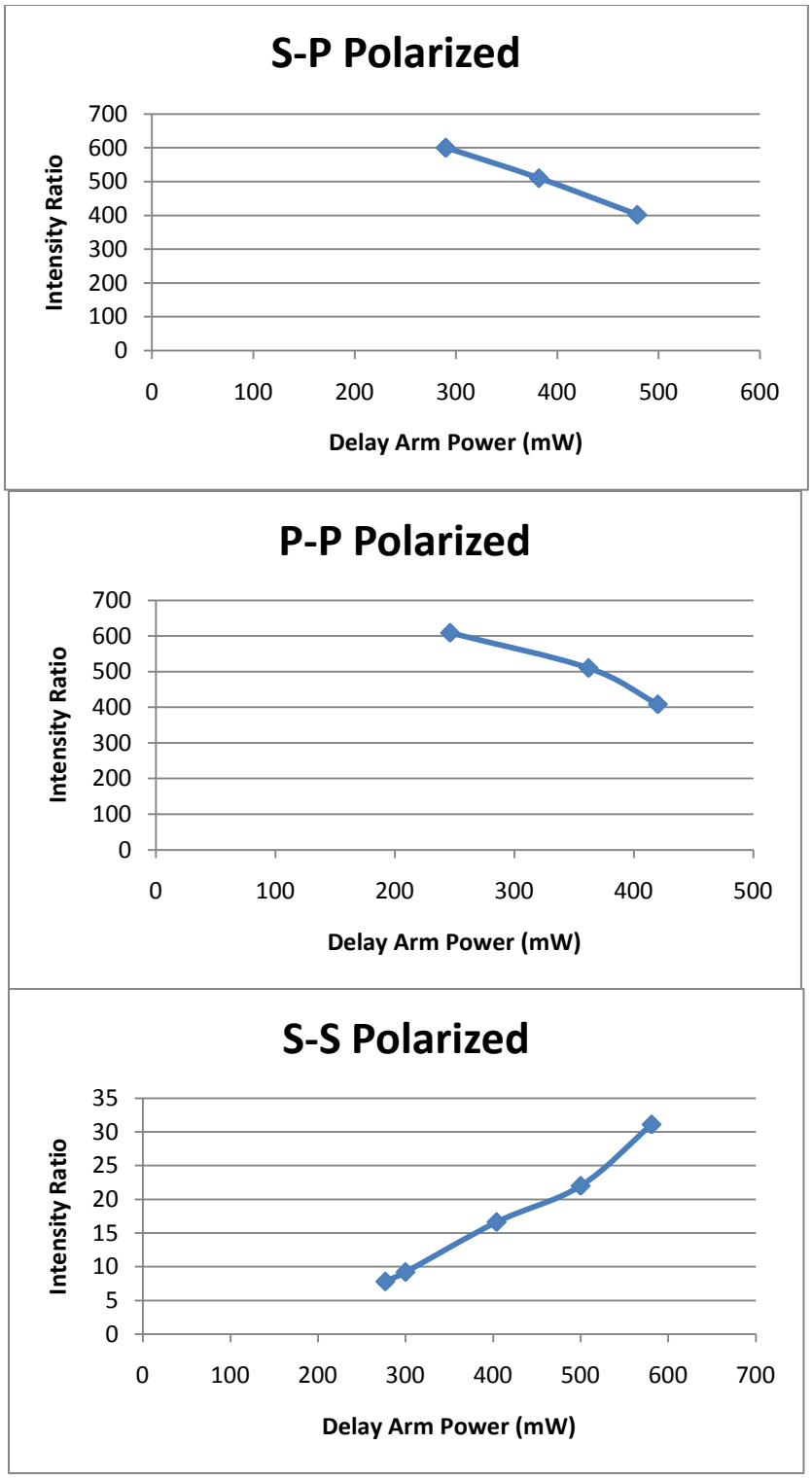


Figure 6: Ratio of peak intensity to background noise (intensity ratio) vs. power through the delay arm (beam 1) for all three polarization sets. Relationship seems to be linear.

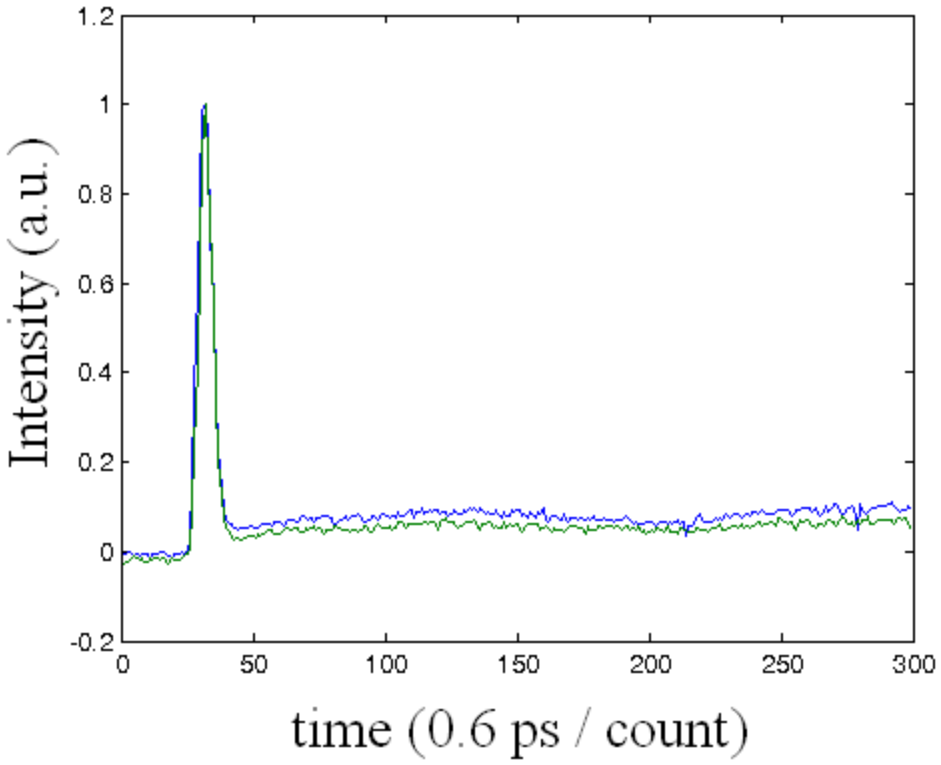


Figure 7: Normalized plot of intensity vs time for s-s polarization. Green trace corresponds to data taken with bluepass filter and blue trace corresponds to data taken without bluepass filter. Curves are normalized to the time zero peak.

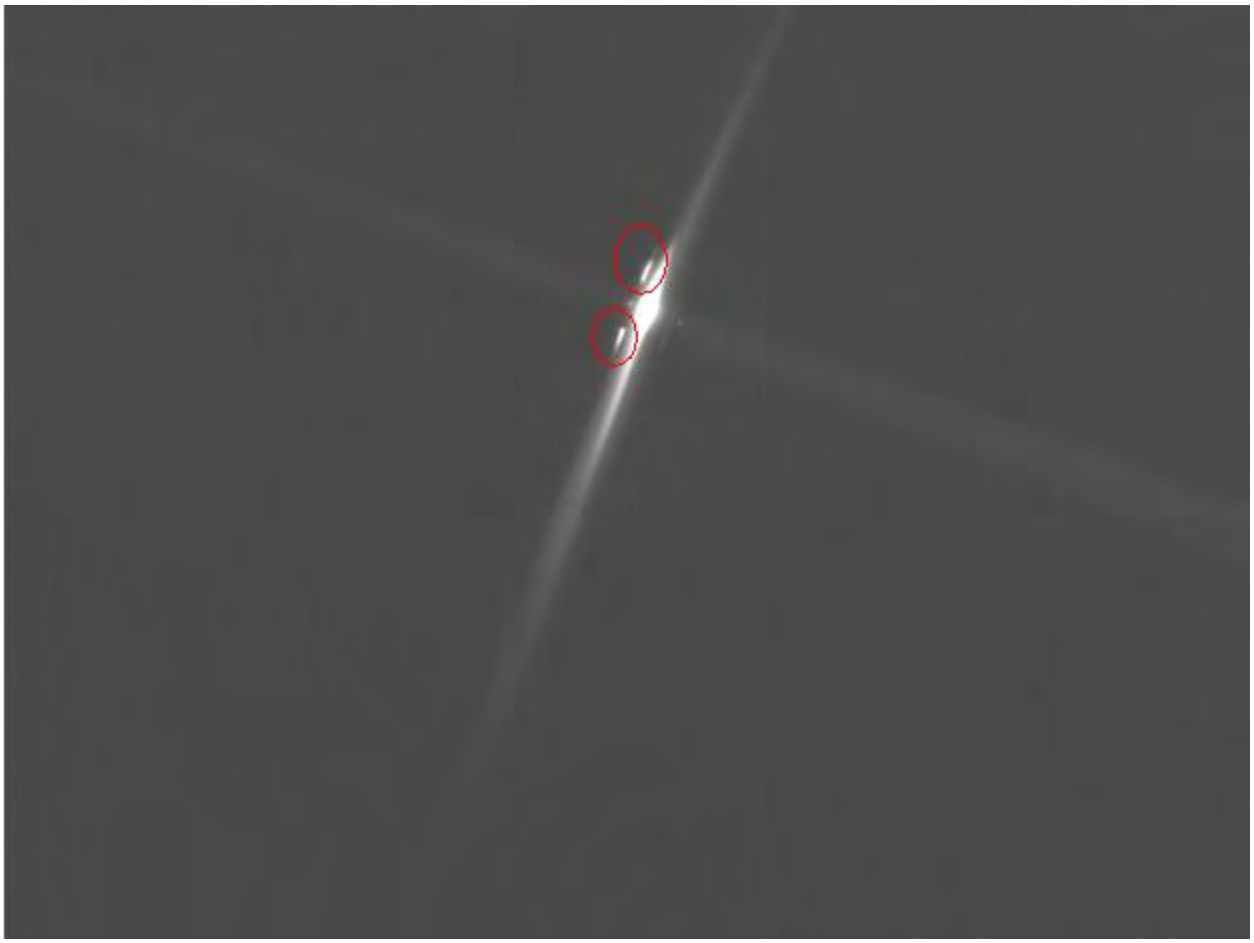

Figure 8: Secondary plasma formation as indicated by red circles. Effect is perhaps due to scattering.

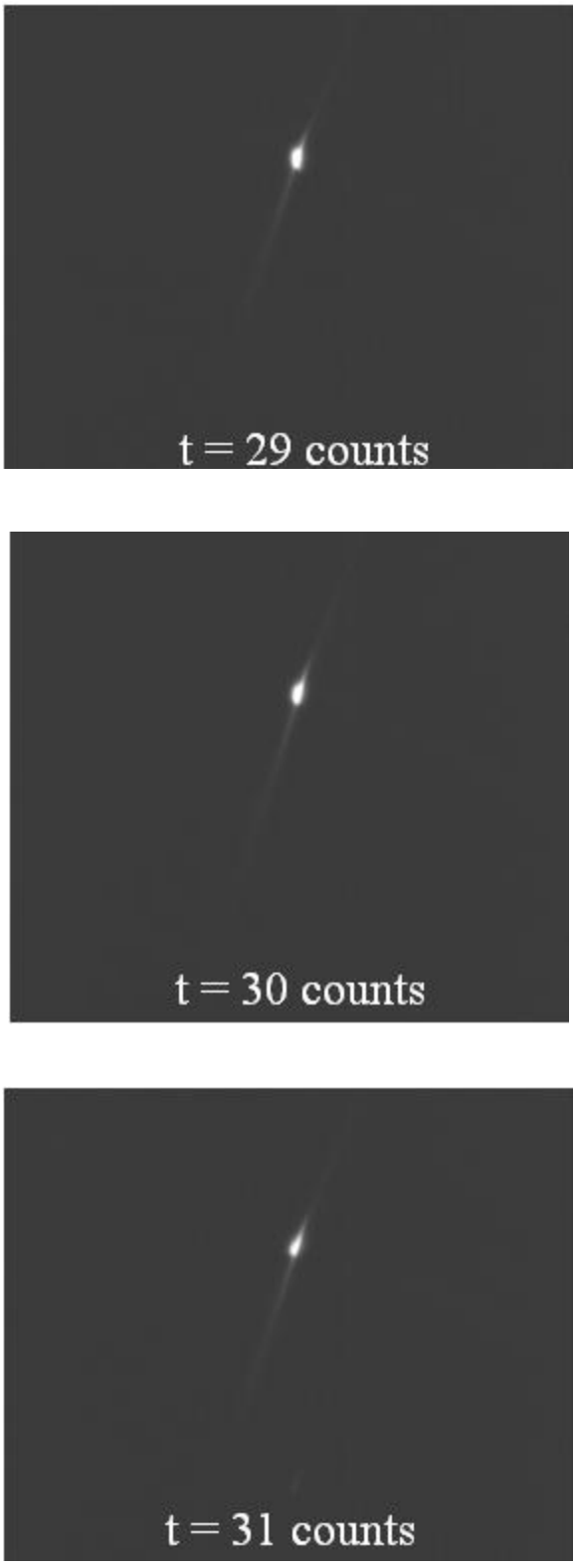


Figure 9: Diagonal rotation of overlap region through time. Plasma exhibits wavefront phenomenon providing an autocorrelation of the two pulses.

# LSST Charge-Coupled Device Calibration

Tiarra Johannas Stout

Office of Science, Science Undergraduate Laboratory Internship (SULI)

Idaho State University

Stanford Linear Accelerator Center Stanford, CA

August 10, 2010

Prepared in partial fulfillment of the requirements of the Office of Science, Department of Energy's Science Undergraduate Laboratory Internship under the direction of Deborah Bard at the Kavli Institute for Particle Astrophysics and Cosmology at the Stanford Linear Accelerator Center.

Participant: _____
Signature

Research Advisor: _____
Signature

Work supported in part by US Department of Energy contract DE-AC02-76SF00515.

# Table of Contents

# Abstract

LSST Charge-Coupled Device Calibration. TIARRA JOHANNAS STOUT (Idaho State University, Pocatello, ID 83209) DEBORAH JOANNE BARD (Stanford Linear Accelerator Center, Menlo Park, CA 94025).

The prototype charge-coupled device created at the Stanford Linear Accelerator Center for the Large Synoptic Survey Telescope must be tested to check its functionality and performance. It was installed into the Calypso telescope in Arizona in November of 2008 for this purpose. Since then it has taken many images of various astronomical objects. By doing photometry on standard stars in these images, we can compare our magnitude results to the known magnitudes of these stars. This comparison allows us to then determine the chip's performance and functional capabilities.

## I. INTRODUCTION

Expecting to see first light in 2016, the Large Synoptic Survey Telescope (LSST) is an extremely large ground based telescope that anticipates funding and will be built in Chile. Described as "Wide-Fast-Deep", the LSST will have an unprecedented wide field of view (ten square degrees for surveys), short exposures (fifteen to thirty seconds and still see faint objects), and the largest digital camera in the world [1].

One of the goals hoped to be achieved with this camera is the measurement of dark matter using strong and weak gravitational lensing [1]. Gravitational lensing occurs when a large cluster of galaxies distorts the light from a galaxy behind this cluster. This causes an arc of light to form around the cluster. By measuring the length of this arc, one can calculate how much matter should be present in the cluster. Since the amount that should be present is vastly greater than the amount of visible matter that can be seen, it is postulated that the difference between these two numbers is made up of dark matter. This is a direct way of measuring the amount of dark matter in the universe [2]. Thousands of galaxy clusters will be seen with LSST, allowing precise measurements of strong lensing effects. Weak lensing is a much smaller effect, distorting the shape of galaxies by only a few percent. The scale of LSST will allow these small effects to be measured with a precision unavailable with current smaller surveys.

Some of the other uses for the LSST will be cataloging the entire sky, observing exploding supernovae and near Earth objects, and probing into the nature of dark energy [1].

Since the LSST is such a large project, one organization alone cannot build it. Therefore many organizations have come together, each one working on a specific part of the telescope's construction. Here at the Stanford Linear Accelerator Center (SLAC) the camera is being designed.

Weighing 2800 kilograms (~6173 lbs), the camera will have approximately 3.2 billion pixels and be 1.6 meters by 3 meters [1]. A charge-coupled device (CCD chip) will be the light

sensor of the camera. A prototype CCD chip has been constructed and installed in the Calypso telescope in Arizona, where its performance and functional capabilities are being tested.

The LSST CCD array will not be one chip, however, but consist of 189 CCD chips arranged into 21 "rafts." Each raft contains nine CCD chips, which are individually divided into sixteen segments [1]. (See figure 1.)

## II. MATERIALS AND METHODS

### *2.1 Calibration of CCD Chip*

Since being installed in Calypso in November of 2008, the prototype CCD chip has taken numerous astronomical images, which has allowed us to test its capabilities. By doing photometry (the measurement of an object's flux or intensity of electromagnetic radiation) on the standard astronomical objects in these images, we can compare our results using the prototype with known results of these well measured objects. If our results produce the same numbers that have been previously documented, then the CCD chip is performing well. To test the prototype, object EGGR 102 (more commonly known as HIP 66578) was observed and the resulting images were processed.

### *2.2 Photometry*

In order to process the images, the program called IRAF (Image Reduction and Analysis Facility) was used. IRAF allows one to manipulate images and convert measurements of star flux from a CCD image to a standard magnitude. It is this standard magnitude that is needed to compare the data taken by the LSST chip to known data of well measured objects.

The first step is to process or clean up the images to remove interference or noise caused by electronic readout noise, thermal electrons, pixel-to-pixel variations, optical non-uniformities, etc, that may later compromise photometry on the actual images [3][4][5]. These effects are removed by taking three types of calibration images, along with science data, throughout the night.

The first type of image is a bias frame or zero second integration. Using a zero second exposure time to flush and read out the chip, these biases establish the readout noise from the chip [3][5]. For data from the Calypso, a one second "dark" is used for this purpose instead of an actual bias. The same goal is accomplished, however.

The second type of calibration image is called a "dark". These images are taken with the shutters closed to establish the pattern of dark current in the chip [3][4][5]. Dark current is the slight electrical current that still flows through the chip even when no photons are present. This effect, however, is negligible when using an effective CCD chip and short exposure times; therefore, for images taken at Calypso, this is not required.

The third image type is the "flat." There are two kinds of flats: dome flats and sky flats. A dome flat is an exposure taken of a white screen while the dome is still closed. This screen is then illuminated by lamps with a well understood spectrum of light. A sky flat is taken of the sky right as the sun is setting or rising, which gives the sky a uniform illumination. These flats show pixel-to-pixel patterns that result from sensitivity variations in the chip or shadows caused by dust or other obstructions [3][4][5].

After the images are processed, one can then do photometry on the desired objects and extract their "instrumental magnitude", which is the magnitude calculated from the number of photon counts received by the CCD chip. This magnitude comes from measuring the area under the curve of the radial profile of the star, which represents the light from both the star and sky background. (See figure 2) The sky is then subtracted out, divided by the exposure time, and the log is taken of the final result [3].

However, it is the absolute magnitude of the star that is desired since it can tell us how far away the star is, its composition, etc. Here one must compile a standard star catalog to find the coefficients of the magnitude equations that will be used to convert the instrumental magnitude into a standard magnitude, which is the measurement of an object's intrinsic brightness. If we are

measuring a well known star, this allows us to compare our results to known results, thereby testing how well our CCD chip is performing.

The catalog format used is from Landolt's UBVRI Standard Stars (2007) of this form:

HIP66578 13:38:50 +70:17:07 12.773 -0.091 -0.875 -0.100 -0.106 -0.206

| | |
|---|---|
| 1 | Object Name |
| 2 | Right Ascension * |
| 3 | Declination * |
| 4 | V Magnitude |
| 5 | BV (B-V color) |
| 6 | UB (U-B color) |
| 7 | VR (V-R color) |
| 8 | RI (R-I color) |
| 9 | VI (V-I color) |

Information for the catalog was taken from the Simbad database.

* Coordinates in FK5 coordinate system

## III. RESULTS

EGGR 102 was measured in the photometric bands i, r, z, and y4, with bands i, z, and y4 being near-infrared filters and r being a visible light filter. Since the standard magnitudes are not known in the z and y4 bands, I only tested our results in the i and r bands. These are the resulting transformation equations along with their calculated coefficients. (See figures 3 and 4)

IFIT : $mi = (V - VI) + i1 + i2 * Xi + i3 * VI + i4 * VI * Xi$

| | |
|---|---|
| mi | instrumental magnitude |
| V | absolute magnitude/V magnitude |
| Xi | airmass |
| VI | color value (difference between two filters) |
| i4 | 0.0 (constant) |
| i1, i2, i3 | coefficients. Calculated at -0.02885237, 0.01845326, and 0.1401964 respectively. |

RFIT : $mr = (V – VR) + r1 + r2 * (Xr – 1.326) + r3 * VR + r4 * VR * Xr$

| | |
|---|---|
| mr | instrumental magnitude |
| V | absolute magnitude/V magnitude |
| Xr | airmass |
| VR | color value (difference between two filters) |
| r4 | 0.0 (constant) |
| r1, r2, r3 | coefficients. Calculated at -0.2086798, 0.7110448, and 2.087208 respectively. |

For the IFIT, five datapoints were used in the final fitting, resulting in a root mean square (RMS) of .005886 after deleting an outlier point. The standard magnitude for EGGR 102 in the i filter is 12.979. Our result was 12.978 +/- .006 after setting the z magnitude (zero point of magnitude scale) in the IRAF photpars parameter to 23.0429. (See figure 3)

The RFIT solution originally did not converge, therefore I corrected the airmass variable (Xr) by subtracting the average airmass of the images from the airmass variable to bring that term closer to zero to shift the intercept and create a higher precision [5]. After modifying the equation, the RMS equaled .007863 using five datapoints. The standard magnitude is 12.873 with our result being 12.465 +/- .008. (See figure 4)

## IV. CONCLUSION

Our preliminary results show that the prototype CCD chip is working well and accurately since our results for the absolute magnitude of EGGR 102 are very near that of its known value and the RMS is less than .01 [5]. However, more data is needed to solidly verify its functionality.

The work done here has also revealed a deficiency in the collected data from Calypso so far. Much of the data taken at Calypso is useless for calibration purposes due to flaws in the images, the images not being of standard astronomical objects, or standard objects being measured in filters that do not contain much data. Future images should be taken of standard stars in common filters for calibration purposes, with an attention on image quality.

## V. FUTURE WORK

Once the calibration is completed, objects with little known data can be observed. New data can also be gathered using the y3 and y4 photometric filters, which were specifically developed by Dr. Kirk Gilmore at the Stanford Linear Accelerator Center (SLAC) for use in the LSST. Further work will also be done on the CCD chip itself, characterizing, and hopefully correcting, the segment variations caused by different zero-point biases, thereby giving the image more uniformity.


## ACKNOWLEDGEMENTS

I would like to thank my mentor Dr. Deborah Bard for her support, willingness to answer my questions, and desire to help me succeed during my time here at SLAC. I would like to thank Dr. Kirk Gilmore as well for his support and direction while my mentor was out of the country. SULI is an extraordinary program, and director Dr. Steve Rock was very helpful throughout the entire experience. However, my greatest thank you goes out to the DOE for funding opportunities like this. Thank you.

**FIGURES**

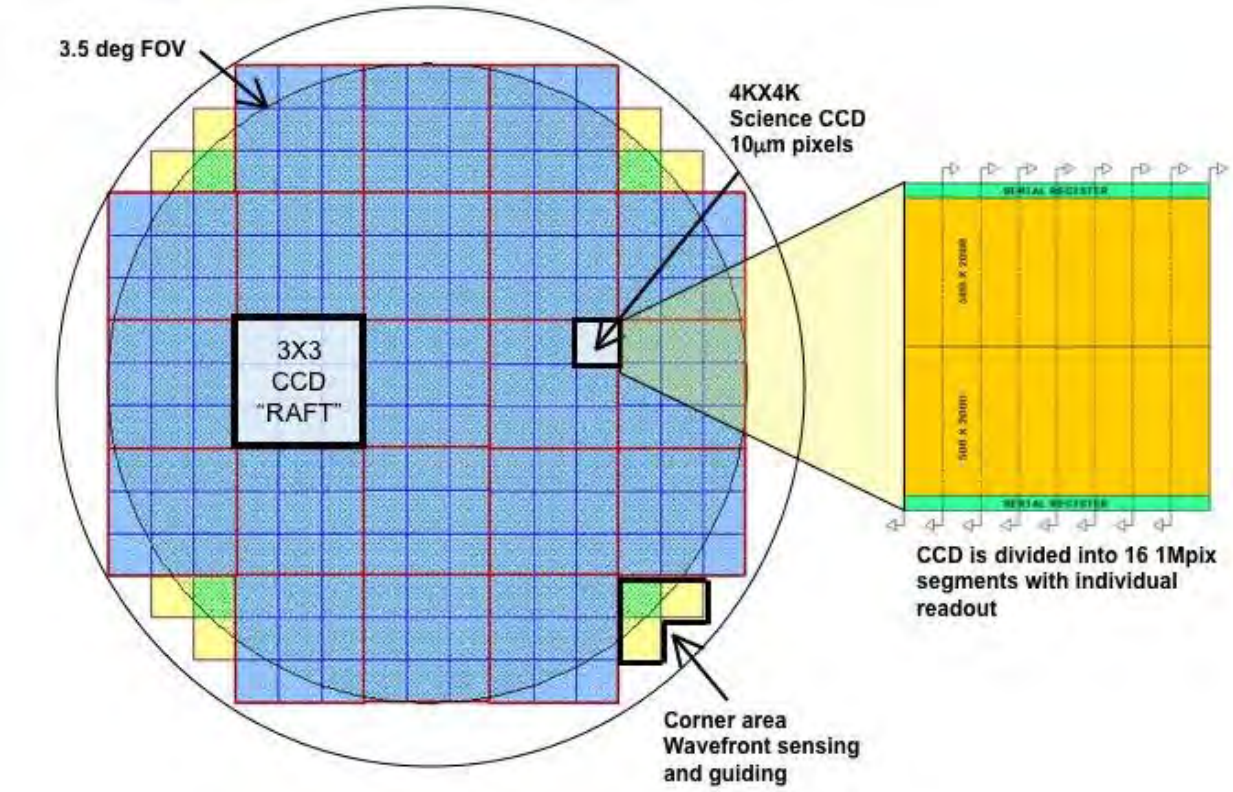


Figure 1: LSST CCD Array. Courtesy of www.lsst.org

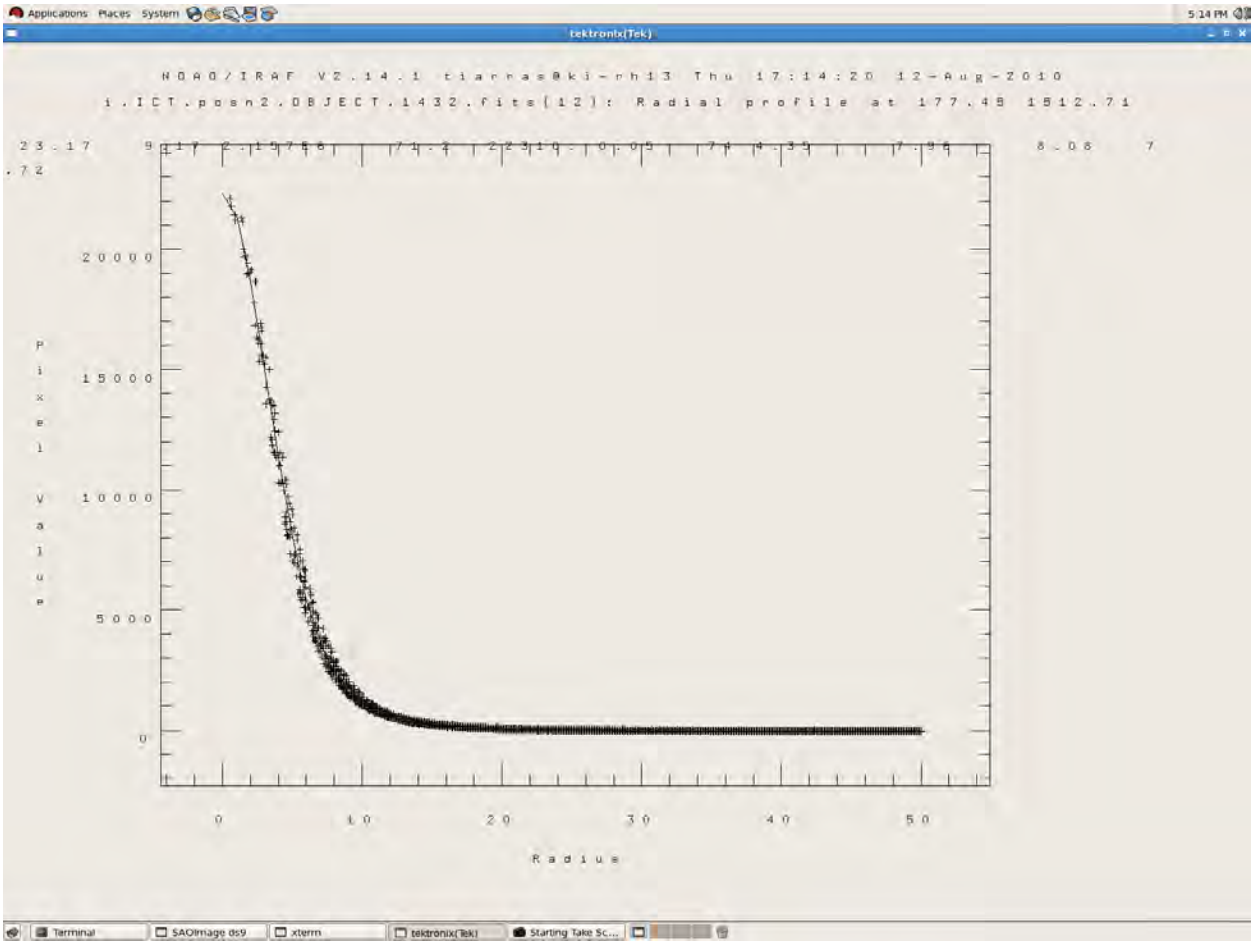


Figure 2: Example of a star radial profile. Produced by Tiarra J. Stout using IRAF and object EGGR 102.

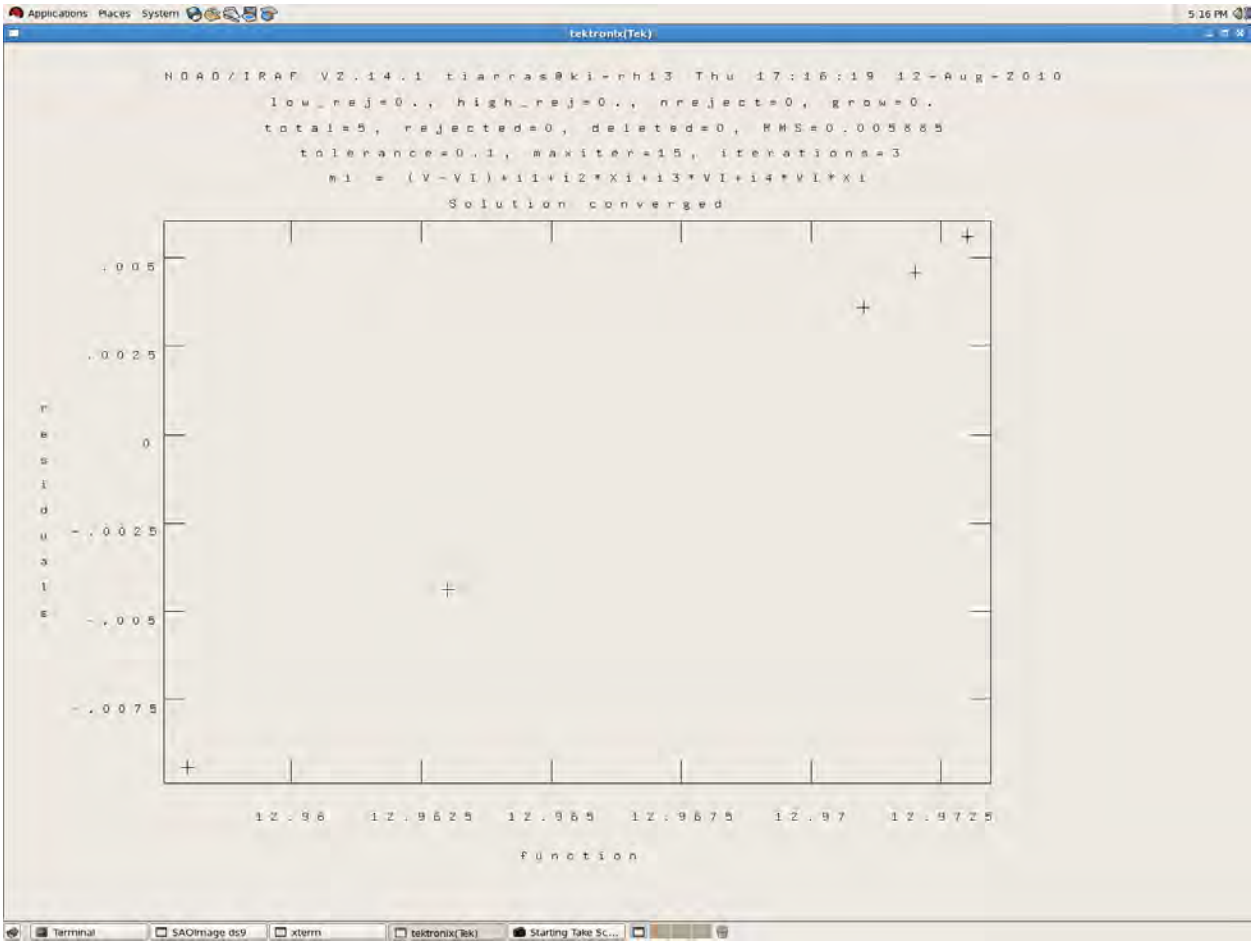


Figure 3: Result of fitting to solve for magnitude coefficients in the i band. The y-axis shows residuals (the error between the fitted magnitudes and the measured magnitudes). The x-axis shows the function, which is the fitted magnitude. Produced by Tiarra J. Stout using IRAF.

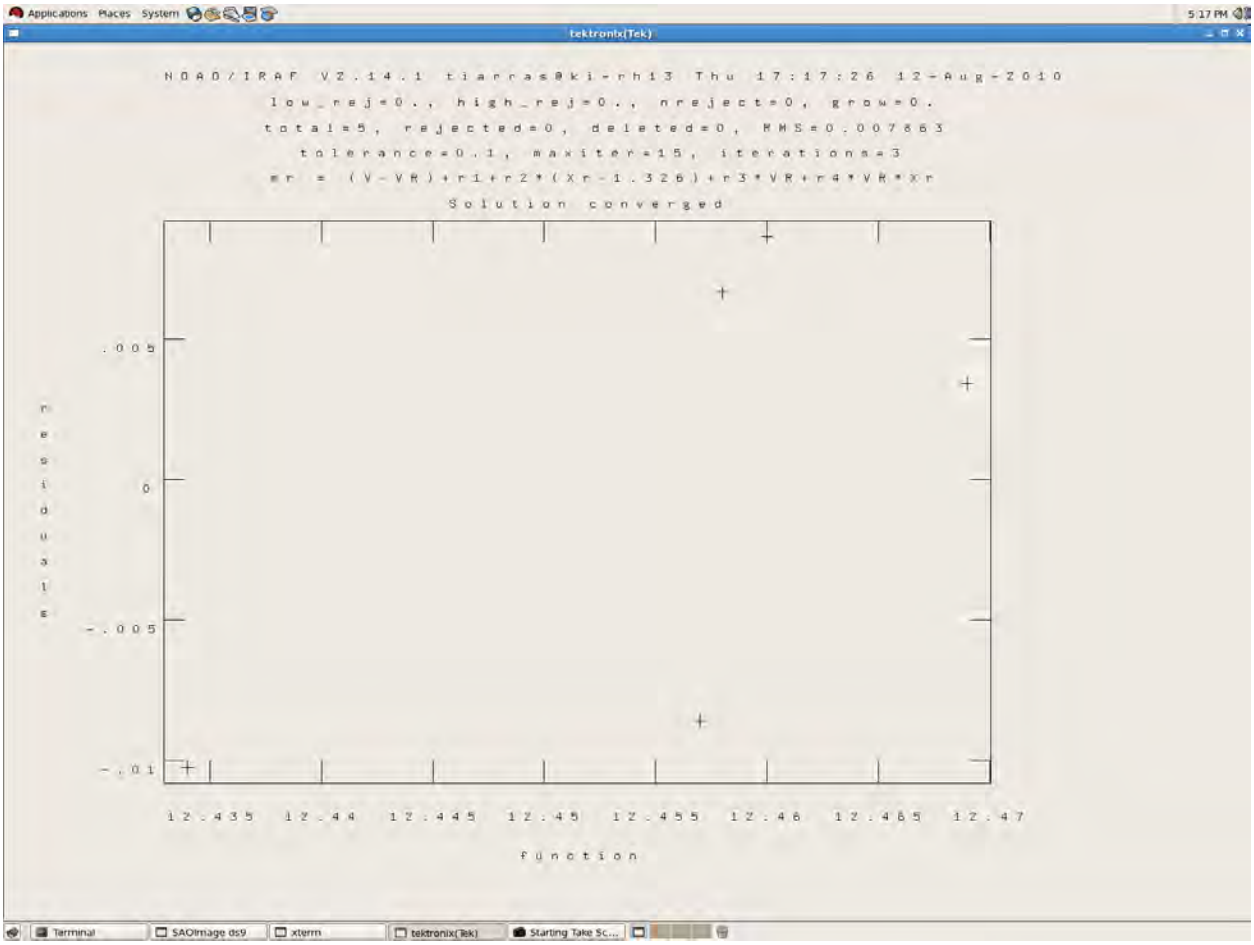


Figure 4: Result of fitting for magnitude coefficients in r band. Produce by Tiarra J. Stout using IRAF.

## REFERENCES


[1] “Large Synoptic Survey Telescope.” Internet: http://www.lsst.org/lsst, August 13, 2010 [July 10, 2010].

[2] Bartelmann, Matthias, *et al.* “Weak Gravitational Lensing.” Physics Report, vol. 340, pp. 291-472, Dec 1999.

[3] Marschall, Laurence A. “CCD Photometry using IRAF at Gettysburg College and the national Undergraduate Research Observatory.” Internet: http://www.nuro.nau.edu/info/iraf.htm, [June 25, 2010].

[4] Massey, Philip, *et al.* “A User’s Guide to Stellar CCD Photometry with IRAF.” Internet: http://iraf.net/irafdocs/daophot2/, April 15, 1992 [June 25, 2010].

[5] Grisetti, Robert. “A Student's Guide to CCD Photometry Data Processing using IRAF at the University of Central Florida.” Internet: http://www.physics.ucf.edu/~yfernandez/iraf/ourmanual.pdf, July 3, 2006. [July 10, 2010].

# Analysis of Femtosecond Timing Noise and Stability in Microwave Components

Michael R. Whalen
Office of Science, Science Undergraduate Laboratory Internship Program

Stevens Institute of Technology

SLAC National Accelerator Laboratory
Stanford, CA

August 14, 2010

Prepared in partial fulfillment of the requirement on the Office of Science, Department of Energy's Science Undergraduate Laboratory Internship under the direction of Josef Frisch at the LCLS Diagnostics Group at SLAC National Accelerator Laboratory.

Participant: _____
Signature

Research Advisor: _____
Signature

Work supported in part by US Department of Energy contract DE-AC02-76SF00515.

## Table of Contents

## ABSTRACT

Analysis of Femtosecond Timing Noise and Stability in Microwave Components.
MICHAEL WHALEN (Stevens Institute of Technology, Hoboken, NJ 07030)
JOSEPH FRISCH (LCLS Diagnostics Group, SLAC National Accelerator Laboratory, Stanford CA, 94025)

To probe chemical dynamics, X-ray pump-probe experiments trigger a change in a sample with an optical laser pulse, followed by an X-ray probe. At the Linac Coherent Light Source, LCLS, timing differences between the optical pulse and x-ray probe have been observed with an accuracy as low as 50 femtoseconds. This sets a lower bound on the number of frames one can arrange over a time scale to recreate a "movie" of the chemical reaction. The timing system is based on phase measurements from signals corresponding to the two laser pulses; these measurements are done by using a double-balanced mixer for detection. To increase the accuracy of the system, this paper studies parameters affecting phase detection systems based on mixers, such as signal input power, noise levels, temperature drift, and the effect these parameters have on components such as the mixers, splitters, amplifiers, and phase shifters. Noise data taken with a spectrum analyzer show that splitters based on ferrite cores perform with less noise than strip-line splitters. The data also shows that noise in specific mixers does not correspond with the changes in sensitivity per input power level. Temperature drift is seen to exist on a scale between 1 and 27 fs/$^0$C for all of the components tested. Results show that any components using more metallic conductor tend to exhibit more noise as well as more temperature drift. The scale of these effects is large enough that specific care should be given when choosing components and designing the housing of high precision microwave mixing systems for use in detection systems such as the LCLS. With these improvements, the timing accuracy can be improved to lower than currently possible.

## *1. Introduction*

The Linac Coherent Light Source (LCLS) currently produces powerful X-ray pulses with energies up to 10KeV. The ability to produce such bright light beams at these wavelengths has given the scientific community a remarkable tool for probing molecules down to the resolution of single atoms. At the LCLS, X-ray pump-probe experiments are carried out to probe the dynamics of molecules. A short, intense optical laser pulse will initiate the molecular change or reaction, followed by an LCLS X-ray pulse used for scattering and analysis. By varying and noting the timing difference between the laser pulse and the x-ray pulse, one can repeat the experiment numerous times with different separations and reconstruct a "movie" of the reaction.

Currently, the LCLS can produce x-ray pulses as short as five femtoseconds. This puts an absolute lower bound on the phase timing difference that can be measured. To determine the timing difference between the optical laser and x-ray pulses, a measurement system consisting of feedback mechanisms and phase shifters is in place. This is to account for cable length differences and small phase drifts between the components. All timing is derived from the same master oscillator, which is used to first accelerate the electrons. Due to the structure of the accelerator, these electrons travel along locked in phase with one crest of the source. Once they reach relativistic speeds, they pass through the undulators, creating a coherent x-ray source. The master source also drives the optical laser pulse, which is shifted to arrive at the same time as the X-ray pulse. To do this, the traveling electron bunch passes through an S-band radio frequency (RF) cavity, which resonates and creates an electric signal. This signal enters the phase detector, which is a mixer, along with the master oscillator signal, and is adjusted by the phase shifter to zero the mixer output, which is the region where the readings are most sensitive. With these current microwave techniques, physicists at Stanford Linear Accelerator Center (SLAC) have been able to measure timing separations with an accuracy of 50 femtoseconds [1]. The two main

concerns with this measurement system are noise levels and drift stability of the electronic devices. Along with the mixers, other microwave components such as amplifiers, phase shifters, low pass filters, attenuators, and splitters add noise to the system. Through testing, criteria for the optimal performance of a system can be deduced.

### *2. Materials and Methods*

This experiment consists of three main setups; the first provides information about the phase difference to voltage output sensitivity of each mixer, the second tests different combinations of components and determines the noise levels associated with each, and the third determines the phase drift associated with temperature changes for each component. The first experiment serves the purpose of gathering sensitivity data necessary to evaluate the noise and drift effects determined in the second and third experiments. This type of data are not specified by the vendors, as these effects only become appreciable when femtosecond time precision is desired; precision at this scale was unattainable before the LCLS was turned on.

### *2.1 Sensitivity in Mixers*

As double-balanced mixers are currently being used to make phase measurements in the LCLS, these are the responsible for determining the sensitivity of phase timing. When two input signals are received by a mixer, through the Local Oscillator (LO) Port and the Radio Frequency (RF) Port, they are processed through a ring diode setup and an output signal is seen from the Intermediate Frequency (IF) Port. A typical Schottky diode can be described by the equation:

$$I = a_1 V + a_2 V^2 + a_3 V^3 + a_4 V^4 + \cdots \quad (1)$$

When this diode is excited by two sinusoidal waves, $\mathrm{Cos}(\omega_1 t)$ and $\mathrm{Cos}(\omega_2 t)$, as in the mixer, the equation thus becomes:

$$I = a_1\big(\mathrm{Cos}(\omega_1 t) + \mathrm{Cos}(\omega_2 t)\big) + a_2\big(\mathrm{Cos}(\omega_1 t) + \mathrm{Cos}(\omega_2 t)\big)^2 + \cdots \quad (2)$$

When this equation is expanded, it contains the term "$2a_2\mathrm{Cos}(\omega_1 t)\mathrm{Cos}(\omega_2 t)$" which has the trigonometric relationship below:

$$2a_2\mathrm{Cos}(\omega_1 t)\mathrm{Cos}(\omega_2 t)=\mathrm{Cos}((\omega_1-\omega_2)t)+\mathrm{Cos}\big((\omega_1+\omega_2)t\big) \quad (3)$$

This is defined as the output of mixing. [2] The two sinusoidal waves describe the LO and RF inputs. The first and second terms on the right side of Equation 3 describe the difference in frequency of the two input signals, and the sum of their frequencies, respectively. Since we are only interested in the difference frequency, the higher frequency term is removed by a low pass filter, as seen in Figure 1.

Three mixers were tested to determine the picoseconds per volt phase difference, which is a measure of the mixers' sensitivities. The Mini-Circuits mixers used were models ZX05-HW-S+, ZFM-4H-S+, and ZFM-150. Two signal generators, Hewlett Packard E4432B ESG-D Series and Hewlett Packard 8656B, were used to generate LO and RF inputs respectively. The RF was set at 476 MHz and the LO at 476.01 MHz to generate at 10 kHz IF output. Both signals passed through a Mini-Circuits VLFX-470 Low Pass Filter with a passband from DC to 470 MHz. While this low pass filter slightly attenuated the primary signal, it served to eliminate higher level harmonics from creating unwanted signals and noise in the mixer. By removing these harmonics, unwanted IF products were also eliminated and the observed noise floor examined in the second part of the experiment was lowered.

Sensitivity readings are taken with LO powers of 5, 10, 15, 17, and 20 dBm for the first two listed mixers along with an additional 0dBm reading taken for the third due to its lower power level specifications for LO inputs. At each of these levels, RF inputs of 0, 5, 10, and 15 dBm were used. As cables have some power loss, a Mini-Circuits PWR-SEN-6GHS+ Power Sensor was used before every measurement right before the input ports to assure the correct power level were entering the mixer. This array of data was taken as such to allow for interpolation of sensitivities for the next parts of the experiment.

The IF output of the mixer is sent through a Mini-Circuits SLP-100+ Low Pass Filter with a passband from DC to 98 MHz to eliminate the summation frequency and only allow the difference frequency to be analyzed in the Tektronix TDS3032 Oscilloscope. With the oscilloscope, the 10 kHz wave for each combination of power inputs is measured for its voltage maximum and minimums and more importantly its sensitivity. To determine phase with a mixer, it is preferable to use the portion of the IF that crosses directly at the zero voltage mark. When the signals are in phase or 180 degrees out of phase, the IF signals are at a maximum or minimum. Around these points, when the phases shift slightly, the corresponding voltage change is small and often undetectable; only changes in power input can be seen as a change in amplitude. When the signals are 90 degrees out of phase, the sinusoidal waves slope is the greatest. Here, the slightest phase shift results in a large voltage change and power input changes will theoretically not affect the sensitivity. By zooming into the zero-intercept on the oscilloscope and measuring the voltage change per time slope, one measures the voltage change produced by a specified phase shift between the two signals. A visual representation of what this actual looks like on the oscilloscopes can be seen in Figure 2. As we know the two signals shift one full cycle in phase at the IF frequency, the observed data can be converted to volts per cycle for the IF, shown in Equation 4 below. Due to the IF frequency's dependence upon the RF frequency, we can finally then convert this to a picoseconds per volt phase shift for the mixer and initial RF, a measure of sensitivity, shown in Equation 5.

$$\boldsymbol{Volts/Cycle}\ [\mathrm{V}] = \boldsymbol{Slope}\ [\mathrm{V/s}] * (\boldsymbol{1/f_{IF}})[\mathrm{s}] \tag{4}$$

$$\boldsymbol{Sensitivity}\ [\mathrm{V/ps}] = \boldsymbol{Volts/Cycle}\ [\mathrm{V}] * \boldsymbol{f_{RF}}\ [\mathrm{s}^{-1}] \tag{5}$$

### *2.2 Noise Measurements*

When trying to optimize a phase detection system, mixer sensitivity alone cannot be used; a ratio of sensitivity to noise must be obtained and analyzed. To measure sensitivity a single RF source is used, as seen in Figure 3. The Hewlett Packard E4432B ESG-D Series Signal Generator is set to 476 MHz, the frequency of the master oscillator for the LCLS. Due to the maximum power of the signal generator being 15dBm, a Mini-Circuits ZHL-2010+ Low Noise Amplifier was placed between the RF source and the low pass filter to obtain the power levels needed to examine a wider range of LO and RF inputs. The low pass filter served to remove any harmonics created by the amplifier. Next, the signal was split by either a Mini-Circuits ZFSC-2-1W+ power splitter or an Anaren 40263 strip-line power splitter. Both were tested to determine differences between magnetic core splitters and strip line splitters. For noise experiments a splitter is used in order to allow both the RF and LO inputs to have exactly the same frequency signal, therefore producing a DC voltage IF. The RF signal is passed through an Aeroflex Weinschel Model 980 Mechanical Phase Shifter in order to adjust the phase difference created by the difference in path lengths leading to the RF and LO ports.

Before noise measurements are taken, the IF output is led into a Fluke 289 True RMS Multimeter. The phase shifter then adjusts the DC output on the voltmeter to read 0 Volts, thereby setting the two inputs 90 degrees out of phase. This sets the mixer at the position of highest sensitivity, which, in practice, will be where phase detection is done. Next, the signal is fed into an Agilent 89441A Vector Signal Analyzer for noise level readings. The power levels these measurements are taken at are LO matches to the sensitivity reading levels while the RF readings were taken as close as possible by use of attenuators before the RF port. Any differences were accounted for by interpolation between sensitivity data. For each power level, the noise floor was determined at four different bandwidths of 100 Hz, 1 kHz, 10 kHz, and 100 kHz. The noise floor voltage divided by the square root of the bandwidth gives a measure of

volts per square root hertz. The noise per root bandwidth over the sensitivity will finally give a noise per sensitivity ratio, which can be used to determine optimization information for the mixers and splitters.

### *2.3 Temperature Drift*

Another factor to consider when choosing components is the DC output voltage drift per temperature change. To determine this temperature drift, the same setup as seen in Figure 3 was used, except the component being tested was placed on a temperature controlled plate. The plate containing the rest of the components was monitored for temperature changes as well. The temperature range for each component varied but was usually between 14°C and 30°C. As done previously in the noise measurements, the signal was fed into the Fluke 289 True RMS Multimeter and set to zero volts output by the phase shifter. However, this time it was done specifically at the top of the temperature range. After being zeroed, the temperature controlled plate and the component being tested were lowered to the bottom of the range, using a Merlin M33 Series chiller. The phase drift, seen as a DC output voltage, was recorded at each integer interval over the temperature range. Without resetting the phase difference, the temperature was increased back to its initial state as readings were taken again.

Two observations about the temperature drift are demonstrated by these measurements. First, if the DC output voltage did not return back to zero, some change in the system most likely occurred and the test loses some validity. Secondly, the average DC voltage change per degree Celsius corresponds directly to the picoseconds phase drift between the two signals. This phase drift per degree Celsius, along with the noise measurements, create two important parameters for choosing optimal components in a high-precision phase-detection system.

### *3. Results*

The sensitivity readings, represented as voltage output per picosecond phase difference can be seen in Figures 4, 5, and 6. Graphing RF input powers against LO input powers give a better visual representation of the most sensitive power inputs and moreover, regions where the sensitivity does not change significantly over different input ranges. The three mixers, Mini-Circuits Models ZX05-HW-S+, ZFM-4H-S+, and ZFM-150, all had the highest sensitivities at the tested inputs of 20 dBm LO and 15 dBm RF with values of 0.05620 V/ps, 0.04430 V/ps, and 0.00897 V/ps respectively. A plateau was also seen above each mixer's recommended LO input, 17dBm for models ZX05-HW-S+ and ZFM-4H-S+, 10dBm for model ZFM-150. Model ZX05-HW-S+'s plateau was above its recommended LO value, where the previous sensitivity trend disappeared. Over the range from 17-20 dBm, this mixer saw on average, a change of less than 0.000592 V/ps. The model ZFM-4H-S+ did not have as distinct a plateau over the recommended LO input; however, the sensitivity trend's slope did decrease considerably. Over the range from 17-20 dBm, on average, sensitivity changes were less than 0.00119 V/ps. The model ZFM-150's plateau was much broader as the recommended LO input was 10 dBm so more readings were taken above its saturated value than for the other mixers. The third mixers plateau spans from 10 to 15dBm LO input and changes on average less than 0.00016 V/ps.

Each specific combination of components for the second experiment was measured for a volts per root hertz noise floor at four bandwidths. These were then divided by the sensitivities calculated earlier for each mixer to determine a noise to sensitivity ratio, NSR, with unit's picoseconds per root hertz. Table 1 contains the average NSR over the four bandwidths for different power inputs for all setups, as well as the minimum NSR value for each. Table 2 compares the input power levels for the optimal NSR and sensitivity.

When individual components of the second experimental setup were placed on a temperature controlled plate for the third experiment, smooth linear changes in the DC offset

were observed. The DC offset change between each degree Celsius change was taken and averaged to arrive at the temperature drift readings listed in Table 3. The ten foot Coaxial Cable reacted most with a 81.58 fs/$^0$C phase drift. While not the most sensitive, or the least noisy, the second mixer showed the least temperature drift with a value of 1.6949 fs/$^0$C.

### *4.1 Discussion-Sensitivity*

From the sensitivity data, the most useful feature is not the maximum sensitivity reading, but the plateau that exists above particular LO inputs, as well as a constant rise in sensitivity for RF inputs. If one's goal is to increase the sensitivity of a mixer to its maximum, applying the largest RF input power the mixer can withstand would be the way to achieve this. However, applying a LO input power above the recommended LO input does not change the sensitivity appreciably. This effect is due to saturation of the diodes in the mixer. Above this power level, the mixer acts as a limiter and increases to the LO power input do not affect the IF output. Operation in this saturated range is optimal for users wishing to keep a consistent sensitivity value when their system contains sources of small amplitude fluctuations.

### *4.2 Component Noise*

While the sensitivity is a useful measurement when choosing a mixer for normal operation, at the LCLS, precision measurements are often limited by the noise associated with each setup. The two types of noise investigated in this project were white and pink noise. White noise is consistent over the entire frequency spectrum and created by phonons, or thermal vibrations, and impurities in the conductors. White noise can only be eliminated so much by temperature control until very expensive and exotic means are necessary to transfer the signal through the temperature change without signal distortion. Pink noise exhibits a 1/f spectrum (equal power per decade of frequency). [3] The noise measurements were taken at a minimum bandwidth of 100Hz with a range of 0-10kHz. What is seen as pink noise at this bandwidth and higher bandwidths can actually be resolved by using a 10Hz bandwidth. When a 10Hz

bandwidth was used, the 0-1kHz range was full of external power source signals at 60Hz and appreciable harmonics of such as high as 600Hz. From this finding, it can be seen that these systems have no significant pink noise. Due to this, all noise measurements are based strictly on the white noise floor.

Beginning with the comparison of the two types of splitters, one made of magnetic circuitry and ferrite cores, the other which is a strip-line splitter etched into a silicon base plate, while both produced similar NSR values, the minimum value for each mixer existed when the magnetic circuitry mixer was used. This trend also exists across the input power spectrum where the NSR is not at its minimum. Differences in noise levels could be explained by construct, such as impurities and stability of internal components.

As for the mixers, while each had similar minimum noise values between 5.70 and 5.85 nV/$\sqrt{Hz}$, the sensitivities made the clear distinction between their NSR's. The minimum NSR's for the mixers were valued from $1.69*10^{-7}$ to $9.16*10^{-7}$ ps/$\sqrt{Hz}$, showing the importance of sensitivity when choosing a mixer. With measurement differences of almost half an order of magnitude among the different mixers, it is apparent that, while the effect is not tremendous, when dealing with mixers in a precision detection system, such as the LCLS, factors such as noise must be tested and taken into account.

For completion, a 20 dB amplifier followed by a 20 dB attenuator was placed between the phase shifter and RF input of the mixer. Noise levels were taken with and without this combination to see how much noise was being added to the system by the amplifier. As it turned out, the amplifiers used in this experiment added no noticeable noise.

### 4.3 *Temperature Drift*

Components such as the mechanical phase shifter and coaxial cable created the largest temperature drift because they contained the longest metal path length, making them most susceptible to expansion with temperature. Not surprisingly, the strip-line splitter's temperature drift was more than twice the magnetic splitter's drift. For unknown reasons, certain mixers were more than an order of magnitude less susceptible to temperature drift. It is presumed answers may lie within the details of the components construction, details withheld by the vendors.

### *4.4 Conclusion*

When designing a highly precise system for making femtosecond phase measurements, it is impractical to build small components such as mixers for such a large project as the LCLS. As these components are not created for the specifications needed, one must judge how important parameters, such as noise levels and temperature stability, are to the project. With the optimal components and parameters, taking a measurement at 200 kHz, typical of LCLS, a timing noise of 0.10420 fs is observed. Combined with the 0.16948 fs timing drift, calculated with the assumption of one-tenth degree Celsius temperature stability, the best combined timing noise for the tested systems is 0.27368 fs. This is an order of magnitude lower than the noise currently seen at the LCLS, implying that with attention given to component testing and analysis, precision of the LCLS phase detection systems can be improved in the future.

## *5. Acknowledgements*

This research was carried out at the SLAC National Accelerator Laboratory between June 21 and August 14, 2010 under the direction of Josef Frisch. I would like to thank the United States Department of Energy, SLAC National Laboratory, and the directors and administrators of the SULI program for making this research possible. I would like to thank my mentor Josef Frisch for his enthusiasm and guidance. I would also like to thank George Burgueno for his help

with procuring the tools necessary to carrying out this research. I would like to thank Cara Perkins for working side by side with me, allowing for all of this research to have been completed.

### *6. References*

[1] A. Brachmann, et al,. *Femtosecond Operation of the LCLS for User Experiments: TUPE066 International Particle Accelerator Conference*, *May 23-28, 2010, Kyoto, Japan*.

[2] Devlin Liam "Mixers," *Plextek Communications Technology Consultants*, July 17, 2003. [Online]. Availible: http://www.plextek.co.uk/papers/mixers2.pdf. [Accessed: July 20, 2010].

[3] P. Horowitz and W. Hill, *The Art of Electronics,* 2nd ed. Cambridge: Cambridge University Press, 1989, pp. 430-432.

## *7. Figures and Tables*

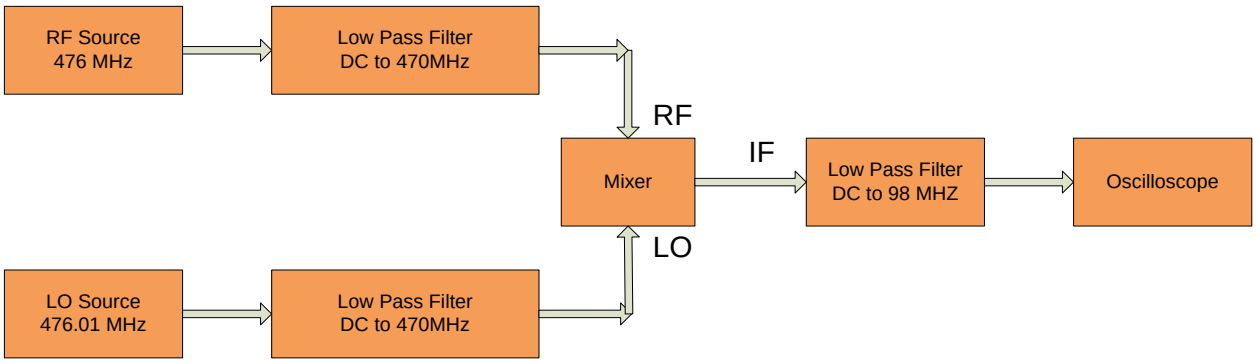


Figure 1: Sensitivity Measurement Setup

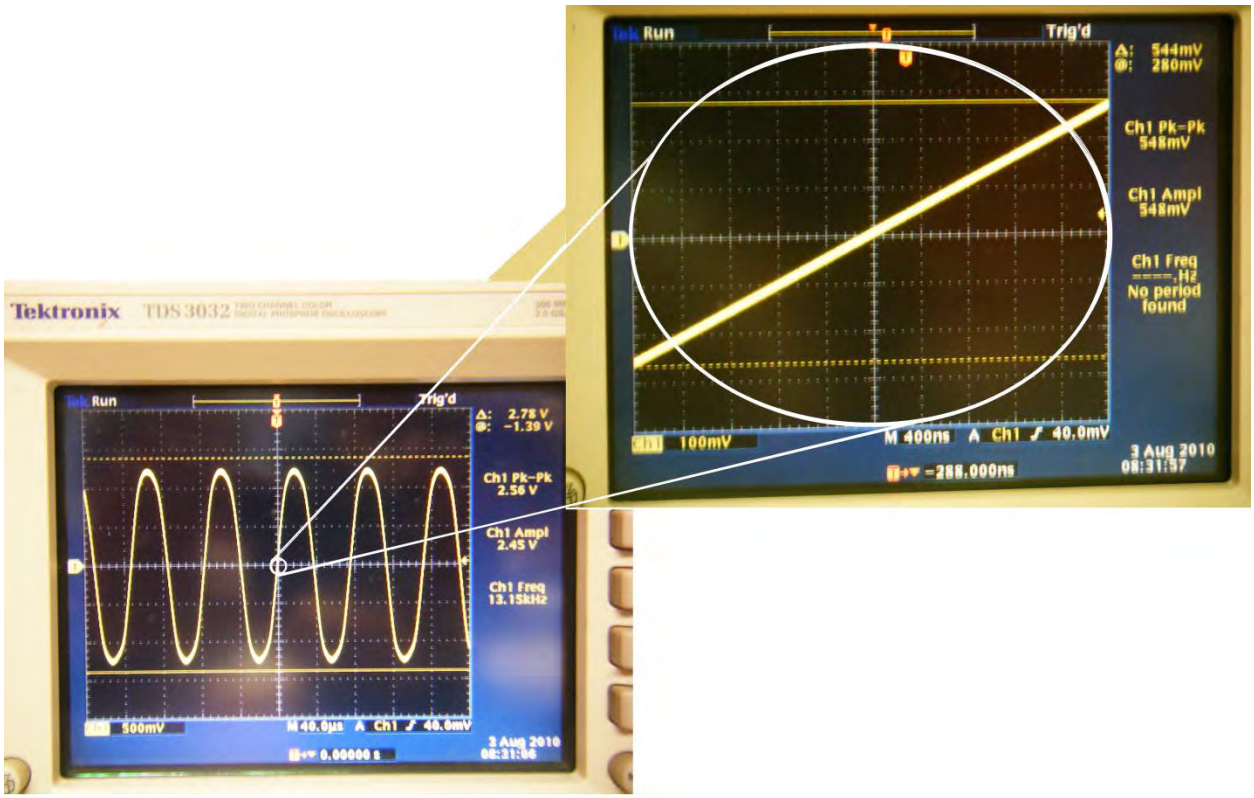


Figure 2: Obtaining data at zero-intercept for maximum sensitivity

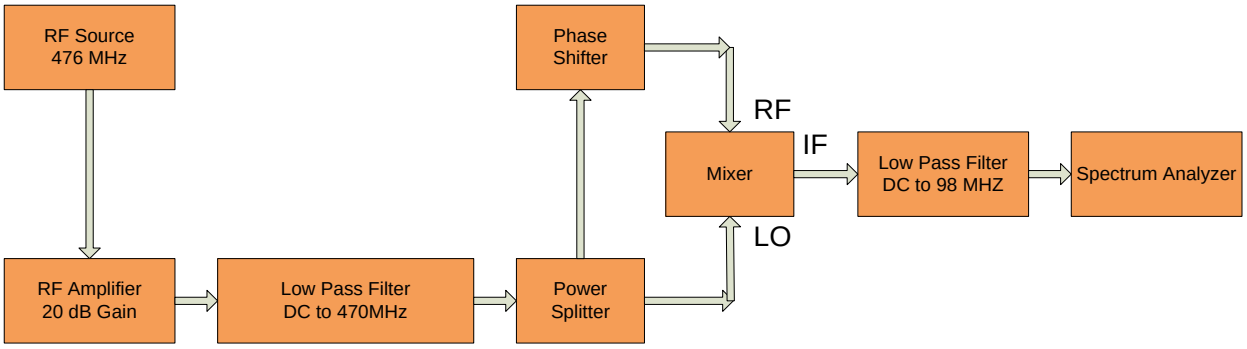


Figure 3: Noise and Drift Measurement Setup

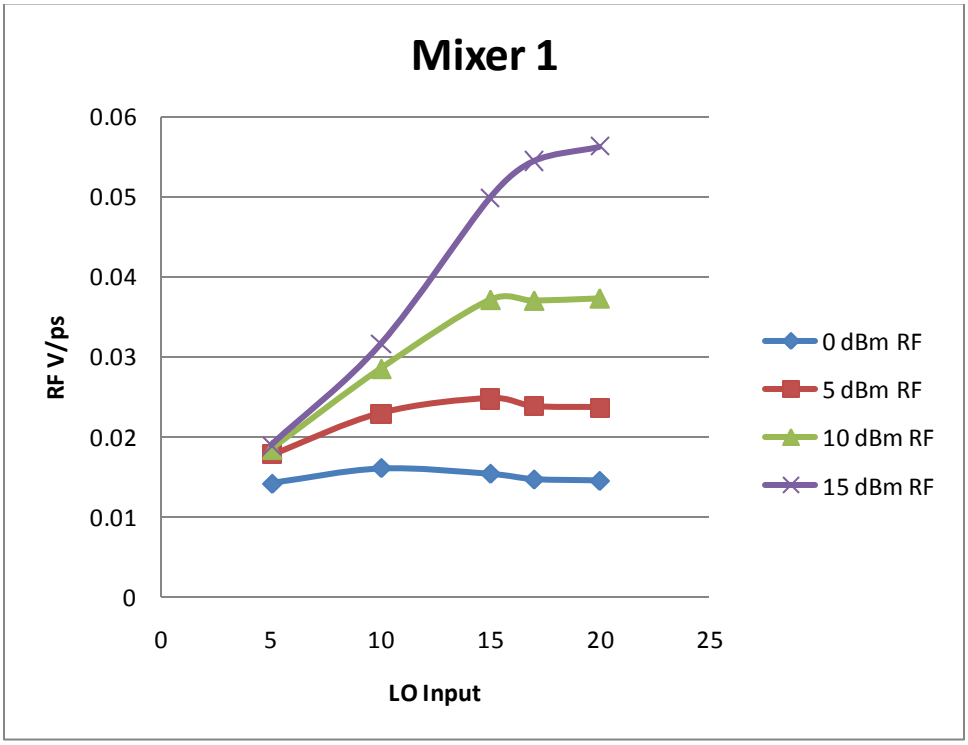


Figure 4: Model ZX05-HW-S+ mixer sensitivity graph

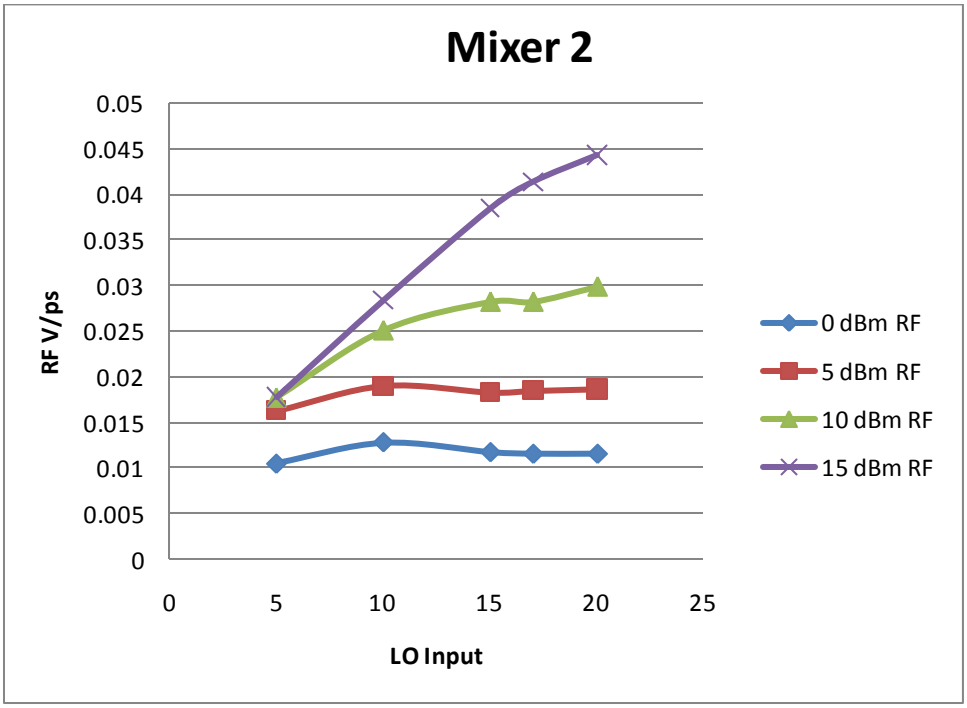


Figure 5: Model ZFM-4H-S+ mixer sensitivity graph

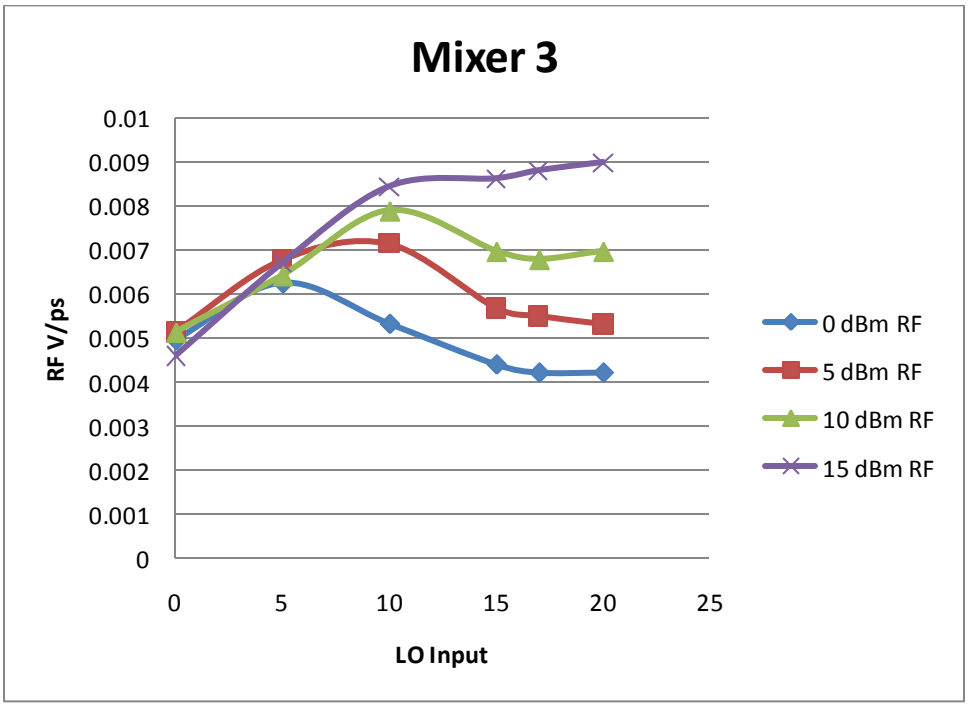


Figure 6: Model ZFM-150 mixer sensitivity graph

| Average NSR [ps/$\sqrt{Hz}$] | | | | |
|---|---|---|---|---|
| Mixer Models<br>M1: Mini-Circuits ZX05-HW-S+<br>M2: Mini-Circuits ZFM-4H-S+<br>M3: Mini-Circuits ZFM-150 | | | Splitter Models<br>S1: Mini-Circuits ZFSC-2-1W+<br>S2: Anaren 40263 | |
| M1, S1 | (RF input power level) *NSR* | | | |
| 5 dBm LO | (0.03) *4.35E-7* | (4.98) *5.06E-7* | (9.78) *4.63E-7* | (14.46) *8.95E-7* |
| 10 dBm LO | (0.42) *4.10E-7* | (4.16) *3.43E-7* | (9.40) *2.53E-7* | (14.46) *9.42E-7* |
| 17 dBm LO | (0.92) *1.39E-6* | (4.87) *1.51E-6* | (10.12) *9.80E-7* | (15.11) *3.72E-7* |
| 20 dBm LO | (1.02) *9.65E-7* | (1.02) *9.78E-7* | (9.95) *4.99E-7* | **(15.32) *1.69E-7*** |
| M1, S2 | | | | |
| 5 dBm LO | (0.09) *4.30E-7* | (4.76) *4.79E-7* | (9.73) *6.20E-7* | (14.96) *1.09E-6* |
| 10 dBm LO | (0.98) *3.91E-7* | (5.21) *3.95E-7* | (8.85) *3.47E-7* | (14.58) *1.10E-6* |
| 17 dBm LO | (0.85) *1.37E-6* | (4.60) *1.60E-6* | (10.53) *1.06E-6* | (14.30) *5.43E-7* |
| 20 dBm LO | (0.78) *9.89E-7* | (4.99) *9.99E-7* | (9.42) *5.19E-7* | **(14.92) *1.70E-7*** |
| M2, S1 | | | | |
| 5 dBm LO | (0.77) *7.09E-7* | (4.76) *4.94E-7* | (8.99) *2.27E-6* | (14.29) *8.70E-7* |
| 10 dBm LO | (0.27) *1.66E-6* | (5.09) *8.74E-7* | (9.91) *3.01E-6* | (14.40) *6.71E-7* |
| 17 dBm LO | (0.79) *6.10E-7* | (4.72) *4.60E-7* | **(10.90) *2.33E-7*** | (15.02) *4.98E-7* |
| 20 dBm LO | (1.01) *5.37E-7* | (5.14) *3.59E-7* | (9.69) *4.60E-7* | (14.95) *6.88E-7* |
| M2, S2 | | | | |
| 5 dBm LO | (0.07) *9.40E-7* | (4.90) *4.85E-7* | (9.51) *1.94E-6* | (14.77) *1.14E-6* |
| 10 dBm LO | (0.79) *1.70E-6* | (4.99) *1.28E-6* | (9.62) *2.72E-7* | (14.99) *3.67E-7* |
| 17 dBm LO | (0.96) *5.43E-7* | (4.84) *3.96E-7* | (9.53) *2.96E-7* | (14.63) *5.41E-7* |
| 20 dBm LO | (1.33) *6.20E-7* | (5.35) *4.59E-7* | **(10.11) *2.51E-7*** | (13.79) *7.22E-7* |
| M3, S1 | | | | |
| 0 dBm LO | (0.08) *1.37E-6* | (5.41) *2.24E-6* | (10.9) *2.10E-6* | (14.59) *2.32E-6* |
| 5 dBm LO | (0.40) *2.19E-6* | (4.51) *1.03E-6* | (9.53) *1.13E-6* | (15.00) *1.10E-6* |
| 10 dBm LO | (0.50) *2.78E-6* | (4.88) *9.90E-7* | (9.37) *1.07E-6* | **(14.63) *9.01E-7*** |
| 17 dBm LO | (1.33) *2.42E-6* | (5.26) *1.53E-6* | (10.54) *1.56E-6* | (14.24) *1.26E-6* |
| M3, S2 | | | | |
| 0 dBm LO | (1.15) *1.40E-6* | (5.93) *2.66E-6* | (9.43) *2.36E-6* | (13.85) *2.22E-6* |
| 5 dBm LO | (0.57) *2.31E-6* | (4.88) *1.51E-6* | (10.42) *1.27E-6* | (14.50) *1.06E-6* |
| 10 dBm LO | (0.07) *2.77E-6* | (5.30) *1.28E-6* | **(9.80) *9.16E-7*** | (14.05) *1.04E-6* |
| 17 dBm LO | (0.64) *2.03E-6* | (4.60) *1.51E-6* | (9.90) *1.45E-6* | (14.90) *1.43E-6* |

Table 1: Average NSR for all mixer, splitter, LO and RF power level combinations (Minimum value for each component combination highlighted in bold.)

| Mixer Models<br><br>M1: Mini-Circuits ZX05-HW-S+<br>M2: Mini-Circuits ZFM-4H-S+<br>M3: Mini-Circuits ZFM-150 | | Splitter Models<br>S1: Mini-Circuits ZFSC-2-1W+<br>S2: Anaren 40263 |
|---|---|---|
| | Minimum NSR (LO, RF) | Maximum Sensitivity (LO, RF) |
| M1, S1 | (20 dBm, 15.32 dBm) | (20 dBm, 15 dBm) |
| M1, S2 | (20 dBm, 14.92 dBm) | (20 dBm, 15 dBm) |
| M2, S1 | (17 dBm, 10.90 dBm) | (20 dBm, 15 dBm) |
| M2, S2 | (20 dBm, 10.11 dBm) | (20 dBm, 15 dBm) |
| M3, S1 | (10dBm, 14.63 dBm) | (20 dBm, 15 dBm) |
| M3, S2 | (10 dBm, 9.80 dBm) | (20 dBm, 15 dBm) |

Table 2: Comparison of minimum NSR and maximum Sensitivity power level inputs

| Component | Temperature Drift (fs/°C) |
|---|---|
| Mini-Circuits Splitter Model ZFSC-2-1W+ | 3.780594406 |
| Anaren Splitter Model 40263 | 8.503419973 |
| Mini-Circuits Mixer Model ZX05-HW-S+ | 26.79407713 |
| Mini-Circuits Mixer Model ZFM-4H-S+ | 1.694897959 |
| Mini-Circuits Mixer Model ZFM-150 | 6.952019732 |
| Aeroflex Phase Shifter Model 980 | 24.56293706 |
| 10' Belden Coaxial 50 Ohm Microwave Cable Model 1673A | 81.58277672 |

Table 3: Temperature Drift

# Development of a Navigator and Imaging Techniques for the Cryogenic Dark Matter Search Detectors

Chris Wilen

Office of Science, Science Undergraduate Laboratory Internship (SULI)

Carleton College

KIPAC SLAC National Accelerator Center

Menlo Park, CA

August 13, 2010

Prepared in partial fulfillment of the requirements of the Office of Science, Department of Energy's Science Undergraduate Laboratory Internship under the direction of Richard Partridge at the Stanford Linear Accelerator Center.

Participant: _____

Signature

Research Advisor: _____

Signature

Work supported in part by US Department of Energy contract DE-AC02-76SF00515.

# TABLE OF CONTENTS

# ABSTRACT

Development of a Navigator and Imaging Techniques for the Cryogenic Dark Matter Search Detectors. CHRIS WILEN (Carleton College, Northfield, MN 55057) RICHARD PARTRIDGE (Stanford Linear Accelerator Center, Stanford, CA 94025)

This project contributes to the detection of flaws in the germanium detectors for the Cryogenic Dark Matter Search (CDMS) experiment. Specifically, after imaging the detector surface with a precise imaging and measuring device, we developed software to stitch the resulting images together, applying any necessary rotations, offsets, and averaging, to produce a smooth image of the whole detector that can be used to detect flaws on the surface of the detector. These images were also tiled appropriately for the Google Maps API to use as a navigation tool, allowing viewers to smoothly zoom and pan across the detector surface. Automated defect identification can now be implemented, increasing the scalability of the germanium detector fabrication.

# INTRODUCTION

The effects of dark matter have been observed throughout the last century on astrophysical scales. Fritz Zwicky was the first to discover evidence of dark matter when he observed the Coma cluster of galaxies in 1933. By looking at the overall brightness of the cluster, and counting the galaxies, he was able to estimate how much mass was contained in the cluster. Observing the outer galaxies, however, Zwicky found his estimate did not match the mass given by Keplerian motion. The difference between the two estimates turned out to be almost 400 times[1], indicating the existence of this unseen mass was a significant result.

Since then, various theories such as modified gravity have been tested, but the one that held up most successfully was that astrophysical structures such as the Coma Cluster were filled with something massive but invisible to our detection methods, named dark matter. Many experiments searching for dark matter have been performed by looking at the movement of galaxies. Evidence for dark matter lies in our own spiral galaxy, which, when measuring the rotation curve by looking at the maximum redshift at different angles, levels out instead of dropping off as would be expected from the visible matter (Figure 1). Gravitational lensing also provides strong evidence for the existence of this invisible, "dark" matter, when light is bent more than it would be from visible matter.

Other observations give indications about the nature of dark matter. It often clusters around and throughout galaxies and other visible matter, so it clearly interacts with visible matter through gravity. Evidence suggests that the interaction with dark matter does not go much further than gravity. One of the strongest arguments for dark matter comes from the recent analysis of the Bullet Cluster (Figure 2). X-ray imaging shows two galaxy clusters colliding in the center, but gravitational lensing shows two concentrations of matter to either side, leading to the conclusion that the clumps of dark matter in each of the clusters went through each other with little interference. This gives strong evidence against modified

gravity theories, which cannot explain this effect[2]. Given dark matter's small cross section and the fact that it is unable to interact electromagnetically with photons, the limits of interaction can be narrowed to dark matter interacting with itself only through gravity and possibly the weak force.

Current estimates based on NASA and the Wilkinson Microwave Anisotropy Probe (WMAP) survey predict that the universe is made of roughly 4.6% atomic matter that we experience, 23% dark matter, and 72% dark energy[3, 4]. Dark matter is significant, making up 85% of matter, and yet we know little about its characteristics. The Cryogenic Dark Matter Search experiment aims to detect it directly on a much smaller, single particle scale, instead of looking only at its gravitational effects in large masses. Specifically we will be looking for interactions between a type of (non-baryonic) dark matter called Weakly Interacting Massive Particles (WIMPS) and atomic matter in germanium detectors.

Because dark matter does not interact electromagnetically, it is assumed to be constantly flowing through the matter around us, unnoticed by any current detectors. For a significant interaction to occur, the WIMPs have to hit the nucleus of the atoms themselves, transferring energy to the atom. For the detector in this experiment, we picked germanium over silicon and other more widely used options because of its high cross section (more area to interact with the dark matter and a higher density leads to a greater probability of detection). When a WIMP interacts with the a germanium nucleus, some energy is transferred to the germanium from the dark matter particle through nuclear recoil. This energy propagates through the germanium in the form of phonons (lattice vibrations) until it reaches patterns of Transition Edge Sensors (TES), located on either side of the germanium crystal.

When they enter the aluminum in these sensors, the phonons break apart some of the cooper pairs (the superconducting carriers), and the resulting quasiparticles are absorbed into a tungsten strip (Figure 3). The whole detector is kept at several milliKelvin, right on the edge of superconductivity for tungsten. As the resistivity of the tungsten changes due to

the quasiparticiles, a negative feedback loop reduces current through the tungsten to keep it at the same temperature. This change in current is measurable and recorded as a WIMP detection.

We needed to be able to distinguish dark matter detections from background radiation and decays of particles around the detector. When a charged particle or other ionizing radiation goes through the germanium, its electric field rips off electrons. By looking at the different signatures of charge build up on small electrodes patterned on surface of the detector, we were able to eliminate detections that looked like decays from atomic matter nearby or electron recoil, and minimize background.

The photolithography used for patterning these sensors on the germanium crystals is much more expensive and error-prone than similar processes for silicon. As a result, a method of reviewing the detectors in each stage of the patterning process, looking at them in detail, and finding errors needs to be established. I developed software to take images of the detector and piece them together into larger tiles that can be processed to find errors. I also created an online navigator to examine these images with.

## MATERIALS AND METHODS

We used a precise imaging and measuring device made by Optical Gauging Products (OGP) to help with the imaging process. Using several points on the detector, we established a coordinate system corresponding with that of the detector for the camera to move along. First, the z-value of three points was taken using adjustment of focus. With a plane representing the surface of the detector created using these points, we then defined the x and y axis, zeroed around a point in the center and lined up with the detector's vertical charge-detecting electrodes. Throughout the CDMS experiment, several detector patterns have been devised, so although the patterns being imaged varied, this procedure of setting up axes generally

worked. We then proceeded to take a series of images, each 640 pixels by 480 pixels, with a 20 pixel overlap, of the detector. This resulted in roughly ten thousand images per detector.

Once the detector had been imaged, the images needed to be compiled into a larger image that one can browse through easily and detect flaws. During this process, for which we used the Java programming language, we could account for small corrections to the imaging process, such as offset, overlap, and rotation (the rotation of the camera was not necessarily aligned with the coordinate system of the detector). Compiling all the images into a single large image took significantly more memory than most computers have, so they were arranged together into larger tiles, each several thousand pixels wide. Any overlap between images was saved as an average of the overlapped areas. Instead of rotating the individual images and putting them together, we rotated the coordinate system and kept the images in their own coordinate system to prevent loss of quality (Figure 4). Blank tiles were not written to save space and processing time.

In the stitching together of the images, we also implemented a technique known as flat field averaging, used to remove systematic variation in light intensity from a non-uniform light source. This procedure involves averaging several blank images (containing no features), and dividing every pixel by the average pixel value of the averaged image. This matrix can then be divided into all other images to remove systematic variations. In color images like the ones worked with here, this needs to be done separately for each color channel.

After the large composite images were created, a navigator needed to be created to view them for the purpose of finding hair-line fractures and other surface flaws. For this we used Ben Legler's image viewer[5] and the Google maps API[6] as a foundation. The Google API takes in many small image tiles and provides an interface through which the user can zoom, move, and measure distances. To make these small tiles we wrote a program to take the composite images created in the previous step and translate and scale them into smaller output tiles labeled correctly (`<zoom level>_<column>_<row>.<filetype>`) along with the

.txt file needed for the Google API.

Processing these images took a long time, so we implemented multi-core threading to split the program between multiple computers or cores. This was done by splitting the rows being processed into different groups for the different processors. As input, we gave the program the number of processes desired for the split, $N$, as well as which process is to be run by each call (thread number), $n$. The program then ran on the rows defined in the range given by:

$$ceil(\frac{n}{N}\lambda) < row < floor(\frac{n+1}{N}\lambda), \tag{1}$$

where $\lambda$ is the total number of rows of images produced. Empty tiles are deleted to save space and processing time.

## RESULTS

In short, the programs we wrote worked well, and produced a useful navigation tool. Each set of 8,000-9,000 images taken by the detector was stitched together with smooth looking interfaces that were barely noticeable. Everything was rotated and offset properly so lines and features going through the images matched to adjacent images with no breaks. The process took roughly an hour to complete on an average modern processor, resulting in almost 15 images per tile, of which there are about 650. Figure 5 shows an example tile of stitched images.

The tiling program took these programs and cut them into approximately 85,000 tiles that worked well with the Google API. The web interface to navigate and view the detectors was easy to use and has proven an excellent tool for examining the detectors. The zoom and pan was smooth and loaded fast, and the additional tools such as the ruler worked perfectly. The tile creation process took around ten to thirteen total run hours, which was

split between two cores. A sample interface can be seen at `http://www.slac.stanford.edu/exp/cdms/CDMS_ImageNavigatorII/IZipG47_Side1_TES/`.

The flat field averaging had a drastic effect on the smoothness seen across the images. Figure 5 shows the difference between tiles where flat field averaging was implemented and where it was not. Because the brightness varied across each image, the lines where the images were stitched together can be clearly seen. In the image where flat fielding is implemented, the systematic lighting differences were taken out and the resulting composite image is smooth and seamless.

## DISCUSSION AND CONCLUSIONS

Although the programs worked well in their purpose, the image sets are large and it took many hours to process them. As the program has to be run after every imaging, improvements in speed would be exceptionally valuable. In the future the results from these programs can also be integrated with software for detecting flaws. For example, software could be written to compare the stitched images to the corresponding sections of the template using a threshold to match the colors. Any differences, where flaws are most likely to be, could then be highlighted and overlaid on the detector using the navigator so one can easily see where flaws and corrections are. This flaw detection is crucial to the overall workings of the detector. The detector needs to be as accurate and precise as possible to isolate dark matter detections from background. Determining flaws in the detectors and making any possible repairs to these areas is an important part of the experiment. Currently the detectors need to be completely examined by hand after each step in the photolithography process. Using automated detection of flaws would allow people to only examine the necessary small areas, resulting in an increase in production speed and scalability of detector fabrication. With 100 or more detectors to be fabricated, this will have a drastic effect on the timing of the

experiment.

## ACKNOWLEDGMENTS

I would like to thank Richard Partridge as my primary mentor throughout the process. Thanks is also due to Rudy Resch and the rest of the CDMS group for advice and suggestions, as well as SLAC National Accelerator Laboratory and the United States Department of Energy for making this experience possible.

## APPENDIX

The input.txt file contains parameters needed to run the programs. Comments can be set using the pound symbol (#). Below are listed the parameters used by the programs. Each parameter should be stated on a new line, with the name of the parameter separated from its value by a tab.

`image_path` The directory path where all the images taken with the OGP are stored.

`save_path` The path to the directory in which all the folders described below reside, including web files.

`autorun_file` The name of the autorun file (which should be in the image_path) which created the images.

`image_name` The name of the image files, with the number of the image replaced by a modulus (%).

`theta` The angle between the coordinate systems of the camera and the detector, in radians.

`pixel_size` The metric length in mm of each pixel. For a x75.3 magnification, this is 5.452um, and for x293 magnification, it is 1.397um.

`blanks` The numbers of the blank images used for the FF averaging, separated by commas.

`tile_width` The width of each composite tile created.

`tile_height` The height of each composite tile created.

There is a precise file structure that should be followed for running Stitcher.java and Tiler.java. Although the image files and the autorun file from the OGP can be stored anywhere, as long as they are in the directory specified by `image_path`, the following files should be included in the `save_path` directory:

`index.htm` The html file that creates the online navigator.

`input.txt` The input file where the parameters above are defined by the user.

`resources` This folder contains the files needed for the navigator, and should not be edited unless to change the interface.

`stitched_images` Images created by Stitcher will be saved here.

`tiles` The tiles created by Tiler for the Google API will be saved to this folder.

# REFERENCES


[1] F. Zwicky, "Spectral displacement of extra galactic nebulae," *Helv. Phys. Acta, 6*, pp. 110–127, 1933.

[2] D. Clowe *et al.*, "A direct empirical proof of the existence of dark matter." *Astrophysics Journal*, 2006.

[3] J. P. Filippini, "A search for wimp dark matter using the first five-tower run of the cryogenic dark matter search," Ph.D. dissertation, (University of California, Berkeley), 2008.

[4] S. W. Leman, "Developement of phonon-mediated transition-edge-sensor x-ray detectors for use in astronomy," Ph.D. dissertation, Stanford University, September 2006.

[5] B. Legler. Gmap image viewer. http://www.rmh.uwyo.edu/gmapviewer/about.php.

[6] Google maps javascript api. http://code.google.com/apis/maps/documentation/javascript/.

[7] (2008, August) The matter of the bullet cluster. http://apod.nasa.gov/apod/ap080823.html.

[8] NASA/CXC/M.Weiss. 4-panel illustrations of cluster collisions. http://chandra.harvard.edu/photo/2006/1e0657/more.html.

# FIGURES

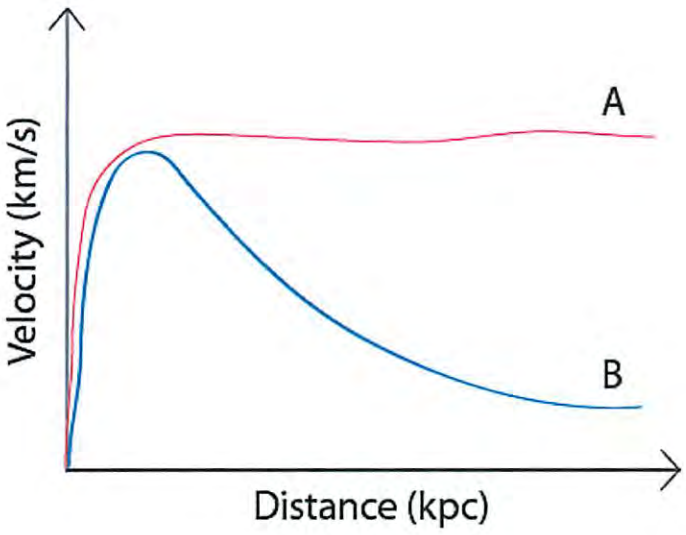


Figure 1: An illustration of the expected and measured rotation curves of the galaxy, showing the average velocity of matter as a function of distance from the center of the galaxy. Assuming Keplerian motion, and the fact that visible matter is concentrated at the center of the galaxy, we would expect rotational velocity to decrease with radius (curve B). The measured relationship (curve A) suggests that a large source of non-light-emitting matter exists in the galaxy or that Newtonian mechanics has flaws.

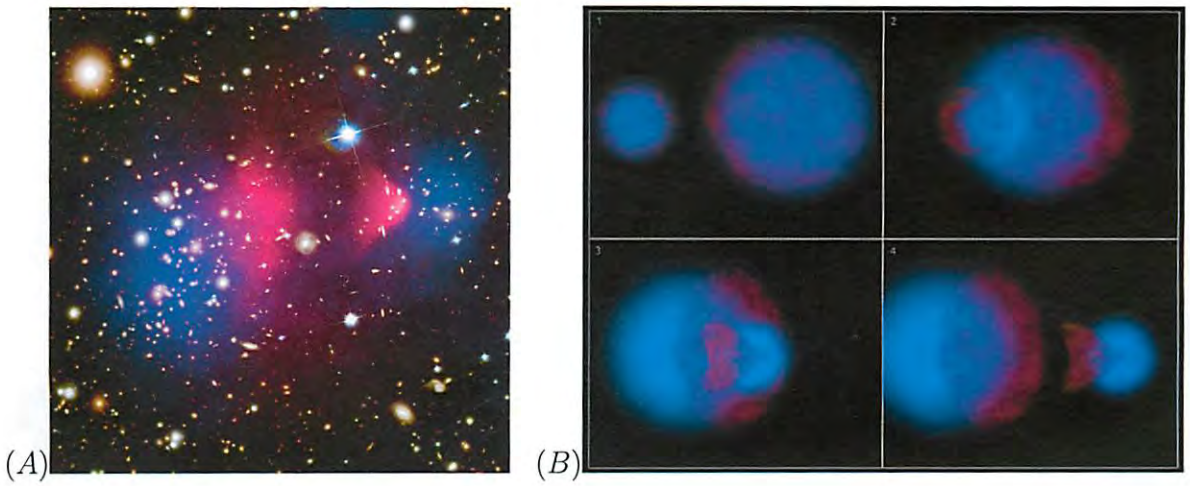

Figure 2: (A) An image of the bullet cluster taken with the Hubble telescope, with an overlay showing the calculated mass distribution in blue.[7] (B) Computer simulations show that a model with weakly interacting dark matter closely match what we see.[8]

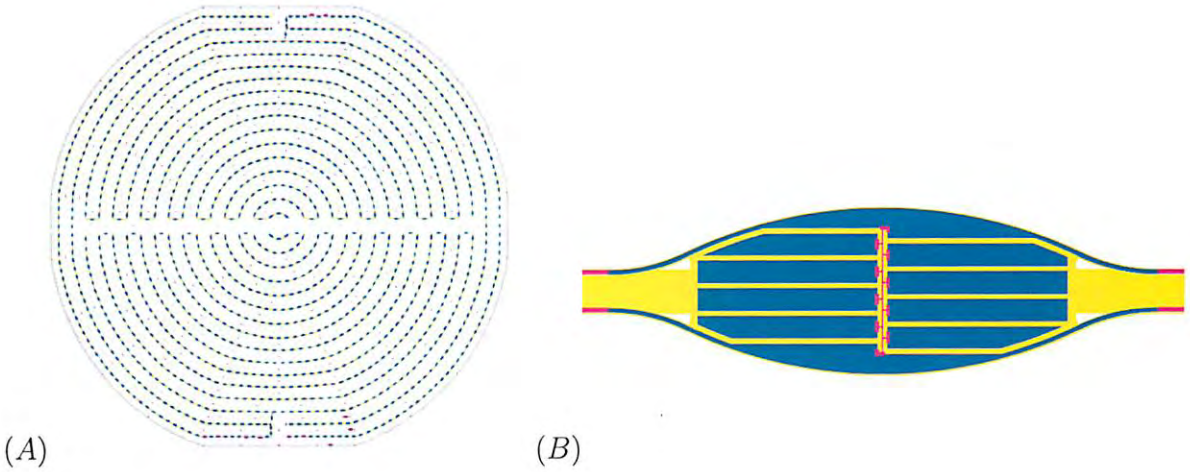

Figure 3: (A) The ends of the spherical germanium detector have nodes arranged in four areas (top, bottom, and two outer) to help with triangulation of the phonons they detect. (B) Phonons break the cooper pairs in the aluminum (blue), which cause a measurable change in current through the tungsten (pink).

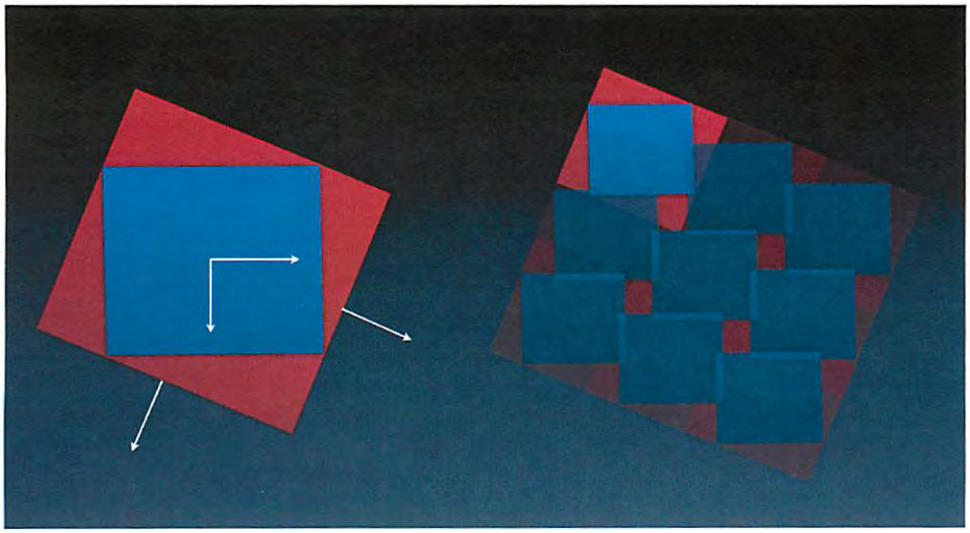

Figure 4: Instead of rotating each image (blue) within the reference frame of the detector (red), we rotated the reference frame of the detector to prevent loss of quality.

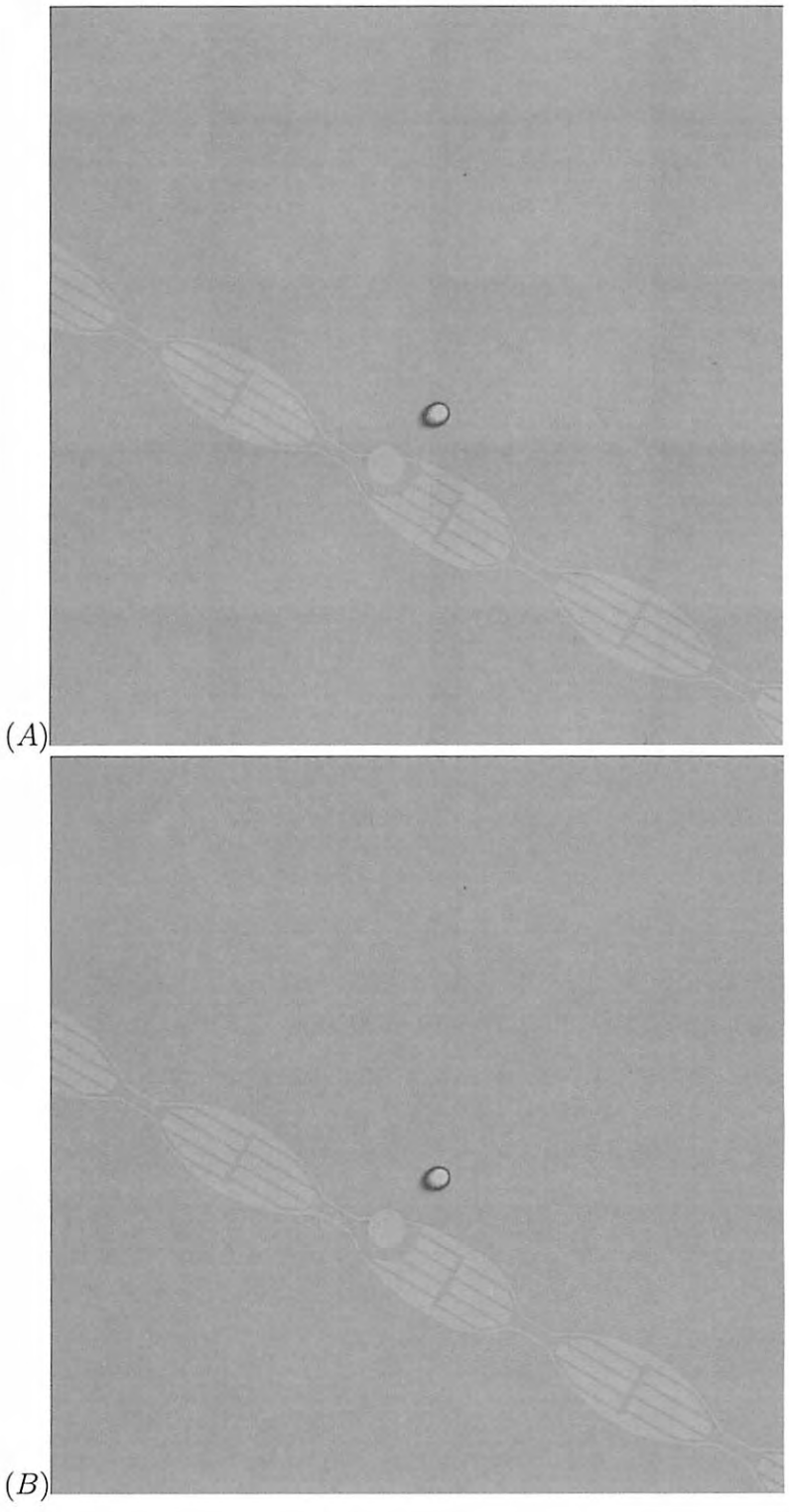


Figure 5: (A) These images of the detector were put together without flat field averaging. The seams where they were stitched together are visible because of the variation in lighting across the image. (B) Using flat fielding, these systematic variations can be removed, creating a much smoother looking image. Note: the difference in contrast is not caused by the flat fielding.

# Feasibility of Close-Range Photogrammetric Models for Geographic Information System

Luke Zhou

Office of Science, Science Undergraduate Laboratory Internship Program

Rice University

SLAC National Accelerator Laboratory

Menlo Park, California

August 13, 2010

Prepared in partial fulfillment of the requirement of the Office of Science, Department of Energy's Science Undergraduate Laboratory Internship under the direction of Brian C. Fuss and Catherine M. LeCocq in the Metrology Department's Alignment Engineering Group at SLAC National Accelerator Laboratory.

Participant: _____
Signature

Research Advisors: _____
Signature

Work supported in part by US Department of Energy contract DE-AC02-76SF00515.

**TABLE OF CONTENTS**

**ABSTRACT**

Using Close-Range Photogrammetry to Create 3D Models of As-Built Structures.
LUKE ZHOU (Rice University, Houston, TX 77005), BRIAN C. FUSS and CATHERINE M. LECOCQ (SLAC National Accelerator Laboratory, Menlo Park, CA 94025).

The objective of this project was to determine the feasibility of using close-range architectural photogrammetry as an alternative three dimensional modeling technique in order to place the digital models in a geographic information system (GIS) at SLAC. With the available equipment and Australis photogrammetry software, the creation of full and accurate models of an example building, Building 281 on SLAC campus, was attempted. After conducting several equipment tests to determine the precision achievable, a complete photogrammetric survey was attempted. The dimensions of the resulting models were then compared against the true dimensions of the building. A complete building model was not evidenced to be obtainable using the current equipment and software. This failure was likely attributable to the limits of the software rather than the precision of the physical equipment. However, partial models of the building were shown to be accurate and determined to still be usable in a GIS. With further development of the photogrammetric software and survey procedure, the desired generation of a complete three dimensional model is likely still feasible.

## INTRODUCTION

Photogrammetry is a method by which images of an object are analyzed to allow for an indirect approach to measuring the size, shape, and position of the object [1]. Combining photogrammetric principles with a computer graphics process makes the construction of accurate three dimensional models of the object possible [1]. This can be done by extracting the 3D coordinates from a set of photographic images taken from all around the object using a photogrammetric software package.

The focus of this project was to test the feasibility of using photogrammetry in the Metrology Department at SLAC National Accelerator Laboratory for the purpose of measuring the dimensions of buildings on the campus to add three dimensional models of the buildings to the SLAC geographic information system (GIS). The GIS will be used to answer geographic queries about various building, utilities and experimental apparatuses within the building. To create a correct base map of SLAC campus, accurate models of the buildings are necessary.

When used in architectural applications such as the GIS, photogrammetry has several practical benefits over the more traditional measuring and computer modeling approaches. As a result of the digital nature of the images taken, photogrammetry allows for a large amount of dimensional data to be quickly recorded and later accessed in a few images. A digital model can then be directly generated from the photogrammetric data stored in the images. In contrast, in order to generate a computer model from scratch, numerous measurements of a building's details would need to be made to model even the simplest of buildings. The surveyor would need to spend large amounts of time at the site of the building and possibly be required to set up cumbersome scaffolding equipment. Given a photogrammetric model, no measurements need to

be made beforehand. In fact, the model can be used if measurements are needed for other purposes.

## METHODS

### *i. Equipment*

In order to conduct a photogrammetric survey of any object, there are three required components: a camera, a targeting system, and photogrammetry software. In short form, a survey can be conducted in three steps. The targets are first placed around an object. Then, a calibrated camera is used to takes photographs of the targets from various angles and positions. Finally, the photographs are used as input data for the photogrammetric software that links the targets appearing in multiple photos to construct a cohesive 3D model.

A modified Nikon D300, shown in Figure 1, was used for this project. All of its internal components are locked into place and functions which would require an inherently unstable lens configuration, such as zoom and autofocus [2], are disabled. The lens and camera were selected to limit the distortion in the images due to the lens and ensure the flatness and regularity of the charged coupled device in the camera [2]. Although amateur cameras are coming into more widespread use [3], for the greatest precision, a metric camera like the modified D300 is preferred. A metric camera gives the advantage of an unchanging geometric configuration of the camera and lens system and thus a known interior orientation [2]. For a non-metric camera, it would be necessary to calibrate the camera before each survey to determine the various distortion parameters (radial, decentering and linear) in the camera and lens. Alternatively, the known parameters of a metric camera can simply be saved and reused between projects.

The bulk of the targets that were used in the photogrammetric survey consist of circular, red (set against a black background), retroreflective targets placed on or around the desired

object. The variety of targets used is shown in Figure 2. These targets allow the photogrammetric software to quickly pinpoint the location of each target in the photographs within 0.2 inches on average. Within the network of the targets, the position of an object's features can be then established. Previous data shows that the Nikon D300 can obtain greater precision, to within one hundred microns [4], but in the context of a building which has dimensions of several tens of feet, within an inch of precision is acceptable. The shape, color, and retroreflective properties of the targets were specifically selected in order to easily pinpoint the centroid of the targets. It is expected that this pinpointing is possible at camera positions that can view the target at an angle of up to 60 degrees off the central axis of the camera. That is, in Figure 3, the target point M is located at an angle *i* of less than 60 degrees from the Z axis corresponding to the camera axis. Beyond this point, even though the targets may still be seen in the photographs, their reflective property diminishes, resulting in a loss of accuracy.

Australis is a photogrammetry program that was designed to allow for automatic measurements of a targeted object. The software scans each image for retroreflective targets. Some of the targets used have a series of red, reflective dots arranged in a particular pattern, or code, which allows for Australis to recognize identically coded targets in multiple pictures and automatically start creating a 3D target network as shown in Figure 4. Comparatively, without the coded targets, the single red dots would be indistinguishable from each other and would have to be manually referenced between images. With the coded targets, however, the position of the single targets can also be accurately and automatically located in relation to the position of the coded targets, creating a denser target network than would be allowed by the number of coded targets alone. In addition to this network of reflective targets, Australis also allows for the manual marking of feature points and lines (e.g., corners, doors, windows) on the building itself.

Similar to the determination of the single reflective targets' locations, the building features' positions are accurately found within the realm of the dense 3D target network.

*ii. Survey Process*

Once the appropriate materials had been obtained, the photogrammetric survey could be carried out. As an example to study the practicality of photogrammetric modeling, Building 281 on SLAC campus was selected for this survey. The survey was taken in three major phases: camera calibration, survey planning and setup, and modeling in Australis.

Although the camera calibration step can be excluded in later surveys due to the metric nature of the Nikon D300 used, it was necessary to conduct an initial calibration for this preliminary study. The calibration was carried out by placing a large and dense network of retroreflective targets on a flat wall. Images were then taken of the target-covered wall using the camera from various heights, positions and orientations. This process was conducted in the dark so that the only significant light source was from the flash of the camera. By running a set of about 25 images of the calibration wall through Australis, the calibration parameters of the camera were determined. The results of repeat tests were in agreement, giving confirmation of the metric nature of the camera. The parameters that were used for the duration of this study are listed in Table 1.

The next phase was the actually planning and conducting of the photogrammetric survey. After various attempts, a reliable process using the available equipment was determined. A minimalistic approach was taken in an attempt to design a survey would be worth the time and effort compared to the traditional approaches to measuring buildings. To begin, the targets were placed. Initially, a scattering of single red, reflective targets was placed on the building to create a network. A higher density of targets was devoted to the corners of the building in order to

reinforce the connection of the two facades forming the corner. The coded targets were then placed. As with the single targets, less emphasis was placed on the long flat sections of the walls compared to more complex areas. To further strengthen the recognition of the corners in the later Australis modeling phase, several targets were placed in the foreground surrounding the building corners. These targets were able to rotate so that the centroids of the targets remained at the exact same coordinates. Without these targets placed around the building, it would have been difficult to angle the camera so that adequate light was able to reflect off of targets on both walls at the corners and thus connect the target networks on each wall. The final set of targets placed were the scale bars that were manufactured such that the centroids of the targets on either end were exactly 30 inches apart (measurable to within 0.02 inches [5]). These scale bars gave the digital 3D model the correct scale in its dimensions. A vertical and a horizontal scale bar were placed on each major wall of the building. An example of a complete target network setup is shown in Figure 5.

One common issue with architectural photogrammetry arises from the presence of obstructions such as trees or other buildings that may block the visibility of the targets and features of the desired building. In the case of Building 281 in this study, the primary concern was the close proximity of another building that limited the distance at which images could be taken and therefore what could be seen by the camera in each image. Various constraints such as this had to be taken into account to determine proper camera positioning for the entire survey before any images could be taken. No set of equations exists to solve every condition that may be faced in any given architectural survey; however, guidelines can be established for the majority of the situations that may be faced. The “3x3” rules for architectural photogrammetry given by [6] can adequately serve such a purpose with some modification and additions made with the

available equipment in mind. In particular, care must be taken to ensure the appearance of key building features in at least three or more convergent images, and photographs must be taken in a ring of positions surrounding the building. These photographs must also be taken from varying heights, with enough overlap so that all targets on and off the building appear in two or more shots. Although more images would likely provide more redundancy and therefore more precision, it would also require more analysis in Australis.

Once the photographs are taken appropriately, the creation of the 3D model in Australis is relatively straightforward. The autoreferencing function in the program can create the basis for the 3D model by recognition of the coded targets. A wireframe of the building can then be generated within the context of the reflective target network by manually marking the building's feature points in multiple images.

*iii. Feasibility Determination*

There were two equally important primary objectives to this project. The first aim was simply to create a three dimensional wireframe model to show that it was possible with the available equipment and software. Once such a model was generated, the next goal was to determine if it is reasonably accurate so that the photogrammetric survey could serve as a replacement for traditional hand surveying and modeling methods. If a 3D photogrammetric model were to be generated but provided inaccurate data, then it would be of little use.

Achievement of the first goal is easily checkable by merely conducting the photogrammetric survey and attempting to model with it in Australis. Most of the equipment and the Australis software can be tested with several simple surveys. The visibility of the targets was checked by placing the targets as would be done in a normal full building survey. Then, several photographs can be taken from various angles to establish the angles from which the targets are

identifiable by Australis. A separate set of surveys is, however, necessary for the rotating targets. Rotating targets were used because they can be seen at any angle by being turned to face the camera. However, a test was conducted to ensure that while rotating, the targets maintained the same centroid position. First, a survey was taken of a façade with the normal distribution of coded and point targets placed on it while the rotating targets were spread out in front facing parallel to the wall. Then, two similar surveys were conducted with half of the targets rotated by 45 degrees to either the left or right. After running the images through Australis and setting the same coordinate system based off non-moving point targets on the wall, the positions of all of the points in the survey, including the rotating targets, were compared between the three similar surveys.

The final test of the equipment and Australis was to plan out and conduct a full survey of a building to ascertain whether or not the use of photogrammetry for the generation of a 3D model was a viable and practical approach. Not only was it necessary to find out if the creation of the model was achievable, but also if the model outputted would be accurate enough to serve as an alternative modeling technique for placement in the GIS.

Although Australis does give results on the precision of the target locations by outputting standard errors and root mean squares, to determine the accuracy of the model, it is necessary to still perform a hand survey with a tape measure to obtain the real measurements. Measurements from both the photogrammetric model and the hand survey must be within one inch of agreement to sufficiently demonstrate that the photogrammetric model is valid and accurate.

## RESULTS

*i. Equipment and Software Testing*

Most of the targets were shown to be easily recognizable in Australis at angles up to 60 degrees off the camera axis. Using nine total rotating targets, the standard deviation of the XYZ coordinates of the 5 rotated targets was comparable to the other 193 targets used in the survey as shown in Table 2.

The construction of a complete three dimensional model from a photogrammetric survey of Building 281 was not shown to be easily achievable. After the photographs were taken, Australis was only able to automatically recognize the target network on the first wall. Even with the rotating targets, Australis was simply unable to automatically recognize the sharp corners. From the meager automatically generated model, it required an additional hour to manually reference points between photographs to create a coherent 3D model of the target network shown in Figure 6. However, bearing in mind alternative methods of computer modeling and the accuracy given by this photogrammetric method, this can still be considered to be a fairly rapid process. Once this initial model was created, marking the feature points of the building to generate the actual building model was attempted. About two of the walls were successfully modeled and are shown in Figure 7. However, as the process continued to the third wall, errors began appearing in points that Australis had already previously established in the model. Quickly, the errors caused Australis to deconstruct the model it had originally created as shown in Figure 8. The minor imprecisions associated with the manual marking of hundreds of points in the 3D model seemed to stretch Australis beyond what it was capable of calculating in a reasonable number of iterations.

*ii. Photogrammetry as a Replacement for Traditional Methods*

Despite its inability to create a three dimensional model of the entire building, Australis still seemed able to generate models of the walls separately without excessive difficulty. These partial models can still be used in a GIS if each wall were individually placed at the correct coordinates. Therefore, it was still worthwhile to assess the accuracy of the dimensions from the partial photogrammetric models.

Using a photogrammetrically-generated wireframe model of two exterior walls faces, shown in Figure 7, an error assessment was conducted to compare the dimensions of the photogrammetric model against the true dimensions of the building.

The results shown in Table 3 will show that the photogrammetric model's measurements are within the desired inch of accuracy. However, as a result of the imprecise marking of the building's feature points, the average standard error, as calculated by Australis, is on the range of several feet. As shown in Table 4, some points display a standard error of up to 35 feet, which is greater than some of the dimensions of the building. At best, the standard error of the coordinates is 2.388 inches. Comparably, when given just the reflective target network, the average standard error was 0.144 inches.

**DISCUSSION**

With the current equipment and software available, it would not be recommended that photogrammetric surveys be conducted for the purpose of creating entire three dimensional models of buildings. The primary reason for this conclusion is the error prone nature of Australis when constructing the wireframe model. The current available method for photogrammetry requires a large amount of set up time before the survey is conducted. If only several quick measurements are necessary, then measurements by hand could often be taken with more ease. In

considering the software aspect, Australis is, at the moment, still far too error prone to be used for creating complete models.

However, because the partial 2-wall models were shown to be accurate, the partial models could instead be inserted into the GIS rather than the full model. Since each model is accurate to within an inch, if placed in the correct coordinates, the separate partial models should line up to create a full model. There is still some concern with the calculated standard errors of many of the coordinates; however, this was not shown to have any bearing on the accuracy of the model. Most likely, these standard errors simply prevent the creation of the full model at this point.

Future work on this project would include further attempts to tweak the positioning of targets and camera positions in a way that would allow Australis to automatically recognize the corner. This project showed that Australis is capable of modeling corners. It is hoped that some survey setup will allow the program to accomplish this automatically.

The eventual goal still remains the same, to model the entirety of a building's exteriors in three dimensions. In due course, the interiors can also be modeled similarly. However, it is likely that the capabilities of the Australis software will need further work before this even the modeling of the exteriors can be effectively and reliably achieved.

**ACKNOWLEDGEMENTS**

I would like to thank the Department of Energy and the SLAC National Accelerator Laboratory for funding and hosting the SULI program and this project. Special thanks is given to my mentors, Catherine LeCocq and Brian Fuss, for their guidance and knowledge throughout the duration of the project. I would also like to thank all of the SULI students and staff at SLAC for their support.

## REFERENCES


[1] M.A.R. Cooper and S. Robson, "Theory of close range photogrammetry," in Close Range Photogrammetry and Machine Vision, K.B. Atkinson, Ed., Latheronwheel, Scotland: Whittles, 1996.

[2] J.G. Fryer, "Camera calibration," in Close Range Photogrammetry and Machine Vision, K.B. Atkinson, Ed., Latheronwheel, Scotland: Whittles, 1996.

[3] T. Luhmann, S. Robson, S. Kyle, and I. Harley, Close Range Photogrammetry: Principles, Techniques and Applications, Dunbeath, Scotland: Whittles, 2006.

[4] C.M. LeCocq, Internal Notes, SLAC, 2010.

[5] "iWitnessPRO Scale Bars," [Online document], [2010 Aug 6], Available at HTTP: http://www.iwitnessphoto.com/products/scale_bar.html

[6] P. Waldhäusl and C. Ogleby, "3 x 3 rules for simple photogrammetric documentation of architecture," International Archives of Photogrammetry and Remote Sensing, vol. XXX, part 5, pp. 426–429, 1994.


## FIGURES


**Figure 1 Modified Nikon D300. Several external and internal modifications were made to hold moving parts in place to create a metric camera.**

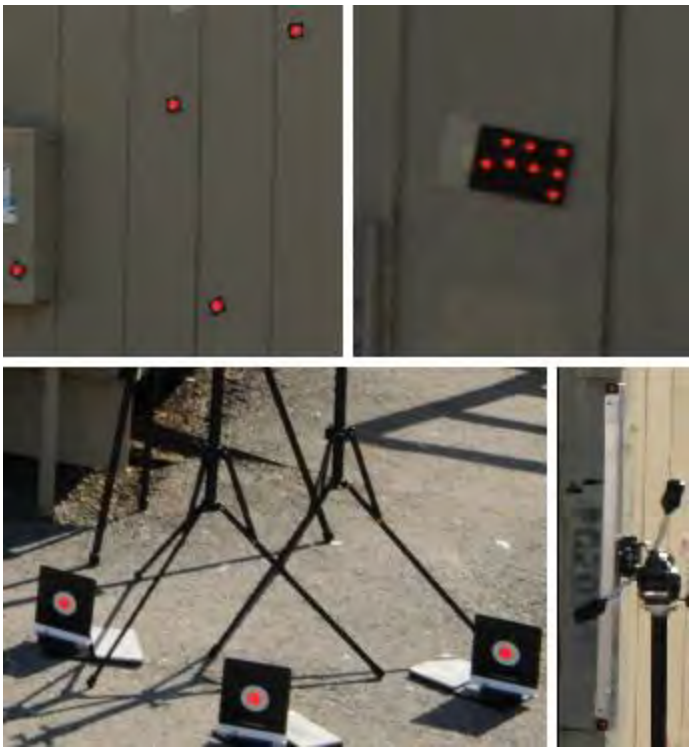

**Figure 2 Single circular targets (upper left) are quickly constructed and used to create a dense network. Coded targets (upper right) have a unique pattern recognizable to Australis. Rotating targets (bottom left) can be turned to be viewed at any camera position while maintaining the same centroid position. Scale bars (bottom right) are 30 inches long to give the entire model proper dimensions.**

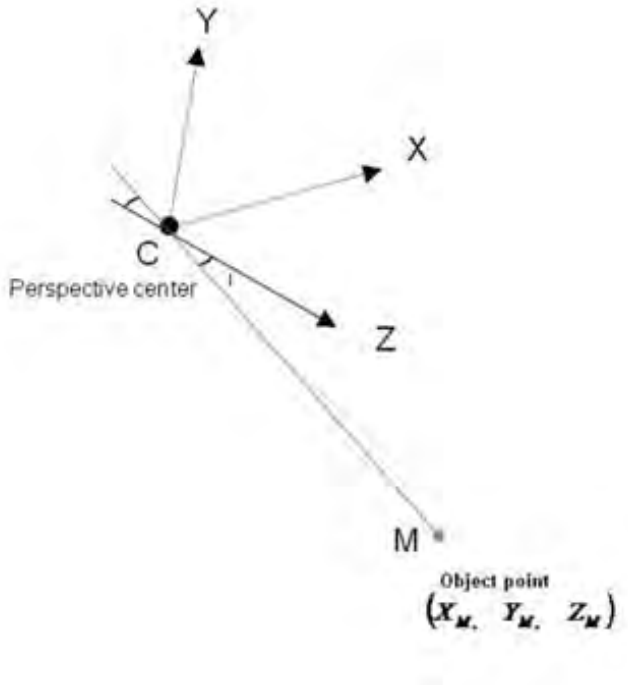


**Figure 3 The Z axis is the central axis of the camera. The XY plane represents the plane of the camer. Object points M at an angle i of less than 60 degrees from the Z axis reflect enough light to view in Australis.**

**METRIC CALIBRATION PARAMETERS**

Resolution = 4288 x 2848 pixels

Pixel width = 0.0055mm, Pixel height = 0.0055mm

| | VALUE | STANDARD ERROR |
|---|---|---|
| Principal distance | c = 18.4801mm | 0.000mm |
| Principal point offset in x-image coordinate | xp = -0.0744mm | 0.000mm |
| Principal point offset in y-image coordinate | yp = 0.0302mm | 0.000mm |
| 3rd-order term of radial distortion correction | K1 = 5.16825e-004 | 2.0104e-007 |
| 5th-order term of radial distortion correction | K2 = -9.97129e-007 | 2.6226e-009 |
| 7th-order term of radial distortion correction | K3 = -2.19117e-009 | 1.0396e-011 |
| Coefficient of decentering distortion | P1 = 4.0131e-005 | 2.048e-007 |
| Coefficient of decentering distortion | P2 = -1.3860e-005 | 1.922e-007 |
| Differential scaling between x & y | B1 = 1.6930e-004 | 1.820e-006 |
| Non-orthogonality between x & y axes | B2 = 6.6916e-005 | 1.846e-006 |

**Table 1 Calibration parameters of the metrically modified Nikon D300.**

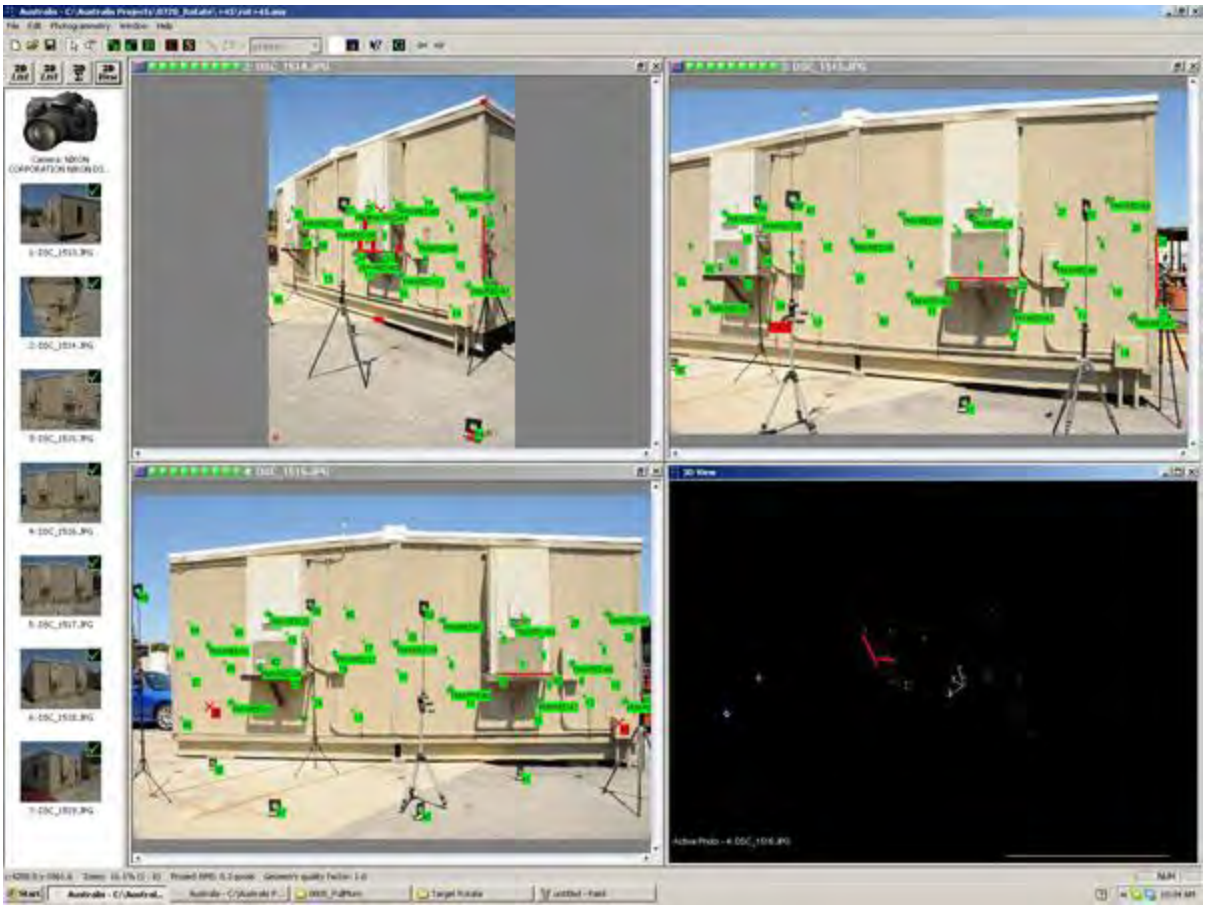

**Figure 2 Matching targets are identified from multiple camera positions to create a 3D target network**

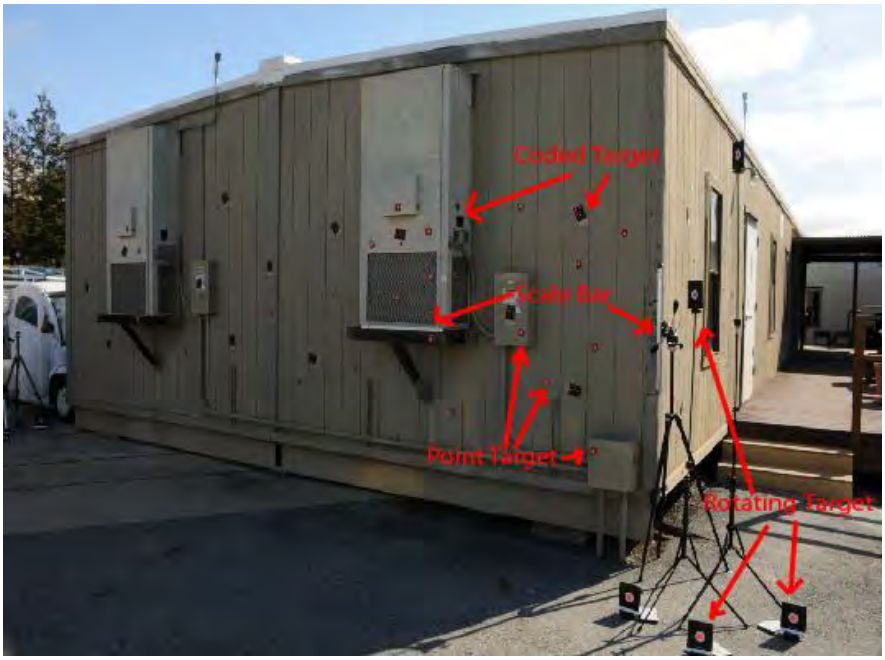


**Figure 3 Complete target network on a façade.**

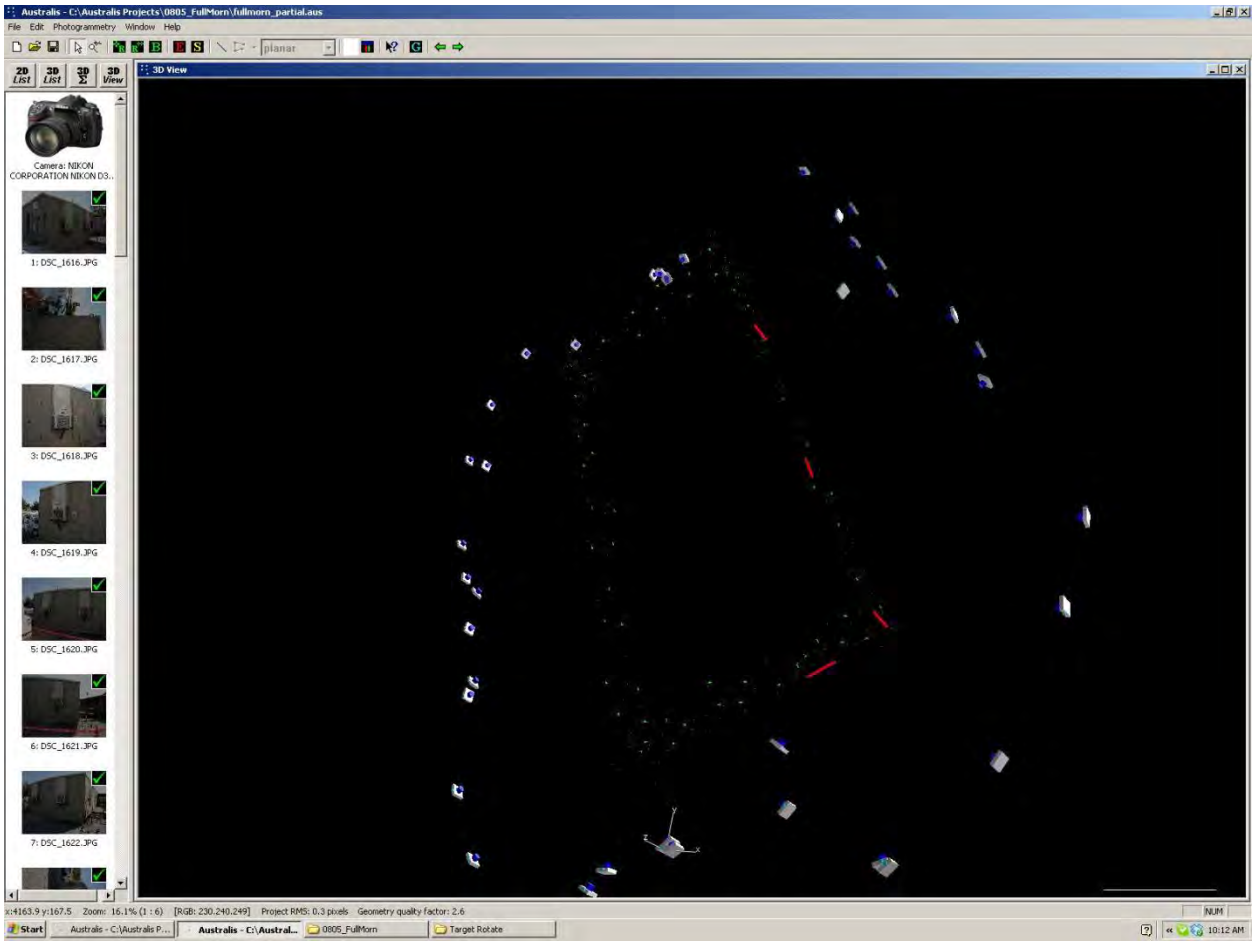


**Figure 4 Three dimensional target network on Building 283 photogrammetrically generated in Australis.**

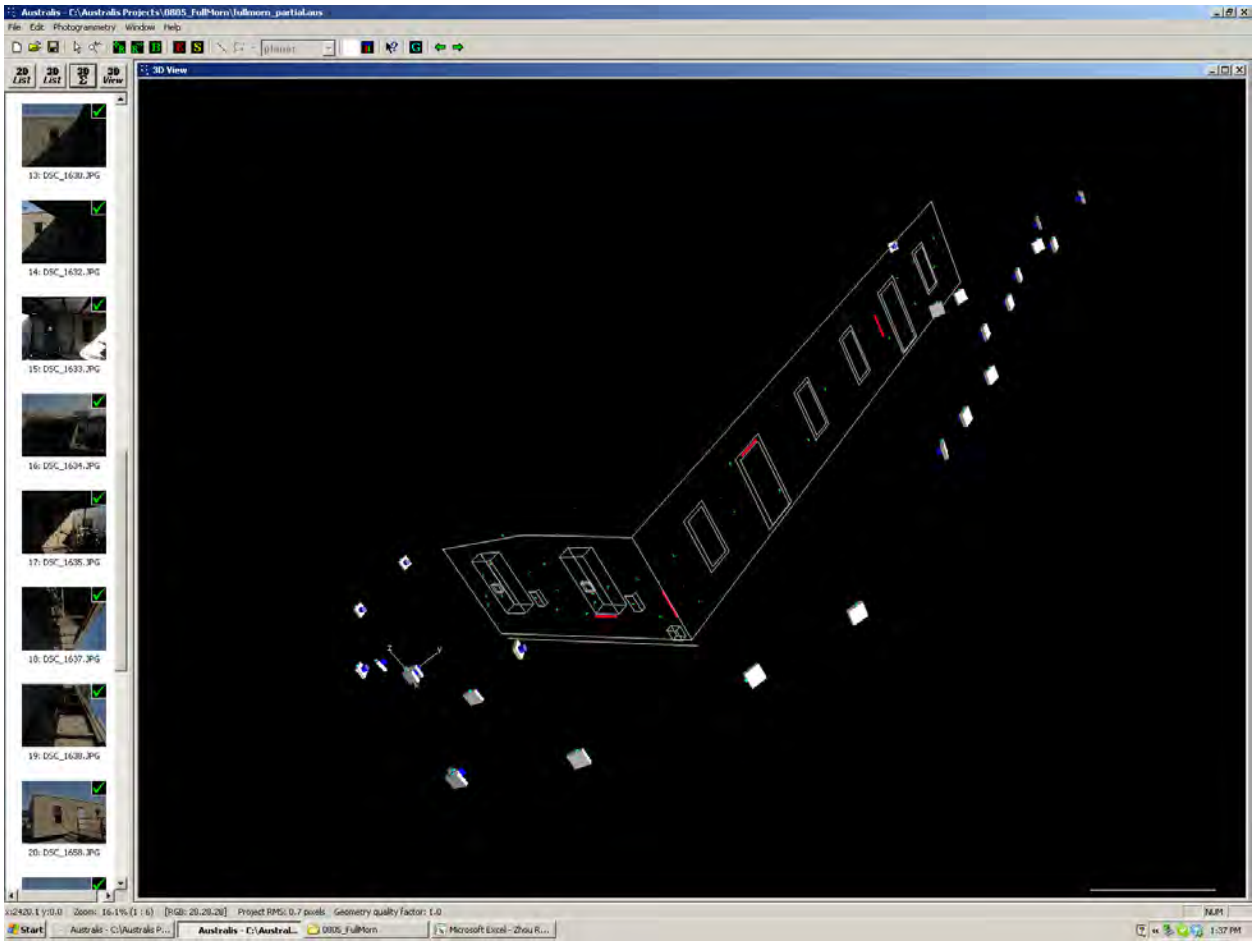


**Figure 5 Photogrammetric 3D wireframe model of two exterior wall of SLAC Building 281.**

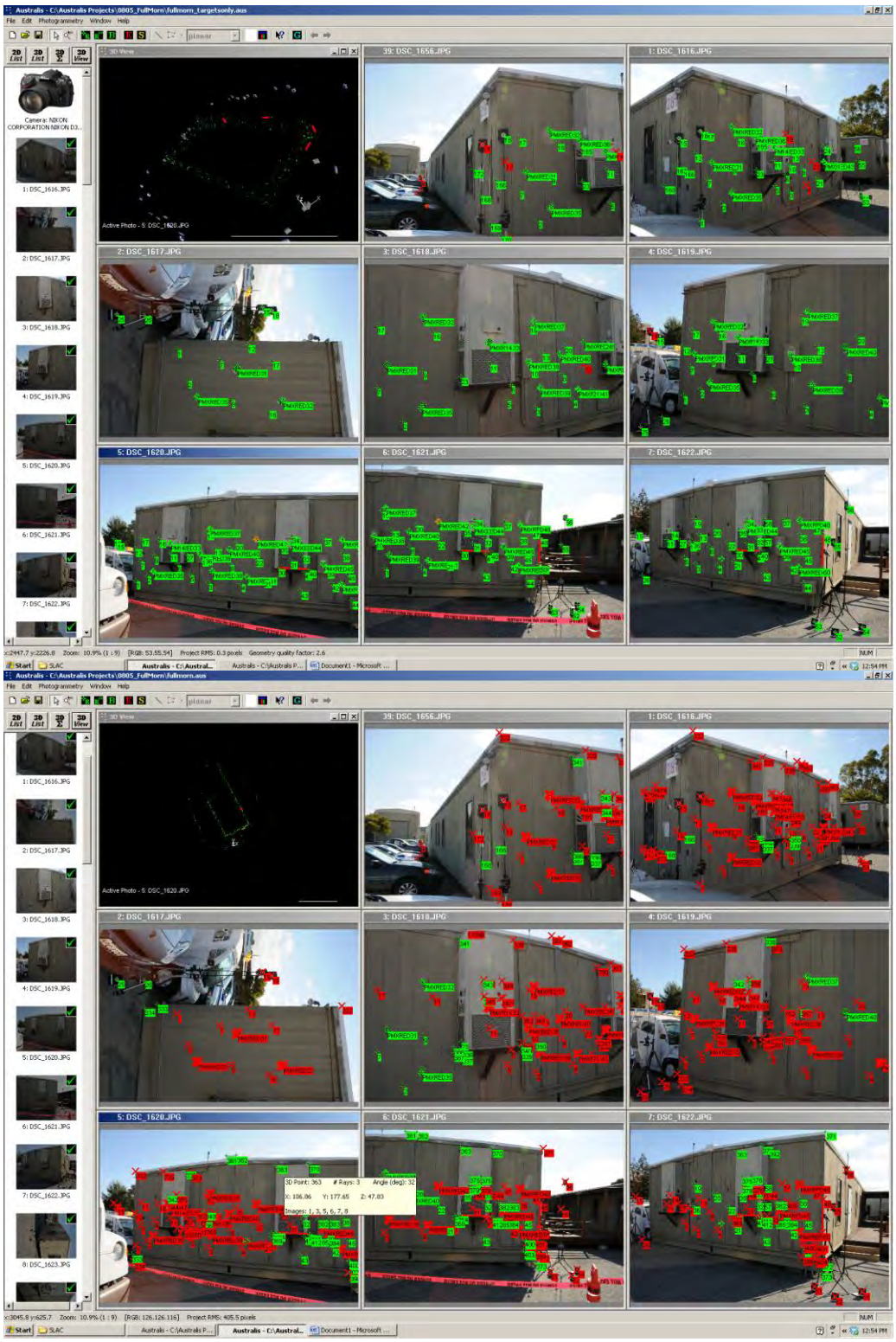

**Figure 6 Although Australis has accurately established the a target network for all four exterior walls in the upper screenshot, as more feature points are marked, Australis is no longer able to calculate the position of many of the originally established points. The digital model is deconstructed and the work is irretrievable.**

| | Standard Deviations (inches) | | |
|---|---|---|---|
| | Average | Minimum | Maximum |
| Rotating Targets | 0.45 | 0.39 | 0.5 |
| Other Targets | 0.39 | 0 | 1.02 |

**Table 2 Standard deviations of the positions of the 5 rotating targets in comparison to the standard deviations of the positions of the 193 stationary targets in a series of photogrammetric surveys of a façade.**

| | Average | Minimum | Maximum |
|---|---|---|---|
| Difference (inches) | 0.22 | 0.0285 | 0.9636 |
| % error | 0.72% | 0.01% | 2.50% |

**Table 3 Differences between 35 actual measurements from hand survey with tape measure and photogrammetric measurements from 3D model.**

| | Standard Errors (inches) | | |
|---|---|---|---|
| | Average | Minimum | Maximum |
| Targets Only | 0.144 | 0.039 | 0.605 |
| With Features | 19.927 | 2.388 | 426.901 |

**Table 4 Standard error, as calculated by Australis, in the position of the points with targets only, as shown in Figure 6, and then with feature points, as shown in Figure 7.**